The synthesis and modification of multi-walled carbon nanotubes (MWCNTs), and their use in dye-sensitized solar cells (DSSCs).

William Katlego Mokone

A thesis submitted to the Faculty of Science.
University of the Witwatersrand
Johannesburg.
In fulfilment for the requirements of the Doctor of Philosophy degree.

Supervisors:

Dr Zikhona Tetana

Prof Neil Coville

Prof Daniel Wamwangi



WITS
UNIVERSITY

May 2023

Declaration.

I **William Katlego Mokone** declare that the work (never been submitted to any other university for any other degree) presented in this thesis for a *Doctor of Philosophy* degree to the University of the Witwatersrand is my own and was performed under the supervision of Dr Zikhona Tetana, Prof Neil Coville and Prof Daniel Wamwangi.



2023

Abstract.

The global community has invested immensely in the research and development of solar, wind, nuclear technologies for energy generation and storage due to the adverse consequences of (i.e., environmental) using fossil fuels for energy generation. Solar energy remains the most viable sources of sustainable and renewable energy and it has led to an explosion in the development of solar technologies such as photovoltaic cells (PVCs). The 3rd generation PVCs, dye Sensitized Solar Cells (DSSCs), have received a lot of attention due to their ease of fabrication, chemical versatility, bidirectional optical absorption energy and structural tunability, low cost and environmental friendliness. The Pt counter electrode (Pt-CE) of the device and alternatives to it have been extensively investigated. Despite having 'good' chemical stability, excellent catalytic activity low sheet resistance and high conductivity, it has relatively high production costs and is susceptible to poisoning by the electrolyte. Multi-walled carbon nanotubes (MWCNTs) and their corresponding heteroatom doped MWCNTs have comparable and in some cases superior electrical and electrochemical properties to that of the Pt electrode. This work was aimed at investigating the synthesis, application of pristine and potentially heteroatom (N, B, P) doped MWCNTs and their corresponding thin films as alternatives to the Pt-CE in DSSCs.

MWCNTs were fabricated using a bimetallic Fe/Co supported on $CaCO_3$ catalyst under different reaction conditions using the chemical vapor deposition (CVD) method. Pristine MWCNTs were fabricated in two studies: (i) The influence of the fabrication method of the bimetallic catalyst. Two catalysts were synthesized under microwave irradiation at constant temperature (*Catalyst 1*) and constant power (*Catalyst 2*), and one under thermal heating (*Catalyst 3*). All three catalysts produced MWCNTs at 700℃ with different properties. (ii) *Catalyst 1* was utilized to investigate the effects of temperature (700, 750, 800℃) in the production of MWCNTs.

The attempted synthesis of heteroatom doped MWCNTs using *Catalyst 1* was performed using two different boron sources (trimethyl borate and tri-isopropyl borate) at: (i) different reaction times (15, 30, 60 min) at 800℃. Trimethyl borate successfully produced MWCNTs with boron in their lattice structure at a reaction time of 15 (0.31%) and 60 min (0.99%). Tri-isopropyl borate failed to add boron to the lattice structure of the obtained MWCNTs at all reaction times. (ii) different reaction temperatures (700, 750, 800℃). A general decrease in yield (%) with an

increase in temperature was observed for both sets of samples. Trimethyl borate produced boron containing MWCNTs (0.99%) at 800℃ only, while tr-isopropyl borate produced them at 700℃ (0.39%) and 750℃ (0.29%).

The influence of carbon source and carrier gas flow rates on the heteroatom doping of MWCNTs using tri-isopropyl borate as a boron source and *Catalyst 3* were investigated. Two factors were considered for this study: the individual flow rates (either carbon source or carrier gas) and the total flow rates (sum of carrier and carbon source gas flow rates). A combination of the lowest carbon source flow rate (50 sccm) and highest carrier gas rate (280 sccm) produced MWCNTs with the highest % yield (36.9%), thermal stability and surface area (41.2 m^2/g). Lastly, the study investigated the influence of varying the total flow rate (290-370 sccm). The total flow rate was found to have significant influence on the yield, crystallinity, thermal stability, and surface area.

The synthesis of boron-nitrogen co-doped MWCNTs was explored using two synthetic approaches; (i) Nitrogen-doped MWCNTs were synthesized using *Catalyst 2* and acetonitrile as a nitrogen source at 800℃, followed by the treatment of the produced N-doped MWCNTs with tri-isopropyl borate to substitute boron into the MWCNTs lattice structure. Nitrogen doped MWCNTs were successfully synthesized with a nitrogen content of 0.97%, after treatment with tri-isopropyl borate, the sample showed the presence of nitrogen (0.25%) and boron (0.79%). (ii) MWCNTs that showed the highest thermal stability in the reaction temperature study (700℃ from tri-isopropyl borate and 750℃ from trimethyl borate) were treated with acetonitrile to incorporate nitrogen into the lattice structure. In both synthetic approaches, nitrogen was successfully added to the lattice structure of both the tri-isopropyl (0.25%) and trimethyl borate (2.47%) derived samples, but neither sample had boron in the lattice structure.

Two synthesis methods were used in the attempted synthesis of phosphorus doped MWCNTs; (i) a triphenyl phosphine solution in toluene was bubbled over *Catalyst 2* at 800℃. This method did not incorporate phosphorus in the structure. (ii) two post doping methods were employed; the 1st method involved the mixing and milling of pristine MWCNTs and solid triphenyl phosphine, the resulting mixture was heated under nitrogen at 800℃. As observed from XPS, this method succeeded in the addition of phosphorus (0.29%) to the lattice structure. The 2nd approach involved the treatment of pristine MWCNTs with a triphenyl phosphine solution

prepared from toluene at 800℃. The obtained sample had a low phosphorus atomic % of 0.07%.

A comprehensive investigation into the dispersion of MWCNTs in water, ethyl acetate, ethanol (EtOH), toluene, chloroform ($CHCl_3$), dichloromethane (DCM) and hexane at different volumes (10, 15, 20 ml) was carried out using UV-vis analysis to identify the solvent with highest dispersive ability. Water and ethyl acetate were found to have the highest dispersive ability, and hexane reported the lowest dispersive ability. The approximation of the band gap energies of the dispersions revealed that dispersion of MWCNTs is reliant on their aspect ratio, particularly average diameter. The influence of different mass (4, 8, 16, 24 mg) of surfactants sodium dodecyl sulfate (SDS) and Dodecyl benzene sulfonic acid (DBSA) on the concentration and stability of ethyl acetate and water dispersions (10 ml) were also investigated.

Pristine and heteroatom doped MWCNTs thin films were prepared using a drop-casting method. Their electrochemical performance using cyclic voltammetry (CV) and electrochemical impedance spectroscopy (EIS) as CE in the reduction of the iodide tri-iodide electrolyte was evaluated relative to that of Pt. The Pt electrode reported two reduction peaks with current densities of -0.65 and -1.27 mA/cm^2. The pristine (-0.01, -0.11 mA/cm^2) and nitrogen doped (-0.05, -0.58 mA/cm^2) MWCNTs thin films had poorer electrocatalytic activity than Pt. However, the addition of nitrogen to pristine MWCNTs improved their electrocatalytic activity as evident in the respective current densities at the reduction peaks. This was also observed in the addition of other heteroatoms boron, oxygen, and phosphorus, which all reported greater catalytic activity than pristine MWCNTs. However, none of the phosphorus containing material surpassed the performance of Pt. One boron (0.31%) doped and nitrogen (2.47%) doped MWCNTs surpassed the performance of Pt with current densities of -1.42 and 1.47 mA/cm^2, respectively. In addition, oxygen (14%) containing MWCNT prepared using trimethyl borate also had better performance (-1.47 mA/cm^2) than Pt.

The characteristics of pristine MWCNTs were found to be reliant on the catalyst synthesis method, with catalysts produced under microwave irradiation producing better quality MWCNTs. The methods employed in the synthesis of boron doped MWCNTs were inefficient in the incorporation of boron to the lattice structure. However, they were proficient at modifying the surface of the material. Pronounced differences in the MWCNTs synthesized were found to be correlated to the individual and total flow rates of the gases used. The ex-situ addition of both nitrogen and boron to the lattice structure was found to be successful when the

addition of nitrogen preceded that of boron. Although the concentration of phosphorus was low, triphenyl phosphine was found to be a promising phosphorous source in the synthesis of phosphorous doped MWCNTs. The dispersion of MWCNTs was found to be dependent on the average diameter of MWCNTs, with different solvents, surfactant and combination thereof having their dispersive ability governed polarity of the solvents, and the average diameter of MWCNTs. Given their superior electrochemical performance, modified MWCNTs (B, N, and O) thin films demonstrated their potential as replacements of Pt as a counter electrode in DSSCs.

Acknowledgements.

My greatest gratitude goes to my supervisor Prof Neil Coville for the extensive amount of chemistry knowledge and wisdom that you have shared with me, and all the productive discussions that we have had. Your guidance has without a doubt gotten me closer to being the scientist I have always wanted to be. To Prof Daniel Wamwangi, for contributing immensely to my understanding of the major aspects of this work, I was always guaranteed to leave our meetings with a richer understanding of the work at hand. I would like to acknowledge Dr Zikhona Tetana for the support and patience in the pursuit of this work.

To the Department of Science and Innovation-National Research Foundation Centre of Excellence in Strong Materials (DSI-NRF CoE-SM), TATA Africa foundation, and African Materials Science and Engineering Network (AMSEN) for funding this research.

I would also like to thank Dr Kamogelo Butsi for being a such a wonderful and supportive friend during the completion of this momentous journey, you made a long and hard journey far easy to complete. To Dr Pumza Mente, for your courageous and encouraging spirit and being a wonderful colleague and friend to work with and for always willing to share your time and talents. To Kamogelo Modisane and Yongezile Mhlana, your friendship and support went a long way in this journey. To Thelma Majola, your kindness, supportive nature, and friendship were amazing at the most important moments. To Lebogang Mosiane, it was always a lovely experience working those late hours, made the laboratory less gloomy. To Nqobile Mabokoe for always creating adventures that rejuvenated me. To Pakama Mahlumba for being such a consistent friend over the years and throughout this journey. To Dr Joyful Mdluli my “thesis buddy” thank you for bringing so much needed humour in such a serious and tough journey. To Mxolisi Sopiseka and Dr Siphiwe Thwala, for being great brothers and sharing in the toughness of the process. To Moniq Lyons, for entertaining my random requests to give input. To Lineo Mxakaza for always being so helpful and being such a life saviour every time I needed access or training with some instruments. To Dr Victor Mashindi for continuous assistance in Electrochemistry. To Sabrina Khoosal and Stephanie Akakios, your encouraging words and constant cheerleading went a significant way to keep me going. To my Manager at L’Oreal, Dr Simon Donck, for being so understanding and accommodating in allowing me to finish this journey. To my partner, Sivuyisiwe Jikele, thank you for being such a safe haven, for being my peace and being so patient with me. To my parents, Simon Oupa Mokone and Martha Tsoteng Mokone, thank you for your love and support in this journey.

Dedication.

This thesis is dedicated to my brother

ISAAC TAU MOKONE

Could have not asked for a better brother.

“There is no worse enemy and no better friend than a brother, for one brother knows another, and in perfect knowledge is strength for good and evil.”

Table of Contents

Abstract. i

Acknowledgements. v

Dedication. vi

List of Abbreviations. x

Chapter 1: Introduction 1

1.1. Hypothesis 7

1.2. Aim 8

1.3. Objectives of the study 8

Chapter 1 References 9

Chapter 2: Literature review 16

2.1. Carbon nanotubes: structure and properties. 16

2.1.1. Synthesis of CNTs 18

2.1.2. Mechanism of CNT growth by CCVD 24

2.1.3. Purification of CNTs 25

2.1.4. Modifications of CNTs. 26

2.2. CNTs thin film fabrication. 29

2.2.1. Types of thin film fabrication methods 30

2.3. Photovoltaic devices. 32

2.3.1. Structure and mechanism of dye sensitized solar cells (DSSCs) 32

Chapter 2 References 35

Chapter 3: Synthesis of pristine MWCNTs using a Fe-Co/$CaCO_3$ catalyst. 53

3.1. Introduction 53

3.2. Materials and Methods 60

3.2.1. Starting Materials 60

3.2.2. Synthesis of 10% Fe-Co/$CaCO_3$ catalyst. 60

3.2.3. Synthesis of pristine MWCNTs. 61

3.2.4. Characterization techniques. 62

3.2. Results and discussions. 63

3.2.1. Synthesis of pristine MWCNTs using microwave heating to prepare the catalyst. 63

3.2.2. Synthesis of MWCNTs: a temperature dependant study. 74

3.2.3. Conclusion. 82

Appendix 3A. 83

Chapter 3 References 85

Chapter 4: An investigation of reaction time, flow rate, temperature, and boron source in the synthesis of boron doped MWCNTs over a Fe-Co/$CaCO_3$ catalyst. 94

4.1. Introduction 94

4.2. Materials and Methods. 96

4.2.1. Starting materials. 96

4.2.2. Synthesis of boron doped MWCNTs. 96

4.2.3. Characterization techniques. 97

4.3. Results and discussion. 98

4.3.1. Attempted synthesis of boron doped MWCNTs (B-doped MWCNTs); reaction time and boron source dependant study. 98

4.3.2. Synthesis of boron doped MWCNTs (B-doped MWCNTs); temperature and boron source dependant study. 117

4.3.2.1. Comparative analysis and summary. 131

4.3.3. Investigation of the gas flow rate on the synthesis of B-doped MWCNTs. 133

4.4. Conclusion. 145

Appendix 4A 148

Chapter 4 References 156

Chapter 5: The synthesis of Boron-Nitrogen Co-doped MWCNTs. 163

5.1. Introduction 163

5.2. Materials and Methods 165

5.2.1. Starting material. 165

5.2.2. Synthesis of boron nitrogen co-doped MWCNTs. 166

5.2.3. Characterization techniques 167

5.3. Results and discussions 167

5.3.1. Synthesis of boron-nitrogen co-doped MWCNTs from nitrogen doped MWCNTs using tri-isopropyl borate as a boron source. 167

5.3.2. Synthesis of boron-nitrogen co-doped MWCNTs from tri-isopropyl borate and trimethyl derived B-doped MWCNTs. 176

5.4. Conclusion. 183

Appendix 5A 184

Chapter 5 References 186

Chapter 6: The synthesis of phosphorous doped MWCNTs. 193

6.1. Introduction. 193

6.2. Materials and Methods. 196

6.2.1. Starting materials. 196
6.2.2. Synthesis of phosphorous doped MWCNTs. 196
6.2.3. Characterization techniques. 197
6.3. Results and discussion 197
6.3.1. The synthesis of phosphorous doped MWCNTs. 197
6.4. Conclusion. 209
Appendix 6A. 210
Chapter 6 References. 211
Chapter 7: The dispersion of pristine MWCNTs in aqueous and organic solvents. 215
7.1. Introduction. 215
7.2. Materials and Methods. 224
7.2.1. Starting material. 224
7.2.2. Dispersion of MWCNTs 224
7.2.2. Characterization techniques. 225
7.3. Results and Discussion 226
7.3.1. The dispersion of pristine MWCNTs in water and organic solvents. 226
7.3.2. The dispersion of MWCNTs in water and ethyl acetate using surfactants. 232
7.4. Conclusion. 237
Appendix 7A. 239
Chapter 7 References. 249
Chapter 8: The fabrication of pristine and heteroatom doped MWCNTs thin films; an electrochemical study. 259
8.1. Materials and methods. 263
8.1.1. Starting material 263
8.1.2. Preparation of the thin films. 263
8.1.3. Electrochemical analysis of MWCNTs thin films. 264
8.2. Results and discussion. 264
8.2.1. Electrochemical analysis of pristine and heteroatom doped MWCNTs. 266
8.3. Conclusion. 277
Chapter 8 References 278
Chapter 9: Conclusion and recommendations. 284
9.1. Recommendations and future work. 289

List of Abbreviations.

1D – One Dimensional

3D – Three Dimensional

AFM – Atomic Force Microscopy

Al_2O_3 – Aluminium Oxide

BET – Brunauer, Emmet and Teller

$CaCO_3$ – Calcium Carbonate

CB – Conduction Band

CCVD – Catalytic Chemical Vapor Deposition

CdTe – Cadmium Telluride

CE – Counter Electrode

CIGS – Copper Indium Gallium Di-Selenide

CMC – Critical Micelle Concentration

CNTs – Carbon Nanotubes

Co-Fe – Cobalt-Iron

Co-Mo – Cobalt-Molybdenum

CTAB - Hexadecyltrimethyl Ammonium Bromide

CV – Cyclic Voltammetry

CVD – Chemical Vapor Deposition

CZTS – Copper Zin Tin Sulfide

DBSA – Dodecyl BenzeneSulfonic Acid

DCM – Dichloromethane

DMF – Dimethyl Formamide

DSSCs – Dye-Sensitized Solar Cells

DTAB – Dodecyltrimethyl Ammonium Bromide

DWCNTs – Double Walled Carbon Nanotubes

E_g – Band Gap

EIS – Electrochemical Impedance Spectroscopy

EPD – Electrophoretic Deposition

EtOH – Ethanol

Fe-Mo – Iron-Molybdenum

FTO – Fluorine Tin Oxide

FWCNTs – Few Walled Carbon Nanotubes

FWHM – Full Width at Half Maximum

GW – Gigawatts

HOMO – Highest Occupied Molecular Orbital

HRTEM – High Resolution Tunnelling Electron Microscope

ITO – Indium Tin Oxide

LBL – Layer-by-Layer

LiF – Lithium Fluoride

LLDP – Linear Low Density Polyethylene

LUMO – Lowest Occupied Molecular Orbital

MgO – Magnesium Oxide

MW – Megawatts

MWCNTs – Multi-Walled Carbon Nanotubes

NMP – *N*-Methyl-2-Pyrrolidone

NTP – Normal Temperature and Pressure

OPVCs – Organic Photovoltaic Cells

PCBM – [6,6]-Phenyl-C_{61}-Butyric Acid Methyl Ester

PCE – Photo-Conversion Efficiency

PDMS – Poly(dimethylsiloxane)

POEM – Poly(oxyethylene)-segmented imine

PV – Photovoltaic

PVCs – Photovoltaic Cells

QC – Quantum Confinement

QD – Quantum Dots

R_{CT} – Sheet Resistance

S. A – South Africa

SCCM – Standard Cubic Centimetre per Minute

SDS – Sodium Dodecyl Sulfonate

SEM – Scanning Electron Microscopy

SiO_2 – Silicon dioxide

SWCNTs – Single Walled Carbon Nanotubes

TEM – Transmission Electron Microscopy

TGA – Thermogravimetric Analysis

THF – Tetrahydrofuran

TPR – Temperature Programmed Reduction

UV – Ultra-Violet

UV-vis – Ultraviolet-Visible

XRD – X-Ray Diffraction

Chapter 1: Introduction

The world is reliant on different forms of energy, their production and supply. Individuals, communities, and nations use all forms of energy to supplement, sustain and improve their way of life. Energy in a form of electricity can be characterized as a human right and it has become the dynamo for the development of human civilization. The living standards of a society may be linked to its electricity consumption.[1, 2] Rapid economic expansion and the increasing global population is expected to lead to an increase in global energy demand, consequently, to enhanced electricity consumption.[3, 4] This has brought into question the future of generation capacity and energy storage. The question is further compounded by the nature of the existing primary sources of energy such as fossil fuels (coal, oil, gas) which are depletable and have adverse environmental consequences such as air pollution. Fossil fuels contribute to undesirable climatic changes such as global warming, which is attributed to the emission of copious amounts of CO_2 into the atmosphere.[4-5] The year 2018 had the highest rate (2%) of carbon emissions on record, and this was correlated to the increase in energy consumption.[6] Approximately 89% of the world have access to electricity (i.e., energy consumption), but this access is globally uneven. Of the 840 million people without access to electricity in 2017, 573 million of them were found in sub-Saharan Africa. Access to electricity is still a challenge in different parts of the world, 153 million people gained access to electricity between the years 2015-2017, which drops to 67 million when population growth is considered.[2]

South Africa (S.A) is currently facing challenges related to an increase in energy consumption/demand which is exacerbated by a near static energy supply. The increase in energy consumption has a direct correlation to the mass electrification programs aimed at achieving universal access to affordable, reliable, and modern energy services.[2, 7-8] Thus far in South Africa, electricity is obtained locally from biomass (dung and wood), natural gas, hydropower, nuclear power, solar and wind. However, the energy generation is dominated by cheap and abundant coal (5th largest reserves globally, 66.7 billion tons)[9] which accounts for 75% and 59% of the total primary energy supply in SA in 2006 and 2016, respectively.[7] This has increased to 72% for the year 2019/2020, with 85% and 92% of generation capacity and electricity production reliant on the use of coal.[9] It has made SA's power generation carbon intensive, and this is reflected in the 2020 European commission report for global CO_2 emissions, which reported a moderate increase of 1.5% for South Africa's fossil fuel CO_2

emissions.[10] The global carbon footprint reduction places a rethink on the reliance of fossil fuels based energy resources to minimize the potential environmental 'catastrophe'.

Given these global challenges, it has become essential to explore alternative energy sources and technologies associated with them through an energy mix initiative. The technologies cover both energy conversion and storage purposes.[4-5] The introduction and integration of renewable energy technologies in electricity production has been identified as a feasible way of achieving universal access to affordable, sustainable, and environmentally friendly energy.[2, 5, 7] The year 2020 saw an increase in global renewable energy capacity by 200 gigawatts (GW) and was anticipated to increase by 10% in 2021. The use of renewable energy for electricity generation is estimated to grow by approximately 50% by the year 2025. [11]

Nations like South Africa (S.A) have policy measures that encourage the development of renewable energy and low carbon sustainable technologies.[7] The conception of the government's *integrated resource plan (2010-2030)* policy has led to capacity developments that procured 6422 megawatts (MW) of renewable energy, however, only 3867 MW is available to the grid. Furthermore, the integration of wind (100 MW) and water (1332 MW) were commissioned from the Sere wind farm and Ingula power plant, respectively.[8] This has led to S.A being ranked as the 12th most attractive investment (R201.8 billion) region for renewable energy.[12]

The different forms of primary sources of renewable energy (i.e., solar, wind, water and nuclear) account for 9.3% of global power generation. Individually, hydropower and nuclear grew by 3.1% and 2.4% in 2019, respectively. However, solar power generation has been dominating the renewable energy market by accounting for 40% growth of all renewable energy.[6] Total renewable energy consumption saw an increase of 17.1 % in 2017, but a decline to 14.9% in 2019.[2] However, despite the strides made in addressing the global carbon footprint using renewable energy and its associated technologies, their production tends to be more mineral intensive than fossil fuel-based technologies.[11]

Solar energy is the driving force of renewable clean technology field with potential to be a more viable alternative to fossil fuels than other renewables. An enormous amount of solar energy is supplied to the earth surface every second in a form of heat and radiation, at "no cost" almost everywhere on the planet.[5,13-15] Depletion is not a risk, but despite its huge potential for the production of electricity beyond its current use, it does have drawbacks. The technologies associated with its use have a high materials footprint.[2, 6, 11 13-14] It is weather dependent, the

sun does not radiate at night, and daily fluctuations in radiant energy intensity are observed. The amount that reaches the earth depends on the time and location.[14, 16-18] These factors have a considerable influence on the types of technologies used and their ability to convert solar energy (i.e., conversion efficiency) into power.

The efficiencies of solar based technologies/photovoltaic devices (PVCs) are largely governed by their components, the material used to fabricate them, and the device architecture used. The diversity of material that can be used and how they can be assembled has allowed a rapid evolution in the development of PVCs, giving rise to different generations of PVCs. This grouping into different generations' function as a guiding yardstick for development, design, and properties enhancement of PVCs.[14]

The 1st generation solar cells are the oldest PVCs, which are primarily associated with relatively high efficiencies and are based on bulk silicon technologies. They are made up of wafers of monocrystalline and polycrystalline silicon. This makes them relatively large and heavy in size, and they require large spaces for installation. Furthermore, to increase efficiency, these devices require many modules/wafers. Hence, despite being commercially available, they are relatively expensive. Additionally, these devices suffer from the active layer being an indirect band gap material with low absorption coefficients.[14-16, 17-18]

The 2nd generation PVCs are more cost effective than 1st generation PVCs because they are based on thin film technology. This characteristic gives the devices a thin light absorbing layer compared to thick silicon wafer. [13,118-19] Furthermore, the thin films may be grown on flexible substrate, thus diversifying their use.[14] Three major types of cells fall under this generation;

(i) *amorphous silicon (a-Si) thin film* PVCs, these devices have reported conversion efficiencies as high as 14% due to the direct band gap and high absorption coefficient of the photoactive layer.[19-20] They have the advantage of being able to operate at high temperature and changing/diverse weather conditions. These types of cells are comparatively cheap and widely available.[14-16]

(ii) (ii) *Cadmium telluride (CdTe)* based PCVs are associated with of low fabrication costs. The material has the advantage of a direct band gap (1.5 eV), high optical absorption coefficient and good chemical stability. The devices still generally present with relatively low conversion efficiencies of 9-10% but have recently presented with conversion efficiencies as high as 22.1%, when fabricated at multi-

junction devices. However, the use of the heavy metal Cd attracts much scrutiny due to its high toxicity and carcinogenic effect. [14-16, 20-24]

(iii) *Copper indium gallium di-selenide (CIGS)* is a quaternary compound of the chalcopyrite family. It is a semiconductor with a direct band gap (1.06-1.7 eV). The highest conversion efficiency recorded for PVCs based on this material have conversion efficiencies up to 22.6%.[16, 20-22] The use of CIGS based solar cells possess the advantage of long life due to the minimal degradation of the material. However, in general the 2nd generation solar cells provide environmental challenges because of cost, toxicity and rarity of the metals used in some of the devices.[14-16, 23-24]

The PVCs of the 3rd generation are one of the most promising new technologies, but they are not commercially viable. They have relatively low conversion efficiencies but are cost effective and have the advantage of ease of production.[14-16, 20] Devices developed thus far include *nano-crystal* PVCs based on quantum dots (QD). These are generally made from semiconducting material of the transition metal groups in the nano-crystal size range as well. Reported conversion efficiencies range from lower than 4% to as high as 13.4%.[21-22] Given the environmental implications of the semiconducting material used in the bulk state of CdTe and CIGS based solar cells, QD semiconducting materials are seen as their potential replacements.[14, 16, 20, 25]

Quaternary semiconducting material such Copper Zinc Tin Sulfide (CZTS) have been used in the fabrication of 'emerging' PVCs. Cu_2ZnSnS_2 (CZTS) *thin film-based* PVCs are reported to be low-cost alternatives due to their abundant and inexpensive elemental constituents. Additionally, these devices are made from relatively "non-toxic" components. The device and its variants have reported > 9% efficiency. However, the addition of Se to the CZTS material, to form the CZTSSe device, has given a record conversion efficiency of 12.6%, attributed to the lower band gap of the new material.[26-29]

Single-junction GaAs based PVCs have high costs but present with some of the highest recorded efficiencies. Two types of these PVCs have reported improved efficiency since their conception; *Single crystal GaAs* based PVCs have recorded efficiencies of approximately 16%, to as high as 28.8%. While the *thin film crystal GaAs* based PVCs have reported efficiencies of > 30% in the span of a decade, and a GaAs sample has shown one of the highest recorded efficiencies (ca. 44%).[16, 21-22]

Perovskite based PVCs are one of the most promising emerging 3rd generation PVCs technologies, they have seen one the most rapid improvements, from approximately 3% to 23.7% in the last decade.[21-22, 30] Despite having low-cost starting material and ease of fabrication, their development and commercialization were impeded by poor stability of the device (i.e., material degradation, poor long term thermal stabilization). [30-32] However, this has seen significant improvements through chemical processes such as halide mixing and cation mixing which allows for the tuning of factors such as the Goldschmidt tolerance factor.[33-34] Depending on the fabrication process, three major types of halide perovskite PVCs emerge with varying magnitudes of photo-conversion efficiencies (PCEs); *mesoporous perovskite*[35-36], *planar perovskite (n-i-p)*[37-38] *and planar perovskite (p-i-n)*[39-40]. [16, 30] Planar *perovskites* have been lagging with their lower photo-conversion efficiencies of 21% compared to the *mesoporous perovskite* of > 22%.[41] Some of the highest reported photo-conversion efficiencies include the thermally stable formamidinium lead iodide ($FAPbI_3$) cell at 25% and tandem silicon cells at > 29%.[42-43]

First fabricated in the 1990s and considered to be one the most developed and emerging 3rd generation PVCs, *dye-sensitized solar cells (DSSCs)* are easy to process and fabricate. They have advantages such as chemical versatility, energy and structural tunability, low cost and environmental friendliness. However, the existing devices have not yielded conversion efficiencies beyond 10-15%.[21-22, 44, 45] Although most of the materials used in the device are relatively cheap, the high costs of the ruthenium (Ru) dye and Pt electrodes has delayed their potential commercialization.[21] However, significant strides have been made in substituting the more expensive components of the device with relatively inexpensive materials, this includes the use of natural and non-metallic organic dyes in the place of Ru based dyes.[46-47] Additionally, alternative electrodes to Pt i.e., carbon and oxide based electrodes have also been investigated and shown to exhibit comparable performance to Pt.[48-49]

The *organic photovoltaic cells (OPVCs)* were first produced in 1985[20] using small organic polymers such as pigments, and they reported low conversion efficiencies (~4%). This subsequently evolved into the usage of semiconducting polymers that led to improved efficiencies of up to ~11%.[21-22] These low efficiencies are attributed to the high band gaps of most organic materials, which limits their ability to harvest the solar spectrum to a large extent.[50-51] Organic materials are susceptible to degradation by water and oxygen, and if used as active layers they can reduce the performance of the PV device. This gives the devices lower stability compared to other PVCs.[51] Despite these disadvantages, the use of organic materials

still gives the resulting devices advantageous properties such as low production costs, ease of processing, mechanical flexibility (especially the resulting thin polymer films), and chemical flexibility. [50-52] Additionally, current research has expanded to the use of OPVCs variants that involve the use of non-fullerene acceptors (NAFs), which has led to improvement in photo-conversion efficiency (18%) and device lifetime or stability.[53-54]

Within these generations/categories of PVCs, different techniques have been integrated in some of the devices to improve their efficiency; established in the 1970s, *Concentrated* PVCs use large mirrors that create converging rays that accumulate onto a specific region over the PVCs, resulting in heat energy that is used for power generation. Depending on the power of lenses used, the PVCs may be classified as low, medium, or high concentration PVCs. They have been found to have conversion efficiencies > 40% and possess an advantage of being scalable to varying size. [14,16,21-22] Other techniques such as the use of Plasmons or plasmonic structures, up/down conversion schemes and waveguides have been utilized in PVCs for improved light harvesting abilities and photo-conversion efficiencies.[55-56]

The technique that birthed the design of *Multi-junction* PVCs was necessitated by the 'desire' to improve the light harvesting ability of PVCs. To achieve this, multiple p-n junctions made from varying semiconducting material (i.e., different band gaps) are utilized. Each material/p-n junction absorb or respond to different wavelengths of light and improves the conversion efficiency of the PVCs by allowing interaction with a broader range of wavelengths.[16, 57] These devices have reported efficiencies over 43%, and those that are commercially available, often tandem cells (two p-n junctions), present with performances of ~30% (e.g., InGaP/GaAs[58] based multi-junction PVCs). However, the use of this technique in some low-cost *a*-Si or organic material thin film PVCs has produced lower efficiencies of up to 10%.[16, 21-22]

The substitution of the DSSCs counter electrode (CE) is the subject of this research. Although diverse materials have been explored, the most widely used CE in DSSCs is platinum (Pt); it has advantages such as good chemical stability, excellent catalytic activity for the reduction of the triiodide ion in the electrolyte, low sheet resistance (essential for reduced energy loss), and high conductivity.[4, 59] However, the use of Pt has not resulted in significant improvements of the efficiency. Alternatives ranging from metal carbides/nitrides,[60-63] metal oxides/sulfides[64-67] to conducting polymers[68-69] have been investigated, and some have been found to have greater efficiencies than when Pt is used.[4] Furthermore, Pt does not have low production cost, and it is susceptible to corrosion or poisoning (i.e., producing platinum iodide species) over time.[70-74]

Given the shortcomings observed in existing CE for the DSSCs, and the restrictions they impose in their use on a large scale, the exploration of alternative CE for enhanced performance and improved conversion efficiencies is justified. Carbon based materials such as carbon black[73], carbon nanoparticles[74], carbon nanotubes (CNTs)[75-76], and graphene nanosheets[71, 77-79] have been explored as alternative CE to Pt for the DSSCs. Amongst these carbon-based materials, CNTs have attracted considerable attention due to their promising and unique properties such as large surface area, superior thermal, mechanical, and specifically electronic properties,.[80-83] Although different types of CNTs (single walled, double walled, few-walled) exist, this research will focus on the use of pristine, and heteroatom doped multi-walled carbon nanotubes (MWCNTs) as CE in DSSCs. The potential offered by the electronic properties of MWCNTs in DSSCs devices has been demonstrated; Lee *et al.* reported a conversion efficiency of 7.67 % for MWCNTs compared to the 7.83 % obtained when Pt was used.[4, 84] Furthermore, Han and co-workers illustrated that MWCNTs based DSSCs not only produce efficiency comparable to Pt based DSSCs, but the material has long lasting stability when exposed to the electrolyte. They also reported a lower charge transfer resistance (R_{CT}, 0.82 $\Omega.cm^2$) compared to Pt (1.8 $\Omega.cm^2$).[4, 85]

However, their electrical conductivities and reduction catalytic activities still cannot considerably exceed those of platinum in DSSCs. To improve the performance of these PVCS with MWCNTs-based CE electrodes, it is important to balance the electrical conductivity and electro-catalytic activity of the material.[78, 86] Heteroatom doping (i.e., N, P or B) has been demonstrated to enhance the electrical conductivity and surface hydrophilicity to facilitate charge-transfer and impart electro-catalytic activities. The electro-catalytic reduction activities of MWCNTs, together with the doping-enhanced electrical conductivities and surface hydrophilicity, has made heteroatom doped MWCNTs potentially ideal low-cost, but very effective CE. [86-91, 35-40, 44] Although the DSSCs device was not fabricated in this work, an electrochemical screening of the pristine and heteroatom doped MWCNTs thin films in the reduction of the DSSCs iodide tri-iodide electrolyte relative to Pt electrolyte was carried out to identify thin film material suitable for the substitution of the Pt-CE.

1.1. Hypothesis

An exceptional CE should possess high electrical conducting properties, good chemical stability, low production cost, low sheet resistance (R_{ct}), large current exchange density, low overvoltage and ease of fabrication. It is well known that MWCNTs are cheap to produce and

show strong potential as the CE for DSSCs due to their high electrical conductivity, fast electron transfer (ballistic transport) and tunable band gap. The modification of MWCNTs has the potential to enhance their electro-activity for applications as CE in DSSCs.

1.2. Aim

The goal of the proposed research is to identify MWCNTs that have the potential to increase the power conversion efficiency and the overall performance characteristics of DSSCs through the development of nitrogen-, boron-, and phosphorus-doped MWCNTs.

1.3. Objectives of the study

- Preparation of the Fe-Co catalyst supported on $CaCO_3$ using microwave and conventional heating
- To synthesize pristine, nitrogen-, boron-, and phosphorus-doped MWCNTs using a chemical vapour deposition over the Fe-Co/$CaCO_3$ catalyst.
- To study the physical and chemical properties of the synthesized doped MWCNTs using various techniques such as transmission electron microscopy, scanning electron microscopy, thermal gravimetric analysis, X-ray photoelectron spectroscopy, and Raman spectroscopy.
- To fabricate CNT based thin film layers on FTO substrates.
- To evaluate the electrochemical properties of CNT thin films and identify those most viable for potential use in DSSCs.

Chapter 1 References

1. J. Antonio. L. S**a**nchez. A. M. Diez-Pascaul. R. P. Capilla. *International Journal of Molecular Sciences.* 2019, **20**, 976.

2. IEA, IRENA, WB, WHO (2019), *Tracking SDG 7: The energy progress report*. 2019, Washington DC. Date accessed: 15-02-2020

3. F. M. Al-Marzouki, S. Abdulla, S. Al-Ameer. *Advances in Materials Science and Engineering*. 2016, 1-3.

4. M. Z. Iqbal, S. Khan. *Solar Energy.* 2018, **160**, 130-152.

5. I. N. Obotowo, I. B. Obot, V. J. Ekpe. *Journal of Molecular Structure.* 2016, **1122**, 80-87.

6. BP statistical review of world energy. *British Petroleum Company limited*. 2019, **60**.

7. R. Perrot, M. Gulati, L. Scholtz, S. Fakir, M. B. Ting, F. Mthembi, L. K. Mytelka, S. Haysom, T. J. Pilusa, E. Muzenda, L. Mujakachi, O. Soumonni. *Earth Wind Fire: Unpacking the Political, Economic and Security implications of discourse on Green Economy.* 2015. Mapungubwe Institute for Strategic Reflection (MISTRA).

8. Integrated resource plan. *Department of mineral resources and energy.* 2019, Republic of South Africa.

9. Annual report. *South African National Energy Development Institute (SANEDI)*. 2019/2020.

10. M. Crippa, D. Guizzardi, M. Muentean, E. Schaaf, E. Sollazzo, F. Monforti-Ferrario, J. G. J. Olivier, E. Vignati. *Fossil CO_2 emissions of all world countries: European Commission.* 2020 Report.

11. The One Earth Editorial Team. *One Earth.* 2021, **4**, 321-322.

12. South African energy sector report, *Department of energy.* Nov 2018, Republic of South Africa.

13. A. H. Chander, M. Krishna, Y. Srikanth. *IOSR Journal of Electrical and Electronics Engineering.* 2015, **10**, 151-154.

14. S. Sharma, K. K. Jain, A. Sharma. *Material science and applications.* 2015, **6**, 1145-1155.

15. M. T. Kibria, A. Ahammed, S. M. Song., F. Hossain., Shams-Ul-Islam. *Proceedings of the 5th International Conference on Environmental aspects of Bangladesh.* 2014.

16. A. M. Bagher, M. M. A. Vahid, M. Mohsen. *American Journal of Optics and Photonics.* 2015, **3**, 94-113.

17. P. C. Choubey, A. Oudhia, R. Dewangan. *Recent Research in Science and Technology.* 2012, **4**, 99-101.

18. B. Srinivas, S. Balaji, M. Nagendra Babu, Y. S. Reddy. *International Journal of Engineering Research-online,* 2015, **3**, 178-182.

19. K. L. Chopra, P. D. Paulson, V. Dutt. *Progress in Photovolatics.* 2012, **12**, 69-92.

20. T. D. Lee, A. V. Ebong. *Renewable and Sustainability Reviews.* 2017, 1286-1297.

21. J. Wu, Z. Lan, J. Lin, M. Huang, Y. Huang, L. Fan, G. Luo, Y. Lin, Y. Xie, Y. Wei. *Chemical Society Reviews.* 2017, **47**, 5975-6023.

22. National Renewable Energy Laboratory (NREL), Best research-cell efficiencies (14-04-2017). *www.commons.wikimedia.org/wiki/file:best_research-cell_efficiencies.png*

23. M. Powolla, S. Paetel, Erik Ahlswede, R. Wuerz, C. D. Wesssendorf. T. M. Friedlmeier. *Applied Physics Review.* 2018, **5**, 041602-(1-29).

24. *www.greentechmedia.com/articles/read/first-solar-hits-record-22-1-conversion-efficiency-for-CdTe-solar-cell.* Date accessed: 22-02-2020.

25. W.A. Badawy. *Journal of Advanced Research.* 2015, **6**, 123-132.

26. W. Wang, T. M. Winkler, O. Gunawan, T. Gokmen, K.T. Todorov, Y. Zhu, D. B. Miltzi. *Advanced Energy Materials.* 2014, **4**, 1301465.

27. S. Englund. *Alternative back contacts for CZTS thin film solar cells*. 2020 {PhD thesis}, Uppsalla university.

28. K. Sun, C. Yan, F. Liu, J. Huang, F. Zhou, J. A. Stride, M. Green, X. Hao. *Advanced Energy Materials.* 2016. **6**, 1600046.

29. D.-H. Son, S.-H. Kim, S.-Y. Kim, Y.-I. Kim. J.-H Sim, S.-N. Park, D.-H. Jeon, D.-K. Hwang, S.-J. Sung, J.-K Kang, K.-J. Yang, D.-H. Kim. *Journal of Materials Chemistry A.* 2019, **7**, 25279-25289.

30. R. Wang, M, Mujahid, Y. Duan, Z.-K. Wang, J. Xue, Y. Yang. *Advanced Functional Materials.* 2019, **29**, 1808843 (1-25).

31. J. L. Yamg, B. D. Siempelkamp, D. Y. Liu, T. L. Kelly. *ACS Nano*. 2015, **9**, 1955-1963.

32. B. Conings, J. Drinjkoningen, N. Gauquelin, A. Babayigit, J. D'Haen, L. D'Olieslaeger, A. Ethirajan, J. Verbeeck, J. Manca, E. Mosconi. F. D. Angelis, H. G. Boyen. *Advanced Energy Materials.* 2015, **5**, 1500477.

33. A. Mei, Y.Sheng, Y. Ming, Y. Rong, W. Zhang, S. Luo, G. Na, C. Tian, X. Hou, Z. Zhang, S. Liu, S. Uchida, T.-W. Kim, Y. Yuan, L. Zhang, Y. Zhou, H. Han. *Joule*. 2020, **4**, 2646-2660.

34. Z. Li, M. Yang, J.-S. Park, J. J. Berry, K. Zhu. *Chemistry of Materials*. 2016, **28**, 284-292.

35. H. S. Kim, C. R. Lee, J. H. Im, K. B. Lee, T. Moehl, A. Marchioro, S. J. Moon, R. Humphrey-Baker, J. H. Yum, J. E. Moser, M. Gratzel, N. G. Park. *Science Report*. 2012, **134**, 591 (1-7).

36. K. Mahmood, B. S. Swain, H. S. Jung. *Nanoscale*. 2014, **6**, 9127-9138.

37. P. Fan, D. Zheng, Y. Zheng, J. Yu. *Electrochimica Acta*. 2018, **238**, 922-930.

38. D. Luo, W. Yang, Z. Wang, A. Sadhanala, Q. Hu, R. Su, R. Shivanna, G. F. Trindade, J. F. Watts, Z. Xu, T. Liu, K. Chen, F. Ye, P. Wu, L. Zhao, J. Wu, Y. Tu, Y. Zhang, X. Yang, R. H. Friend, Q. Gong, H. J. Snaith, R. Zhu. *Science*. 2018, **360**, 1442-1446.

39. H. Yang, J. Zhang, C. Zhang, Z. Lin, D. Chen, X. Sun, X. Xi, G. Han, Y. Hao. *Solar Energy*. 2016, **139**, 190-198.

40. C. Tian, E. Castro, G. Betancourt-Solis, Z. Nan, O. Fernandez-Delgado, S. Jankuru, L. Echegoyen. *New Journal of Chemistry*. 2018, **42**, 2896-2902.

41. Q. Jiang, Z. Chu, P. Wang, X. Yang, H. Liu, Y. Wang, Z. Yin, J. Wu, X. Zhang, J. You. *Advanced Materials.* 2017, **29**, 1703852 (1-7)

42. J. Jeong, M. Kim, J. Seo, H. Lu, P. Alhawat, A. Mishra, Y. Yang, M. A. Hope, F. T. Eickemyer, M. Kim, Y. J. Yoon, I. W. Choi, B. P. Darwich, S. J. Choi, Y. Jo, J. H. Lee, B. Walker, S. M. Zakeeruddin, L. Emsley, U. Rothlisberger, A. Hagfeldt, D. S. Kim, M. Grätzel, J. Y. Kim. *Nature.* 2021, **592**, 381-385.

43. A. Al-Ashouri, E. Köhnen, B. Li, A. Magomedov, H. Hempel, P. Caprioglio, J. A. Márques, A. B. M. Vilches, E. Kasparavicius, J. A. Smith, N. Phung, D. Menzel, M. Grischek, L. Kegelmann, D. Skroblin, C. Gollwitzer, T. Malinauskas, M. Jošt, G. Matić, B. Rech, R. Schlatmann, M. Topić, L. Korte, A. Abate, B. Stannowski, D. Neher, M. Stolterfoht, T. Unold. V. Getautis, S. Albrecht. *Science*. 2020, **370**, 1300-1309.

44. I. N. Obotowo, I. B. Obot, V. J. Ekpe. *Journal of Molecular structure.* 2016, **1122**, 80-87.

45. A. Hagfeldt, G. Boschloo, L. Sun, L. Kloo, H. Perterson, *Chemical Reviews*. 2011, **11**, 6595.

46. J. Peter, I. Vijaya, S. Anandan, K, Ramachandran. P. Nithiananthi. *International Journal of Energy Research.* 2021, **45**, 7764-7782.

47. M. R. N. Thomas, V. J. K. Lourdusamy, A. A. Dhandayuthapani, V. Jayakumar. *Environmental Science and Pollution Research.* 2021, **28**, 28911-28925.

48. S. Yun, P. D. Lund, A. Hinsch. *Energy and Environmental Science*. 2015, **8**, 3495-3514.

49. S. Gnanasekar, P. Kollu, S. K. Jeong, A. N. Grace. *Scientific Reports*. 2019, **9**, 5177 (1-12)

50. H. Hoppe, N. S. Saricifcti. *Advances in Polymer Science*. 2008, **214**, 1-86.

51. N. Yeh, P. Yeh. *Renewable and Sustainable Energy Reviews*. 2013, **21**, 420-431.

52. M. B. Askari. *Sustainable Energy*. 2014, **2**, 85-90.

53. L. Ma, S. Zhang, J. Wang, Y. Xu, J. Hou. *Chemical Communications.* 2020, **56**, 14337-14352.

54. J. Zhang, H. S. Tan, X. Guo, A. Facchetti, H. Yan. *Nature Energy.* 2018, **3**, 720-731.

55. Y. Zhang, C. Y. Yam, G. C. Schatz. *Journal of Physical Chemistry Letters.* 2016, **7**, 1852-1858.

56. P. Prabhathan, V. M. Murukeshan. *Plasmonics*. 2016, **11**, 253-260.

57. A. M. Green. *Third Generation Photovoltaics: Advanced Solar Energy Conversion.* (2003). Springer, page 65.

58. T. Takamoto,M. Kaneiwa, M. Imaizumi, M. Yamaguchi. *Progress in Photovoltaics: Research and Applications.* 2005, **13**, 495-511.

59. Y.-A. Leu, M.-H, Yeh, L.-Y. Lin, T.-J. Li, L.-Y. Chang. S.-Y. Shen, Y.-S. Li, G.-L, Chen, W.-H. Chiang, J.-J. Lin, K.-C. Ho. *ACS Sustainable Chemistry and Engineering*. 2017, **5**, 537-546.

60. J. S. Jang, D. J. Ham, E. Ramasamy, J. Lee, J. S. Lee. *Chemical Communication.* 2010, **46**, 8600-8602.

61. J. He, J. M. Pringle, Y-B. Cheng. *The Journal of Physical Chemistry C.* 2014, **118**, 16818-16824.

62. A.-R. Ko, J.-K. Oh, Y.-W. Lee, S.-B. Han, K-W. Park. *Materials Letters.* 2011, **65**, 2220-2223.

63. M. Wu, H. Guo, Y.-N. Lin, K. Wu, T. Ma, A. Hegfeldt. *The Journal of Physical Chemistry C*. 2014, **118**, 12625-12631.

64. L. Cheng, Y. Hou, B. Zhang, S. Yang, J. W. Guo, L. Wu, H.G. Yang. *Chemical Communication*. 2013, **49**, 5945-5947.

65. C.-W. Kung, H,-W. Chen, C,-Y. Lin, K,-C. Huang, R. Vittal, K,-C. Ho. *ACS Nano*. 2012, **6**, 7016-7025.

66. X. Liu, G. Yue, H. Zheng. *RSC Advances*. 2017, **7**, 12474-12478.

67. X. Zheng, J. Guo, Y. Shi, F. Xiong, W-H, Zhang, T. Ma, C. Li. *Chemical Communications*. 2013, **49**, 9645-9647.

68. Y. Saito, W. Kubo, T. Kitamura, Y. Wada, S. Yanagida. *Journal of Photochemistry and Photobiology A.* 2004, **164**, 153-157.

69. J. Wu, Q. Li, L. Fan, Z. Lan, P. Li, J. Lin, S. Hao. *Journal of Power Sources.* 2008, **181**, 172-176.

70. M. McCune, W. Zhang, Y. Deng. *Nano Letters*. 2012, **12**, 3656-3662.

71. W. Hong, Y. Xu, G. Lu, C. Li, G. Shi. *Electrochemistry Communications*. 2008, **10**, 1555-1558.

72. H. Han, U. Bach, Y.-B. Cheng, R. A. Caruso, C. MacRae. *Applied Physics Letters*. 2009, **94**, 103102.

73. T. N. Murakami, S. Wang, Q. Ito, M. K. Nazeeruddin, T. Bessho, I. Cesar, P. Liska, R. Humphry-Baker, P. Comte, P. Pechy, M. Gratzel. *Journal of the Electrochemistry Society*. 2006, **153**, A2255-A2261.

74. R. R. Jia, J. Z. Chen, J. H. Zhao, J. F. Zheng, C. Song, L. Li, Z. P. Zhu. *Journal of Materials Chemistry*. 2010, **20**, 10829-10834.

75. Z. Yang, T. Chen, R. He, G. Guan, H. Li, L. Qiu, H. Peng. *Advanced Materials*. 2011, **23**, 5436-5439.

76. J. Han, H. Kim, D. Y. Kim, S. M. Jo, S. Y. Jang. *ACS Nano*. 2010, **4**, 3503-3509.

77. H. Choi, H. Kim, S. Hwang, Y. Han, M. Jeon. *Journal of Materials Chemistry*. 2011, **21**, 7548-7551.

78. J. D. Roy-Mayhew, D. J. Bozym, C. Punckt, I. A. Aksay. *ACS Nano*. 2010, **4**, 6203-6211.

79. D.W. Zhang, X. D. Li, H. B. Li, S. Chen, Z. Sun, X. J. Yin, S. M. Huang. *Carbon.* 2011, **49**, 5382-5388.

80. Z. N. Tetana. *Boron and nitrogen doped carbons for photochemical degradation reactions.* 2013 {PhD Thesis}. University of the Witwatersrand.

81. *WWW.NanoWerk.com* {date accessed: 01-02-2020}

82. P. Serp, M. Corrias, P. Kalck. *Applied Catalysis A: General*. 2003, **253**, 337-358.

83. Y. Li. K. A. Watso, M. J. Fallbach, S. Ghase, J. G. Smith, D. M. Delozier, W. Cao, R. E. Crooks, J. W. Connel. *ACS Nano*. 2009, **3**, 2081-2094.

84. W. J. Lee, E. Ramasamy, D. Y. Lee, J. S. Song. *ACS Applied Materials and Interfaces*. 2009, **1**, 1145-1149.

85. L. Han, N. Koide, Y. Chiba, A. Islam, R. Komiya, N. Fuke, A. Fukui, R. Yamanaka. *Applied Physics Letters.* 2005, **86**, 213501 (1-3).

86. C. Mattevi, G. Eda, S. Agnoli, S. Miller, K. A. Mkhoyan, O. Celik, D. Mostrogiovanni, G. Granozzi, E. Garfunkel, M. Chhowalla. *Advanced Functional Materials*. 2009, **19**, 2577-2583.

87. Z. N. Tetana, S. D. Mhlanga, G. Bepete, R. W. M. Krause, N. J. Coville. *South African Journal of Chemistry*. 2012, **65**, 39-49.

88. S. B. Yang, X. L. Feng, X. C. Wang, K. Müllen. *Angewandte Chemie.* 2011, **123**, 5451-5455; *Angewandte Chemie International Edition*. 2011, **50**, 5339 –5343.

89. X.Wang, J. S. Lee, Q. Zhu, J. Liu, Y.Wang, S. Dai, *Chemistry of Materials*. 2010, **22**, 2178-2180.

90. L. T. Qu, Y. Liu, J. B. Baek, L. M. Dai. *ACS Nano*. 2010, **4**, 1321-1326.

91. D. S. Yu, Q. Zhang, L. M. Dai, *Journal of American Chemical Society*. 2010, **132**, 15127-15129.

Chapter 2: Literature review

The performance of any photovoltaic cell is dependent on the architecture/design of the said device, but the type of material used in the device is of more significance. Fundamentally the basic structure of photovoltaic devices such as DSSCs consists of a photoanode, electrolyte and a cathode (i.e., counter electrode).[1-2] Each component has a different role, hence, no one component is more essential than the other. A delicate balance between them and how they 'interact' with each other needs to be established to obtain an optimal performance from the device.

Counter electrodes (CEs) are responsible for completing the circuitry and maintaining the stability of a device by collecting electrons from the external circuit. Numerous characteristics make for a successful CE; the material should possess exceptional electrical conducting properties, good chemical stability, low production cost, low sheet resistance (R_{ct}), large current exchange density, and low overvoltage for reducing the redox system (i.e., iodide triiodide). Furthermore, methods of processing and fabrication of the CEs has a significant impact on their application and performance.[1-10] CNTs have received considerable attention for satisfying many of these criterias.[10] Not only do they possess favourable electronic characteristics, but due to their high thermal stability, mechanical tensile strength and high aspect ratio etc., they have been utilized extensively in various electronic applications such as in sensors[11-12], capacitors[13-14] and solar cells[10, 15-21].

2.1. Carbon nanotubes: structure and properties.

CNTs are one dimensional (1D), cylindrical (i.e., tubular) carbon network structures that have carbon atoms existing in a sp^2 hybridized state, creating a repeating conjugated pi-bond pattern that produces a honeycomb like lattice. There are different types of CNTs (**Figure 2.1**), and these are classified according to the number of their walls (i.e., tubes). A single-walled CNT (SWCNT) consists of a one atom thick wall that can be less 1 nm in diameter. Double-walled CNTs (DWCNTs) consist of two concentric tubes made of a carbon network. Multi-walled CNTs (MWCNTs) are made up of two or more of these walls i.e., encapsulating layers of concentric tubes that can reach a diameter over 100 nm. Few-walled carbon nanotubes (FWCNTs) have 3-9 layers of concentric tubes. These different CNTs can be differentiated by techniques such as scanning electron microscopy (SEM) or high-resolution transmission electron microscopy (HRTEM). For example, in the images produced from HRTEM, a

SWCNT appears as two parallel "lines", while a MWCNT appears as multiple parallel "lines".[22-29]

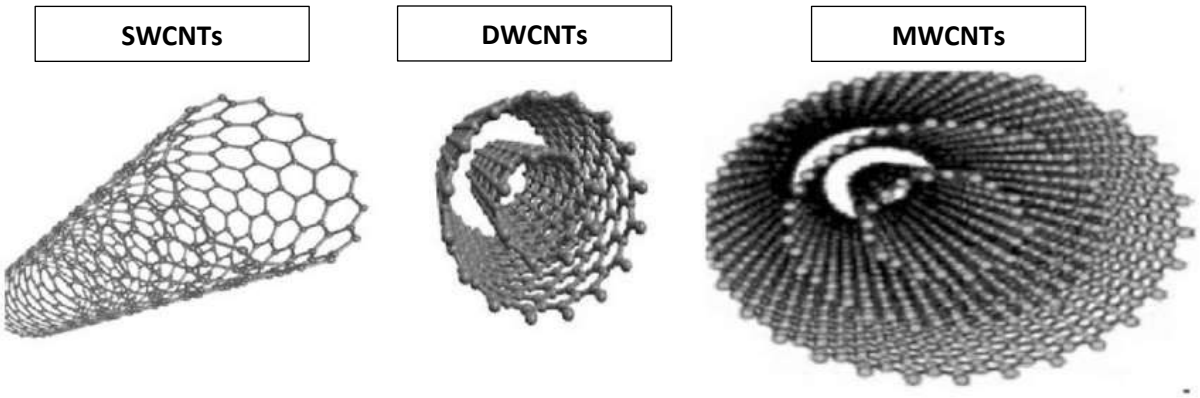


Figure 2.1: Types of Carbon nanotubes (CNTs)

One of the most common ways that the CNT structure is described is by visualizing it as a graphene sheet that is rolled into a tube. Depending on the direction it is rolled, it results in three types of CNT tubular structures: *zigzag*, *armchair*, and *chiral*. These differ is size and diameter, and they can be identified and classified by analyzing the cross-sectional structure of the CNT (i.e., by considering the pattern/arrangement of the pi-bonds across the diameter of the tubes).[22, 30-31]

All three structures differ in structural properties such as diameter, length and wrapping angle (i.e., degree of wrapping). These differences determine their electronic and electron transport properties, and consequently their conductivity. Armchair CNTs tend to be metallic in nature, while zigzag and chiral CNTs are semiconductors. The chirality vectors are good indicators (proportional) of the CNT diameter and wrapping angle.[22, 30-34]

The electron mobility and transport are dramatically different in metallic and semiconducting CNTs. Those with semiconducting behavior have a band gap (E_g) that varies with diameter (d) as $E_g \approx \frac{1}{d}$, and CNTs with metallic behavior, due to their secondary band gap, have $E_g \approx \frac{1}{d^2}$.[33, 36-38] The conductivity of the material is also influenced by quantum effects such as quantum confinement (QC) i.e., the confinement of charge carriers in one or more directions.[33] QC effects become dominant as the diameter of a material is reduced and becomes comparable to the de-Broglie wavelength of the confined charge carriers (i.e. an electron).[39]

The length of the CNTs influence their electron transport properties, more specifically the mobility and transport of electrons along the nanotubes. Resistance is proportional to the length of the nanotubes, for example, CNTs shorter than 500 nm with a metal contact have been found

to have a minimum resistance of 6-7 kΩ, and these values are proportional to changes in the length of CNTs at a rate of 6 kΩ.[35, 40-41]

MWCNTs can be relatively complex compared to their counterpart SWCNTs. Each layer can be rolled up differently to give either zig-zag, armchair or chiral structures, thus resulting in various sequential arrangements of the layers (i.e. zig-zag-armchair-chiral or chiral-zig-zag-armchair etc.). This variation in the sequence of the layers can either be regular or random, the simplest form of MWCNTs is when all the layers are identical. The large amounts of possible arrangements of these layers makes conductivity in MWCNTs relatively complex, this is aggravated by existing inter-wall reactions and coupling that non-uniformly redistributes the charge/current over individual tubes. However, these factors also ensure that MWCNTs are 'always' conducting.[22, 35, 42-43] Parameters that govern and determine the behavior of CNTs such as chirality, diameter, and length, depend on their method of synthesis and the conditions under which they are synthesized.

2.1.1. Synthesis of CNTs

Extensive research has gone into the synthesis of CNTs, and existing methods produce CNTs with different physical, chemical characteristics and purity. The *arc discharge* method was one of the first major methods utilized. The method involves the application of a direct current arc voltage with a microsecond pulse duration at low pressures across two graphite electrodes immersed in a liquid solution or an inert gas such as argon. The temperatures that result are high enough to form a plasma, leading to the sublimation of the carbon located at the anode. The gap between the electrodes is kept constant by adjusting the position of the anode to stabilize the plasma for long reaction times (i.e., seconds to minutes). The carbon sublimation produces a complex mixture of products that are deposited on different parts of the reactor.[35, 44-50]

When the reaction is performed with no catalyst, soot containing fullerenes are deposited on the walls of the reactor, while deposits of MWCNTs that are formed (together with graphite nanoparticles) are deposited on the cathode. The MWCNTs obtained have inner tube diameters varying from 1-3 nm, while the outer wall tubes have a diameter range of 2-25 nm. Their length is found to be no more than 1 m. The inclusion of metal catalysts in the reaction leads to the production of carbon deposits containing MWCNTs, metal filled MWCNTs, graphitic nanoparticles etc., and the soot produced contains MWCNTs, metal filled MWCNTs and SWCNTs. The SWCNTs obtained have closed tips and a diameter range of 1.1-1.4 nm. The

complex mixture of products that are produced provides a challenge when it comes to isolating the MWCNTs and SWCNTs from the deposits and soot.[44-46]

Other variants of the arc discharge method with varying design and parameters have been used. One example is the *pulsed/intermittent arc discharge* method which allows longer pulse durations of a few milliseconds.[44] The utilization of this method in water produced a sediment composed of MWCNTs with lengths ranging from 100-500 nm.[51] The *plasma rotating arc discharge* method involves the rotation of the electrodes, and work performed by Lee and co-workers using pure graphite and helium gas revealed that an increase in yield of CNTs occurred when the rotation speed of the anode was increased.[52] In the *alternating current arc discharge* method, a discharge current is set relative to a discharge voltage allowing for longer continuous reaction times ranging from 1-2 hours. Experiments also involving the variation in the angle (30-180) between the electrodes that are immersed in different hydrocarbons have been performed. These produced well graphitized 10-25 nm diameter MWCNTs with the highest purity observed at an angle of 90.[44, 50, 53]

The *laser ablation* method is another method utilized in the production of CNTs, the vaporization of graphite using a laser beam is used. A metal-graphite composite is placed in a high temperature furnace, and a laser beam of a specific wavelength (e.g., 532 nm) is focused onto the metal graphite material and scanned uniformly across the target surface to maintain a smooth, uniform face vaporization. This method produces CNTs of high purity and favors the production of SWCNTs but may result in some carbon deposits. The laser may be pulsed, double beamed or continuous, and the wavelength of the laser depends on the material made from the laser (XeCl excimer, CO_2, Nd:YAG, KrF excimer). [44, 54-62] Furthermore, one type of laser made from a specific type of material (e.g., XeCl excimer, CO_2) may still produce varying wavelengths.[62-64]

Graphite has also been used in a *ball milling process* to produce CNTs and this process yields more MWCNTs than SWCNTs. It is a two-step process. In the first step, graphite is ground in a stainless-steel container containing four hardened steel balls for approximately 150 hours to produce the nanotube nuclei, this is followed by an annealing step that activates nanotube growth.[22]

The *Hydrothermal* synthetic method involves the hydrothermal treatment of precursors or combination thereof such as polyethylene plus water, ethylene glycol etc. over a catalyst at a specific temperature, and in some cases at high pressure.[44, 65-67] Non-catalytic reactions have

been used to produce MWCNTs from amorphous carbon in hydrothermal fluids.[68] The method provides advantages such as; the absence of hydrocarbon or carrier gases in the process, being able to use low temperatures in the process, and using starting materials that are stable at ambient temperatures and are readily available.[44] A variety of CNTs have been produced from this method. These include closed and open end MWCNTs with a large inner core diameter range of 20-800 nm[65], and some nanotubes with a wall thickness of 7-25 nm[66].

CNTs may also be synthesized using the *Electrolysis* method, which involves the use of alkali and alkaline-earth chloride salts. The metals go through an electro-extraction process onto a graphite electrode, subsequently leading to the formation of CNTs. The erosion of the cathode during the electrolytic process produces a mixture of products ranging from MWCNTs, SWCNTs, carbon encapsulated metal particles and amorphous carbon. It has unique advantages: the reaction occurs in a condensed phase, it has ease of apparatus assembly, use of a cost-effective material, and low energy consumption.[44, 69-73]

One of the most cost effective, high purity, high yield, large scale production, and commonly used methods for the selective synthesis of CNTs is the *chemical vapor deposition* (CVD) method. It is a versatile technique that allows for various modifications in both design and reaction condition, thus giving rise to different kinds of CVD based methods. The experiments are largely carried out at atmospheric pressure in a flow furnace that is either horizontal, or vertical (allows for pressure variation (**Figure 2.2**)). The horizontal configuration (**Figure 2.2.A**) is the one that is generally used; in this mode the catalyst is placed on a quartz glass boat that is in turn placed in a quartz tube. The tube is placed in a horizontal furnace, and an inert gas (to prevent the carbon from oxidizing) together with a hydrocarbon are passed through it, over a catalyst bed, to give the product.[35, 44, 74]

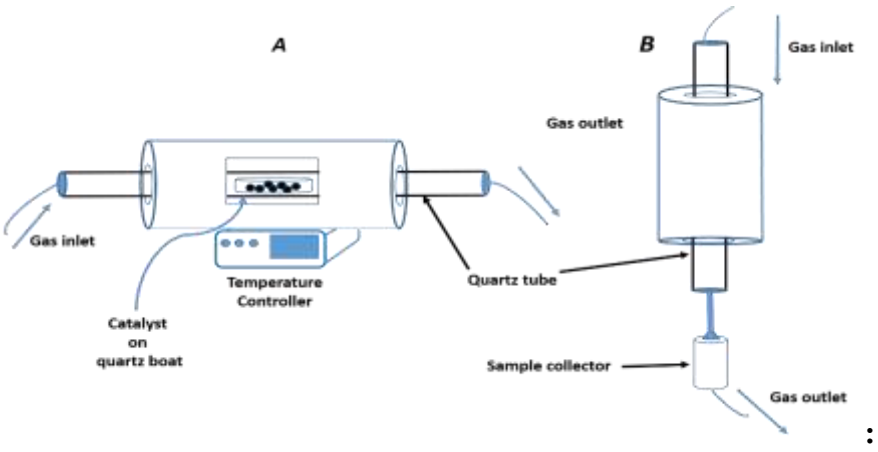


Figure 2.2: *CVD diagram: A)* Horizontal furnace, *B)* Vertical furnace

Slight variations and additions to the design of the CVD allows for selective CNTs growth in different forms such as powder and aligned forests, with the tubes taking different shapes (i.e. straight, curved).[44, 75-76] Vertically aligned SWCNTs and DWCNTs may be produced from modified CVD methods such as *water-assisted-CVD*[77], *O_2-assisted-CVD*[78], *microwave-plasma-enhanced-CVD*[79-80] (can also produce curved and randomly orientated CNTs[81]), and *hot-filament-enhanced-CVD* processes.[82,44] Alcohol based CVD and injection CVD can also produce multi-branched and mainly straight CNTs, respectively.[53, 83-84]

There exists some CNTs synthetic methods that are non-catalytic in nature,[68, 85-88] although this is still debatable.[89-90] CVD methods generally require the use of a metal-based catalyst, i.e., the decomposition of hydrocarbons (i.e., carbon source) over metal-based catalysts deposited on a support. This version of the CVD is referred to as catalytic chemical vapor deposition (CCVD).[35, 44] The choice of the catalyst, support, and combination thereof are significant factors in the type, quality and yields of CNTs that are produced. Their diameter and growth may be controlled by the size of catalyst active particles (i.e., metals used) and their dispersion on the support. Furthermore, this provides room for the controlled growth of CNTs through patterning of the catalyst surface, to not only diversify the kind produced, but their application as well.[44, 91-92]

The metal of choice as a catalyst is an important factor in determining the morphology and growth of CNTs. Different transition metals have been used, with Fe, Co, Ni, and Mo reported to be the most effective catalysts and bimetallic versions of these catalyst present better results. Some rare earth oxides and natural minerals have also been used successfully as catalysts.[44, 93] Support materials have also been extensively studied to illustrate their significance, for example Balogh *et al*. studied the use of Co, Fe and Co-Fe bimetallic catalysts supported on zeolite and $CaCO_3$. The use of zeolite was found to produce better bundle like structures of CNTs than those made over $CaCO_3$.[94] Fe-Mo bimetallic catalyst supported on MgO have been effective in the production of SWCNTs and DWCNTs, while Co-Mo supported on MgO has produced high yield of pure MWCNTs.[95-98] Other types of supports investigated include oxides such as Al_2O_3, SiO_2, etc.[90, 99] The significance of the metal-substrate/support combination is further illustrated in the study by Liu and co-workers.[77] They showed that the use of a Fe/Si catalyst produced a product without amorphous carbon compared to when a Fe/stainless steel catalyst was used. Furthermore, Fe/sapphire and Ni/Fe/glass produced CNTs with random orientation while the use of Fe/Si and Fe/stainless steel produced well aligned CNTs.[44, 77] Beyond the type of catalyst/support combination, the preparation method for these catalysts is

also an important factor. Hernadi *et al.* studied and reported the significance of catalyst preparation.[100-101] In one of their studies they reported on the decomposition of acetylene at 700 ^{o}C over a Co/zeolite catalyst. The catalyst prepared using the ion-exchange method was inactive in the synthesis of CNTs, relative to the highly active catalyst prepared from an impregnation method.[100] The diameter of catalyst metal particles determines the type of CNTs that are produced. Thus, 1 nm metal particles tend to produce SWCNTs, while MWCNTs are generally obtained from metal particles that have a diameter of 10-50 nm.[102]

In addition to the catalyst, the source of carbon, the hydrocarbon (type, volume) due to its chemical and thermodynamic properties plays a role in the nature, lifetime, quality, and yield of CNTs produced. The synthesis of CNTs using gas precursors efficiently is reliant on the concentration and reactivity of intermediates generated in the gas phase from the pyrolysis process.[102] Consequently, intermediates with excellent physisorption and chemisorption properties on a variety of catalysts are essential for the initiation of CNTs growth, thus making the chemical structure of the hydrocarbon important. Generally, higher yields and deposition rates are observed when unsaturated hydrocarbons rather than saturated carbons are used.[102-106] Furthermore, saturated hydrocarbons tend to favor the synthesis of SWCNTs, they produce highly graphitized material with fewer walls. However, this does not mean unsaturated hydrocarbons may not be used in the production of SWCNTs. This has been demonstrated using highly diluted unsaturated hydrocarbons to produce SWCNTs, and the use of saturated hydrocarbons to produce MWCNTs.[102, 107] One is spoiled for choice in the type of carbon sources that may be used in the production of CNTs; from saturated chemicals such as methane[108-109], hexane[110], and propane[111] to unsaturated chemicals such as benzene[112], acetylene[113-114] and toluene[115]. High molecular weight carbon sources like kerosene[115], natural gas[116] and asphalt[117] have also been utilized.[102] For gas-based precursors such as methane and acetylene, their flow rate into the reaction chamber plays a role in the growth and quality of CNTs. For example, a study by Chee *et al.* reported the synthesis of MWCNTs using acetylene at different flow rates; they found that the yield increased with an increase in flow rate (at controlled temperature). Furthermore, at 700 and 30 sccm (acetylene) MWCNTs of higher purity were produced compared to those made at 700 and 15 sccm.[118] Zhan *et al.* illustrated this phenomena further by showing that increasing the flow rate of methane from 50 ml/min to 200 ml/min at constant temperature, time and carrier gas flow rate, increased the carbon % yield.[119] The general direct proportionality that is observed between flow rate and carbon yields

can be rationalized by the use of the larger amount of carbon being available at higher flow rates.[120]

Another significant factor in the synthesis of CNTs using CVD is the type or combination of *carrier gases* used, and their flow rates. Primarily, their function is to create an inert atmosphere, i.e. to remove oxygen or any gas that may react with either the carbon precursor or catalyst, and more importantly to prevent the oxidation of carbon material product.[35] Common gases used include N_2, Ar, H_2 and He, and these have also been used as mixtures viz. N_2/Ar, H_2/N_2, Ar/H_2 etc.[35, 102, 121] Lee and co-workers studied the influence of Ar gas with a flow rate in the range of 2000-3000 sccm and showed that the average length of CNTs produced increased as the flow rate increased. Decreasing the flow rate below 2000 sccm produced CNTs with a shorter length. The flow rate was also found to influence the average diameter, with 2000 sccm and 3000 sccm producing CNTs with an average diameter of 70 nm and 100 nm, respectively.[121] Zhan *et al* found that the use of H_2 not only slowed down the deactivation of the catalyst but also influenced the graphitization of the material and carbon yield. However, for a H_2 flow rate range of 0-80 ml/min the study indicated that the graphitization and carbon yields increased from 0-20 ml/min, but decreased from 40-80 ml/min.[119]

In all the CVD method variants, the reaction conditions such as temperature, pressure and reaction time play a central role. Temperature plays a significant factor in the type of carbon precursor that is used. Methane tends to be used at temperatures > 800 ^{o}C, while precursors such as acetylene and ethylene are generally used on the lower end temperatures of 500-850 ^{o}C.[102, 122-123] Low temperatures tend to produce MWCNTs, while higher temperatures tend to be selective for SWCNTs. This selectivity is a consequence of the precursors used for the synthesis of MWCNTs (i.e., acetylene, benzene) being stable at lower temperatures, while those that are used to obtain SWCNTs are stable at higher temperatures.[102, 124-127]

The pressure of the reaction can influence the types and carbon yield of the CNT material produced. The pressure study reported by Ni *et al*. indicated that an increase in carbon yield occurred from 7.5 torr to 78 torr, and at higher methane pressures reduced deactivation of the catalyst was observed.[128] The reaction time played a role in determining characteristics such as length, diameter and carbon yield of the CNTs formed.[129-130] Generally the carbon yield and the length of the tubes increased with reaction time, provided that the catalyst was not deactivated/poisoned and remained physically accessible to the carbon precursor. The carbon yield and length are directly proportional to the reaction time because longer reaction times

increase the amount of carbon available for deposition. This increase in length and yield is not infinite and there exists a critical reaction time for different reaction conditions after which they begin to decline. [119-120, 130]

2.1.2. Mechanism of CNT growth by CCVD

It is evident that no one factor determines the type and nature of CNTs produced. It is rather the optimization of these factors relative to each that gives either SWCNTs or MWCNTs, and determine properties such as chirality, diameter, and length of CNTs produced. Due to all the extensive combinations in reaction conditions and precursors, the mechanisms for CNT growth is still debated, but there is a mechanism to explain the CCVD synthesis of CNTs that is widely agreed upon.[131-132] The three step vapour-liquid-solid model suggests that the growth of CNTs on the surface of a metal catalyst occurs when the carbon produced by a precursor absorbs on the metal, and dissociates to give elemental carbon atoms. Subsequently the carbons form a liquid metastable carbide that results from the dissolving of the carbon atoms by the metal particle. The CNTs growth begins after the dissolved carbon atoms are saturated in the metal particles, and the solid carbon precipitates from the metal particles.[131-134] This model provides a foundation for explaining and understanding the two existing, widely accepted mechanisms for CNTs growth.

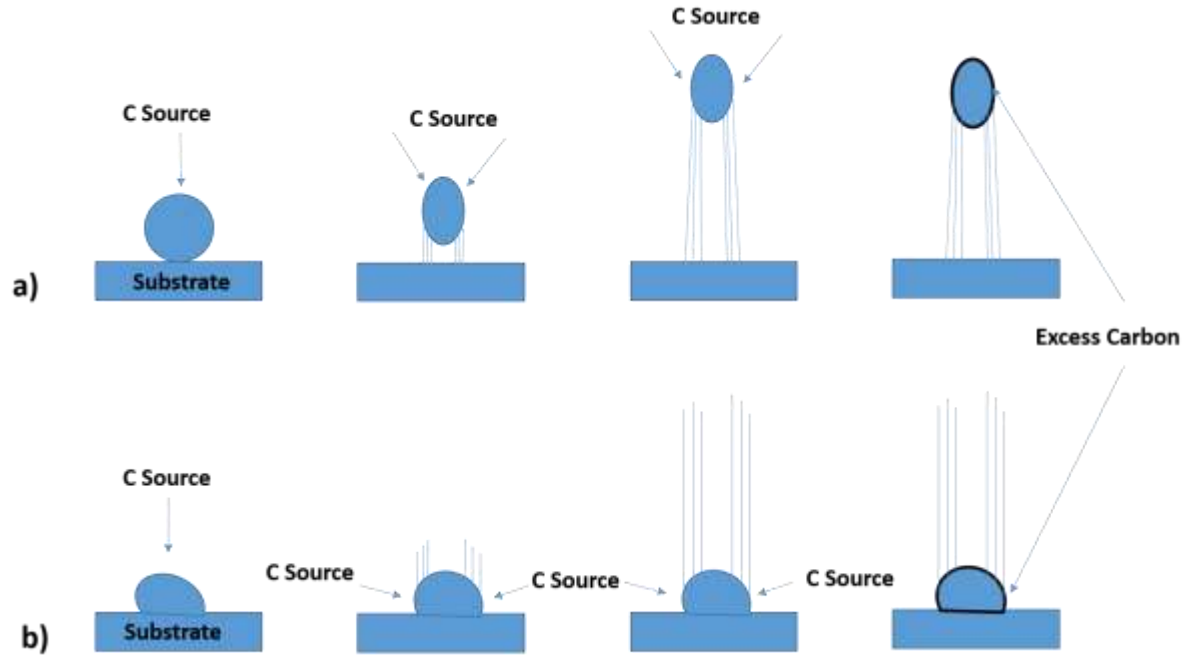


Figure 2: *CVD growth mechanism*; a) tip growth, b) base growth

The two mechanisms are referred to as the base growth and tip growth models (**Figure 2**). The tip growth mechanism (**Figure 2a**) occurs when the metal catalyst interaction with the substrate is weak, consequently, when the CNTs precipitate from the metal particle, they extend from the bottom of the metal. This detaches the metal off the substrate, leaving the top of the catalyst exposed. This provides a site for carbon precursor decomposition, and growth in length of the CNTs. The growth process is terminated when the catalyst is covered with excess carbon. The base growth mechanism (**Figure 2b**) occurs when the catalyst-substrate interaction is strong, the catalyst remains rooted to the substrate with subsequent carbon deposition occurring at the edge of the catalyst while the CNTs grows upward into a graphitic cylinder.[102, 131-136] The diameter of the metal catalyst not only directs the type of CNT formed, but in the case of MWCNTs, the number of layers are directly proportional to the diameter of the metal catalyst diameter.[137-138]

2.1.3. Purification of CNTs

The purification method of choice for CNTs depends on the synthetic method used to produce them, and the by-products that are generated from said method. Substantial research has gone into investigating the purification and methods. These can be destructive or non-destructive to the nanotubes.[139-145] The arc discharge method produces well graphitized and high quality CNTs together with other carbonaceous material. The isolation of the CNTs from other carbonaceous material has been achieved by non-destructive separation methods that involve stabilization of the nanomaterials in a surfactant solution.[139, 146] The CNTs are dispersed in the solution and reversibly incorporated into the micelles without having their structure altered. The process may be followed by centrifugation and filtration, to separate the amorphous carbon and macroscopic particles from the CNTs. A flocculation process (aggregation of micelles due to increased surfactant concentration) may also be used to separate the CNTs by length. Size exclusion chromatography can separate CNTs through a column with controlled pore sizes, restricting the larger particles, and creating separate fractions by length.[147-151]

Although the non-destructive methods produce high purity CNTs, they cannot be used to purify large amounts of samples and they tend to be time consuming. These methods fall short when it comes to the purification of CNTs synthesized using catalytic-support (i.e. CCVD) based methods, or samples that contain metal based impurities.[146, 152] The purification of these types of samples requires multiple steps, and this can be potentially destructive to the CNTs in the sample.[146, 153] Purification by oxidation has been shown to be useful, with the process involving

either a gas or liquid based method. Gas based oxidation using gases such as O_3/O_2[154], Br_2 (in water)[155-156], Cl_2[157] in air and high temperatures are better suited for the removal of other carbonaceous material. However, they are not effective for the removal of metallic or metal oxide impurities. [139, 158-159]

Liquid based oxidation using acids have been found to be a more viable option for the removal of both carbonaceous and metal-based impurities. The method does not selectively oxidize or remove the impurities, but also oxidizes the CNTs in the crude sample as well.[154] Thus, it is essential to mitigate this competitive oxidation by minimizing the number of impurities in the sample by having a reduced number of purifications steps and using relatively dilute acids.[146] This method also plays a role in choosing the type of support for a catalyst. For example, the use of MgO or $CaCO_3$ as support allows for the support to be readily washed off from the CNTs crude sample.[27, 146, 160] Oxidizing agents used include strong acids such as HNO_3 [144, 161], H_2SO_4, HCl[156], $HClO_4$ or a weak acid such as H_2O_2[154]. A study by Hiura *et al.* illustrated that 'non-acidic' oxidizing agents such as $KMnO_4$ may be utilized, and its use in the large-scale purification of CNTs samples reported a slower oxidation rate relative to the use of HNO_3 and H_2SO_4.[162]

2.1.4. Modifications of CNTs.

CNTs deemed to have 'no defects' are found to be almost chemically inert. However, CNTs are generally produced with varying types of intrinsic defects that may be structural (atom topological arrangement) or elemental (presence or absence of certain elements). The defects may also be introduced intentionally into the material during and/or by post synthesis methods. The topological structure of CNTs is largely made up of a repeated hexagonal sp^2 carbon lattice, but these units can be disrupted by the presence of structural defects in the form of four, five, seven or eight membered rings, stemming from vacancies and adatoms in the lattice. Some of the most common intrinsic defects observed in CNTs are called bumby, zipper and Stone-Wales defects.[163-168]

Although CNTs exhibits high strain and high surface energy throughout the structure because of high curvature, the presence of pentagons and heptagons in certain positions (with varying possible arrangements) tends to exacerbate the effect. They also influence the type of defects, and where they may be introduced.[163, 169-170] The types (i.e., intrinsic, or extrinsic), positions and distribution of defects are important as they not only influence the reactivity of the CNTs, but also other characteristics such as their water transport[171], toxicological[172-173], mechanical[174],

and electrical properties[164, 175-177]. The two major processes normally used to introduce defects to the material are functionalization and doping.

2.1.4.1. Functionalization of CNTs

The process of functionalization is generally aimed at improving the CNT processability and solubility to broaden their applications.[176, 178] The process may be chemical or physical, and the extent of each depends on factors such as the type, size of CNTs, and if they are arranged randomly or are aligned relative to each other. Physical processes such as exohedral functionalization by use of a polymer[179] or surfactant[139, 180] are non-covalent in nature, and involve only strong Van de Waal interactions. On the other hand, covalent exohedral functionalization involves the chemical attachment of chemical groups on the sidewalls, defect sites and tips/endcaps of the CNTs.[162-163, 176, 181-182]

Various techniques ranging from oxidative purification[154] (liquid or gas based), cycloadditions[183], Diels-Alder reactions[184], ozonolysis[185] etc have been utilized to achieve this, and the choice of method is influenced by the type of functional groups one wishes to add to the CNTs. This process leads to a change in the sp^2 hybridized nature of the carbon atoms in the basal structure to sp^3.[163, 176, 181] Oxidative functionalization has a dual function in processing CNTs; it can serve to remove impurities (**see section 2.1.2**),[154] and to add functional groups to the material. However, liquid-based oxidation is preferred to gas based oxidation due to the mild, slow nature of the process in producing oxidized CNTs in high yield. Furthermore, the oxidation process not only introduces defects to the surface but may lead to cleavage of CNTs and the opening of their tips. Due to the presence of structural defects (e.g., pentagonal), the tips are more susceptible to oxidation.[154, 162-163, 176] Covalent functionalization also influences the electrical and electrochemical nature of the material by increasing the number of defect sites for electro-catalytic activity but does have the potential to lower the conductivity by damaging the conjugated structure in the graphitic basal plane.[186]

2.1.4.2. Heteroatom doping of CNTs.

Heteroatom doping (e.g., by N, B, and P) offers a better alternative to introducing electro-catalytic active sites to the carbon network with a minimized change of conjugation length (i.e., minimized damage to the graphitic basal plane). The minimal damage to the conjugated structure and its length is a consequence of how the dopants exist in the network structure of the material. In a nitrogen doped material, nitrogen has been reported to exist as four types of

species; oxidized pyridinic, pyrrolic, and quaternary (**Figure 2.4**), and all these species can exist in varying concentrations.[186-188 32]

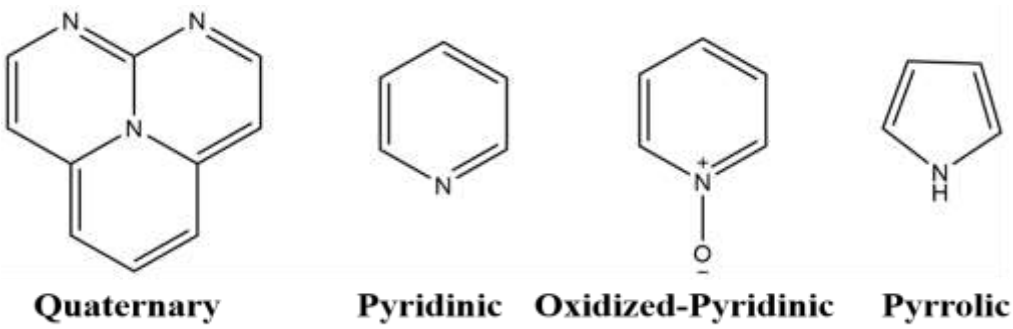


Figure 2.4: Nitrogen based species incorporated in graphitic carbon.

The nitrogen atoms not only provide electro-catalytic active sites, but the delocalized lone pair of electrons participate in electron transport across the conjugated length of a network structure. The substitution of carbon with nitrogen leads to the production of an n-type semiconductor and reduces the gap between the conduction band and the Fermi-level. Increased conductivity of the CNTs is observed as the nitrogen content increased.[189-190]

In boron doped materials, boron has been found to exist in three ways; BC_3, BCO_2 and BC_2O all of which provide electro-catalytic active sites. The empty p-orbitals of the boron atom also initiate and participate in electron transport along the conjugated length in a network structure. The presence of boron has been shown to lead to improved electro-catalytic activity, electrical conductivity, and lower charge transfer resistance.[175, 191-193] Leu *et al.* illustrated, that boron not only provides more catalytic sites and free charge carriers, but also its presence led to higher electrical conductivity by giving rise to semi-metallic characteristics in the material by lowering its Fermi-level.[191]

There exist two general methods for the synthesis of heteroatom doped CNTs; *a) in situ* doping; in this process the synthesis of a material occurs concurrently with the doping process and the material is formed with heteroatom based defects, and *b) post doping;* this involves the treatment of CNTs with heteroatom precursors such as CH_3CN[187], NH_3 for N-doping, or $C_9H_{21}BO_3$, $C_3H_9BO_3$ for B-doping after CNT synthesis.[194-195] Both these methods may be incorporated in the *CVD* methods described in section **2.1.2.** The precursors may be solid or liquid. The boron *post-doping* process usually involves high synthesis temperatures using solid precursors such as boric acid or boron oxide.[175, 188, 191, 194, 196]

Heteroatom doping can improve the electrical conductivity and surface hydrophilicity to facilitate charge-transfer and enhance electro-catalytic activities to the CNTs. The electro-catalytic reduction activities, together with the doping-enhanced electrical conductivities, and improved surface hydrophilicity, have made heteroatom doped carbon nanomaterials ideal as a low-cost material, effective for electronic based applications (e.g., counter electrodes in DSSCs). [175, 186-187, 192, 197-199]

2.2. CNTs thin film fabrication.

Thin film technology has been applied to varying materials such as ZnO[200], TiNi[201], CdTe[202], Ta_2O_5[203] etc., and has seen extensive applications in fields involving optical devices[204], telecommunication devices[205], sensors[206], energy conversion[207-208] and storage devices[209]. The diversity observed in their application and properties is a due to a unique 'averaged behavior' compared to their isolated parent material or their bulk form. They possess high surface to volume ratios, and their 'behavior' allows for better reproducibility. The morphology (e.g., thickness, smoothness) and stability of the thin films, which depends on their preparation methods, determines how and where the thin film should be utilized.[35, 210-211]

CNTs present with a number of exceptional properties, but their high aspect ratio (i.e., length to diameter) leaves them intertwined and interconnected in a network that encourages the formation of thin films. The thin films may be obtained from samples that have either random networks or aligned arrays of CNTs. The obtained 2D conducting films have a high mechanical flexibility and conductivity, so much so, that at times they are considered as a novel material.[35, 210, 212-213] This is partly due to the mixture of metallic and semiconducting CNTs that have their properties 'averaging out' as they interact, thus giving the film its novel properties.[214-215] Methods used for thin film fabrication are generally categorized into two: direct growth (i.e. from *CVD*) and solution based growth. The direct growth method has disadvantages such as the leaving behind of residual catalyst, and this leads to substrate compatibility related issues in electronic applications. The high aspect ratio which results in strong Van de Waals interactions makes the processing of CNTs for solution-based methods problematic. The strong Van de Waal forces and interconnectedness of the CNTs gives them their reduced solubility/dispersibility in varying solvents. Failure to sufficiently disperse CNTs produces films that are not smooth in nature, and leads to reduced conductivity in the resulting film. [35, 212, 215]

CNTs are produced in powder form and their utilization as a counter electrode (CE) must be preceded by a step that transforms them into thin films. There exist different ways to separate CNTs and increase their dispersibility; *a)* surface functionalization which encourages their dispersion in aqueous and polar medium, but as highlighted in section **2.1.4.1**, this method creates covalent bonds and damages the structure of the CNTs.[216-218] *b)* dispersal in organic solvents under different conditions[219-220], and *c*) the use of surfactants and polymers in solvents to aid their dispersion.[139, 147, 221-223] The use of solvents without assistance leads to insufficient dispersion, resulting in increased aggregation, especially at high concentrations of CNTs. However, the dispersion aids need to be removed post dispersion, while some surfactants and polymers are easily washed off with water, others may require heat treatment.[35, 219-220]

2.2.1. Types of thin film fabrication methods

The "direct growth method for film deposition" can produce thin films on different substrates, and a single deposition or multiple depositions onto the substrate must be made to produce the film. The method involves the exposure of a substrate to two or more vaporized substances. They are thermally decomposed with gases to form the thin film on the substrate surface. In some cases, a catalyst is added to promote the growth process. The characteristics of the film produced are influenced by several reaction parameters such as gas flow rate, pressure, temperature, and catalyst. [35, 212, 224-225]

The CVD method can produce CNT based films that are uniform and have a high density and conductivity. This may be attributed to the tubes obtained in the film having few defects and 'excellent' CNT-CNT interactions. The method also has the advantage of producing films with high reproducibility and adhesion at high deposition rates. However, the method has several limitations: a) it provides difficulties in producing a mechanically "satisfying" CNT composite film, b) the deposition of multicomponent materials from multiple sources with well controlled stoichiometry is not a trivial process, and c) the method requires harsh conditions such as high temperature and a vacuum. Furthermore, the substrates used may be incompatible with the devices they are to be applied to.[35, 212, 226]

Apart from the direct growth method used in the CNTs film deposition, solution-based film fabrication has received a lot of attention in industry and academia. This is a consequence of advantages such as low temperature processing, no need for high vacuum systems, and its cost effectiveness. There are different kinds of solution methods that have been reported.[35, 212] The *spray coating* deposition method has been used to produce CNTs based thin films. The

dispersed CNTs (in solution) are sprayed onto a heated substrate, and they form a thin layer by undergoing a pyrolytic decomposition in which excess solvents and by-products escape as vapor. Advantages offered by this method include the production of thick films with a large surface area and relatively large thickness. The stability (i.e., adhesion to substrate) of the film is affected by the substrate used, hence this method allows for the use of different substrates, and thus gives an added advantage of producing materials suited for a diverse range of devices.[35, 212, 227-228]

The *dip coating* deposition method involves the immersion of a substrate into a dispersed CNT mixture at a constant speed for a specific amount of time. When that time has elapsed, to avoid 'jitters', the substrate is removed from the solution at a constant speed. The substrate emerges with a thin layer of CNTs solution attached, and as it dries, a thin solid layer is formed. The drying step determines the quality of the film produced. Several factors govern the amount of coating on the substrate: the viscosity of the solution, immersion time, withdrawal of substrate, and the interaction between the substrate solution (the CNTs) and the substrate. Dip-coating offers the advantage of having the potential to be used for large scale coating of a substrate, and it does not require costly sophisticated apparatus. However, because the substrate is coated on both sides, the method restricts the application of the film produced.[35, 212, 229-230]

The *spin coating* method has been widely used; in this method a small amount of CNTs solution is deposited at the center of a substrate. The substrate is spun at high speed, spreading, and covers the surface using a centrifugal force, thus forming a thin film. The solution concentration, viscosity, angular speed, and spin time determine the thickness of the film. This method is accompanied by several drawbacks: it cannot be used for large scale coating purposes as most of the material would be flung off the substrate during the process, this makes multilayer coating inefficient and not easily manageable.[35, 212, 231-233]

The *drop casting* method involves the drop wise deposition of a solution onto a substrate. It is an easy process to perform and has low cost. It is like the spray coating method but provides controllable coating. The morphology of the films produced depends on the droplet size, the momentum of the droplet, and the rate at which it wets the surface of the substrate upon impact (i.e., by the viscosity of the solvent used). However, the method is limited to the production of small area films.[35, 234-235]

The last method discussed pertains to a solution-based deposition by *vacuum filtration*. It is widely used for the fabrication of CNT film composites. It involves the separation of CNTs

composites from the solvent and their compaction into films. This is achieved by applying different pressures between two sides of a Buchner funnel from which a thin film result. The method has been found to produce very thick films that restrict their range of application.[212, 236]

The production of CNTs based films described above is dependent on the dispersion, addition and removal of dispersion aids, binder materials for improving adhesion and stability, and choice of substrate in producing CNTs based thin films of 'excellent' quality.[35, 212] There also exists other solution-based methods that have not been discussed above that have been utilized to produce thin films. These include the sol-gel method[237], electrophoretic deposition (EDP)[238], pulse electrodeposition[239], sputter deposition[240], and layer-by-layer (LBL) self-assembly deposition[241].

2.3. Photovoltaic devices.

The different kinds of photovoltaic devices, and their development has become an essential factor in global energy production, using the sun's (solar) energy. They are classified according to their components and fabrication. As highlighted in chapter 1, DSSCs possess advantages such as chemical versatility, energy and structural tunability, low cost and environmental friendliness.[242-245]

2.3.1. Structure and mechanism of dye sensitized solar cells (DSSCs)

A typical DSSC device (**Figure 2.5**) consists of:

(i) a *working electrode* made up of three components forming a transparent photoanode. It is generally made from a semiconducting oxide such as TiO_2[246], ZnO[247], Nb_2O_5[248] deposited on a conducting glass such as fluorine tin oxide (FTO) or indium tin oxide (ITO). TiO_2 (normally anatase) is the most used oxide due to its high energy band gap and ability to impede photo-corrosion. However, the dye breadth of absorption in the UV region is small; thus, the fabricated film is immersed in a photosensitive luminescent dye (sensitizer) which is either metal based or metal free to increase the light absorbing ability. It is essential that it has a broad absorption spectrum (UV-vis, near infrared). The dyes are normally made from molecules with pi-conjugated systems and function to generate photoexcited electrons, while the TiO_2 (with a dye adsorbed on its surface) is the semiconductor responsible for electron injection.[10, 249-255] Other factors regarding the TiO_2, such as

the thickness of the layer[256] and the precursors[257-258], influences the performance of the DSSCs. Furthermore, the combination of these components of the photoanode give it its character. For example, Mashreghi *et al*. reported a decrease in conversion efficiency when the area of the photoanode increased.[259]

(ii) an *electrolyte* that serves as a mediator to regenerate the dye sensitizer once it has emitted its photoexcited electrons to restore it to its original state. Different electrolytes such as Br^-/Br_2^-,[260] SCN^-/SCN_2[261] and Co^{2+}/Co^{3+} [262] have been utilized, but I^-/I_3^- has been shown to have the highest efficiency. Despite this, its utilization in DSSCs has shortcomings such as high volatility and poor long-term stability. It also leads to the corrosion of Pt, ITO/FTO and TiO_2, thus causing photodegradation and dye-desorption. [10, 249-255]

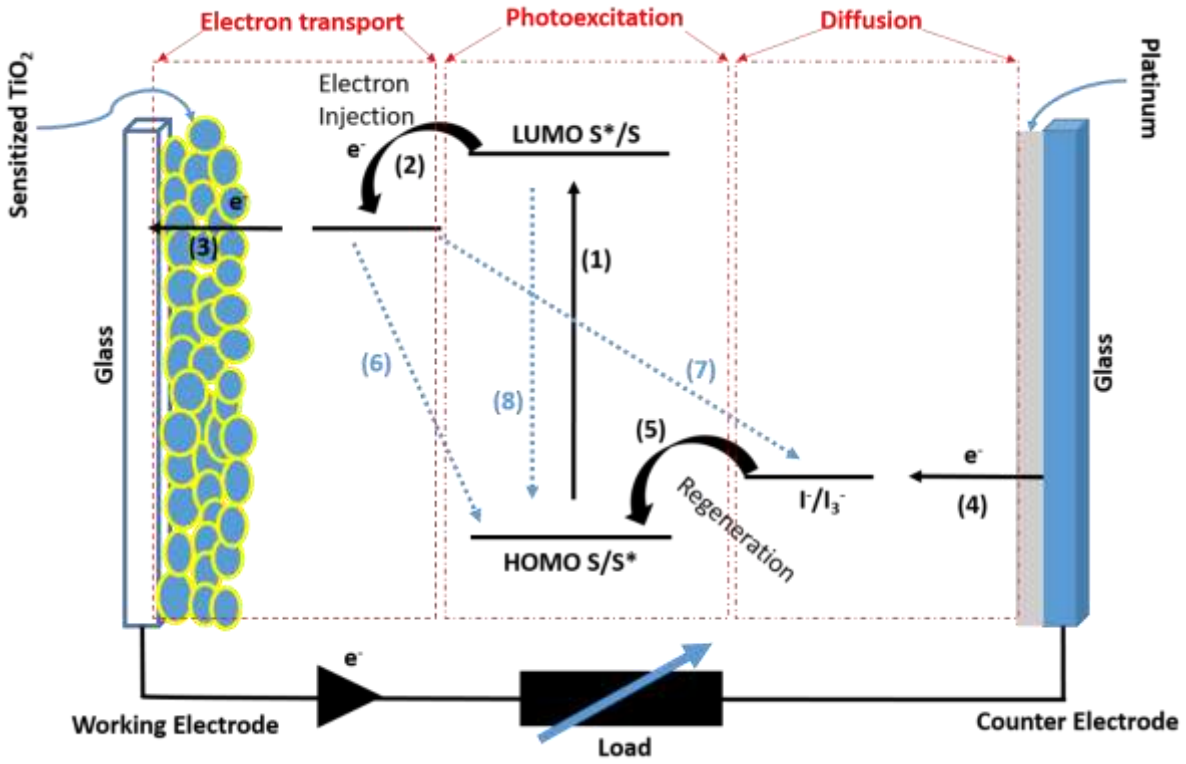


Figure 2.5: Representation of DSSC and corresponding energy level diagrams, NOTE: S represents the dye in its de-excited state, and S* represents the dye in its excited state. Recombination processes represented by dashed blue arrows.

(iii) A *counter electrode* (CE) that serves as a cathode and regulates the DSSC performance by catalyzing the reduction of the iodide-triiodide redox species. Diverse types of materials have been utilized[10] but have generally failed to surpass

the most widely used Pt counter electrode. It possesses most of the characteristics that make a 'good' electrode, such as 'good' chemical stability, excellent catalytic activity for the reduction of the triiodide ion in the electrolyte, low sheet resistance (essential for reduced energy loss), and high conductivity. However, apart from the relatively high production costs, Pt use is 'limited' in terms of reserves in nature. [10, 249-255]

The DSSC begins to operate when it is exposed to sunlight. In the process (1) the dye absorbs solar energy and the electrons in its highest occupied molecular orbital (HOMO) are excited into its lowest unoccupied molecular orbital (LUMO). (2) The electrons in the LUMO are injected into the conduction band (CB) of the TiO_2, (3) which transports the electrons to the external circuit. The completion of these three steps requires that the HOMO for the sensitizer to be higher than the conduction band of TiO_2. (4) The electrons reach the CE where the triiodide ions have migrated, reducing them to iodide ions. (5) The iodide species migrate towards the photoanode where they are oxidized to restore the dye to its original state. This requires the HOMO level to be lower than that of the electrolyte level. The redox system serves to prevent the decomposition of the dye. [10, 249-255]

This mechanism has shortcomings. The amount of time that it takes for the electron to travel from the HOMO to the LUMO level (1) (See **Figure 2.5**), from the LUMO to the CB of TiO_2 (2), and consequently into the external circuit (3) takes pico to microseconds. However, the time it takes the electrons to travel through the external circuit to the CE, through the electrolyte (by a redox process) back to working electrode to reduce the dye to its original state (4) occurs at a lower rate, microseconds. During this time, recombination can occur (**Figure 2.5**). The first kind of recombination that may occur is the de-excitation of the electrons in the LUMO back to the HOMO level (8). Here the electrolyte and TiO_2 are in contact, and electrons that are successfully injected into the CB of TiO_2 can be recombined with the triiodide ion (7) and the oxidized dye (6) instead of traveling to the external circuit. Therefore, enhancing the performance and conversion efficiency (η) of the DSSCs involves the suppression of these recombination processes. [10, 249-255] This may be achieved by minimizing direct contact between the photoanode and the electrolyte by making the external boundaries of the dye hydrophobic. Furthermore, dye aggregation on the TiO_2 surface can be prevented by adding co-adsorbents to the dye.[249]

Chapter 2 References

1. A. H. Halami, B. Rajab, J. Abed, M. Faraj, A. A. Hawili, H. Alawadhi. *Energy*. 2019, **174**, 526-533.
2. M. Hiramoto, Y. Shinmura. *Organic Solar cells*. *Springer Handbook Electronic and Photonic Materials.* 2017, Chapter 54, 1329-1338.
3. R. R. Jia, J. Z. Chen, J. H. Zhao, J. F. Zheng, C. Song, L. Li, Z. P. Zhu. *Journal of Materials Chemistry*. 2010, **20**, 10829-10834.
4. Z. Yang, T. Chen, R. He, G. Guan, H. Li, L. Qiu, H. Peng. *Advanced Materials*. 2011, **23**, 5436-5439.
5. J. Han, H. Kim, D. Y. Kim, S. M. Jo, S. Y. Jang. *ACS Nano.* 2010, **4**, 3503-3509.
6. H. Choi, H. Kim, S. Hwang, Y. Han, M. Jeon. *Journal of Materials Chemistry*. 2011, **21**, 7548-7551.
7. J. D. Roy-Mayhew, D. J. Bozym, C. Punckt, I. A. Aksay, *ACS Nano*. 2010, **4**, 6203-6211.
8. D.W. Zhang, X. D. Li, H. B. Li, S. Chen, Z. Sun, X. J. Yin, S. M. Huang. *Carbon*. 2011, **49**, 5382-5388.
9. M. Law, L. E. Greene, S. C. Johnson, R. Saykally, P. Yang. *Nature Materials.* 2005, **4(6)**, 455-459.
10. M. Z. Iqbal, S. Khan. *Solar Energy.* 2018, **160**, 130-152.
11. V. M. Aroutiounian, A. Z. Adamyan, E. A. Khachaturyan, Z. N. Adamyan, K. Hernadi, Z. Pallai, Z. Nemeth, L. Forro, A. Magrez, E. Horvath. *Sensors and Actuators B: Chemical.* 2013, **177**, 308-315.
12. K.-Y. Choi, J.-S. Park, K.-B. Park, H. J. Kim, H.-D. Park, S.-D. Kim. *Sensors and Actuators B: Chemical.* 2010, **150**, 65-72.
13. L. Li, Z. Lou, W. Han, D. Chen, K. Jiang, G. Shen. *Advanced Materials Technologies*. 2017, **2**, 1600282 (1-8).

14. D. A. John, S. Banerjee, G. W. Bohannan, K. Biswas. *Applied Physics Letters*. 2017, **110**, 163504 (1-5).

15. Y. Chen, H. Gao, Y. Luo. *Applied Physics Letters.* 2011, **99**, 143309.

16. C. Li. Y. Chen, Y. Wang, Z. Iqbal, M. Chhowalla, S. Mitra. *Journal of Materials Chemistry.* 2007, **17**, 2406-2411.

17. W. J. Lee, E. Ramasamy, D. Y. Lee, J. S. Song. *ACS Applied Materials and Interfaces*. 2009, **1**, 1145-1149.

18. L. Han, N. Koide, Y. Chiba, A. Islam, R. Komiya, N. Fuke, A. Fukui, R. Yamanaka. *Applied Physics Letters.* 2005, **86**, 213501 (1-3).

19. M. W. Rowell, M. A. Topinka, M. D. Mcgehee. *Applied Physics Letters*. 2006, **88**, 233506 (1-3).

20. H.-J. Shin, S. S. Jeon, S. S. Im. *Synthetic Metals.* 2011, **161**, 1284-1288.

21. H. Hanaei, M. K. Assadi, R. Saidur. *Renewable and Sustainable Energy Reviews.* 2016, **59**, 620-635.

22. *WWW.NanoWerk.com/nanotechnology/introduction/introduction_to_nanotechnology_22.php (Date accessed: 01-02-2020)*

23. Y. Tang, J. Lu, D. Liu, X. Yan, C. Yao, H. Zhu. *Hindawi Journal of Nanomaterials.* 2017, 7601869 (1-11).

24. X. Lu, Z. Chen. *Chemical Reviews*. 2005, **105**, 3643-3696.

25. S. Iijima. *Nature*. 1991, **354**, 56-58.

26. S. Iijima, T. Ichihashi. *Nature*, 1993, **363**, 603-605.

27. E. Flahaut, R. Bacsa, A. Peigney, C. Laurent. *Chemical Communications*. 2003, 1442-1443.

28. K. P. Gong, F. Du, Z. H. Xia, M. Durstock, L. M. Dai. *Science*. 2009, **323**, 760-764.

29. H. Qi, C. Chian, J. Liu. *Chemistry of Materials*. 2006, **18**, 5691-5695.

30. D. Das, H. Rahaman. *New York: CRC Press Taylor and Francis Group*. 2015, **196**, p9781138822313.

31. R. Saito, M. Fujita, G. Dresselhaus, M. S. Dresselhaus. *Physical Review B*. 1992, **46**, 1804-1811.

32. M. S. Dresselhaus, G. Dresselhaus, R. Saito. *Carbon.* 1995, **33**, 883-891.

33. R. A. Jishi, J. Bragin, L. Lou. *Physical Review B*. 1991, **59**, 9862-9865.

34. R. A. Jishi, D. Inomota, K. Nakao, M. S. Dresselhaus, G. Dresselhaus. *Journal of the Physics Society of Japan*. 1994, **63**, 2252-2260.

35. L. Hu, D. S. Hetch, G. Grüner. *Chemical Reviews.* 2010, **110**, 5790-5844.

36. J. W. Mintmire, C. T. White. *Physical Review Letters.* 1998, **81**, 2506-2509.

37. C. L. Kane, E. J. Mele. *Physical Review Letters.* 1997, **78**, 1932-1935.

38. S. D. Saito, G. Dresselhaus, M. S. Dresselhaus. *Imperial College Press: London.* 1998.

39. E. G. Barbagiovanni, D. J. Lockwood, P. J. Simpson. *Applied Physics Reviews*. 2014, **1**, 011302 (1-47).

40. S. Li, Z. Yu, C. Rutherglen, P. J. Burke. *Nano Letters*. 2004, **4**, 2003-2007.

41. P. Sundqvist, F. J. Garcia-Vidal, F. Flores, M. Moreno-Moreno, C. Gómez-Navarro, J. S. Bunch, J. Gómez-Herrero. *Nano Letters.* 2007, **7**, 2568-2573.

42. *www.azonano.com/article.aspx?articleID=1564* (Date accessed: 05-02-2020)

43. *www.nanoshel.com/properties-of-mwcnt* (Date accessed: 05-02-2020)

44. A. Szabó, C. Perri, A. Csató, G. Giordano, D. Vuono, J. B. Nagy. *Materials*. 2010, **3**, 3092-3140.

45. A. Fonseca, J. B. Nagy. *Kluwer Academic Publishers: Dordrecht, The Netherlands.* 2001, **372**, 75-84.

46. J. Journet, W. K. Maser, P. Bernier, A. Loiseau, M. L. de la Chapelle, S. Lefrant, P. Deniard, R. Lee, J. E, Fisher. *Nature*. 1997, **388**, 756-758.

47. S.-D. Wang, M.-H. Chang, K. M.-D. Lan, Ch-Ch. Wu, J.-J. Cheng, H.-K. Chang. *Carbon*. 2005, **43**, 1778-1814.

48. M. Ishigami, J. Cumings, A. Zettl, S. Chen. *Chemical Physics Letters.* 2000, **319**, 457-459.

49. Y.-H. Wang, S.-Ch. Chiu. K.-M. Lin, Y.-Y. Li. *Carbon*. 2004, **42**, 2535-2541.

50. M. Cadek, R. Murphy, B. McCarthy, A. Drury, B. Larh, R. C. Barklie, M. in het Panhuis, J. N. Coleman, W. J. Blau. *Carbon*. 2002, **40**, 923-928.

51. K. Imasaka, Y. Kanakate, Y. Ohshiro, J. Suehiro, M. Hara. *Thin Solid Films.* 2006, 250-254.

52. S. J. Lee, H. K. Baik. J. Yoo, J. H. Han. *Diamond and Related Materials*. 2002, **11**, 914-917.

53. Z. E. Horvath, K. Kertesz, L. Petho, A. A. Koos, L. Tapaszto, Z. Vertesy, Z. Osvath, Al. Darabont, P. Nemes-Incze, Zs. Sarkozi, L. P. Biro. *Current Applied Physics*. 2006, **6**, 135-140.

54. M. Kusaba, Y, Tsunawaki. *Thin Solid Films*. 2006, 255-258.

55. G. Radhakrishnan, P. M. Adams, L. S. Bernstein. *Thin Solid Films.* 2006, **515**, 1142-1146.

56. H. Zhang, Y. Ding, Ch. Wu, Y. chen, Y. Zhu, Y. He. *Physica B.* 2003, **325**, 224-229.

57. E. Muñoz, W. K. Maser, A. M. Benito, M. T. Martinez, G. F. de la Fuente, Y. Maniette, A. Righi, E. Anglaret, J. L. Sauvajol. *Carbon*. 2000, **38**, 1445-1451.

58. W. K. Maser, A. M. Benito, E. Muñoz, G. M. de Val, M. T. Martinez, A. Larrea, G. F. de la Fuente. *Nanotechnology*. 2001, **12**, 147-151.

59. M. Yudasaka, R. Yamada, N. Sensui, T. Wilkins, T. Ichihashi, S. Iijima. *Journal of Physical Chemistry B.* 1999, **103**, 6224-6229.

60. M. Zhang, M. Yudasaka, S. Iijima. *Chemical Physics Letters*. 2001, **331**, 196-200.

61. D. Nishide, H. Kataura, S. Suzuki, K. Tsukagoshi, Y. Aoyagi, Y. Achiba. *Chemical Physics Letters.* 2003, **372**, 45-50.

62. M. Yudasaka, T. Komatsu, T. Ichihashi, Y. Achiba, S. Iijima. *Journal of Physical Chemistry B.* 1998, **102**, 4892-4896.

63. J. Chrzanowska, J. Hoffman, A Małolepszy, T. A. Kowalewski, Z. Szymanski, L. Stobinski. *Basic Solid State Physics B.* 2015, **252**, 1860-1867.

64. N. Braidy, M. A. El Khakani, G. A. Botton. *Carbon*. 2002, **40**, 2835-2842.

65. Y. Gogotsi, J. A. Libera, M. Yoshimura. *Journal of Materials Research.* 2000, **15**, 2591-2594.

66. Y. Gogotsi, N. Naguib, J. A. Libera. *Chemical Physics Letters*. 2002, **365**, 354-360.

67. S. Manafi, H. Nadali, H. R. Irani. *Materials Letters*. 2008, **62**, 4175-4176.

68. J. M. Caldero-Morono, S. S, Swamy, T. Fujino, M. Yoshimura. *Chemical Physics Letters*. 2000, **329**, 317-322.

69. W. K. Hsu, J. P. Hare, M. Terrones, H. W. Kroto, D. R. M. Walton, P. J. H. Harris. *Nature*. 1995, **377**, 687.

70. J. B. Bai, A.-L. Hamon, A. Marraud, B. Jouffrey, V. Zymla. *Chemical Physics Letters.* 2002, **365**, 184-188.

71. Q. Zeng, Z. Li, Y. Zhou. *Journal of Natural Gas Chemistry.* 2006, **15**, 235-246.

72. N. Gorbert. *Materials Today*. 2007, **10**, 28-35.

73. I. A. Novoselova, N. F. Oliinyk, S. V. Volkvok, A. A. Konchits. I. B. Yanchuk. V. s. Yefanov, F. P. kolesnik, M. V, Karpets. *Physica E.* 2008, **39**, 155-158.

74. S. B. Sinnott, R. Andrews. *Critical Reviews in Solid State Materials Sciences*. 2001, **26**, 145-249.

75. E. Flahaut, A. Gividaraj, A. Peigney, C. Laurent, A. Rousset, C. N. R. Rao. *Chemical Physics letters.* 1999, **300**, 236-242.

76. S. S. Fan, M. G. Chapline, N. R. Franklin, T. W. Tombler, A. M. Cassel, H. J. Dai. *Science.* 1999, **283**, 512-514.

77. G. Y. Liu, D. Y. Zhong, S. H. Xia, S. F. Cheng, Y. G. Ding, Y. J. Lu, Y. J. Shao, H. Y. Li, L. J. Hangfu, E. G. Wang. *Applied Surface Science*. 2003, **215**, 209-213.

78. S. Chaisitsak, A. Yamada, M. Konagi. *Diamond and Related Materials.* 2004, **13**, 438-444.

79. K. Hata, D. H. Futaba, K. Nizuno, T. Namai, M. Yamura, S. Iijima. *Science*. 2004, **306**, 1362-1364.

80. G. Zhang, D. Mann, L. Zhang, A. Javey, Y. Li, E. Yenilmez, Q. Wang, J. P. McVittie. Y. Nishi, J. Gibbons, H. Dai. *Proceedings of the National Academy of Sciences of the United States of America*. 2005, **103**, 16141-16145.

81. J. L. Qi, X. Wang, H. W. Tian, Y. S. Peng, C. Liu, W. T. Zheng. *Journal of Alloys and Compounds.* 2009, **486**, 265-272.

82. M. Zhu, J. Wang, R. A. Outlaw, K. Hou, D. M. Manos, D. C. Holloway. *Diamond and Related Materials*. 2007, **16**, 196-201.

83. E. Terado, M. Redrado, E. Munoz, W. K. Maser, A. M. Benito, M. T. Martinez. *Materials Science and Engineering C*. 2006, **26**, 1158-1188.

84. S. Wei. W. P. Kang, J. L. Davidson, J. H. Huang. *Diamond and Related Materials.* 2006, **15**, 1828-1833.

85. Z. G. Cambaz, G. Yushin, S. Osswald, V. Mochalin, Y. Gogotsi. *Carbon*. 2008, **46**, 841-849.

86. G. Yushin, Y. Gogotsi, A. Nikitin. *Nanomaterials Handbook. CRC Press*. 2006, 237-280.

87. M. Kusunoki, T. Suzuki, C. Honjo, T. Hirimaya, N. Shibata. *Chemical Physics Letters*. 2002, **366**, 458-462.

88. J. Harrison, S. N. Sambandam, J. J. Boeckl, W. C. Mitchel, W. E. Collins, W. Lu. *Journal of Applied Physics*. 2007, **101**, 104311 (1-5).

89. J. J. Schneider, N. I. Maksimova, J. Engstler, R. Joshi, R. Schierholz. R. Feile. *Inorganica Chimica Acta*. 2008, **361**, 1770-1778.

90. H. Gao, C. Mu, F. Wang, D. Xu, K. Wu, Y. Xie. *Journal of Applied Physics*. 2003, **93**, 5602-5605.

91. Z. F. Ren, Z. P. Huang D. Z. Wang, J. G. Wen, J. W. Xu. J. H. Wang, L. E. Calvet, J. Chen, J. F. Klemic, M. A. Reed. *Applied Physics Letters*. 1999, **75**, 1086-1088.

92. J. M. Bonard, H. Kind, T. Stockli, L. A. Nilsson. *Solid State Electronics.* 2001, **45**, 893-914.

93. I. Willems, Z. Kónya, J.-F. Colomer, G. van Tendeloo, N. Nagaraju, A. Fonseca, J. B. Nagy. *Chemical Physics Letters*. 2000, **317**, 71-76.

94. Z. Balogh, Gy, Halasi, B. Korbely, K. Hernadi. *Applied Catalysis A: General.* 2008, **344,** 191-197.

95. H. Ago, N. Uehara, N. Yoshihara, M. Tsuji, M. Yumura, N. Tomonaga, T. Setoguchi. *Carbon*. 2006, **44**, 2912-2918.

96. Y. Soneda, L. Duclaux, F. Béguin. *Carbon*. 2002, **40**, 955-971.

97. L. Qingwen, Y. Hao, C. Yan, Z. Jin, L. Zhongfan. *Journal of Materials Chemistry.* 2002, **12**, 1179-1183.

98. C. Valles, M. Perez-Mendoza, W. K. Maser, M. T. Martinez, L. Alvarez, J. L. Sauvajol, A. M. Benito, C. Valles. *Carbon.* 2009, **47**, 998-1004.

99. E. Flahaut, A. Govindaraj, A. Peigney, Ch, Laurent, A. Rousset, C. N. R. Rao. *Chemical Physical Letters.* 1999, **300**, 236-242.

100. K. Hernadi, A. Fonseca, J. B. Nagy, D. Bernaerts, A. Fudala, A. A. Lucas. *Zeolites.* 1996, **17**, 416-423.

101. K. Hernadi, A. Fonseca, P. Piedigrosso, M. Delvaux, J. B. Nagy, D. Bernaerts, J. Riga. *Catalyst Letters*. 1997, **48**, 229-238.

102. H. B. Abdullah, I. Ramli, I. Ismailm N. A. Yusof. *Pertanika Journal of Science and Technology*. 2017, **25**, 379-396.

103. K. Mizuno. K. Hata, T. Saito, M. Yumura, S. Iijima. *The Journal of Physical Chemistry B*. 2005, **109b,** 2632-2637.

104. J. Prasek, J. Drbohlavova, J. Chomoucka, J. Hubalek, O. Jasek, V. adam, R. Kizek. *Journal of Materials Chemistry*. 2011, **21**, 15872-15884.

105. Y. T. Lee. J. H. Han, S. H. Choi, J. B. Yoo, C. Y. Park, T. Jung, S. G. Yu, J. Lee, W. Yi, J. M. Kim. *Surface and Coatings Technology*. 2003, **169-170**, 384-352.

106. Q. Li, H. Yan, J. Zhang, Z. Liu. *Carbon*. 2004, **42**, 829-835.

107. K. Hernadi, A. Fonseca, J. B. Nagy, A. Siska, I. Kiricsi. *Applied Catalysis A: General*. 2000, **199,** 245-255.

108. N. Izadi, A. M. Rashidi, B. A. Horri, M. R. Mosoudi, H. R. Bozorgzadeh, A. Zeraatkar. *Solid State Sciences*. 2011, **13**, 1242-1250.

109. K. Hata, D. N. Futaba, K. Mizuno, T. Manai, M. Yumura, S. Iijima. *Science*. 2004, **306**, 1362-1364.

110. K. Y. Tran, B. Heinrichis, J. F. Colomer, J. P. Pirad, S. Lambert. *Applied Catalysis A: General*. 2007, **318**, 63-69.

111. A. Bachmatiuk, R. J. Kalenezuk, M. H. Rummeli, T. Gemming, E. Borowiak-Palen. *Materials Science-Poland*. 2008, **26**, 105-111.

112. M. Escobar, M. S. Moreno, R. J. Candal, M. C. Marchi, A. Caso, P. I. Polosecki, G. H. Rubiolo, S. Goyanes. *Applied Surface Science.* 2007, **254**, 251-256.

113. G. Allaedini, S. M. Tasirin, P. Aminayi. *Journal of Alloys and Compounds.* 2015, **647**, 809-814.

114. Z. Y. Zhan, Y. N. Zhang, G. Z. Sun, L. X. Zheng, K. Liao. *Applied Surface Science.* 2011, **257**, 7704-7708.

115. T. Altalhi, M. Ginic-Markovic, N. Han, S. Clarke, D. Losic. *Membranes (Basel)*. 2010, **1**, 37-47.

116. L. Tapasztó, K. Kertész, Z. Vértesy, Z. E. Horváth, A. A. Koós. Z. Osváth, Zs. Sárközi, Al. Darabont, L. P. Biró. *Carbon*. 2005, **43**, 970-977.

117. X. Liu, Y. Yang, H. Liu, W. Ji, C. Zhang, B. Xu. *Materials Letters.* 2007, **61**, 3916-3919.

118. T. J. Chee, M. Aziz, A. F. Ismail. *Jurnal Teknologi.* 2008, **49**, 141-147.

119. S. Zhan, Y. Tian, Y. Cui, H. Wu, Y. Wang, S. Ye, Y. Chen. *China Particuology*. 2007, **5**, 213-219.

120. I. A. Mohammed, M. T. Bankole, A. S. Abdulkareem, S. S. Ochigbo, A. S. Afolabi, O. K. Abubakre. *South African Journal of Chemical Engineering*. 2017, **24**, 17-42.

121. C. J. Lee, S. C. Lyu, H.-W. Kim, C.-Y. Park, C.-W. Yang. *Chemical Physics Letters*. 2002, **359**, 109-114.

122. K. J. MacKenzie, O. M. Dunens, A. T. Harris. *Industrial Engineering and Chemistry Research*. 2010, **49**, 5323-5338.

123. J. P. Tessonnier, D. S. Su. *ChemSusChem*. 2011, **4**, 824-847.

124. Z. Niu, Y. Fang. *Journal of Crystal Growth*. 2006, **297**, 288-233.

125. I. Abdullahi, N. Sakulchaichareon, J. E. Herrera. *Diamond and Related Materials*. 2014, **41**, 84-93.

126. M. Monthioux. *Carbon Meta-Nanotubes: Synthesis, Properties and Applications*. *United Kingdom, UK: John Wiley and Sons Ltd.* 2011.

127. J. Gallego, G. Sierra, F. Mondragon, J. Barrault, C. Batiot-Dupeyrat. *Applied Catalysis A: General*. 2011, **397**, 73-81.

128. L. Ni, K. Kuroda, L.-P. Zhou, T. Kizuka, K. Matsuishi, J. Nakamura. *Carbon*. 2006, **44**, 2265-2272.

129. E. Dündar-Tekkaya, N. Karatepe. *Fullerenes, Nanotubes and Carbon nanostructures.* 2104, **23**, 535-541.

130. G. Saeed. M. Umer. Farooq. *Optoelectronics and Advanced Materials-Rapid Communications*. 2013, **7**, 707-711.

131. M. Kumar, Y. Ando. *Journal of Nanoscience and Nanotechnology.* 2010, **10**, 3739-3758.

132. D. Mann. *Carbon nanotubes: properties and application. Taylor and Francis Group. Boca Raton*. 2006, **Chapter 2**, 19-49.

133. M. Kumar, Y. Ando. *Nanotechnology Perceptions.* 2010, **8**, 147-170.

134. A. Gohier. C. P. Ewels, T. M. Minea. M. A. Djouadi. *Carbon*. 2008, **46**, 1331-1338.

135. R. T. K. Baker. M. A. Barber, P. S. Harris. F. S. Feates, R. J. Waite. *Journal of Catalysis.* 1972, **26**, 51-62.

136. R. T. K. Baker, R. J. Waite. *Journal of Catalysis.* 1975, **37**, 101-105.

137. J. P. Gore, A. Sane. *Carbon Nanotube-Synthesis, Characterizations, Applications. InTech. Croatia.* 2011, 121-146.

138. S. B. Sinnot, R. Andrews, D. Qian, A. M. Rao, Z. Mao, E. C. Dickey, F. Derbyshire. *Chemical Physic Letters.* 1999, **315**, 25-30.

139. J.-M Bonard, T. Stora, J.-P. Salvetat, F. Maier, T. Stöckli, C. Duschl, L. Forró, W. A. de Heer, A. Châtelain. *Advanced Materials*. 1997, **9**, 827-831.

140. P. X. Hou, S. Bai, Q. H. Yang, C. Liu, H. M. Cheng. *Carbon*, 2002, **40**, 81-85.

141. A. C. Dillion, T. Genneu, K. M. Jones, J. L. Alleman, P. A. Parilla, M. J. Heben. *Advanced Materials.* 1999, **103**, 1354-1358.

142. A. G. Rinzler, J. Liu, H. Dai, P. Nikolaev, F. J. Rodríguez, P. J. Boul. A. H. Lu, D. Heymann, D. T. Colbert, R. S. Lee. J. E. Fischer, A. M, Rao. P. C. Eklund, R. E. Smalley. *Applied Physics A.* 1998, **67**, 29-37.

143. W. A. de Heer, P. M. Ayajan. A. Chëtelain, T. Gerfin, R. Humphrey-Baker, L. Forro, D. Ugarte. *Science*. 1995, **268**, 845-847.

144. K. Hernadi, A. Fonseca, J. B. Nagy, B. Bernaerts. J. Riga, A. Lucas. *Synthetic Metals*. 1996, **77**, 31-34.

145. S. Bandow. *Journal of Applied Physics.* 1996, **80**, 1020-1027.

146. E. Couteau, K. Hernadi, J. W. Seo, L. Thiên-Nga, Cs. Mikó, R. Gaál. L. Forró. *Chemical Physical Letters*. 2003, **378**, 9-17.

147. R. J. Hunter. *Introduction to Morden Colloid Science*. *Oxford University Press, Oxford*. 1993.

148. G. S. Duesberg, J. Muster, H. J. Byrne, S. Roth, M. Burghard. *Applied Physics A.* 1999, **69**, 269-274.

149. E. J. Wanless, W. A. Drucker. *Journal of Physical Chemistry.* 1996, **100**, 3207-3214.

150. G. S. Duesberg, M. Burghard, J. Muster, G. Philipp, S. Roth. *Chemical Communications.* 1998, **3**, 435-436.

151. S. Asakura, F. Oosawa. *Journal of Chemical Physics.* 1954, **22**, 1255-1256.

152. F. T. Edelman, *Angewandte Chemie International Edition*. 1999, **38**, 1381-1387.

153. P.-X. Hou, C. Liu, H.-M. Cheng. *Carbon*. 2008, **46**, 2003-2025.

154. K. Hernadi, A. Siska, L. Thiên-Nga. L. Forró, I. Kiricsi. *Solid State Ionics*. 2001, **142-142**, 203-209.

155. Y. K. Chen, M. L. H. Green, J. Hammer, R. M. Lago, S. C. Tsang. *Advanced Materials.* 1996, **8**, 1012-1015.

156. P. X. Hou, S. Bai, Q. H. Yang, C. Liu, H. M. Cheng. *Carbon*. 2002, **40**, 81-85.

157. E. L. Khim Chng, H. L. Poh, Z. Sofer. M. Pumera. *Physical Chemistry Chemical Physics*. 2013, **15**, 5615-5619.

158. S. C. Tsang, P. F. J. Harris, M. L. H. Green. *Nature*. 1993, **362**, 520-522.

159. L. S. K. Pang, J. D. Saxby, S. Peter. Chatfield. *Journal of Physical Chemistry*. 1993, **97**, 6941-6942.

160. J.-F. Colomer, C. Stephan, S. Lefrant, G. van Tendeloo, I. Willems, Z. Kónya, A. Fonseca, Ch. Laurent, J. B. Nagy. *Chemical Physics Letters.* 2000, **317**, 83-89.

161. L. Vaccarani, C. Goze, R. Aznar, V. Micholet, C. Journet, P. Bernier. *Synthetic Metals.* 1999, **103**, 2492-2493.

162. H. Hiura, T. W. Ebbesen, K. Tanigaki. *Advanced Materials*. 1995, **7**, 275-276.

163. N. Yao, V. Lordi, S. X. C. Ma, E. Dujardine, A. Krishnan, M. M. J. Treacy, T. W. Ebessen. *Journal of Material Science.* 1998, **13**, 2432-2437.

164. L. A. Algharagholy. *Journal of Electronic Materials.* 2019, **48**, 2301-2306.

165. A. M. Patel, N. Gosai, A. Y. Joshi. *Applied Mechanics and Materials.* 2015, **813-814**, 145-150.

166. H.-Y. He, B.-C, Pan. *Frontiers of Physics in China.* 2009, **4**, 297-306.

167. A. H. Brozena, J. D. Leads, Y. Zhang, J. T. Fourkas, Y. Wang. *ACS Nano*. 2014, **8**, 4239-4247.

168. J. Zhu, A. S. Childress, M. Karakaya, S. Dandeliya, A. Srivastava, Y. Lin, A. M. Rao, R. Podila. *Advanced Materials*. 2016, **28**, 7185-7192.

169. P. M. Ajayan, T. Ichihashi, S. Iijima. *Chemical Physics Letters.* 1993, **202**, 384-388.

170. S. Iijima, T. Ichihashi, Y. Ando. *Nature*. 1992, **356**, 776-778.

171. W. D. Nicholls, M. K. Borg, D. A. Lockerby, J. M. Reese. *Molecular Simulation*. 2012, **38**, 781-785.

172. I. Fenoglio, G. Greco, M. Tomatis, J. Muller, E. Raymundo-Piñero, F. Bénguin. A. Fonseca, J. B. Nagy, D. Lison, B. Fubini. *Chemical Research in Toxicology.* 2008, **21**, 1690-1697.

173. M. Terrones. *Acta Microscópica*. 2007, **16**, 33-34.

174. R. Rafiee, R. Pourazizi. *Materials Research*. 2014, **17**, 758-766.

175. M.-H. Yeh, Y.-A. Leu, W.-H. Chiang, Y.-S. Li, G.-L. Chen, T.-J. Li, L.-Y. Chang, L.-Y. Lin, K.-C. Ho. *Journal of Power Sources.* 2018, **375**, 29-36.

176. C. H. Lau, R. Cerveni, S. R. Clarke, M. G. Markovic, J. G. Matisons, S. C. Hawkins, C. P. Huynh. G. P. Simon. *Journal of Nanoparticle Research.* 2008, **10**, 77-88.

177. S. Saito. *Science*. 1997, **278**, 77-78.

178. M. Zhang, L. Su. L. Mao. *Carbon*. 2006, **44**, 276-283.

179. R. Murphy, J. N. Coleman, M. Cadek, B. McCarthy, M. Bent, A. Drury, R. C. Barklie, W. J. Blau. *Journal of Physical Chemistry B.* 2002, **106**, 3087-3091.

180. E. E. Tkayla, M. Ghislandi, G. de With, C. E. Koning. *Current Opinion in Colloid and Interface Science.* 2012, **17**, 225-232.

181. M. A. M. Motchelaho, H. Xiong, M. Moyo, L. L. Jewell, N. J. Coville. *Journal of Molecular Catalysis A: Chemical*. 2011, **335**, 189-198.

182. M. A. Hamon, C. H. Jian, M. Chen, E. L. Apparao, M. Rao, P. C. Eklund. P. C. Haddon. *Advanced Materials*. 1999, **11**, 834-840.

183. M.-L. Sham, J.-K. Kim. *Carbon*. 2006, **44**, 768-777.

184. M. Holzinger, O. Vostrowsky, F. Hennrich, M. Kappes, R. Weiss, F. Jellen. *Angewandte Chemie International Edition*. 2001, **40**, 4002-4005.

185. S. Banerjee, S. S. Wong. *Journal of Physical Chemistry B*. 2002, **106**, 12144-12151.

186. C. Mattevi, G. Eda, S. Agnoli, S. Miller, K. A. Mkhoyan, O. Celik, D. Mostrogiovanni, G. Granozzi, E. Garfunkel, M. Chhowalla, *Advanced Functional Materials*. 2009, **19**, 2577-2583.

187. Z. N. Tetana, S. D. Mhlanga, G. Bepete, R. W. M. Krause, N. J. Coville. *South African Journal of Chemistry*. 2012, **65**, 39-49.

188. S. van Dommele, A. Romero-Izquirdo, R. Brydson, K. P. de Jong. J. H. Bitter. *Carbon*. 2008, **46**, 138-148.

189. O. Stephan, P. Ajayan. *Science*. 1994, **266**, 1863-1865.

190. M. Terrones, P. M. Ajayan, F. Banhart, X. Blasé, D. L. Carrol, J.-C. Charlier, R. Czerw, B. Foley, N. Grobert, R. Kamalakaran, P. Kohler-Redlich, M. Ruhle, T. Seeger, H. Terrones. *Applied Physics A: Materials.* 2002, **74**, 355-361.

191. Y.-A. Leu, M.-H. Yeh, L-Y. Lin, T.-J. Li, L.-Y. Chang, S.-Y. Shen, Y.-S. Li, G.-L. Chen, W.-H. Chiang, J.-J. Lin. K.-C. Hao. *ACS Sustainable Chemistry and Engineering.* 2017, **5**, 537-546.

192. J. Han, L. L. Zhang, S. Lee, J. Oh, K. S. Lee. J. R. Potts, J. Ji, X. Zhao, R. S. Ruoff, S. Park. *ACS Nano*. 2013, **7**, 19-26.

193. W.-H. Chiang, C.-Y. Hsieh, S.-C. Lo, Y.-C. Chang, T. Kawai, Y. Nonoguchi. *Carbon*. 2016, **109**, 49-56.

194. Z. N. Tetana. *Boron and nitrogen doped carbons for photochemical degradation reactions. University of the Witwatersrand.* PhD thesis; 2013.

195. C. P. Ewels, M. Glerup. *Journal of Nanoscience and Nanotechnology.* 2005, **5**, 1345-1363.

196. T. Hamada, K. Suzuki, T. Kohno, T. Suguira. *Carbon*. 2002, **40**, 1203-1210.

197. X.Wang, J. S. Lee, Q. Zhu, J. Liu, Y.Wang, S. Dai. *Chemistry of Materials*. 2010, **22**, 2178-2180.

198. L. T. Qu, Y. Liu, J. B. Baek, L. M. Dai. *Acs Nano*. 2010, **4**, 1321-1326.

199. D. S. Yu, Q. Zhang, L. M. Dai. *Journal of American Chemical Society*. 2010, **132**, 15127-15129.

200. T. J. Coutts, X. Li, T. M. Barnes, B. M. Keyes, C. L. Perkins, S. E. Asher, S. B. Zhang, S.-H. Wei, S. Limpijumnong. *Zinc Oxide Bulk, Thin Films and Nanostructures; Processing, Properties and Applications. Elsevier*. 2006. Chapter 3, page 43-84.

201. Y. Fu, H. Du, W. Huang, S. Zhang, M. Hu. *Sensors and Actuators A: Physical.* 2004, **112**, 395-408.

202. X. Wu. *Solar Energy*. 2004, **77**, 803-814.

203. C. Chaneliere, J. L. Autran, R. A. B. Devine, B. Balland. *Materials Science and Engineering: R: Reports.* 1998, **22**, 269-322.

204. H. Kangarlou, A. Rafizadeh. *Optik-International Journal for Light and Electronic Optics.* 2013, **124**, 2787-2790.

205. L.-J Meng, F. Placido. *Surface and Coatings Technology*. 2003, **166**, 44-50.

206. G. Ozaydin-Ince, A. M. Coclite, K. K. Gleason. *Reports of Progress in Physics.* 2012, **75**, 016501(1-41).

207. T. López-Luke, A. Wolcott, L.-P. Xu, S. Chen, Z. Wen, J. Li, E. De La Rosa, J. Z. Zhang. *Journal of Physical Chemistry C*. 2008, **112**, 1282-1292.

208. C. J. Petti, M. M. Hilali, G. Prabhu. *Handbook of Thin Film Deposition (3rd edition)*. 2012, 313-359.

209. P. Ngene, R. J. Westerwaal, S. Sachdeva, W. H. Louis, C. P. M. de Smet, B. Dam. *Angewandte Chemie*. 2014, **126**, 12277-12281.

210. K. Mylvaganam, Y. Chen, W. Liu, M. Liu, L. Zhang. *Anti-Abrasive Nanocoatings.* 2015, 543-567.

211. S. E. Snow, P. J. Novak, M. P. Cambell, D. Park. *Applied Physics Letters.* 2003, **82**, 2145-2147.

212. L. Fu, A. M. Yu. *Reviews of Advanced Materials.* 2014, **36**, 40-61.

213. I. Yahya, S. M. Mustaza, H. Abdullah. *Transparent Conducting Films*. 2018, chapter 4, 53-71.

214. E. Bekyarova, M. E. Itkis, N. Cabrera, B. Zhao, A. P. Yu, J. B. Gao, R. C. Haddon. *Journal of the American Chemical Society.* 2005, **127**, 5990-5995.

215. A. B. Kaiser, V. Skakalova, S. Roth. *Physica E.* 2008, **40**, 2311-2318.

216. B. Smith, K. Wepansnick, K. E. Schrote, A. R. Bertele, W. P. Ball, C. O'Melia, D. H. Fairbrother. *Environmental Science and Technology.* 2009, **43**, 819-825.

217. I. D. Rosca, F. Watari, M. Uo, T. Akasaka. *Carbon.* 2005, **43**, 3124-3131.

218. N. Savage, S. M. Diallo. *Journal of Nanoparticle Research.* 2005, **7**, 331-342.

219. G. Sun, Z. Liu, G. Chen. *NANO: Brief Reports and Reviews.* 2010, **5**, 103-109.

220. K. Jagadish, S. Srikantaswamy, K. Byrappa, L. Shruthi, M. R. Abhilash. *Journal of Nanomaterials: Hindawi.* 2015, 1-6.

221. L. Vaisman, H. D. Wagner, G. Marom. *Advances in Colloid and Interface Science.* 2006, **128-130**, 37-46.

222. W. H. Duan, Q. Wang, F. Collins. *Chemical Science.* 2011, **2**, 1407-1413.

223. S. M. Strano, A. C. Dyke, L. M. Usrey, W. P. Barone, J. M. Allen, W. H. Shan, C. Kittrell, H. R. Hauge, M. J. Tour, E. R. Smalley. *Science*. 2003, **301**, 1519-1522.

224. M. Zhang, S. L. Fang, A. A. Zakhidov, S. B. Lee, A. E. Aliev, C. D. Williams, K. R. Atkinson, R. H. Baughman. *Science*. 2005, **309**, 1215-1219.

225. X. Dong, B. Li, A. Wei, X. Cao, M. B. Chan-Park, H. Zhang, L.-J. Li, W. Huang, P. Chen. *Carbon*. 2011, **49**, 2944-2949.

226. L. Marot, T. de los Arcos, A. M. Bünzli, C. Wäckerlin, R. Steiner, P. Oelhafen, E. Meyer, D. Mathys, P. Spätig, G. Covarel. *Surface and Coatings Technology.* 2012, **212**, 223-228.

227. E. Ramasamy, W. J. Lee, D. Y. Lee, J. S. Song. *Electrochemistry Communications.* 2008, **10**, 1087-1089.

228. A. Schindler, J. Brill, N. Fruehauf, J. P. Novak, Z. Yaniv. *Physica E: Low-dimensional Systems and Nanostructures.* 2007, **37**, 119-123.

229. N. Saran, K. Parikh, D.-S. Suh, E. Muñoz, H. Kolla, S. K. Manohar. *Journal of American Chemical Society.* 2004, **126**, 4462-4463.

230. V. Bliznyuk, S. Singamaneni, R. Kattumenu. *Applied Physics Letters*. 2006, **88**, 164101 (1-3).

231. M. A. Seo, J. H. Yim, Y. H. Ahn, F. Rotermund, D. S. Kim. S. Lee, H. Lim. *Applied Physics Letters*. 2008, **93**, 231905 (1-3).

232. B. Safadi, R. Andrews, E. A. Grulke. *Journal of Applied Polymer Science*. 2002, **84**, 2660-2669.

233. W. Ding, V. Koutsos, J. H. Si, Z. X. Song. *Advanced Materials Research.* 2012, **569**, 15-18.

234. M. Eslamian, F. Soltani-Kordshuli. *Journal of Coatings Technology and Research.* 2018, **15**, 271-280.

235. E. Eslamian, F. Zabihi. *Nanoscale Research Letters*. 2015, **10**, 462 (1-5).

236. C. Luo, X. Zuo, L. Wang, S. Song, J. Wang, C. Fan, Y. Chao. *Nano Letters*. 2008, **8**, 4454-4458.

237. L. Berguiga, J. Bellessa, F. Vocanson, E. Bernstein, J. C. Plenet. *Optical Materials.* 2006, **28**, 167-171.

238. J. Zhang, Y. Wang, J. Zang, G. Xin, Y. Yuan, X. Qu. *Carbon*. 2012, **50**, 5196-5202.

239. F. Su, C. Liu, J. Guo, P. Huang. *Surface and Coatings Technology.* 2013, **217**, 94-104.

240. N. Alexeyeva, J. Kozlova, V. Sammelselg, P. Ritslaid, H. Mändar, K. Tammeveski. *Applied Surface Science.* 2010, **256**, 3040-3046.

241. A. Yu, X. Zhang, H. Zhang, D. Han, A. R. Knight. *Electrochimica Acta*. 2011, **56**, 9015-9019.

242. I. N. Obotowo, I. B. Obot, V. J. Ekpe. *Journal of Molecular structure.* 2016, **1122**, 80-87.

243. A. Hagfeldt, G. Boschloo, L. Sun, L. Kloo, H. Perterson, *Chemical Reviews*. 2011, **11**, 6595.

244. H. Hoppe, N. S. Saricifcti. *Advances in Polymer Science*. 2008, **214**, 1-86.

245. N. Yeh, P. Yeh. *Renewable and Sustainable Energy Reviews*. 2013, **21**, 420-431.

246. M . Hočevar, U. O. Krašovec, M. Berginc, G. Dražič, N. Hauptman, M. Topič. *Journal of Sol-Gel Science and Technology.* 2008, **48**, 156-162.

247. K. Tennakone, G. R. R. A. Kumara, I. R. M. Kottegoda, P. VPS. *Chemical Communications.* 1999, **1**, 15-16.

248. K. Sayama, H. Sugihara, H. Arakawa. *Chemistry of Materials.*1998, **10**, 3825-3832.

249. K. Sharma, V. Sharma, S. S. Sharma. *Nanoscale Research Letters*. 2018, **13**, 1-46.

250. J. Wu, Z. Lan, J. Lin, M. Huang, Y. Huang, L. Fan, G. Luo, Y. Lin, Y. Xie, Y. Wei. *Chemical Society Reviews.* 2017, **46**, 5975-6023.

251. M. Chen, L.-L. Shao. *Chemical Engineering Journal*. 2016, **304**, 629-645.

252. A. Jena, S. P. Mohanty, P. Kumar, J. Naduvath, D. Gondane, P. Lekha, J. Das, H. K. Narula, S. Mallick, P. Bhargava. *Transactions of the Indian Ceramic Society.* 2012, **71**, 1-16.

253. F. M. Al-Marzouki, S. Abdalla, S. Al-Ameer. *Advances in Materials Science and Engineering: Hindawi.* 2016, 4928710 (1-13).

254. T. Brown, F. De Rossi, F. Di Giacomo, G. Mincuzzi, V. Zadetto, A. Reale, A. Di Carlo. *Journal of Material Chemistry A.* 2014, **2**, 10788-10817.

255. N. Kumara, A. Lim, C. M. Lim, M. I. Petra, P. Ekanayake. *Renewable and Sustainable Energy Reviews.* 2017, **78**, 301-317.

256. I. ShinH. Seo, M.-K. Son, J.-K. Kim, K. Prabakar, H.-J. Kim. *Current Applied Physics.* 2010, **10**, S422-S424.

257. A. Mashreghi, M. Ghasemi. *Renewable Energy*. 2015, **75**, 481-488.

258. A. Mashreghi, F. Davoudi. *Materials Science in Semiconductor Processing.* 2015, **30**, 618-624.

259. A. Mashreghi, F. B. Moghadam. *Journal of Solid State Electrochemistry.* 2016, **20**, 1361-1368.

260. S. Ferrere, A. Zaban, B. A. Gregg. *Journal of Physical Chemistry B*. 1997, **101**, 4490-4493.

261. G. Oskam, B. V. Bergeron, G. J. Meyer, P. C. Searson. *Journal of Physical Chemistry B.* 2001, **105**, 6867-6873.

262. H. Nusbaumer, J. E. Moser, S. M. Zakeeruddin, M. K. Nazeeruddin, M. Grätzel. *Journal of Physical Chemistry B.* 2001, **105**, 10461-10464.

Chapter 3: Synthesis of pristine MWCNTs using a Fe-Co/$CaCO_3$ catalyst.

3.1. Introduction

Carbon nanotubes (CNTs) have become a pivotal part in the development of a carbon-based nanotechnology world. Many different types of CNTs have been produced with unique characteristics. Due to their diverse and unique methods of production and subsequent different properties, the CNTs with single or multi-walls have been extensively investigated and utilized in biomedical applications[1-3], drug delivery systems[4-6], and electronic devices[7-8] such as super-capacitors[9-10], sensors[11-12], fuel cells[13-14] and photovoltaic devices[15-20]. Multi-walled carbon nanotubes (MWCNTs) have exhibited great utility in these various applications because of their high mechanical, electrical and thermal properties.[21-23]

Various methods such as the *arc discharge*[24-25], *laser ablation*[26-27], *ball milling*[28-29], *hydrothermal*[30-31], *electrolysis*[32-33], and the *chemical vapour deposition (CVD)*[22, 34-35] have been developed for the production of different types of MWCNTs. The *CVD* method, more specifically its variant, the *catalytic chemical vapour deposition (CCVD)* method, for the large-scale products of CNTs, has attained the status of being the most used process for a cost effective, high purity, high yielding synthesis of MWCNTs.[36-38] In this method many factors determine the type and quality of MWCNTs produced. These include the type of catalyst and its support material, the carbon source (e.g., ethylene, methane), the reaction atmosphere (i.e., N_2, Ar, H_2), temperature (normally around 700-1000℃, although lower and higher temperature have been reported), pressure, reaction time, and the flow rate of carbon source and carrier gases.[22, 37, 39-41]

The catalyst support of choice and its preparation method play a special role in the production of MWCNTs. Metal nanoparticles are used as catalysts. The technique for their deposition and dispersion onto the support, and their particle size determine the morphological properties of the MWCNTs (i.e., diameter, length etc).[42-44] Furthermore, the support has been demonstrated to control the size of the metal nanoparticles, and thus influence the morphology of the MWCNTs produced. Metals ranging from Co, Al, Fe, Ni, Mo on different supports such as SiO_2, Al_2O_3, MgO have been used to prepare pristine MWCNTs with different morphologies and properties, some examples are shown in Table 3.1.[25]

Table 3.1: Synthesis of pristine MWCNTs using *CCVD* method under different conditions.

Conditions (temperature, time, carbon source, carrier gas.)	**Catalyst/Support.**	**Catalyst preparation method.**	**Reported MWCNTs Characteristics.**	**References**
650 ℃, 30 min, C_2H_2, H_2.	Fe/MgO.	Liquid impregnation and co-impregnation process.	Cluster of uniformly packed, high purity MWCNTs: Outer diameter of 20-30 nm.	45
400-600℃, 1 h, C_2H_2, N_2.	Ni/MgO, Co_3O_4/MgO, Fe_3O_4/MgO.	Wet impregnation method.	Average diameter: 16 nm, 29 nm, 70 nm.	46
700-800℃, 10 h, CH_4,	Fe/Al_2O_3 Fe-Co/Al_2O_3	Fused catalyst method.	Combination of short and long, straight, hollow cores and bamboo MWCNTs with average diameter of 12 nm	47
800℃, 1 h, C_2H_2, H_2-Ar	Ferrocene	---	Vertically aligned MWCNTs.**	48
700-800℃, 45-55 min, acetylene, Ar.	Fe-Co/Kaolin.	Wet impregnation method.	Granular and thick tubular intercalated bundles.**	49

800-1000℃, 15-35 min, C_2H_2, Ar.	NiO/Al_2O_3.	Wet impregnation method.	Well aligned with a combination of twisted and entangled MWCNTs. Outer diameter ranges from 14-65 nm	50
600-800℃, 60 min, ethylene-H_2, Ar.	Fe_2O_3/Al_2O_3	Co-precipitation.	Dense and aligned forests. Outer diameter of 20-30 nm.	51
650℃, 30 min, C_2H_2, H_2 and N_2.	Ferrocene/Water hyacinth	Incipient wetness impregnation method.	Entangled Bamboo like structures.**	52

** Diameters not reported

Despite the extensive variety of CNTs that can be obtained from the use of the *CCVD* method, it still presents challenges such as the removal of the catalyst-support and the carbon by-products. For example, it has been demonstrated that the removal of supports such as silica gel and zeolites is difficult and require multiple steps that may damage the structure of CNTs.[49, 53] A diversity of metal catalysts have been used, but Fe and Co, and more specifically their bimetallic version, Fe-Co, have been reported to be one of the most active catalyst systems. Indeed, major success has been achieved in producing MWCNTs using Fe, Co, Fe-Co.[54-58] Furthermore, given the challenges associated with the removal of the support post synthesis, it is essential to choose a support that can be 'readily' removed.

Supports such as MgO and $CaCO_3$ have become attractive because they can be easily removed/washed off post synthesis (Table 3.2).[45, 59-69] The advantages of using $CaCO_3$ includes that it decomposes into CaO and CO_2 during the reaction (for temperatures > 700).[59] CaO can be washed off using dilute acids such as HCl, H_2SO_4, HNO_3 etc.[66] For example, Cheng and co-workers produced CNTs in high yield from using $CaCO_3$ as support.[54] Couteau *et al.* performed a large scale production of highly pure MWCNTs using acetylene as a carbon source over

various Fe, Co, and Fe-Co catalysts supported on $CaCO_3$,[66] some examples are shown in Table 3.2.

Table 3.2: Synthesis of pristine MWCNTs using *CCVD* method over an Fe-Co/$CaCO_3$ catalyst.

Conditions (temperature, time, carbon source, carrier gas.)	**Catalyst preparation method.**	**Purification method.**	**Reported MWCNTs morphology.**	**References**
700℃, 1 h, C_2H_2, Ar.	Wet impregnation method	30% HNO_3 and H_2SO_4 under reflux.	Densely distributed MWCNTs with reduced agglomeration. Average diameter of 25 nm	60
700℃, 1 h, C_2H_2, Ar.	Wet impregnation method	Mixture of 30% H_2SO_4 and 10% HNO_3 (*v/v* 3:1) under sonication.	Randomly oriented with smaller degree of entanglement. Average diameter of 23-73 nm.	61
720℃, 30 min, C_2H_2, N_2.	Wet impregnation method	Stirred in HCl for 30 min, followed by stirring in distilled water overnight.	Entangled and agglomerated MWCNTs with rough surfaces and average diameter of 5-25 nm.	62

700℃, 1 h, C_2H_2, N_2.	Wet impregnation method	Treated with 55% HNO_3 under reflux.	Randomly arranged MWCTNs with open tips with an average diameter of 9.8 nm.	63
700℃, 1 h, C_2H_2, N_2.	Wet impregnation method	Two methods: treated with 30% and 55% HNO_3 under reflux.	MWCNTs presenting with both smooth and rough surfaces. With an outer and inner average diameter of 8-18 nm and 20-35 nm, respectively.	64
700-900℃, 1 h, C_2H_2, N_2.	Fe-Co/$CaCO_3$	Stirred in 30% HNO_3 for 30 min.	Irregular coiled spaghetti like shape MWCNTs. Inner and outer diameter ranges: 7-79 nm and 29-108 nm, respectively.	65
720℃, 30 min, C_2H_2, N_2.	Co/$CaCO_3$, Fe(II)/$CaCO_3$, Fe(III)/$CaCO_3$, Fe(II)-Co/$CaCO_3$,	Sonicated in dilute 30% HNO_3 for 30 min.	Well graphitized wall structures.**	66

	Fe(III)-Co/$CaCO_3$.			
750, 30 min, C_2H_2, N_2.	Fe-Co/$CaCO_3$	30% HNO_3 under reflux for 24 h.	Length < 10 μm, average diameter: 58 nm	67
700, 1 h, C_2H_2, N_2.	Fe-Co/$CaCO_3$	No purification method reported.	Graphitic nanomaterial, MWCNTs not well defined**	68
720, C_2H_2, N_2.	Fe-Co/$CaCO_3$	30% HNO_3 under sonication for 30 min.	Only SEM images reported**	69

** Diameters not reported

The use Fe-Co/$CaCO_3$ to produce MWCNTs using the CVD method and its subsequent removal (Table 3.2) have been investigated. Reports indicate that Fe-Co/$CaCO_3$ catalyst prepared using the different methods (even when the precursors are the same), can yield MWCNTs with varying properties.[60-69] However, an investigation by Mhlanga *et al*. using Fe-Co/$CaCO_3$ catalysts made from different precursors (nitrate solutions versus acetate solutions) using three different methods (wet impregnation, deposition precipitation and reverse micelles) indicated no significant differences in the CNT sizes or physical properties when the particle sizes of the catalyst were the same.[70] Despite what appears to be contradicting reports, different reaction conditions (time, drying time, calcination temperature, stirring speed) in the synthesis of the catalyst appear to determine the properties of the obtained catalyst, and the produced MWCNTs.[61]

The use of the Fe-Co/$CaCO_3$ catalyst offers advantages such as ease of production and availability of a variety of preparation methods and has exhibited great utility and versatility in the production of diverse MWCNTs. Several simple methodologies exist for the removal of the catalyst from the obtained samples. The catalyst removal can be achieved under different

reaction conditions, i.e., different temperatures, reaction times etc or combination thereof. It is with this backdrop that the study in this chapter is based.

In this chapter the influence of Fe-Co/$CaCO_3$ preparation methods on the type of MWCNTs produced is assessed. Fe-Co/$CaCO_3$ catalysts were prepared using the same precursors using different heating media and reaction times. Conventional/thermal heating is the most used method in the production of the Fe-Co/$CaCO_3$ catalyst. It can be difficult to control the uniformity of the properties of the catalyst produced using this methodology. On the other hand, microwave irradiation offers a fast and efficient method that can give highly reproducible reactions and allows for high heating rates and shorter reaction times.[71-74]

To elucidate the significance of Fe-Co/$CaCO_3$ production methods on the properties of MWCNTs, two studies were carried out:

1. Three Fe-Co/$CaCO_3$ catalysts were synthesized using the wet impregnation method, one was prepared using thermal heating, and two using microwave irradiation. The influence of microwave irradiation time and consequently amount of energy supplied to the reaction was also explored. These were then used to produce MWCNTs using identical reaction conditions.

2. The effects of temperature (700℃, 750℃, 800℃) on the synthesis of MWCNTs using one of the Fe-Co/$CaCO_3$ catalyst obtained from microwave irradiation were also investigated.

3.2. Materials and Methods

3.2.1. Starting Materials

The materials used in all the experiments were of analytical grade and required no additional purification. Calcium carbonate ($CaCO_3$, 98%), iron (III) nitrate nonahydrate ($Fe(NO_3)_3 9H_2O$, 98%), cobalt(II) nitrate hexahydrate ($Co(NO_3)_2 6H_2O$, 98%), ethylene glycol (99%), and 55% nitric acid (HNO_3) were bought from Sigma Aldrich South Africa. The water used in all the experiments was distilled. The gases (ethylene (C_2H_2) and nitrogen (N_2), 99.99%) utilized were obtained from Afrox, South Africa.

3.2.2. Synthesis of 10% Fe-Co/$CaCO_3$ catalyst.

A 10% Fe-Co/$CaCO_3$ catalyst was prepared using the incipient wetness impregnation method under three different conditions. Method A and B involved microwave irradiation, while method C utilized conventional heating. The catalysts were prepared from $CaCO_3$ $Fe(NO_3)_3 9H_2O$, $Co(NO_3)_2 6H_2O$ and ethylene glycol (Sigma Aldrich), except for the substitution of ethylene glycol with water in method C. The reagents did not require any additional purification or processing prior to use.

Method A

Metal nitrates, $Fe(NO_3)_3 9H_2O$ (3.6 g) and $Co(NO_3)_2 6H_2O$ (2.4 g), were milled together to enhance their solubility, and dissolved in ethylene glycol (25 ml). $CaCO_3$ (9.0 g) was dissolved in ethylene glycol (35 ml), and the metal nitrate solution was added dropwise to it and the resulting solution was left to stir for 15 min, followed by sonication for 26 min. The solution was distributed equally by weight into 4 microwave vessels. These were subsequently placed under microwave irradiation for 1 h (preceded by 40 min ramping time) at a constant temperature of 160 ℃ , with the power set not to exceed 500 watts. The resulting mixture was filtered under vacuum, and a wet brown solid was isolated and dried at 120 ℃ for 12 h. The dried solid was ground, sieved (< 150 μm) and calcined at 400 ℃ for 16 h to remove the nitrates, resulting in the synthesis of a brown solid (*catalyst 1*).

Method B

Metal nitrates, $Fe(NO_3)_3 9H_2O$ (3.6 g) and $Co(NO_3)_2 6H_2O$ (2.4 g), were milled together to enhance their solubility, and dissolved in ethylene glycol (25 ml). $CaCO_3$ (9.0 g) was dissolved in ethylene glycol (35 ml), and the metal nitrate solution was added dropwise to it and the

resulting solution was left to stir for 15 min, followed by sonication for 26 min. The solution was distributed equally by weight into 4 microwave vessels. These were subsequently heated under microwave irradiation at a constant power of 500 watts, with the temperature fluctuating between 160-170 ℃ for 10 min. The resulting mixture of was filtered under vacuum, and a wet brown solid was isolated and dried at 120 ℃ for 12 h. The dried solid was ground, sieved (< 150 μm) and calcined at 400 ℃ for 16 h to remove the nitrates, resulting in formation of a brown solid (*catalyst 2*).

Method C.

A mixture of $Fe(NO_3)_3 9H_2O$ (3.6 g) and $Co(NO_3)_2 6H_2O$ (2.4 g) was milled together to enhance their solubility, and was dissolved in distilled water (25 ml). The resulting solution was added drop wise to a $CaCO_3$ (9.0 g) solution (35 ml distilled water) and left to stir for 15 min, followed by sonication for 26 min. The solution was stirred while heating at 160 for 5h. The resulting mixture was filtered, and the wet brown solid dried at 120 ℃ for 12 h. The dried solid was ground, sieved (150 μm) and calcined at 400 ℃ for 16 h to remove the nitrates, giving a brown solid product (*catalyst 3*).

3.2.3. Synthesis of pristine MWCNTs.

Pristine MWCNTs were made using the horizontal CCVD synthetic method. Fe-Co/$CaCO_3$ (300 mg) catalyst was weighed into a quartz boat in a tubular quartz tube in a furnace in horizontal mode. The tube was connected to two gas lines supplying acetylene (C_2H_2 (90 sccm)) and N_2 (240 sccm) gases that function as a source of carbon and as a carrier gas, respectively. The temperature of the furnace was increased (10 ℃/min) to the desired reaction temperature under a N_2 atmosphere. Once the desired temperature was reached, C_2H_2 gas was introduced concurrently with the N_2 gas to the reaction chamber for 1 h. The reaction was cooled down to room temperature using compressed air, and the MWCNTs product collected from the boat. The obtained MWCNTs samples were treated with an excess of HNO_3 (55%) in a round bottom flask and left stirring under reflux at 110 ℃ for 4 h. The resulting solution was left to cool to room temperature. The resulting solution was diluted with water, filtered, and washed until the filtrate had a neutral pH. The obtained black solid was left to dry at 100 ℃ for 12h in an oven.

Two studies were carried out: (i) *Catalyst 1* was used in a temperature study (700 ℃, 750 ℃, and 800 ℃) where three samples of pristine MWCNTs were obtained. (ii) *Catalysts 1, catalyst*

2 and *catalyst 3* were used in the preparation of pristine MWCNTs at 700 ℃ to investigate the influence of catalyst preparation on the nature of the MWCNTs produced.

The carbon yield (%) of each sample was determined relative to the amount of carbon supplied by acetylene to the reaction chamber. Considering the flow rate of acetylene (90 SCCM) and the duration (60 min) it was pumped into the reaction chamber; the carbon yield (%) was determined using two methods, in both methods the normal temperature and pressure (NTP) were assumed (20 ℃ or 293.15K and 1 atm). The volume of acetylene supplied into the chamber in 60 min was first calculated as shown below.

$$V = flow\ rate \times reaction\ time = 90\frac{cm^3}{min} \times 60min = 5400\ cm^3 = 5.4\ l \ldots\ldots\ldots \textbf{(3.1)}$$

In method 1 the gas law equation ($PV = nRT$) was utilized to obtain the number of moles (n), and the molar mass equation ($M = m/n$) was used to determine the theoretical mass of carbon. Method 2 used the density equation ($\rho = m/V$) to determine the theoretical mass of carbon. For both methods the % yield was calculated using the actual mass (after purification) and theoretical mass;

$$\%\ yield = \frac{Actual\ yield\ (after\ purification)}{Theoretical\ yield} \times 100 \ldots\ldots\ldots\ldots \textbf{(3.2)}$$

A complete example of the calculations is shown below using sample PP700. The % yield from both methods are listed in Table 3.4, values from both methods were reported to show that both methods gave values with small deviations from each other. However, Method 2 may be the more accurate method as it does not assume ideal gas behaviour from acetylene.

Method 1	Method 2
$n = \frac{PV}{RT} = \frac{(1\ atm)(5.4\ l)}{(0.0820)(293.15K)} = 0.2246$ mol	$m = \rho V = 0.001092\frac{g}{cm^3} \times 5400\ cm^3 = 5.897\ g$
$m = Mn = 0.2246\ mol \times 26.04\frac{g}{mol} = 5.849\ g$	$\%\ yield = \frac{1.585\ g}{5.897\ g} \times 100 = 26.9$
$\%\ yield = \frac{1.585\ g}{5.849\ g} \times 100 = 27.1\ \%$	

3.2.4. Characterization techniques.

The structural properties of the catalysts and MWCNTs were determined using Powder X-ray diffraction (XRD) analysis on a Bruker D2 phaser using nickel filtered copper radiation =

0.15406 nm, and an angle scan range of 2θ = 10-90°. Additionally, XRD was used to investigate the purity of the MWCNTs. Raman spectroscopy measurements were obtained using a 514.5 nm laser line from an argon ion laser to determine the structural characteristics of the MWCNTs. Scanning electron microscopy (SEM, ZEISS SIGMA FESEM instrument) was used to obtain images that gave information about the morphology of the samples. Physical properties such as surface area, pore volume and size were determined using the Brunauer, Emmet, and Teller (BET) method under isothermal conditions (-196 ℃, using liquid nitrogen). Measurements were obtained via N_2 adsorption on a Micromeritics TriStar 3000 instrument. The thermal properties of the materials were studied using thermo-gravimetric analysis (TGA) under air (20 ml/min) over a temperature range of 35-900 ℃, on a PerkinElmer TGA4000 instrument. Temperature programmed reduction (TPR, 50-900 ℃) analysis was performed on the obtained catalysts under hydrogen (H_2) on a Micrometrics AutoChem II instrument.

3.2. Results and discussions.

3.2.1. Synthesis of pristine MWCNTs using microwave heating to prepare the catalyst.

The synthesized catalysts were characterized to highlight the differences in their properties because of the different reaction conditions. The surface area analysis (Table 3.3) of the catalysts was performed using the BET method, and *catalyst 1* and *3* reported low surface areas consistent with literature reports.[59-62] Catalyst *2* exhibited a surface area larger than both catalysts. *Catalyst 3* was synthesized using a method reported by Chiwaye *et al*. and the low surface area was consistent with this report.[59] In the case of *catalyst 1* and *catalyst 2*, longer irradiation time (i.e., supply of more energy to the system) gave a catalyst with larger pore volume and size, while short irradiation times (i.e., supply of less energy to the system) gave a catalyst with a larger surface area and a smaller pore size. This could suggest that with longer irradiation times led to the decomposition of the catalyst support.

Table 3.3: Brunauer-Emmet-Teller surface area data

Sample	Surface area (m^2/g)	Pore volume (cm^3/g)	Pore size (nm)
Catalyst 1	5.5	0.105	75
Catalyst 2	14.4	0.054	15
Catalyst 3	4.5	0.045	39

The thermal properties of the prepared catalysts were investigated using thermogravimetric analysis (TGA, **Figure 3.1**) between 35-900 ℃; small losses in mass (2%) were observed between 400-700 ℃ for all three catalysts, with *catalyst 2* exhibiting the least amount of mass loss in this range. *Chiwaye et al.* attributed this mass loss to the production of CO_2 during the formation of bimetallic and trimetallic oxides such as $Ca_2Fe_2O_5$/$Ca_2Co_2O_5$ and Ca_2FeCoO_5, respectively. These oxides contributed to the ~ 40% mass residue observed in all samples.[59] The similarities in the data to *Chiwaye et al.* suggest that a Fe/Co (5%/5%) $CaCO_3$ (i.e., 10% Fe-Co/$CaCO_3$) was successfully synthesized.[59] Although not discussed in this chapter, the TPR (**Appendix 3A, Figure 3.14**) data corroborated the differences in the obtained catalyst.

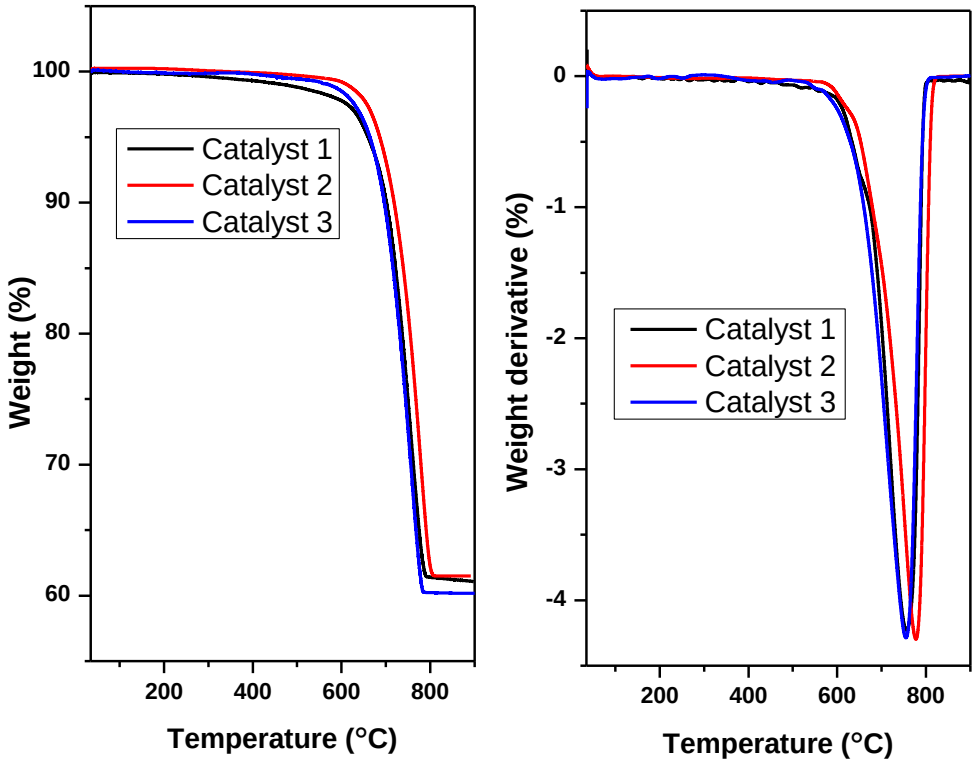


Figure 3.1: Thermogravimetric analysis of Fe-Co/$CaCO_3$ catalysts.

The bimetallic catalysts were used in the synthesis of MWCNTs at 700 ℃. The as-synthesized samples P700, P700-1 and P700-2 were produced from *Catalyst 1, 2,* and *3*, respectively. The samples were treated with HNO_3 to remove the catalyst residue to give three purified samples denoted PP700, PP700-1 and PP700-2. Scanning electron microscopy analysis (SEM images, **Figure 3.2a-b**) of the purified MWCNTs revealed the presence of nanotubes in each sample, the nanotubes were randomly arranged, agglomerated, and entangled.

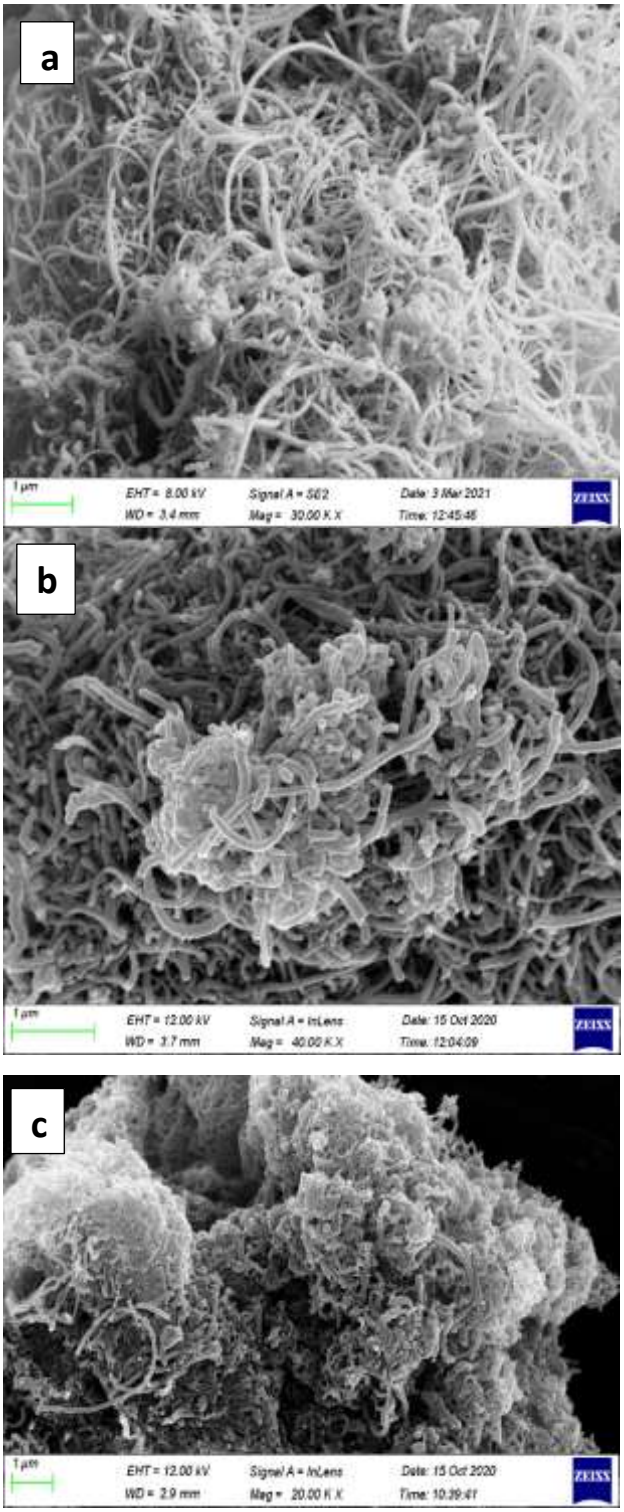


Figure 3.2: SEM analysis of pristine MWCNTs *a)* Sample PP700, *b)* sample PP700-1, *c)* sample PP700-2.

Sample P700 produced from *catalyst 1* had the highest carbon yield (Table 3.4), followed by sample P700-1 (*catalyst 2*) and P700-2 (*catalyst 3*), respectively. This indicates that the preparation methods for the catalyst not only determines their properties, but the yield of CNTs obtained from said catalyst. Microwave irradiation, and particularly longer irradiation times (i.e., larger amount of energy) in catalyst preparation led to the production of higher yields of MWCNTs.

Table 3.4: Carbon yield (%) of pristine MWCNTs

Sample	Total Mass Purified (g)	Yield (%) *	Yield (%) **
PP700	1.585	27.0	26.8
PP700-1	0.625	10.7	10.6
PP700-2	0.499	8.5	8.4

*Calculated using method 1. ** Calculated using method 2.

The XRD pattern (**Figure 3.3a**) of these samples shows Bragg reflections arising from the 002 (~26°), 100 (~43°), and 101 (~44-45°) sp^2 hybridized carbon planes. The spectrum also shows that the P700 sample contained less impurities generated from the catalyst, compared to samples P700-1 and P700-2. The samples were treated with 55% HNO_3 to remove the catalyst residue, a treatment known to oxidize and functionalize the MWCNTs.[75-77] XRD analysis of the samples obtained after treatment with HNO_3 (PP700, PP700-1 and PP700-2) corroborated the removal of the catalyst (**Figure 3.3b**). No major shifts in the carbon graphitic planes 002 (~26°), 100 (~43°) and 101 (~44-45°) were observed, and these peak positions correspond to the reported XRD data of MWCNTs.[78-83]

The Bragg reflections showed a small variation in peak position: PP700 < PP700-2 < PP700-1 for all the graphitic planes. The 002 plane peaks showed an asymmetry in the line shape, which may be attributed to several factors that lead to their broadening: (i) differences in crystallite size and their distribution (ii) the preferred orientation of said crystallite, (iii) variable diameter distribution, (iv) tensile strain and compression forces largely arising from the diameter of the tubes (v) successive layers with different chirality. [84-87]

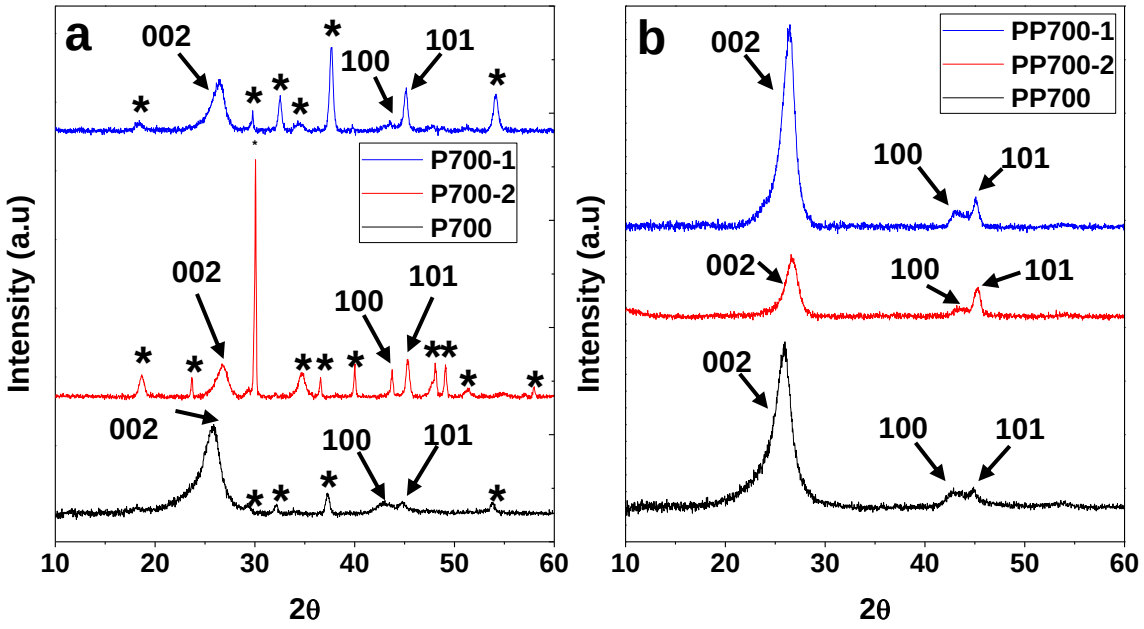


Figure 3.3: XRD pattern of pristine MWCNTs: *a)* un-purified MWCNTs, *b)* purified MWCNTs. *Catalyst residue.

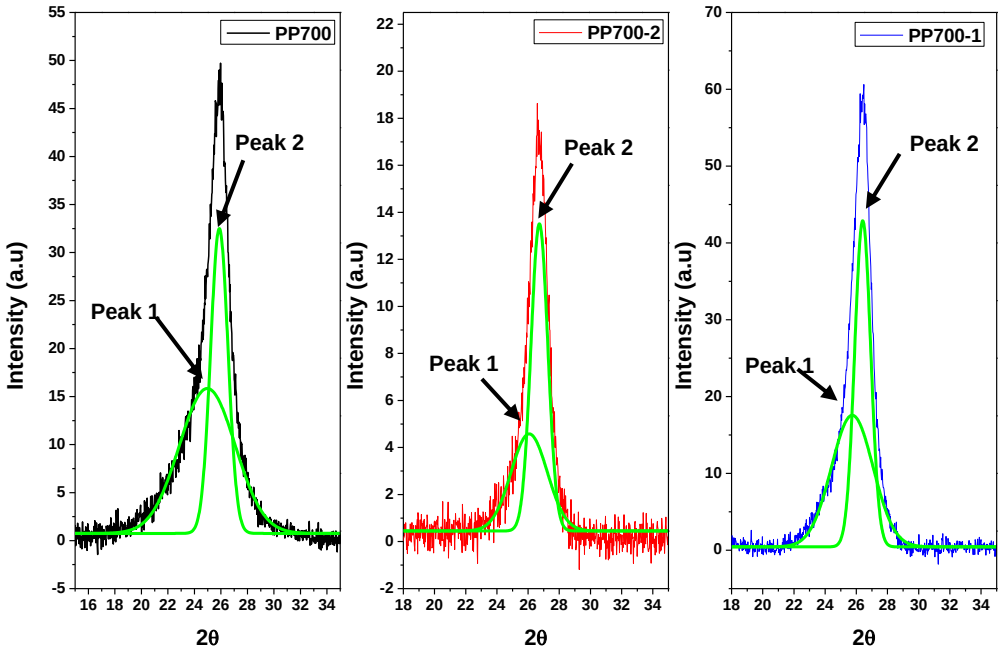


Figure 3.4: XRD pattern of deconvoluted 002 peaks using a Gaussian spectral function,

The peaks of the 3 samples due to the 002 plane, were deconvoluted using the Gaussian spectral functions (**Figure 3.4).** This method gave a better fit compared to a Voigt spectral function used in the work reported by Singh *et al.*[84] and Mofokeng *et al*[88]. The Scherrer equation was used to calculate the crystallite size (L_a, Table 3.5) from the 002 peak positions, and the peak broadening factor FWHM (β, Table 3.5) was determined using a Gaussian function. Using the

major peak (peak 2, **Figure 3.4**) it was determined that the crystallite size of the samples was in the order PP700 < PP700-2 < PP700-1, while the full width at half maximum (FWHM) showed the opposite trend, indicating that as the crystallite size decreased broader peaks were obtained. Different reports have attributed peak 1 to several factors; Mofokeng *et al* and Bandow *et al* attributed it to the presence of nanotubes with different diameters in one sample[84] and dispersed inner diameters[89], respectively. On the other hand, Kiang *et al* ascribed it to the continuous reduction in d-spacing with increasing diameter of the shells/tubes of the MWCNTs (i.e., the distance between shells of a nanotube is not constant).[90] However, in addition to these factors instrumental broadening due to X-ray source and beam divergence, including sample preparation, can also contribute to the asymmetry observed.[91]

Table 3.5: The crystallite size and interlayer spacing of the obtained MWCNTs.

Sample code	002 plane peak position (°)	L_a (nm)	FWHM (°)	d_{002} (Å)	g (%)
PP700	25.87	5.0	1.543	3.440	0.00
PP700-2	26.41	6.4	1.208	3.372	81.2
PP700-1	26.72	6.1	1.268	3.333	(124)*

*Did not meet the Marie and Mering's validity range.[63]

Although the d-spacing is determined from the XRD data, it is essential to note that literature reports have reported that due to factors such as helix angle changes in the material[86] and unequal spacing of graphitic layers due to the differences in strain of inner and outer walls[84], the d-spacing determined from XRD data tends to be slightly larger than when measured from high resolution transmission electron microscopy (HRTEM).[63, 93-96] The interlayer spacing (d_{002}, Table 3.5) of the MWCNTs were calculated using the Bragg equation (3). The interlayer spacing (d-spacing) is inversely proportional to θ, and the samples reveal that d_{002} (PP700) > d_{002} (PP700-2) > d_{002} (PP700-1).

$$n\lambda = 2dsin\theta \text{……..} \quad \textbf{(3.3)}$$

$$\text{g (\%)} = \frac{3.440 - d_{002}}{3.440 - 3.354} \times 100 \text{ …….} \quad \textbf{(3.4)}$$

The graphitization degree of each sample was investigated and calculated using the Maire and Mering formula (4): where g is the graphitization degree of a sample, 3.440 is the d-spacing of

carbon material with a turbo-static structural arrangement, and 3.354 is the value of the d-spacing in an ideal defect-free graphite crystal. [63, 87-88, 92-96] The graphitization degree has a validity range of $0 \leq g \leq 1$ (i.e., 0-100 %), but this does not always hold due to factors such as the orientation of carbon layers (symmetrical versus turbostatic) and defects due to chemical treatments such as functionalization.[65] Turbostatic carbon has structural arrangements between amorphous carbon and crystalline carbon, but in graphite like layered material, such as CNTs, it describes random layer arrangements and orientations which have reduced the three-dimensional (3D) ordering of the graphitic layers relative to each other.[97] Sample PP700 presented with a graphitization degree of zero, with a d-spacing equal to that of a turbostatic carbon arrangement. Sample PP700-2 presented with a better graphitization degree relative to PP700. However, sample PP700-1 failed to obey the validity range, which indicated the possible presence of layers with a high degree of random arrangement and orientation relative to each other.

Raman spectroscopy was used to characterize and compare the structural features of the produced purified MWCNTs. The characteristic carbon graphitic *D* and *G* peaks were observed in the 1st order region (**Figure 3.5a-c**) for all samples at approximately 1350 and 1580 cm^{-1}, respectively. The *D* peak arises due to the A_{1g} symmetry forbidden breathing mode, which is active because of the presence of disorder and surface defects in a graphitic structure, while the *G* band is due to the presence E_{2g} vibrations of sp^2 hybridized carbon atoms. All peaks exhibited an asymmetry that indicated the presence of multiple peak components that were isolated by deconvolution, using a Lorentzian spectral function. [70,84, 88, 98-103] The isolated components D_1 (~ 1200 cm^{-1}), D_2 (~ 1500 cm^{-1}) and D' (~ 1616 cm^{-1}) have been attributed to disordered graphitic lattice from the A_{1g} symmetry, amorphous carbon, and disorder on the surface graphene layers of the E_{2g} vibrational mode, respectively.[88, 101, 104-106] Due to the presence of these multiple peak components, the ratio coefficient (i.e., extent of order/disorder) was determined using the area of the *D* and *G* peaks (I_D/I_G). Interestingly, the use of intensity ratios yielded the same trend, and it is listed in **Appendix 3A Table 3.10** with the rest of the Raman Lorentzian fitted data. Samples PP700-2 (1.48) and PP700 (1.66) presented with the lowest I_D/I_G ratio indicating that *catalyst 3* and *catalyst* 1 produced MWCNTs with the highest crystallinity, respectively. Furthermore, it indicated that shorter irradiation time in catalyst preparation gave MWCNTs with better crystallinity. Although the intensity of the *G* band relative to the *D* band is larger for PP700 compared to PP700-2, the *D'* band has a higher intensity in PP700 than in PP700-2. This indicates the existence of more defects on the surface

of the graphene layers in PP700 relative to PP700-2, thus PP700-2 presented with the lowest I_D/I_G ratio.

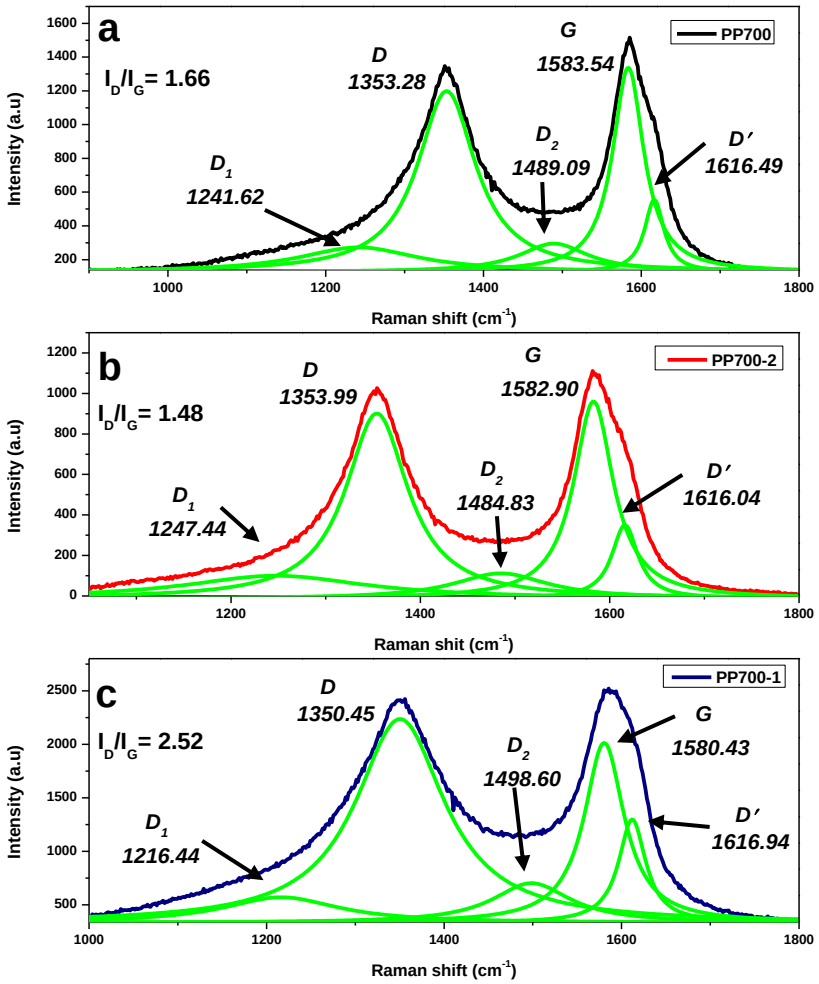


Figure 3.5a-c: 1st order Raman Lorentzian fitted peaks of purified pristine MWCNTs prepared using different catalysts.

An additional peak in the 2nd order region (**Figure 3.6a-c**) of the Raman spectra was also observed. This is due to the overtone of the D-band which arises from a double resonance process. The *G´*, *D+G* and *2G* bands are attributed to the *2D*, $2E_{2g}$ and $D+E_{2g}$ frequency modes. These bands were fitted using a Lorentzian function. The splitting in the peak indicates the presence of stacked graphitic layers, and thus corroborates the successful production of MWCNTs. The *G´* band is a good indicator of the crystallinity and number of layers in the material.[108-113] The $I_{G'}/I_G$ ratio can give information about the long-range sp^2 order in the material, high ratio indicates good long-range order, and consequently better crystallinity.[114-116] The $I_{G'}/I_G$ ratios for all three samples (**Appendix 3A, Table 3.10**) revealed that long-range

ordering and consequently crystallinity for sample PP700-2 (1.06) > PP700-1 (0.66) > PP700 (0.59).

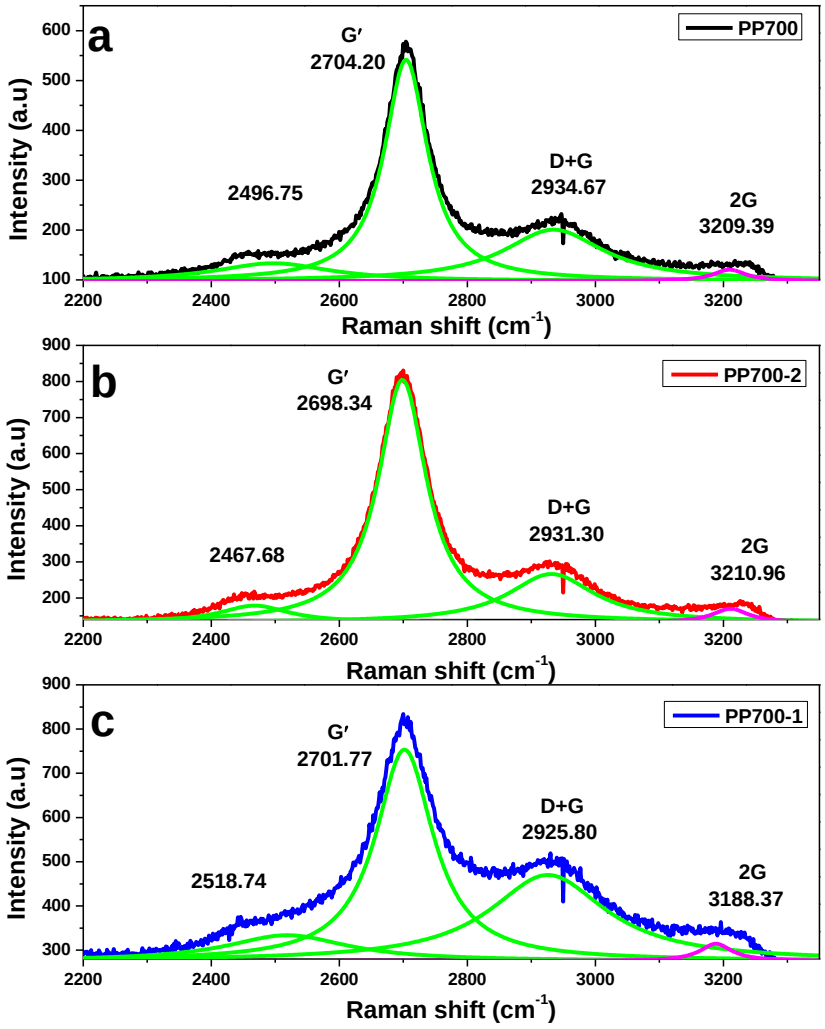


Figure 3.6a-c: 2nd order Raman Lorentzian fitted peaks of purified pristine MWCNTs prepared using different catalysts.

The thermal properties of the un-purified MWCNTs were investigated using TGA (**Figure 3.7a-b**). The TGA curve revealed that the catalyst residual weight was different for the impure samples, with *catalyst A* (P700, < 5%) < *catalyst 3* (P700-1, 25%) < *catalyst 2* (P700-2, 34%). Weight gain was observed at 400℃ for samples P700-2 and P700-1, which was attributed to the presence of incompletely oxidized catalysts that formed metal oxides from residual metal.[117-118] Samples P700-2 and P700-1 were also found to have two forms of MWCNTs decomposing at different temperatures; P700-2 presented with two distinct decomposition temperatures at 640℃ and 734℃, and P700-1 at slightly lower temperatures of 620℃ and

730℃. Sample P700 presented with an asymmetry that also revealed the presence of two forms of MWCNTs that decomposed at different temperatures (710℃ and 760℃).

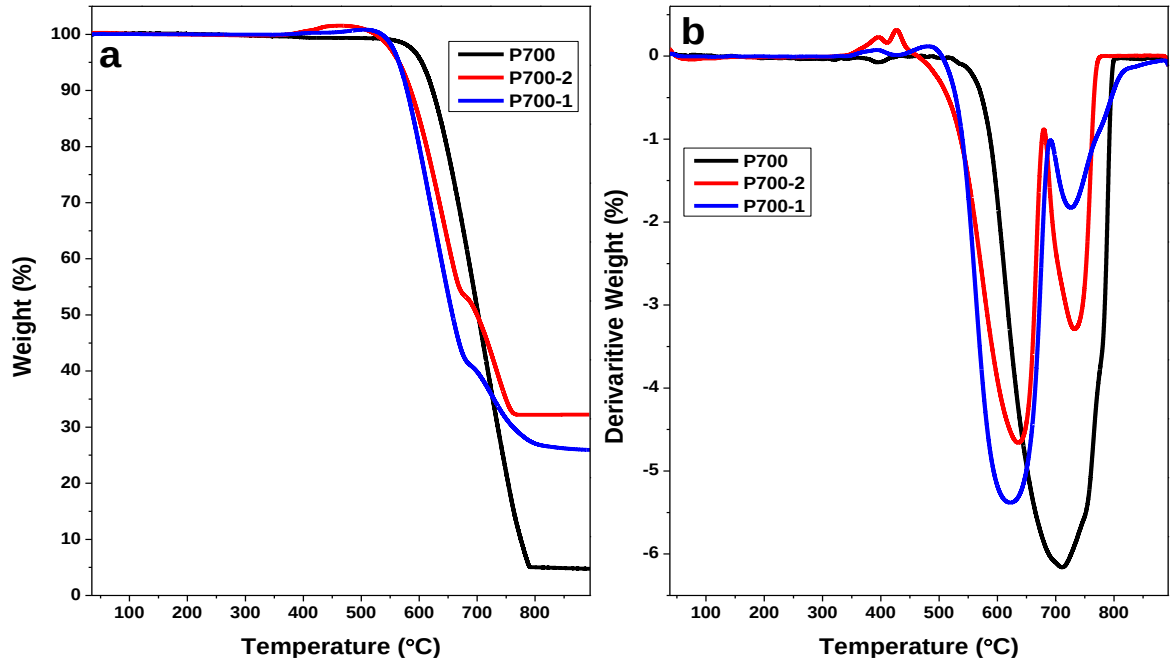


Figure 3.7a-b: Thermogravimetric analysis of un-purified MWCNTs obtained from different catalysts.

After treatment of the samples with HNO_3, the TGA curves indicated a successful removal of the catalyst residue for P700 to give sample PP700 (**Figure 3.8a-b**). While samples P700-2 and P700-1 still exhibited some catalyst residue after treatment with the acid (PP700-2 (8%) and PP700-1 (4%)). All the oxidized samples exhibited weight-loss at temperatures below 500℃, which is attributed to the presence of amorphous carbon and/or the removal of functional groups added to the MWCNTs during the purification/oxidation process.[117, 119-122] Sample PP700 was found to be the most thermally stable with a decomposition temperature of 700℃, followed by PP700-2 at 630℃ and PP700-1 at 580℃. The low decomposition temperature for sample PP700-1 is consistent with the Raman data which revealed that it has a higher density of disorder and had the smallest diameter (corroborated by XRD analysis).

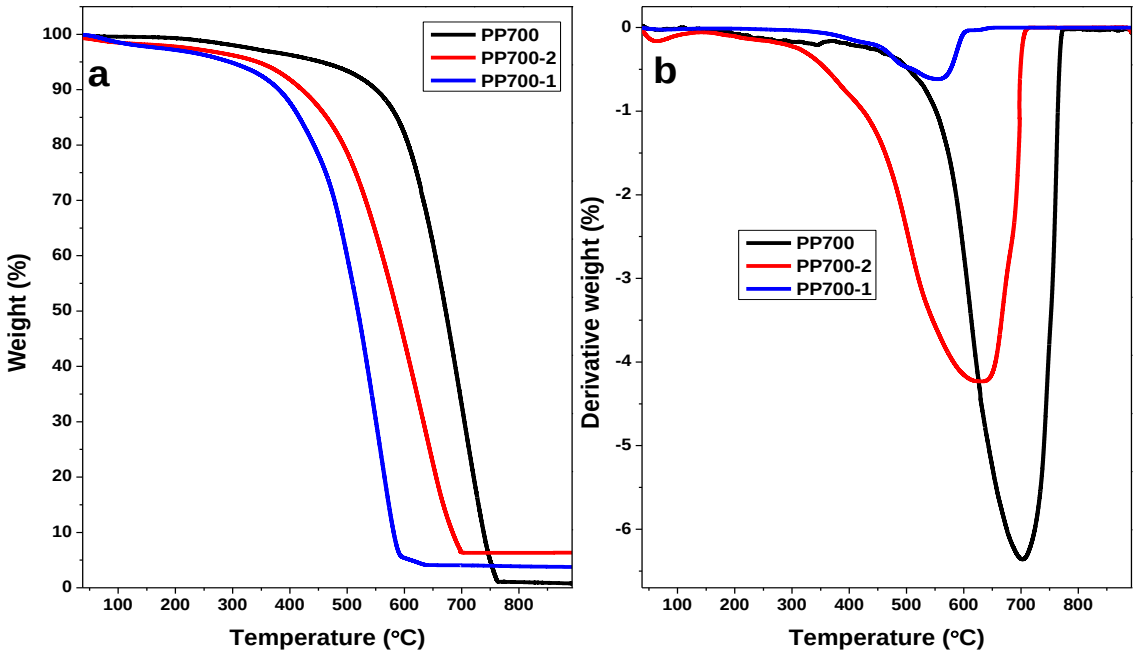


Figure 3.8a-b: Thermogravimetric analysis of purified MWCNTs obtained from different catalysts.

Despite PP700-2 reporting a lower disorder than sample PP700, it presented with a lower decomposition temperature. However, the asymmetry of the derivative weight curve indicated the presence of MWCNTs in PP700-2 with comparable thermal stability (~690℃) to PP700 (~700℃). This can be attributed to several factors such as length, for example, the acid oxidation process has been shown to not only reduce the thermal stability of a material, by shortening the length of nanotubes.[122-125] Consequently, it is conceivable that the lower thermal stability for sample PP700-2 could be explained by the length of nanotubes, which may have been shortened during the purification/oxidation process or the sample inherently contains shorter nanotubes. However, if the MWCNTs were shortened during the purification process, it suggests that the reactivity of the MWCNTs in the PP700-2 sample to the acid differ to that of PP700 and PP700-1. In addition, the presence of catalyst residue (in particular Fe) has been shown to decrease the decomposition temperature of MWCNTs; sample PP700-2 had the highest content of catalyst residue (8%) compared to PP700 which presented with the lowest concentration of catalyst residue (< 1%), thus could have contributed to its lower thermal stability. [122, 126-130] MWCNTs prepared from catalysts that were produced using microwave irradiation have better thermal stability compared to thermal heating. Additionally, the use of longer irradiation times for catalyst preparation gave the most thermally stable MWCNTs.

The surface area studies (Table 3.6) revealed that *catalyst 1* (PP700) produced MWCNTs with the largest surface area, followed by *catalyst 2* (PP700-1) and *catalyst 3* (PP700-2). Using microwave irradiation for catalyst preparation led to the production of MWCNTs with high surface areas (PP700 vs PP700-1) relative to thermal heating. However, decreasing the power used (i.e., lower irradiation time) gave smaller surface area compared to thermal heating i.e., PP700-2 vs PP700-1.

Table 3.6: BET Surface area data of purified MWCNTs

Sample	Surface area (m^2/g)	Pore volume (cm^3/g)	Pore size (nm)
PP700	96.1	0.37	15
PP700-2	63.8	0.35	26
PP700-1	74.9	0.41	22

3.2.2. Synthesis of MWCNTs: a temperature dependant study.

The catalyst dependant study reported in the previous section revealed that Fe-Co/$CaCO_3$ catalysts prepared using thermal heating (*catalyst 3*) produced MWCNTs with inferior properties compared to those obtained a catalyst prepared under microwave irradiation (*catalysts 1 and 2*). The influence of temperature on the synthesis of MWCNTs using the Fe-Co/$CaCO_3$ prepared from either thermal heating or microwave irradiation has not been explored. So, since *catalyst 1* produced MWCNTs with more desirable properties (higher yield (%), high surface area and thermal stability), this section explored the influence of temperature (700℃, 750℃ and 800℃) on the production of MWCNTs. The as-synthesized samples (P700, P750, P800) were purified using HNO_3 to give samples PP700, PP750 and PP800, respectively. The yield of MWCNTs (Table 3.7) decreased with an increase in temperature.

Table 3.7: Carbon yield (%) of purified pristine MWCNTs

Sample	Total Mass (g) purified	Yield (%) *
PP700	1.585	26.8
PP750	0.935	15.8

PP800	0.475	8.0

*Calculated using method 2

SEM analysis (**Figure 3.9**) of the purified products indicated the successful synthesis of MWCNTs. The CNTs in the SEM images showed different diameters and lengths with tubes randomly arranged, agglomerated, and entangled. Additionally, sample PP750 had some sheet like material that wrapped around some of the nanotubes but were absent in the PP700 and PP800 samples. The material could be amorphous carbon. Sample PP800 had nanotubes with both smooth and rough surfaces.

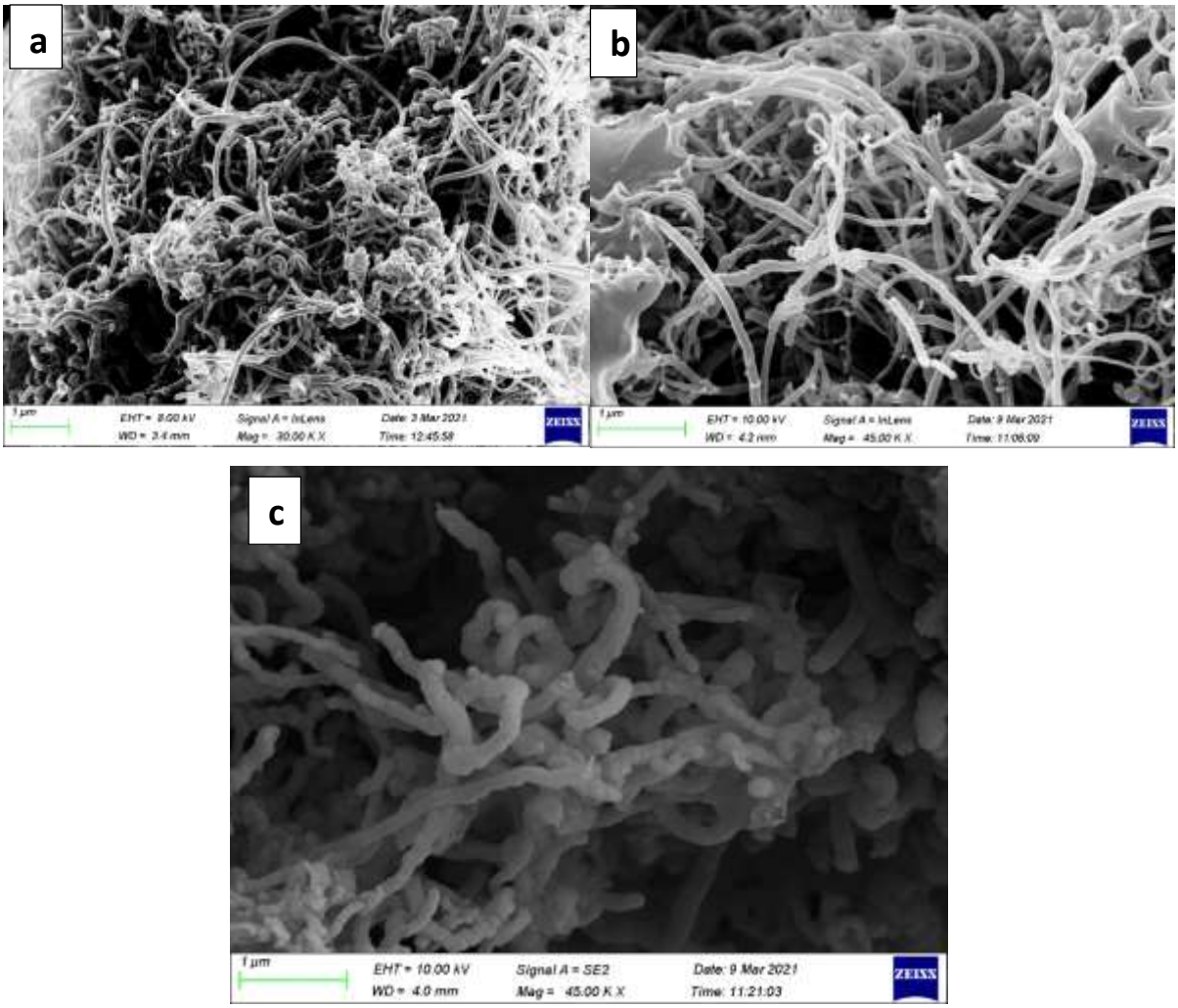


Figure 3.9: SEM analysis of pristine MWCNTs *a)* Sample PP700, *b)* sample PP750, *c)* sample PP800.

XRD analysis of the as-synthesized samples (P700, P750, and P800) reported the characteristic peaks of the 002, 100 and 101 carbon graphitic planes (**Figure 3.10a**). The XRD pattern also

showed by-products due to the catalyst. XRD analysis of the purified samples (PP700, PP750, PP800) indicated removal of most of the catalyst residue (**Figure 3.10b**).

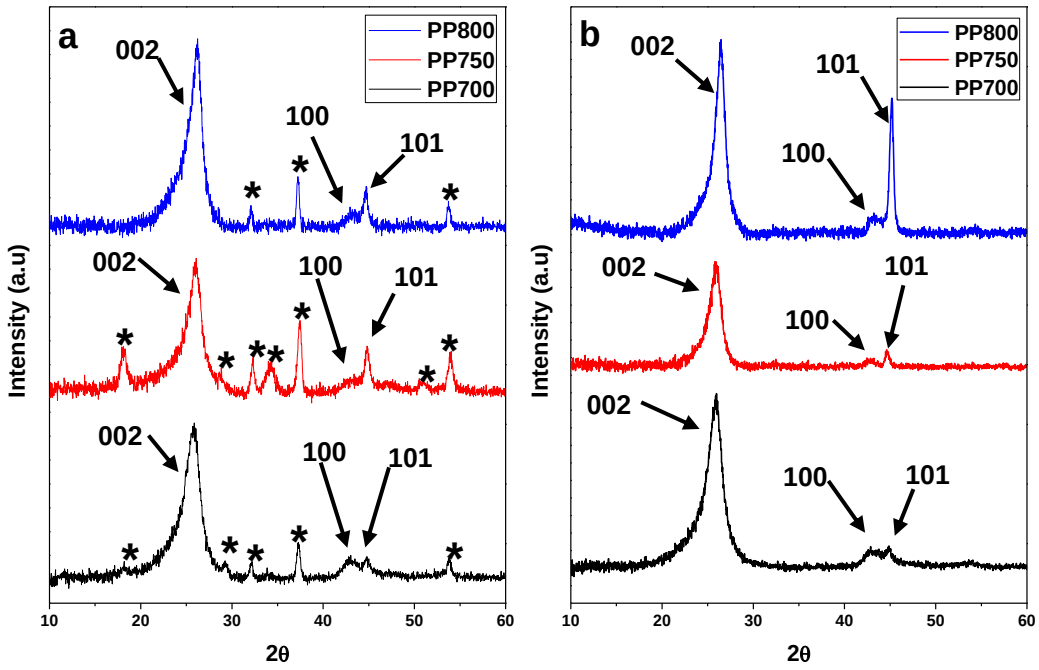


Figure 3.10: XRD spectra of (*a*) as-synthesized MWCNTs, *b)* purified MWCNTs. *Catalyst residue.

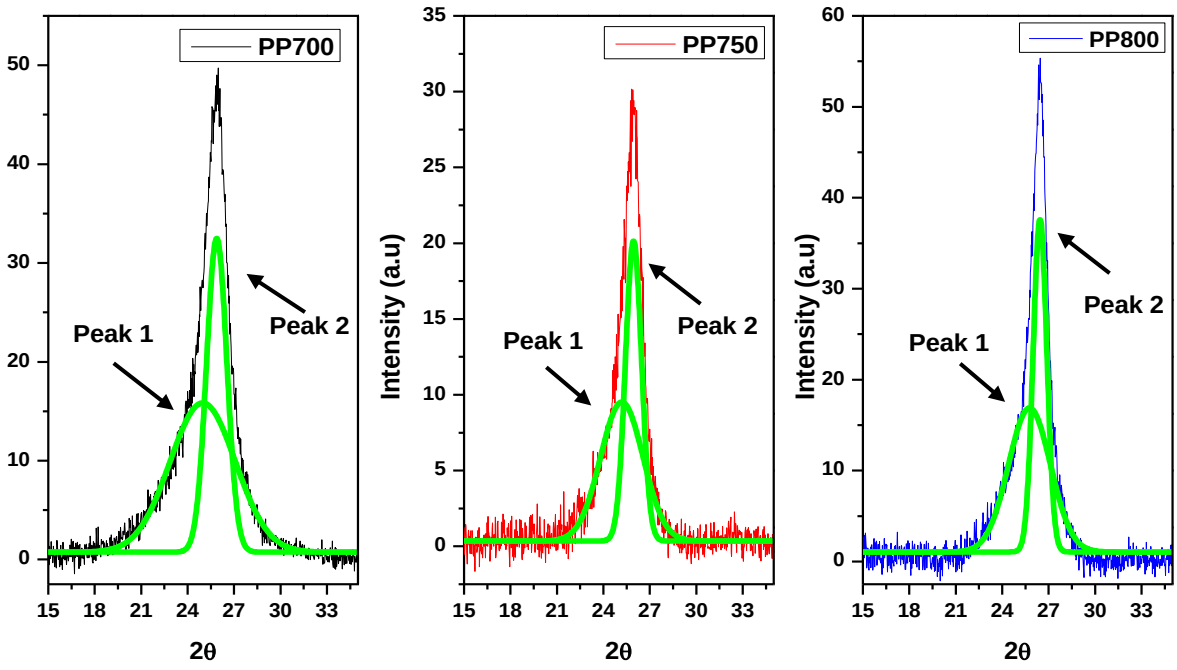


Figure 3.11: XRD spectra of deconvoluted 002 peaks using Voigt spectral function.

Analysis of the 002 Peak 2 (**Figure 3.11)** by deconvolution using a Voigt spectral function was used to determine the crystallite size (Table 3.8) of the CNTs. It was found that as the reaction temperature increased the Bragg angle and crystallite size of the obtained MWCNTs increased. Equation 3.4 was used to determine and study the graphitization degree (g) of the purified samples (Table 3.8), and g was found to be directly proportional to the reaction temperature. PP700 presented with d-spacing equal to carbon material with turbostatic arrangement of the graphitic layers, while PP800 had a higher g value.[93-96] The graphitization degree indicated that as the reaction temperature increased the random stacking of the graphitic layers was reduced, and the presence of highly ordered 3D graphite increased. The d-spacing of the samples had an inverse correlation to the synthetic temperature; this may be attributed to the difference in average diameter of the MWCNTs.[84] The trend in the d-spacing suggests that the average diameter increased with temperatures, PP800 > PP700 ≅ PP750.[84, 95, 97-98] Furthermore, the inverse correlation of the FWHM to the reaction temperature also supports the observation of an increase in average diameter with reaction temperature since small average diameter tubes tend to have high curvature, and consequently a high strain contributing to broadening (i.e., larger FWHM) of the 002 peak.[84, 95, 97-98]

Table 3.8: The crystallite size and d-spacing of the obtained purified MWCNTs.

Sample code	002 plane peak position (°)	L_a (nm)	FWHM (°)	d_{002} (Å)	g (%)
PP700	25.87	5.018	1.543	3.441	0.00
PP750	25.94	6.336	1.222	3.432	9.30
PP800	26.44	7.433	1.041	3.368	83.7

The structural information of the material was investigated using Raman spectroscopy (**Figure 3.12a-c**) and the characteristic *D* and *G* bands typical of the presence of carbon graphitic material was observed in the 1st order region at approximately 1350 and 1580 cm^{-1}, respectively.[84, 88, 99-104, 119] It was found that the I_D/I_G ratio, and consequently the crystallinity/sp^2 hybridized clusters were directly proportional to the synthesis temperature. This was corroborated by the reduction in intensity of the *G* band relative to the *D* band with an increase in reaction temperature.[84]

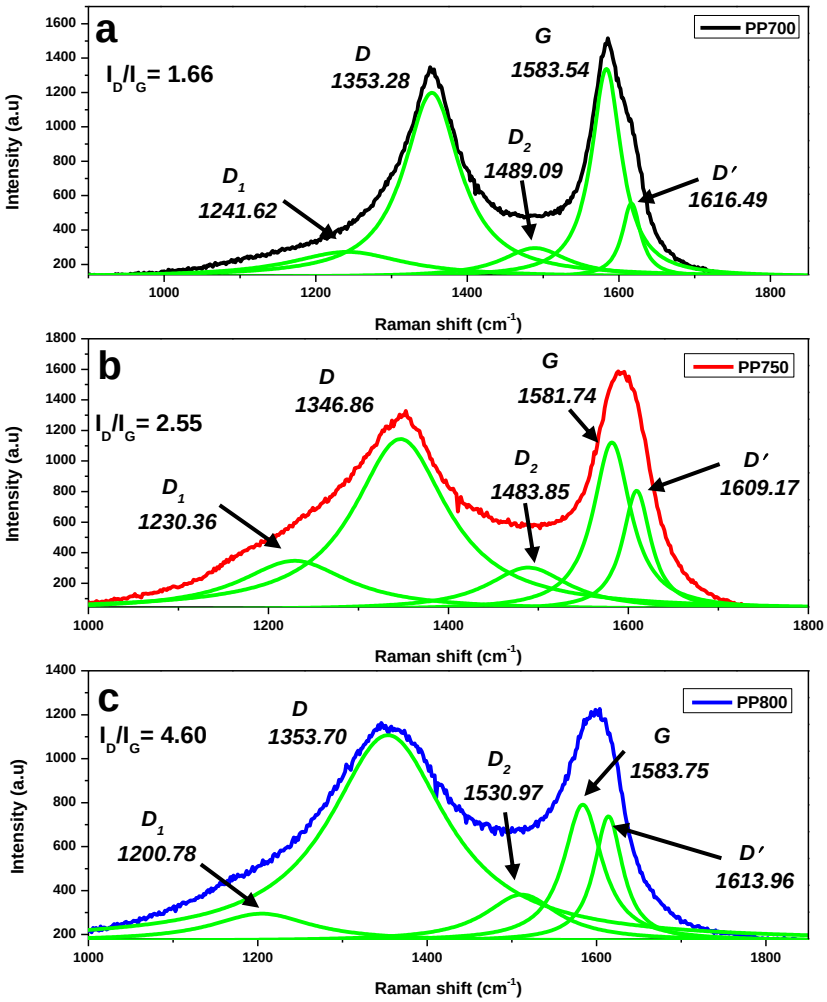


Figure 3.12a-c: 1st order Raman Lorentzian fitted peaks of purified pristine MWCNTs prepared at different temperatures.

The $I_{G'}/I_G$ long range order for sample PP800 (0.70) > PP700 (0.59) > PP750 (0.45), indicating that long range order of a material increases with an increase in temperature. The XRD data revealed that the average diameter increased with synthesis temperature, and this is corroborated by the reduced intensity of the *G´* band with an increase in temperature. The smaller the intensity the greater the number of graphitic layers and consequently the smaller the average diameter.[110-111] Additionally, the *G* band in the 1st order region reduced in intensity relative to the *D* band, a property also consistent with large diameter nanotubes.[84] This reduction with temperature indicated that the average diameter of the nanotubes is directly correlated to their synthetic temperature. Furthermore, the *G´* and *D+G* bands of the PP800 sample overlap significantly and are comparable in intensity, which is consistent with a high number of layers and consequently the large average diameter.[110-111]

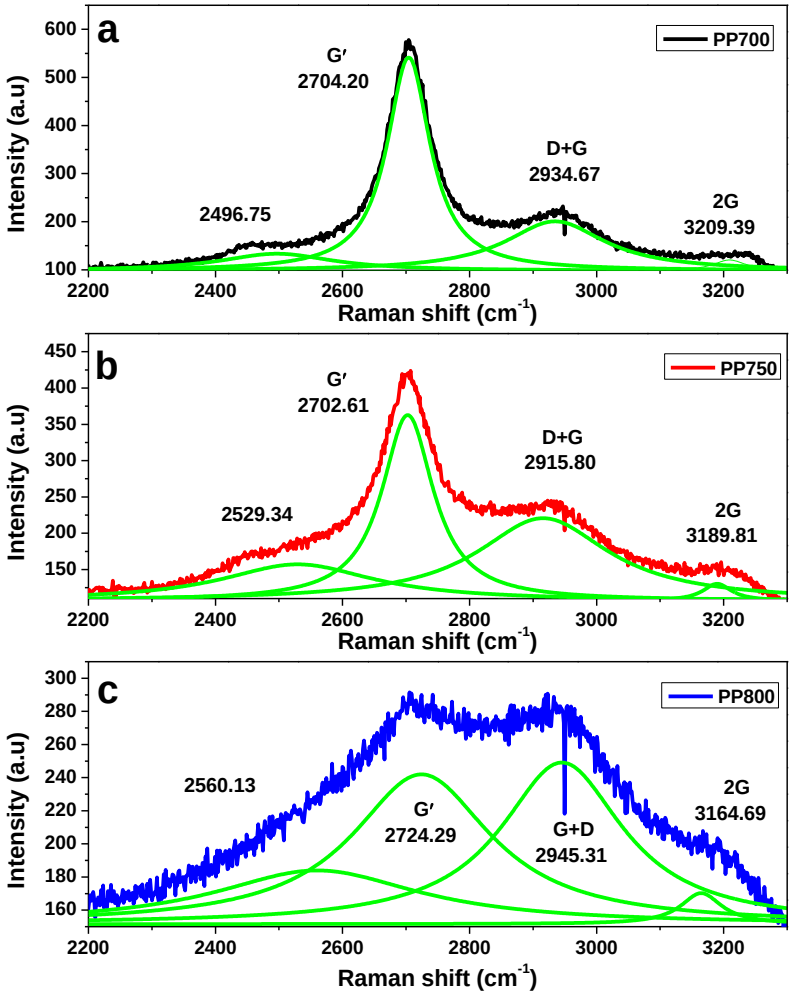


Figure 3.12a-c: 2nd order Raman Lorentzian fitted peaks of purified pristine MWCNTs prepared at different temperatures.

Thermogravimetric analysis was used to investigate the structural and thermal properties of MWCNTs prepared at different temperatures (**Figure 3.13a-c**). It was found that as the reaction temperature increased the yield (%) of carbon material decreased, P700 (95%) > P750 (87%) > P800 (69%). The derivative curve revealed the formation of metal oxides at 400 ℃ resulting from the presence of incompletely oxidized metals for samples prepared at 750 ℃ and 800 ℃.[117-118] Furthermore, the TGA indicated that as the temperature increased the formation of two distinct graphitic crystalline material became more pronounced; PP700 (710℃ and 760℃), PP750 (620 ℃ and 685 ℃), and PP800 (670 ℃ and 740 ℃).

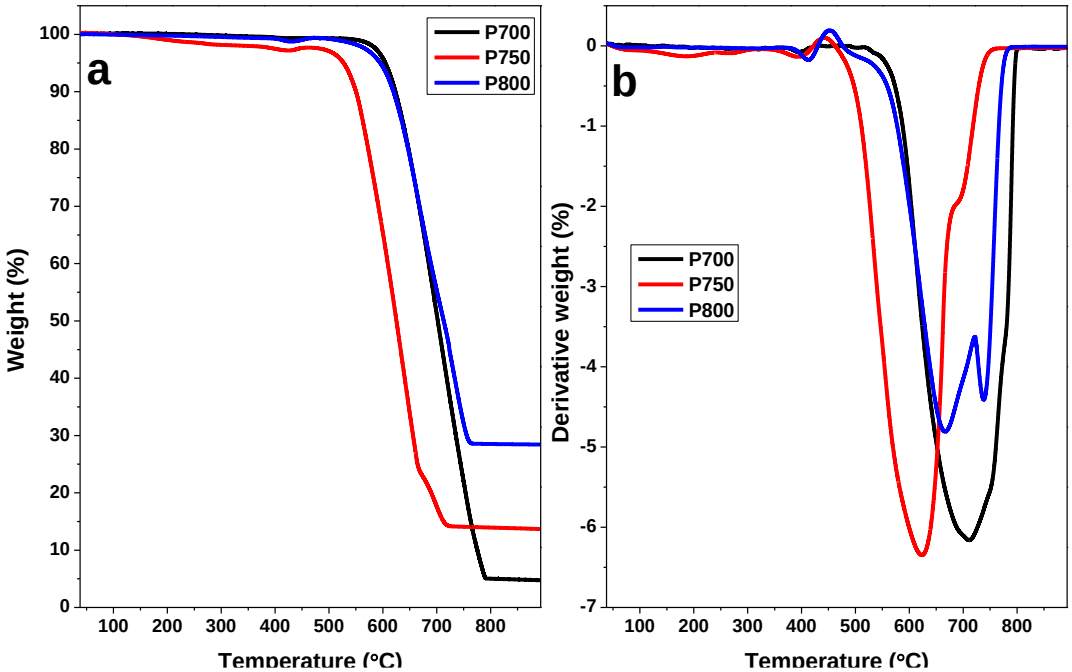


Figure 3.12a-b: Thermogravimetric analysis of un-purified MWCNTs obtained from a temperature dependant study.

The TGA analysis (**Figure 3.13a-b**) of MWCNTs treated with HNO_3 revealed that the purity (i.e., concentration of catalyst residue) of the samples decreased with increase in temperature. The first weight loss was observed at a temperature less than 100℃ for sample PP750 and PP800, which may be attributed to the removal of moisture adsorbed onto the material. The next mass loss attributed to the decomposition of amorphous carbon was observed at 400 ℃.[117, 120-121] The thermal stability decreased for material produced at higher synthesis temperatures, i.e., PP700 (700 ℃) > PP800 (555 ℃ and 615 ℃) ≥ PP750 (555 ℃). This was consistent with the Raman data which showed that sample PP700 had a larger concentration of the sp^2 hybridized clusters. However, despite having the highest concentration of defects, sample PP800 reported thermal stability better than PP750 because of the high long-range order reported for the material.[122, 129-130]

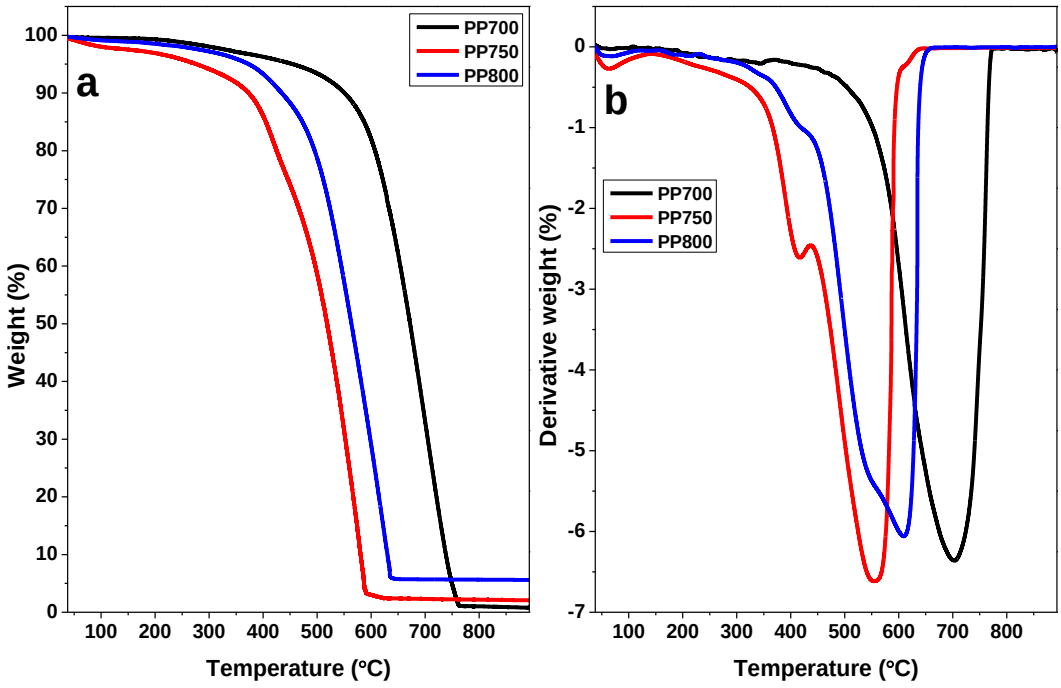


Figure 3.13a-b: Thermogravimetric analysis of purified MWCNTs obtained from a temperature dependant study.

Surface area (Table 3.9) studies indicated that the surface area and pore volume of the material produced decreased with an increase in temperature. This is consistent with the deductions made from XRD and Raman analysis which indicated that the average diameter of the prepared material increased with the reaction temperature. So, given that the average diameter is inversely proportional to surface area,[117, 128] it followed that the surface area decreased with an increase in synthesis temperature.

Table 3.9: Surface area data for purified MWCNTs

Sample	Surface area (m^2/g)	Pore volume (cm^3/g)	Pore size (nm)
PP700	96.1	0.367	15
PP750	35.9	0.172	19
PP800	15.0	0.111	29

3.2.3. Conclusion.

The influence of catalyst fabrication methods on the type of MWCNTs produced was investigated, the prepared catalysts produced MWCNTs with different properties. *Catalyst 1* (PP700) and *catalyst 2* (PP700-1) were prepared under microwave irradiation and produced MWCNTs with a higher carbon yield (%) than MWCNTs made from *catalyst 3,* prepared using thermal heating. The carbon yield (%) MWCNTs obtained from *catalyst 1* were found to be consistent with typical CVD yields of approximately 30%,[131] while they were significantly lower for MWCNTs derived from *catalyst 3* and *catalyst 2.* Thus, making the synthesis of MWCNTs from *catalyst 1* more scalable. *Catalyst 3* gave MWCNTs with the lowest crystallinity and thermal stability. Furthermore, the samples obtained from *catalyst 1* and *2* had higher surface area than those obtained from *catalyst 3. Catalyst 1* and *2* were prepared using different reaction times and different microwave power; *catalyst 2* was prepared at a constant power of 500 Watts for 10 min, while *catalyst 2* was prepared at a constant temperature (varying power; 0-500 Watts) for 1 h. *Catalyst 1* (PP700) which was prepared from a higher supply of irradiation energy to the system gave a higher yield of MWCNTs with better thermal stability and a larger surface area than those prepared from *catalyst 2*. However, *catalyst 2* produced MWCNTs with a lower concentration of defects relative to *catalyst 1*. Microwave irradiation resulted in catalysts that produced MWCNTs with higher yields, higher surface area, better crystallinity, and higher thermal stability than the catalyst produced from conventional heating. In addition, longer irradiation times produced a catalyst that led to the production of MWCNTs with higher yield (%), surface area and thermal stability. Overall, this study indicated that the properties of MWCNTs may be tailored by adjusting the parameters of the method used to prepare the catalyst.

Catalyst 1 was used to investigate the influence of temperature (700 ℃, 750 ℃ and 800 ℃) on the production of pristine MWCNTs. The carbon yield (%) and purity of the produced MWCNTs decreased at higher reaction temperatures to yields much lower than expected of the CVD method. The decrease in % yield with an increase in temperature was ascribed to the impact of high temperatures on the integrity of the catalyst. At temperatures higher than 700℃, the support begins to decompose and formed CaO, while the metal catalysts also formed oxides. A combination of these factors made the catalyst less effective in the production of MWCNTs. The crystallinity and surface area were also found to be directly proportional to the reaction temperature. Furthermore, the thermal stability of the samples also decreased with an

increase in temperature. This study revealed that *catalyst 1* produces good quality and a higher yield of MWCNTs at lower temperatures.

Appendix 3A.

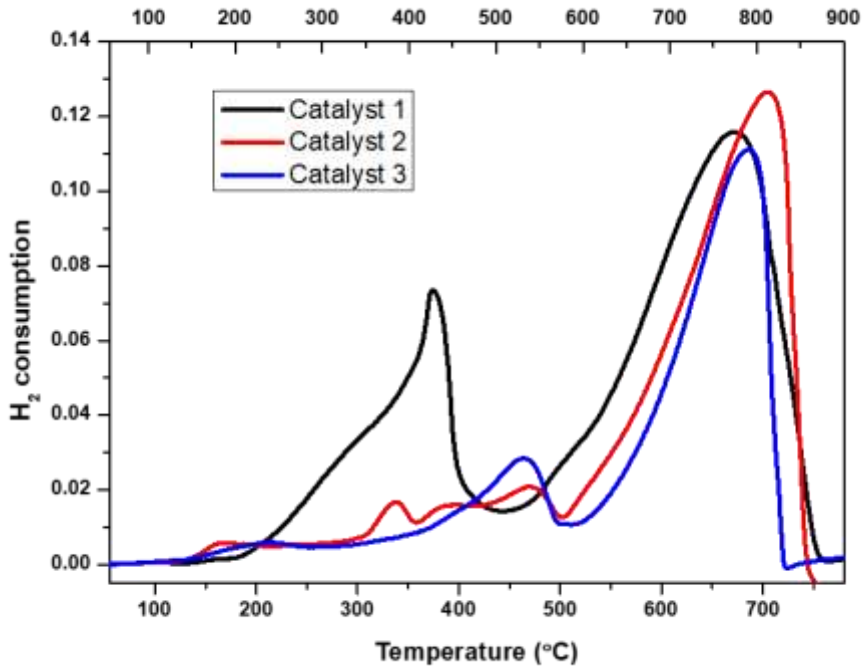


Figure 3.14: Temperature programmed reduction study of Fe-Co/$CaCO_3$ catalysts.

Table 3.10: Catalyst dependant study Raman analysis curve fitted Lorentzian data.

Sample	Area (D-peak)	Area (G-peak)	Intensity (D-peak)	Intensity (G-peak)	Area (G`-peak)	Ratio* I_D/I_G	Ratio $I_{G'}/I_G$
PP700	150932.25	91053.82	1071.66	1211.06	57318.65	0.88	0.59
PP700-2	115004.74	77803.89	914.44	973.80	82528.95	0.93	1.06
PP700-1	364995.46	144594.02	1903.63	1680.50	96703.73	1.41	0.67

*Calculated from intensity peak.

Table 3.11: Temperature dependant study Raman analysis curve fitted Lorentzian data.

Sample	Area (D-peak)	Area (G-peak)	Intensity (D-peak)	Intensity (G-peak)	Area (G`-peak)	Ratio* I_D/I_G	Ratio (Area used) $I_{G'}/I_G$
PP700	150932.25	91053.82	1071.66	1211.06	53718.65	0.88	0.59
PP750	222484.91	87203.04	1117.01	1095.55	39722.01	1.01	0.45
PP800	247864.01	53855.24	936.17	620.52	37785.03	1.50	0.70

*Calculated from intensity

Chapter 3 References

1. J. Simon, E. Flahaut, M. Golzio. *Materials*. 2019, **12**, 624-644.
2. A. N. Chakoli, J. M. He, Y. D. Huang. *Materials Today Communications*. 2018, **15**, 128-133.
3. M. Roldo, D. G. Fatouros. *Annual Reports Section "C" Physical Chemistry.* 2013, **109**, 10-35.
4. H. Wang, J. Li, X. Zhang, Z. Ouyang, Q. Li, Z. Su, G. Wei. *RSC Advances.* 2013, **3**, 9304-9310.
5. H. He, L. A. Pham-Huy, P. Dramou, D. Xiao, P. Zuo, C. Pham-Huy. *Biomed Research International.* 2013, **2013**, 1-12.
6. W. Zhang, Z. Zhang, Y. Zhang. *Nano Research Letters.* 2011, **6**, 555-576.
7. L.-M. Peng, Z. Zhang, S. Wang. *Materials Today Communications.* 2014, **17**, 433-442.
8. P. Avouris, J. Chen. *Materials Today: Nanotubes Electronics and Optoelectronics.* 2006, **9**, 46-54.
9. S. H. Aboutalebi, A. T. Chidembo, M. Salari, K. Konstantinov, D. Wexler, H. K. Liu, S. X. Dou. *Energy and Environmental Science.* 2011, **4**, 1855-1865.
10. L. Li, Z. Lou, W. Han, D. Chen, K. Jiang, G. Shen. *Advanced Materials Technologies.* 2017, **2**, 1600282 (1-8).
11. M. Sireesha, V. J. Babu, A. S. K. Kiran, S. Ramakrishna. *Nanocomposites*. 2018, **4**, 36-57.
12. A. Boyd, I. Dube, G. Feredov, M. Paranjape, P. Barbara. *Carbon*. 2014, **69**, 417-423.
13. C. Gupta, P. H. Maheshwari, S. R. Dhakate. *Materials for Renewable and Sustainable energy.* 2016, **5**, 1-11.
14. C. Lou, H. Xie, Q. Wang, G. Luo, C. Liu. *Journal of Nanomaterials.* 2015, 560392 (1-10).

15. U. Mehmood, Z. Malaibari, F. A. Rabani, A. U. Rehman, S. H. A. Ahmad, M. A. Atieh, M. S. Kamal. *Electrochimica Acta.* 2016, **203**, 162-170.

16. B. Siwach, S. Sharma, D. Mohan. *Journal of Integrated Science and Technology*. 2017, **5**, 1-4.

17. P. C. Mahakul, K. Sa, B. V. R. S. Subramanyam, P. Mahanadia. *Materials Chemistry and Physics.* 2019, **226**, 113-117.

18. S. Kim, O. Dovjuu, S.-H. Choi, H. Jeong, J.-T. Park. *Coatings.* 2019, **9**, 250-262.

19. S. Paul, B. Rajbongshi, B. Bora, R. G. Nair. S. K. Samdarshi. *New Carbon Materials.* 2017, **32**, 27-34.

20. L. Chen, X. Pan, D. Zheng, Y. Gao, X. Jiang, M. Xu, H. Chen. *Nanotechnology*. 2010, **21**, 345201(1-9).

21. C. Laurent, A. Peigney, A. Rousset. *Journal of Materials Chemistry.* 1998, **8**, 1263-1272.

22. V. Jourdain, C. Bichara. *Carbon.* 2013, **58**, 2-39.

23. K.-H. Ahn, S.-M. Kim, I. J. Yu. *Safety and Health at work.* 2011, **2**, 65-69.

24. L. Hu, D. S. Hetch, G. Grüner. *Chemical Reviews.* 2010, **110**, 5790-5844.

25. A. Szabó, C. Perri, A. Csató, G. Giordano, D. Vuono, J. B. Nagy. *Materials*. 2010, **3**, 3092-3140.

26. M. Yudasaka, T. Komatsu, T. Ichihashi, Y. Achiba, S. Iijima. *Journal of Physical Chemistry B.* 1998, **102**, 4892-4896.

27. J. Chrzanowska, J. Hoffman, A Małolepszy, T. A. Kowalewski, Z. Szymanski, L. Stobinski. *Basic Solid State Physics B.* 2015, **252**, 1860-1867.

28. *WWW.NanoWerk.com/nanotechnology/introduction/introduction_to_nanotechnology_22.php (Date accessed: 01-02-2020)*

29. S. J. Yoo, S. H. Han, W. J. Kim. *Carbon*. 2013, **61**, 487-500.

30. Y. Gogotsi, J. A. Libera, M. Yoshimura. *Journal of Materials Research.* 2000. **15**, 2591-2594.

31. Y. Gogotsi, N. Naguib, J. A. Libera. *Chemical Physics Letters*. 2002, **365**, 354-360.

32. J. B. Bai, A.-L. Hamon, A. Marraud, B. Jouffrey, V. Zymla. *Chemical Physics Letters.* 2002, **365**, 184-188.

33. Q. Zeng, Z. Li, Y. Zhou. *Journal of Natural Gas Chemistry.* 2006, **15**, 235-246.

34. A. C. Dupuis. *Progress in material science.* 2005, **50**, 929-961.

35. I. Kunadian, R. Andrews, D. Qian, M. P. Mengüç. *Carbon.* 2009, **47**, 384-395.

36. Y. M. Manawi, Ihsanullah, A. Samara, T. Al-Ansari, M. A. Atieh. *Materials.* 2018, **11**, 822-858.

37. F. Danafar, A. Fakhru'l-Razi, M. A. S. Mohd, D. R. B. Awang. *Chemical engineering Research and Design.* 2011, **89**, 214-223.

38. F. Wei, Q. Zhang, W.-Z. Qian, H. Yu, Y. Wang, G.-H. Luo, G.-H. Xu, D.-Z. Wang. *Powder Technology.* 2008, **183**, 10-20.

39. S. Zhan, Y. Tian, Y. Cui, H. Wu, Y. Wang, S. Ye, Y. Chen. *China Particuology*. 2007, **5**, 213-219.

40. L. Ni, K. Kuroda, L.-P. Zhou, T. Kizuka, K. Matsuishi, J. Nakamura. *Carbon*. 2006, **44**, 2265-2272.

41. G. Saeed. M. Umer. Farooq. *Optoelectronics and Advanced Materials-Rapid Communications*. 2013, **7**, 707-711.

42. M. Kumar, Y. Ando. *Journal of Nanoscience and Nanotechnology.* 2010, **10**, 3739-3758.

43. J. P. Gore, A. Sane. *Carbon Nanotube-Synthesis, Characterizations, Applications. InTech. Croatia.* 2011, 121-146.

44. S. B. Sinnot, R. Andrews, D. Qian, A. M. Rao, Z. Mao, E. C. Dickey, F. Derbyshire. *Chemical Physic Letters.* 1999, **315**, 25-30.

45. T. Arunkumar, R. Karthikeyan, R. R. Subramani, K. Viswanathan, M. Anish. *International Journal of Ambient Energy.* 2020, **41**, 452-456.

46. Y. Soneda, L. Duclaux, F. Béguin. *Carbon*. 2002, **40**, 955-971.

47. D. Torres, J. L. Pinilla, I. Suelves. *International Journal of Hydrogen Energy.* 2020, **45**, 19313-19323.

48. Y. Khan, S. Shukrulla, M. Y. Naz, A. Ghaffarm, I. Ahmad, S. Alsuhaibani. *Digest Journal of Nanomaterials and Biostructures.* 2017, **12**, 957-963.

49. A. Oyewemi, A. S. Abdulkareem, J. O. Tijani, M. T. Bankole, O. K. Abubakre, A. S. Afolabi, W. D. Roos. *Arabian Journal for Science and Engineering.* 2019, **44**, 5411-5432.

50. S. Venkatesan, B. Visvalingam, G. Mannathusamy, V. Viswanathan, A. G. Rao. *International Nano Letters.* 2018, **8**, 297-308.

51. S. Shukrullah, M. Y. Naz, N. M. Mohamed. K. A. Ibrahim, A. Ghaffar, N. M. AbdEl-Salam. *Journal of nanomaterials.* 2019, **2019**, 4642859(1-12).

52. S. Sasrimuang, O. Chuchuen, A. Artnaseaw. *Green Processing and Synthesis.* 2020, **9**, 340-348.

53. V. Ivanov, J. B. Nagy, P. Lambin, A. Lucas, X. B. Zhang, X. F. Zhang, D. Bernaerts, G. Van Tendeloo, S. Amelinckx, J. Van Landuyt. *Chemical Physics Letters.* 1994, **223**, 329-335.

54. J. Cheng, X. Zhang, Z. Luo, F. Liu, Y. Ye, W. Yin, W. Liu, Y. Han. *Materials Chemistry and Physics.* 2006, **95**, 5-11.

55. E. Dervishi, Z. Li, A. R. Biris, D. Lupu, S. S. Ttrigwell, A. S. Biris. *Chemistry of Materials.* 2007, **19**, 179-184.

56. T. C. Schmitt, A. S. Biris, D. W. Miller, A. R. Biris, D. Lupu, S. S. Trigwell, Z. U. Rahman. *Carbon*. 2006, **44**, 2032-2038.

57. Z. N. Tetana. *Boron and Nitrogen Doped Carbons for Photochemical Degradation Reactions. University of the Witwatersrand.* PhD thesis; 2013.

58. C. H. See, A. Husin, A. T. Harris. *Chemical Engineering and Technology.* 2009, **32**, 1280-1284.

59. N. Chiwaye, L. L. Jewell, D. G. Billing, D. Naidoo, M. Ncube, N. J. Coville. *Materials Research Bulletin.* 2014, **56**, 98-106.

60. M. T. Bankole, I. A. Mohammed, A. S. Abdulkareem, J. O. Tijani, S. S. Ochigbo, O. K. Abubakre, A. S. Afolabi. *Journal of Alloys and Compounds.* 2018, **749**, 85-102.

61. S. O. Ibrahim, K. U. Isah, A. S. Abdulkareem, U. Ahmadu, J. O. Tijani, W. D. Roos. *Journal of Material Science: Materials in Electronics.* 2020. Published online, DOI: *https://doi.org/10.1007/s10854-020-03550-s10854-020-03550-0*

62. Z. Li, E. Dervishi, Y. Xu, X. Ma, V. Saini, A. S. Biris, R. Little, A. R. Biris, D. Lupu. *The Journal of Chemical Physics.* 2008, **129**, 074712 (1-6)

63. X. Mathebula. *Photocatalytic Degradation of Methyl Violet in Water using TiO_2/Cellulos-N-MWCNTs. University of the Witwatersrand.* MSc dissertation; 2018.

64. A. M. M. Motchelabo. *Iron and Cobalt Catalysts Supported on Carbon Nanotubes for Use in the Fischer-Tropsch Synthesis. University of the Witwatersrand.* PhD thesis; 2011.

65. W. K. Maboya, N. J. Coville, S. D. Mhlanga. *South African Journal of Chemistry.* 2016, **69**, 15-26.

66. E. Couteau, K. Hernadi, J. W. Seo, L. Thiên-Nga, Cs. Mikó, R. Gaál. L. Forró. *Chemical Physical Letters*. 2003, **378**, 9-17.

67. L. F. Giraldo, M. Echeverri, B. L. López. *Macromolecular Symposia.* 2007, **258**, 119-128.

68. E. D. Dikio, A. J. Kupeta, F. T. Thema. *Journal of Chemistry.* 2014, **2014**, 641823 (1-6). doi.org/10.1155/2014/641823

69. H. Karimi-Maleh, S. Mehdipour-Ataei, M. Hatami, M. A. Khalilzadeh. *Journal of Analytical Chemistry.* 2014, **69**, 162-168.

70. S. D. Mhlanga, K. C. Mondal, R. Carter, M. J. Witcomb, N. J. Coville. *South African journal of chemistry.* 2009, **62**, 67-76.

71. P. T. Anastas and J. Warner. *Green Chemistry. Theory and Practice. Oxford University Press. Oxford,* 1998.

72. A. de la Hoz, A. Diaz-Ortiz, P. Prieto. *Chapter: Microwave-Assisted Green Organic Synthesis in Alternative Energy Sources for Green Chemistry.* 2016, pp 1-33.

73. A. Morsali, L. Hashemi. *Advanced in Inorganic Chemistry.* 2020, **76**, 33-72.

74. M. S. Dahiya, V. K. Tomer, S. Duhan. *Applications of Nanocomposite Materials in Drug Delivery*. 2018, 737-760.

75. K. Hernadi, A. Fonseca, J. B. Nagy, B. Bernaerts. J. Riga, A. Lucas. *Synthetic Metals*. 1996, **77**, 31-34.

76. L. Vaccarani, C. Goze, R. Aznar, V. Micholet, C. Journet, P. Bernier. *Synthetic Metals.* 1999, **103**, 2492-2493.

77. H. Hiura, T. W. Ebbesen, K. Tanigaki. *Advanced Materials*. 1995, **7**, 275-276.

78. V. K. Gupta, T. A. Saleh. *Carbon Nanotubes-From Research to Application.* 2011, Chapter 17, 295-312.

79. Z. Fathi, R.-A. K. Nejad, H. Mahmoodzadeh, T. N. Satari. *Journal of Plant Protection Research*. 2017, **57**, 228-236.

80. M. A. Salam, R. Burk. *Arabian Journal of Chemistry.* 2017, **10**, S921-S927.

81. X. He, X. Xu, G. Bo, Y. Yan. *RSC Advances.* 2020, **10**, 2180-2190.

82. J. Li, S. Ye, T. Li, X. Li, X. Yang, S. Ding. *Procedia Engineering.* 2015, **102b,** 492-498.

83. F. Zhou, Y. Wang, W. Wu, T. Jing, S. Mei, Y. Zhou. *Scientific Reports.* 2016, **6**, 38000 (1-12).

84. D. K. Singh, P. K. Lyer, P. K. Giri. *Diamond and Related Materials.* 2010, **19**, 1281-1288.

85. C. F. Holder, R. E. Schaak. *ACS Nano.* 2019, **13**, 7359-7365.

86. T. Belin, F. Epron. *Material Science and Engineering B.* 2005, **119**, 105-118.

87. D. Reznik, C. H. Olk, D. A. Neumann, J. R. D. Copley. *Physical Review B.* 1995, **52**, 116-124.

88. T. P. Mofokeng, Z. N. Tetana, K. I. Ozoemena. *Carbon.* 2020, **169**, 312-326.

89. S. Bandow, *Japanese Journal of Applied Physics Part 2.* 1997, **36**, L1403-1405.

90. C. H. Kiang, M. Endo, P. M. Ajayan, G. Dresselhaus, M. S. Dresselhaus. *Physical Review Letter*. 1998, **81**, 1869-1872.

91. M. Shiraishi, M. Inakagi, *Carbon alloys: Novel Concepts to Develop Carbon Science and Technology*. 2003, 161-173.

92. M. Liu, J. M. Cowley. *Carbon*. 1994, **32**, 393-403.

93. J. Majewska, B. Michalkiewicz. *Applied Physics A*. 2013, **111**, 1013-1016.

94. D. Hou, K. Li, R. Ma, Q. Liu. *Journal of Materiomics.* 2020, **6**, 628-641.

95. C. N. Barnakov, G. P. Khokhlova, A. N. Popova, S. A. Sozinov, Z. R. Ismagilov. *Eurasian Chemico-Technological Journal.* 2015, **17**, 87-93.

96. K. Kinoshita, K. Zaghib. *Journal of Power Sources.* 2002, **110**, 416-423.

97. P. Ruz, S. Banerjee, M. Pandey, V. Sudarsan, P. U. Sastry, R. J. Kshirsagar. *Solid State Sciences.* 2016, **62**, 105-111.

98. S. L. H. Rebelo, A. Guedes, M. E. Szefcyk, A. M. Pereira, J. P. Araújo, C. Freire. *Physical Chemistry Chemical Physics.* 2016, **18**, 12784-12796.

99. A. Sadezky. H. Muckenhuber, H. Grothe, R. Niessner, U. Pöschl. *Carbon*. 2005, **43**, 1731-1742.

100. A. Jorio, M. A. Pimenta, A. G. S. Filho, R. Saito, G. Dresselhaus. M. S. Dresselhaus. *New Journal of Physics.* 2003, **5**, 139.1-139.17.

101. A. C. Ferrari, J. Robertson. *Physical Review B.* 2001, **64**, 075414 (1-13).

102. A. C. Ferrari, J. Robertson. *Physical Review B.* 1999, **61**, 14095-14107.

103. Z. Xing, Y. Qi, Z. Tian, J. Xu, Y. Yuan, C. Bommier, J. Lu, W. Tong, D. Jiang, X. Ji. *Chemistry of Materials.* 2017, **29**, 7288-7295.

104. R. Al-Jishi, G. Dresselhaus. *Physical Review B*. 1982, **26**, 4514-4522.

105. Y. Wang, D. C. Alsmeyer, R. I. McCreery. *Chemistry of Materials.* 1990, **2**, 557-563.

106. T. Jawhiri, A. Roid, J. Casado. *Physical Review B*. 2000, **61**, 14095.

107. L. Bokobza, J. Zhang. *Express Polymer Letters.* 2012, **6**, 601-608.

108. E. F. Antunes, A. O. Lobo, E. J. Corat, V. J. Trava-Airoldi, A. A. Martin, C. Veŕssimo. *Carbon*. 2006, **44**, 2202-2211.

109. M. S. Dresselhaus, G. Dresselhaus, M. Hoffman. *Vibrational Spectroscopy*. 2007, **45b,** 71-81.

110. M. S. Dresselhaus, A. Jorio, M. Hofmann, G. Dresselhaus, R. Saito. *Nano Letters.* 2010, **10**, 751-758.

111. M. S. Dresselhaus, G. Dresselhaus, M. Hofmann. *Philosophical Transactions of the Royal Society.* 2008, **366**, 231-236.

112. L. M. Malard, M. A. Pimenta, G. Dresslhaus, M. S. Dresselhaus. *Physics Reports.* 2009, **473**, 51-87.

113. M. S. Dresselhaus, G. Dresselhaus, R. Saito, A. Jorio. *Physics Reports.* 2005, **409**, 47-99.

114. S. Santangelo, G. Messina, G. Faggio, M. Lanza, C. Milone. *Journal of Raman Spectroscopy.* 2011, **42**, 593-602.

115. R. A. Dileo, B. J. Landi, R. P. Raffaelle. *Journal of Applied Physics.* 2007, **101**, 064307 (1-5).

116. S. Santangelo, M. Dhanagopal, G. Faggio, G. Messina, A. Pistone, M. Lanza, C. Milone. *Diamond and Related Materials.* 2010, **19**, 599-603.

117. Z. N. Tetana, S. D. Mhlanga, G. Bepete, R. W. M. Krause, N. J. Coville. *South African Journal of Chemistry.* 2012, **56**, 39-49.

118. J. W. Chiang, B. E. Brinson, A. Y. Huang, P. A. Willis, M. J. Bronikowski, J. L. Margrave, R. E. Smalley, R. H. Hauge. *Journal of Physical Chemistry B.* 2001, **105**, 8297-8301.

119. K. Hernadi, A. Fonseca, P. Piedigrosso, M. Delvaux, J. B. Nagy, D. Bernaerts, J. Riga. *Catalyst Letters*. 1997, **48**, 229-238.

120. B. J. Landi, C. D. Cress, C. M. Evans, R. P. Raffaelle. *Chemistry of Materials*. 2005, **17**, 6819-6834.

121. Z. J. Shi, Y. F. Lian, F. H. Liao, X. H. Zhou, Z. N. Gu, Y. Zhang, S. Iijima, H. D. Li, K. T. Yue, S. L. Zhang. *Journal of Physics and Chemistry of Solids.* 2000, **61**, 1031-1036.

122. J. H. Lehman M. Terrones, E. Mansfield, K. E. Hurst, V. Meunier. *Carbon.* 2011, **49**, 2581-2602.

123. P. Liu, T. Wang. *Applied Physics A: Materials Science and Processing.* 2009, **97**, 771-775.

124. S. Santangelo, G. Messina, G. Faggio, M. Lanza, A. Pistone, C. Milone. *Journal of Material Science.* 2010, **45**, 783-792.

125. K. Don-Young, Y. S. Young, K. Soon-Min, J. Hyoung-Joon. *Molecular Crystals and Liquid Crystals.* 2009, **510**, 79-86.

126. H. Li, N. Zhao, C. He, C. Shi, X. Du, J. Li. *Materials Science and Engineering A.* 2008, **473**, 355-359.

127. G. S. B. McKee, C. P. Deck, K. S. Vecchio. *Carbon.* 2009, **47**, 2085-2094.

128. A. Peigney, Ch, Laurent, E. Flahaut, R. R. Bacsa, A. Rousset. *Carbon.* 2001, **39**, 507-514.

129. Z. Li, E. Dervishi, Y. Xu, V. Saini, M. Mahmood, O. D. Oshin, A. R. Biris. A. S. Biris. *Catalysis Letters.* 2009, **131**, 356-363.

130. D. Y. Kim, C. M. Yang, Y. S. Park, K. Kim, S. Y. Jeong, J. H. Han, Y. H. Lee. *Chemical Physics Letters.* 2005, **413**, 135-141.

131. K. Raji, C. B. Sobhan. *Nanotechnology Reviews.* 2013, **2**, 73-105.

Chapter 4: An investigation of reaction time, flow rate, temperature, and boron source in the synthesis of boron doped MWCNTs over a Fe-Co/$CaCO_3$ catalyst.

4.1. Introduction

MWCNTs are a type of carbon allotrope that are typically described as rolled up sheets of graphene encapsulating each other. [1-6] The existing diversity of synthesis and modification methods has led to an explosion in the diversity of morphologies such as different diameters, lengths, number of rolled layers and the manner these layers are rolled (i.e., chirality) etc. to access their exceptional chemical properties and expand their area of application.[7-11] Heteroatom doping is one technique used to modify the properties of CNTs. Doping has been typically performed using N, B, and P atoms, and the doped MWCNTs have been reported to have reduced resistivity, increased thermal stability, reduced thermal conductivity, improved conductivity, and electrocatalytic activity compared to their pristine counterparts.[12-21]

Boron has been used extensively as a dopant; it contains three valence electrons and an electron deficient p-orbital that allows the initiation of electron flow when incorporated in the chemically inert sp^2 carbon structure. Furthermore, it increases the number of active sites essential for improving electrochemical properties of the material. Boron doped MWCNTs possess an increased amount of hole charge carriers, giving them better electrical conductivity.[12-15] The concentration of boron in the carbon structure influences the morphology of the MWCNTs, and the extent to which their different properties can be improved. Yeh *et al.* investigated the electrochemical properties of B-doped materials with different boron concentrations (0.40, 2.09, 3.38, 3.92 %) by using the materials as counter electrodes in dye-sensitized solar cells. They reported an improvement in conversion efficiency for all the B-doped materials compared to the pristine MWCNTs. Furthermore, the material with the lowest boron concentration reported the highest conversion efficiency and electrocatalytic activity, improved electronic conductivity, and lower charge transfer resistance relative to materials with the higher concentrations.[12]

Different methods have been employed in the production of B-doped MWCNTs; arc-discharge,[22-26] laser ablation,[27-30] and catalytic vapour deposition[30-40]. These methods produce

B-doped MWCNTs with varying concentrations of boron, and consequently varying characteristics. The *CVD* method offers the advantage of producing higher yields of boron doped material with a diverse range of characteristics. The doping process may be performed in two major ways: *in situ* or *post doping* via the *CVD* method. The *in-situ* method involves the formation of B-doped MWCNTs by simultaneously supplying the carbon and boron precursor into the reaction chamber, while the *post doping* method is a two-step process that requires the synthesis of the MWCNTs first, and this is followed by the addition of the boron precursor to produce B-doped MWCNTs. [41-42]

As with the production of pristine MWCNTs using the *CVD* method, the type and quality of B-doped MWCNTs depends on the temperature, pressure, type of catalyst, carrier gas (i.e., type and flow rate), carbon precursor (including flow rate of a gas), and boron precursor. The production of elemental boron or boron complexes can be an expensive process and tends to present with environmental challenges. [41, 43-44]. A diverse range of B containing precursors have been used in either the liquid, gas or solid states and have been employed to make B-CNTs. *Tetana et al.* investigated and successfully produced B-doped MWCNTs via an *in-situ* process at different temperatures (700, 750, 800, 850, 900℃) using $C_3H_9BO_3$ and C_2H_2 over a Fe-Co/$CaCO_3$ catalyst as a boron and carbon source, respectively. At temperatures > 800 ℃ B-doped MWCNTs were produced with other carbonaceous material. They reported the highest boron concentration of 1.6% for the reaction performed at 800 ℃. They also reported the formation of boron oxide during the reaction, which contaminated and weakened the integrity of the quartz tube used.[41]

Despite being highly toxic and flammable B_2H_6 gas has been successfully utilized in the synthesis of B-doped MWCNTs and other forms of CNTs.[45-48] Solid boron precursors such as B_2O_3 have shown success in the production of B-doped CNTs, but for effecting doping, high synthetic temperatures were needed. This ultimately created additional and unintended defects in the carbon structure.[41, 49-51] Other boron precursors that have been utilized include $C_8H_7BO_4$[52], triethylborane[53-54], boric acid[55-56], triphenylborane[57-58], and boron trichloride[59-60].

Although an extensive amount of work has gone into developing different methods to produce boron doped CNTs, precise control of boron concentration in the carbon structure remains a major challenge.[41, 61-62] The purpose of the work in this chapter is to produce B-doped MWCNTs over a Fe-Co/$CaCO_3$ catalyst using acetylene and two boron sources, trimethyl borate ($C_3H_9BO_3$) and tri-isopropyl ($C_9H_{21}BO_3$), using the same reaction conditions. This was

to determine the preferable boron source of the two and to evaluate the influence of the carbon to boron ratio on the properties of MWCNTs produced. Additionally, both precursors were used in a temperature dependant and in time dependant studies to assess the influence of reaction temperature and time on the amount of boron incorporated in the MWCTNs structure. Furthermore, $C_9H_{21}BO_3$ was used to produce B-doped MWCNTs at different flow rates of the carbon precursor and carrier gas. The diversity of conditions explored in this work allowed for the extensive comparison and examination of the morphology, elemental configuration, and defect levels of the B-doped MWCNTs produced.

4.2. Materials and Methods.

4.2.1. Starting materials.

Trimethyl borate (≥ 98%), tri-isopropyl borate (≥ 98%), and 55% nitric acid (HNO_3) of reagent standard were purchased from Sigma-Aldrich, South Africa. Distilled water was used in all the experiments that required water. The gases, acetylene (C_2H_2) and nitrogen (N_2), were supplied by Afrox, South Africa.

4.2.2. Synthesis of boron doped MWCNTs.

A quartz boat equipped with 10% Fe-Co/$CaCO_3$ (300 mg) catalyst was placed in a tubular quartz tube in a horizontal furnace. The tube was connected to two gas lines supplying C_2H_2 and N_2 that functioned as carbon source and carrier gases, respectively. The B-doped MWCNTs were obtained by increasing the temperature of the furnace at $10℃/min$ to the desired temperature under a N_2 atmosphere. Once the desired temperature was obtained, the C_2H_2 and N_2 gases were bubbled through the boron source, $C_3H_9BO_3$ or $C_9H_{21}BO_3$ into the reaction chamber for 1 h. The reaction was cooled down to room temperature using compressed air. The boat containing a black solid of MWCNTs was retrieved and the product collected. The B-doped MWCNTs samples were added to an excess of HNO_3 (55%) in a round bottom flask and left stirring under reflux at 110℃ for 4 h. The resulting solution was left to cool to room temperature. It was diluted with water, filtered, and washed until the filtrate had a neutral pH. The obtained black solid was left to dry at 100℃ for 12 h in an oven.

The different studies were carried out as followed:

i) *Catalyst 1* (**Chapter 3, Section 3.2.1 Method A**) was used in a temperature dependant study (700℃, 750℃, and 800℃) for the production B-doped MWCNTs using both $C_3H_9BO_3$ and $C_9H_{21}BO_3$ as boron sources. C_2H_2 and N_2 gases had flow

rates of 90 sccm and 240 sccm, respectively. Additionally, was also used to conduct a time dependant study (15 and 30 min) using $C_3H_9BO_3$ and $C_9H_{21}BO_3$ as boron sources at 800℃, with C_2H_2 (90 sccm) and N_2 (240 sccm) used as carbon and carrier gas sources, respectively.

ii) C*atalyst 3* it (**Chapter 3, Section 3.2.1 Method C**) was also used in the preparation of B-doped MWCNTs at 800 ℃. The flow rates of the carbon source and carrier gases were varied, and $C_9H_{21}BO_3$ was used as a boron source.

The carbon yield (%) of the purified B-doped MWCNTs prepared using tri-isopropyl borate (BP800-*15-i*, BP800-*30-i*, BP800-*60-i*) and trimethyl borate (BP800-*15-m*, BP800-*30-m*, BP800-*60-m*) were determined relative to the C_2H_2 gas used at normal temperature (20℃) and pressure (1 atm) (NTP). The yield was calculated as described below:

$$V_{C_2H_2} = C_2H_2\ flow\ rate \times reaction\ time = 90\ sccm \times 60\ min = 5400\ cm^3$$

$$V_{C_2H_2} = 90\ sccm \times 30\ min = 2700\ cm^3$$

$$V_{C_2H_2} = 90\ sccm \times 15\ min = 1350\ cm^3$$

$$m_{theoretical} = \rho_{C_2H_2} V_{C_2H_2} = 0.001092 \frac{g}{cm^3} \times V_{C_2H_2}$$

$$\%\ yield = \frac{Mass\ of\ purified\ sample}{Theoretical\ mass} \text{.....(4.1)}$$

4.2.3. Characterization techniques.

The structural characteristics of the materials were studied using powder X-ray diffraction (PXRD, angle scan range of 2θ = 10-90°) analysis on a Bruker D2 phaser with a nickel filtered copper radiation λ_{K_α} = 0.15406 nm, and Raman spectroscopy using an argon ion laser with a 514.5 nm laser line. Furthermore, images from the transmission electron microscope (TEM, FEI Tecnai T12 instrument) and scanning electron microscope (SEM, ZEISS SIGMA 03-30 FESEM instrument) were used in determining the morphology of the material. The Brunauer, Emmet, and Teller (BET) method under isothermal conditions (-196℃, using liquid nitrogen) was used to determine the surface area, pore volumes and sizes of the material (Micromeritics TriSta 3000 instrument). A PerkinElmer TGA4000 instrument was used to investigate the thermal properties of the obtained boron doped MWCNTs over a temperature range of 35-900℃ under an atmosphere of air (20 ml/min).

4.3. Results and discussion.

4.3.1. Attempted synthesis of boron doped MWCNTs (B-doped MWCNTs); reaction time and boron source dependant study.

The reaction time (15, 30, 60 min) was investigated for the synthesis of B-doped MWCNTs using tri-isopropyl borate and trimethyl borate as boron sources at 800℃ over the Fe-Co/$CaCO_3$ catalyst. The catalyst residue in the as-synthesized MWCNTs were removed through an oxidative process using 55% HNO_3, and the carbon yield (%) of the purified B-doped MWCNTs prepared using tri-isopropyl borate (BP800-*15-i*, BP800-*30-i*, BP800-*60-i*) and trimethyl borate (BP800-*15-m*, BP800-*30-m*, BP800-*60-m*) were determined (Table 1).

Table 4.1: Carbon yield (%) of MWCNTs derived from tri-isopropyl borate and trimethyl borate.

Sample	Total Mass of purified samples (g)	Carbon yield (%)
BP800-*15-i*	0.5451	37.0
BP800-*30-i*	0.7239	24.6
BP800-*60-i*	1.5850	26.9
BP800-*15-m*	0.5980	40.6
BP800-*30-m*	0.7107	24.1
BP800-*60-m*	0.8530	14.5

The carbon yield (%) (Table 4.1) was found to decrease with reaction time when both boron sources were used. In both cases, the highest % yield was achieved at a reaction time of 15 min. The decrease in % yield was found to be more pronounced with an increase in reaction time when trimethyl borate was used compared to tri-isopropyl borate. Additionally, the difference in % yield at a reaction time of 30 min was found to be insignificant in both cases.

The successful synthesis of all B-doped samples was corroborated by TEM analysis (**Figure 4.1a-f**), and the obtained images also used to estimate the average diameter of nanotubes in each sample. All samples reported MWCNTs with varying lengths, diameter, and a

combination of MWCNTs with open and closed tips. Additionally, all samples contained some MWCNTs with a coiled morphology, but was more prominent in sample BP800-60-*i*. Furthermore, all samples that had MWCNTs a mixture of both smooth and rough surfaces. In both sets of samples, a reaction time of 30 min, produced the highest average diameter, with the use of trimethyl borate (BP800-30-*m*) producing the larger average diameter (59 nm) relative to the use of tri-isopropyl borate (52 nm, BP800-30-*i*). However, sample BP800-30-*i* reported a wider diameter distribution than BP800-30-*m.* The lowest average diameter recorded for both sets of samples was at a reaction time of 60 min, with BP800-60-*i* reporting a wider diameter distribution. Except for samples prepared at a reaction time of 30 min, the use of trimethyl borate produced MWCNTs with smaller average diameters than tri-isopropyl borate.

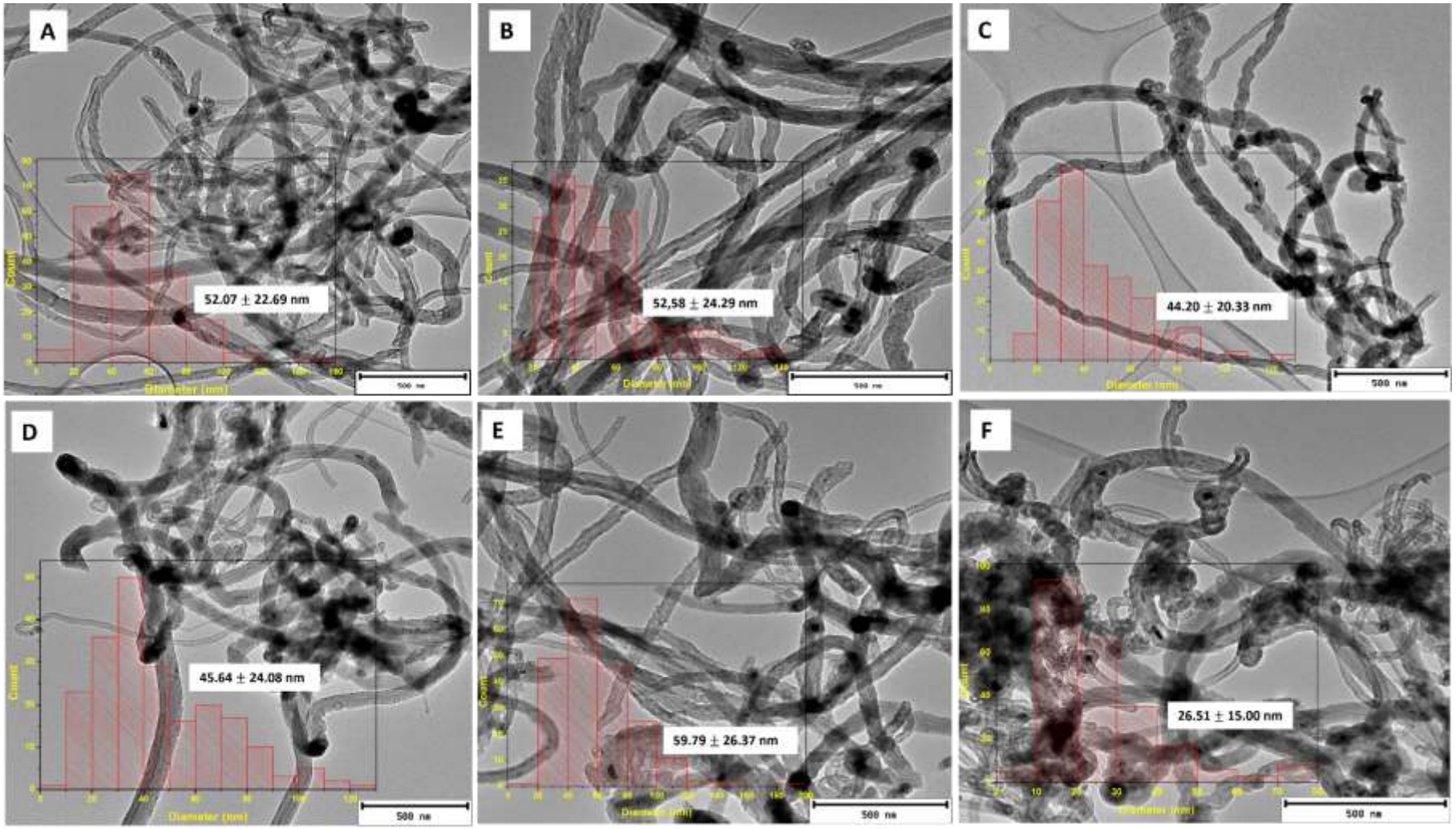


Figure 4.1: TEM images of B-doped MWCNTs *a)* sample BP800-*15-i*, *b)* sample BP800-*30-i*, *c)* sample BP800-*60-i*, *d)* sample BP800-*15-m*, *e)* sample BP800-*30-m*, *f)* sample BP800-*60-m.*

The XRD analysis of the obtained as synthesized (**Figure 4.2a-b**) and purified (**Figure 4.2c-d**) MWCNTs reported the characteristic peaks due to the 002, 100 and 101 graphitic planes at approximately 26°, 43°, 44-45°, respectively. In addition to the catalyst residue peaks observed in the as-synthesized MWCNTs of both sets of samples, boron trioxide peaks (**Figure 4.2b**) were observed in MWCNTs samples prepared from trimethyl borate. XRD patterns (**Figure 4.2c-d**) of the purified and functionalized MWCNTs, confirmed the removal of the residue for both sets of samples, and of boron trioxide in the case of material derived from trimethyl borate. Sample BP800-*60-i* (**Figure 4.2c**) was the only one that still presented with a noticeable amount of catalyst residue.

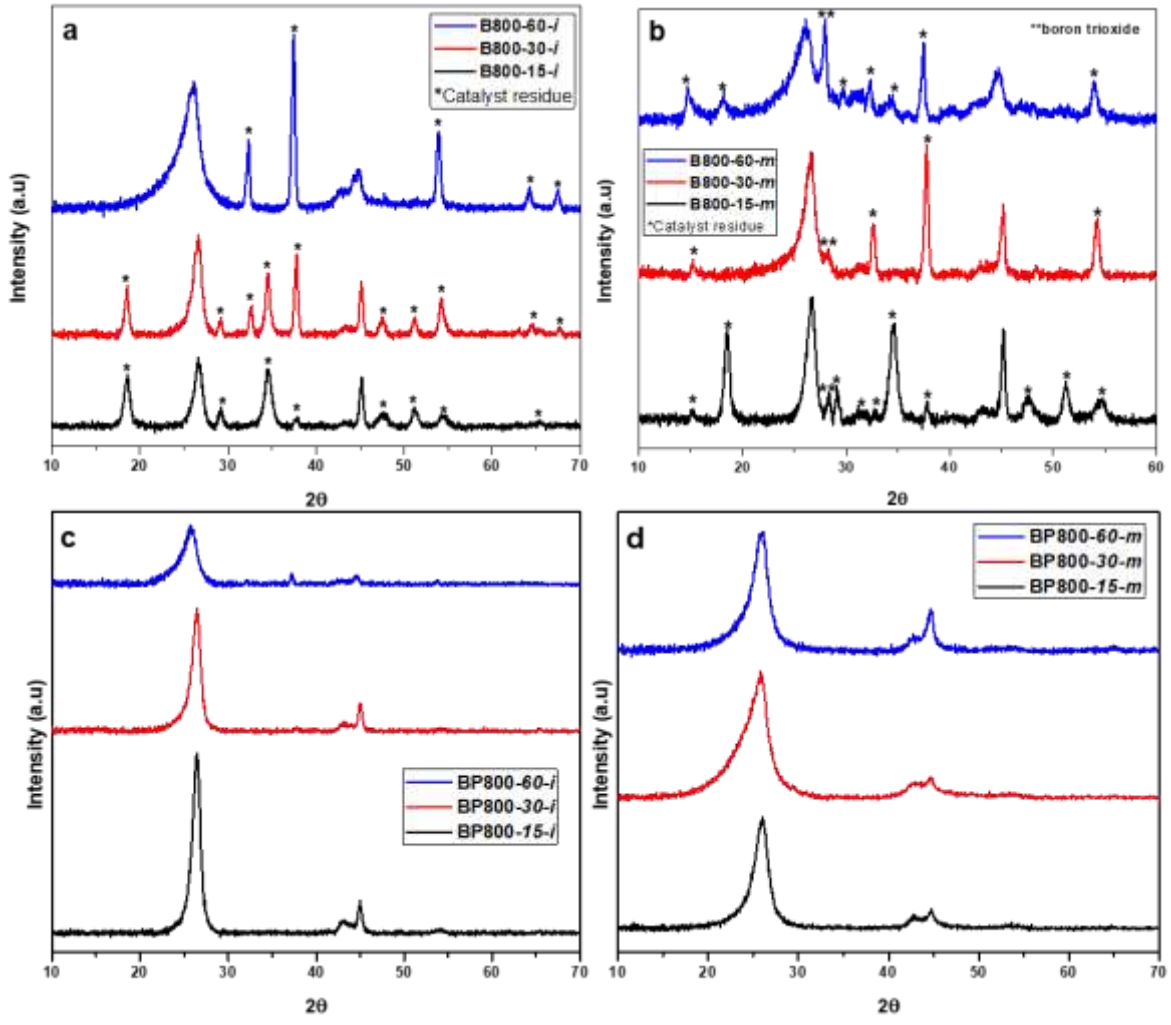


Figure 4.2: XRD analysis of *a)* as-synthesized tri-isopropyl borate derived B-doped MWCNTs, *b)* as-synthesized trimethyl borate derived B-doped MWCNTs *c)* purified tri-isopropyl borate derived B-doped MWCNTs, *d)* purified trimethyl borate derived B-doped MWCNTs.

The Bragg reflections (002 plane, Table 4.2) for samples BP800-15-*i* (26.48°) and BP800-30-*i* (26.43°) were similar to those of the pristine MWCNTs (26.44°, see sample PP800 XRD spectrum in **Appendix 4A Figure 4.29**), but a downward shift in the position of the 002 peak was observed for sample BP800-60-*i* (25.83°). A downward shift in the 002 peak was observed for all the purified MWCNTs prepared from trimethyl borate. A downward shift in the peak position has been reported to indicate a successful boron addition to the lattice structure of MWCNTs. [41, 63-66]

Table 4.2: The d-spacing and graphitization degree (g) of the obtained MWCNTs.

Sample code	002 plane peak position (°)	FHWM (°)	d_{002} (Å)	g (%)
BP800-15-*i*	26.48	0.7382	3.363	89.5
BP800-30-*i*	26.43	0.8161	3.369	82.6
BP800-60-*i*	25.83	1.145	3.446	*(-7.0)
BP800-15-*m*	25.98	1.180	3.427	15.1
BP800-30-*m*	25.81	1.189	3.449	*(-10.46)
BP800-60-*m*	25.93	1.150	3.433	8.1
PP800	26.44	1.041	3.368	83.7

*Validity range is between 0-100%, outside this range turbostratic arrangement of layers and increased defect density is observed.[65]

All the purified samples presented with asymmetric 002 peaks that were deconvoluted using the Voigt spectral function **(Figure 4.3a-f)**. The asymmetry could be attributed to the sample containing a mixture of morphologies (e.g., diameter), as seen in the TEM analysis of the samples. The FWHM (Table 4.2) of MWCNTs prepared from tri-isopropyl borate indicated that the asymmetry of the 002 peak became more prominent as the reaction time increased. This suggests that an increase in reaction time produced MWCNTs with improved crystallinity. reaction time did not report a significant influence on the FHWM, and consequently the crystallinity of the MWNCTs prepared from trimethyl borate. This suggested that reaction time

had more influence on the differences in crystallinity in the production of MWCNTs when tri-isopropyl borate was used as a boron source.

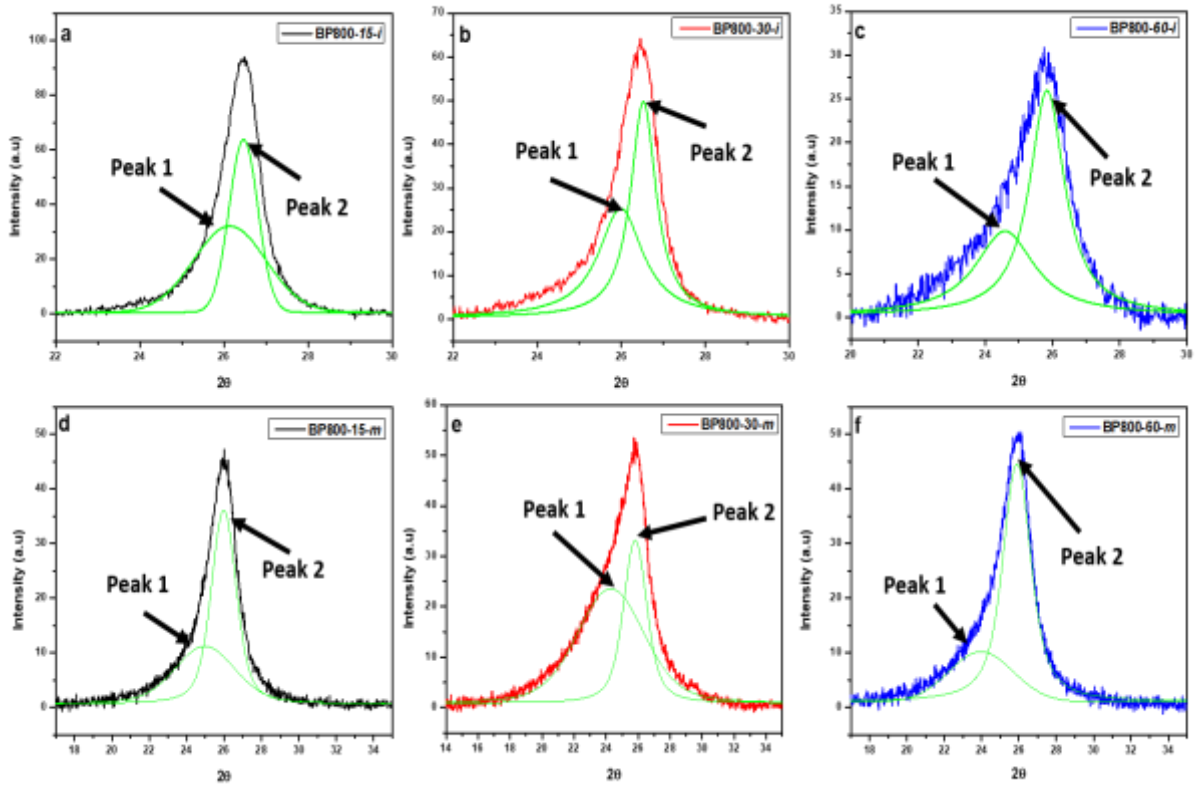


Figure 4.3: XRD spectra of deconvoluted 002 peaks using Voigt spectral function: *a-c)* 002 peak of purified B-doped MWCNTs prepared from tri-isopropyl borate, *d-f)* 002 peak of purified B-doped MWCNTs prepared from trimethyl borate.

The d-spacing (d_{002}, Table 4.2) was determined using the Bragg equation (4.2); samples BP800-15-*i* and BP800-30-*i* presented with d-spacing comparable to each other and the pristine MWCNTs (PP800), while BP800-60-*i* gave the largest d-spacing. The MWCNTs synthesized from trimethyl borate reported a d-spacing larger than those of the pristine MWCNTs. Although the d-spacing may be attributed to a combination of several factors,[41, 64, 67-72] the larger d-spacing for sample BP800-60-*i* (3.446) and all the MWCNTs prepared from trimethyl borate suggested a successful incorporation of boron into the lattice structure, and they correspond to typical values reported in literature for B-doped MWCNTs. [41, 63, 65-66]

$$n\lambda = 2dsin\theta \text{……..} \textbf{(4.2)}$$

$$g\ (\%) = \frac{3.440 - d_{002}}{3.440 - 3.354} \times 100 \text{ ……..} \textbf{(4.3)}$$

The graphitization degree (g) was determined and investigated using the Maire and Mering formula (4.3).[73-76] Graphitization degree evaluates the deviation of material from an ideal defect free graphite like crystal (i.e., crystallinity) and the 3D arrangement of the graphitic layers relative to each other. Additionally, the former is also subject to the uniform or non-uniform distribution of defects in each layer throughout the crystal. A low g signals significant deviation from an ideal defect free graphite and a turbostratic arrangement of the layers, hence, it could give qualitative information on the presence of any defects or incorporation of boron into the sample's lattice structure. [65, 67-69] Both sets of samples reported g values less than that of the pristine MWCNTs sample. The g for tri-isopropyl borate derived MWCNTs decreased with an increase in reaction time, with sample BP800-60-*i* failing to obey the validity range ($0 \leq g \leq 100$). A general decrease in g for the trimethyl borate derived MWCNTs was also observed, but it was sample BP800-30-*m* that did not obey the validity range. This indicated that samples BP800-60-*i* and BP800-30-*m* reported a higher degree of turbostratic arrangement of the layers, and a high density of defects that may be due to the successful incorporation (non-uniform) of boron into the lattice structure. This is consistent with the large d-spacings for both samples, which is generally attributed to boron containing MWCNTs. [41, 63, 65-66] The g values for both sets of samples indicated that trimethyl borate was more effective in the modification of MWCNTs than tri-isopropyl borate.

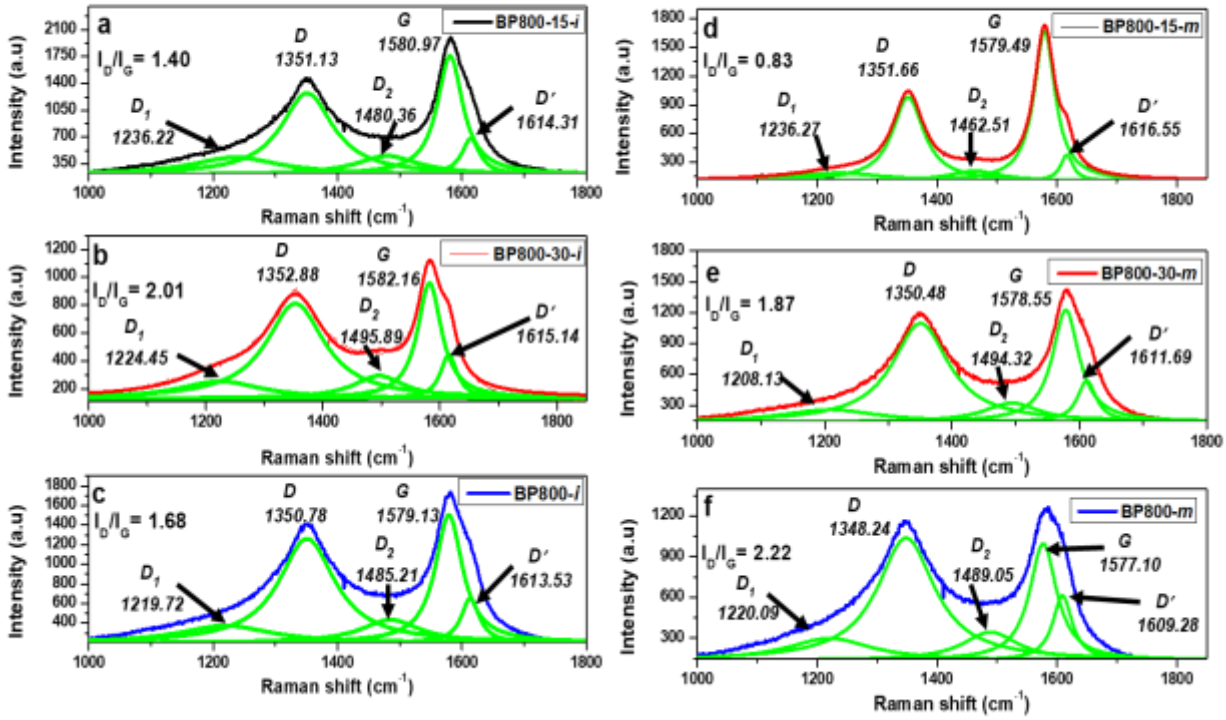


Figure 4.4: *a-c)* 1st order Raman Lorentzian fitted peaks for purified B-doped MWCNTs prepared from tri-isopropyl borate, *d-f)* 1st order Raman Lorentzian fitted peaks for purified B-doped MWCNTs prepared from trimethyl borate.

Raman spectroscopy (**Figure 4.4**, full data reported in **Appendix 4A** Table 4.14) was also used to investigate the structural properties of the purified/functionalized MWCNTs. The characteristic *D* (1350 cm^{-1}) and *G* (1580 cm^{-1}) bands arising from the A_{1g} symmetry forbidden breathing mode and E_{2g} vibrations of sp^2 hybridized carbon atoms, respectively, were observed. The bands exhibited an asymmetry that was associated with the presence of multiple components, and a Lorentzian function was used to isolate them.[35, 39, 77-83] The area of the *D* and *G* bands was used to calculate the ratio coefficient for determining the relative order/disorder in each material. All synthesized MWCNTs samples presented with a lower I_D/I_G ratio than the corresponding pristine MWCNTs and this could be attributed to the catalytic graphitization effect that boron is known to have in the synthesis of MWCNTs.[41] The I_D/I_G ratio was found to increase with reaction time for both sets of samples, however, the ratio increased up to a reaction time of 30 min and then reduced at a reaction time of 60 min for samples prepared using tri-isopropyl borate. In addition, the intensity and width of the *D* peak was also found to increase with an increase in reaction time. This suggested that the density of

defects was larger for material produced at higher reaction times. This was corroborated further by the increase and decrease in intensity of the *D'* and *G* bands as the reaction time increased, respectively.

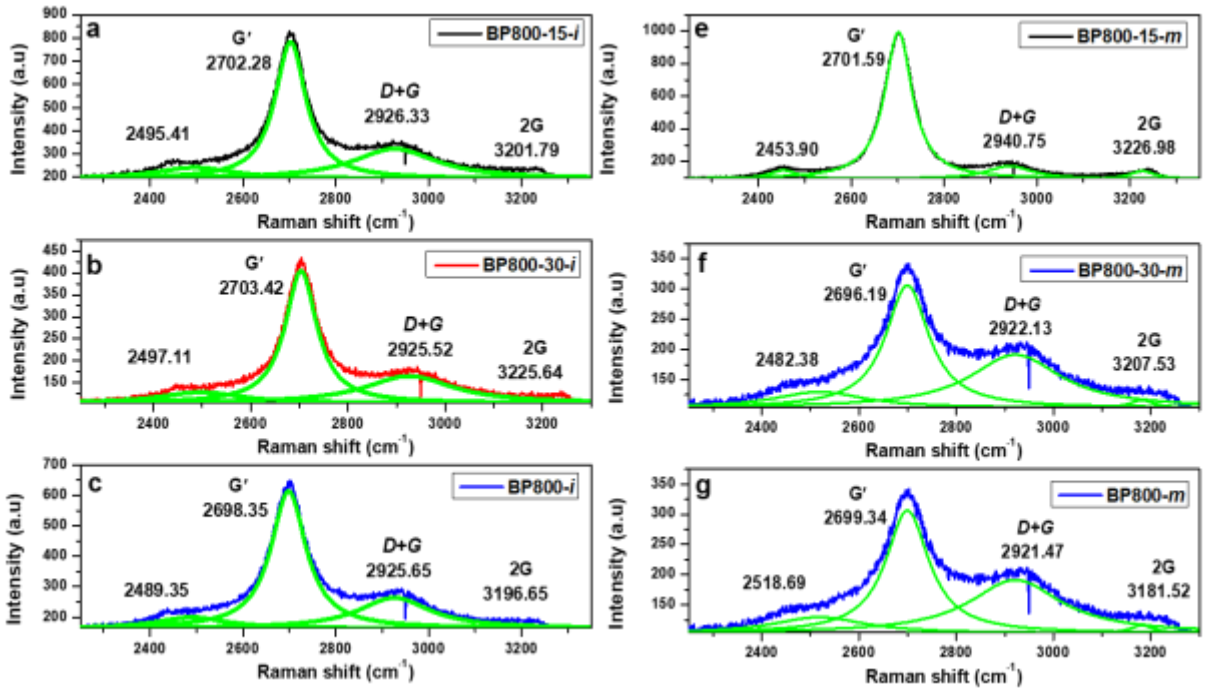


Figure 4.5: *a-c)* 2nd order Raman Lorentzian fitted peaks for purified tri-isopropyl borate derived B-doped MWCNTs, *d-f)* 2nd order Raman Lorentzian fitted for purified trimethyl borate derived B-doped MWCNTs.

The 2nd order region of the Raman spectra (**Figure 4.5**, full data reported in **Appendix 4A** Table 4.12) revealed multiple peaks associated with the presence of multiple graphitic layers, the observed *G', D+G* and *2G* bands that arise from the overtone of the *D* band and a double resonance process from the *2D*, $2E_{2g}$ and $D+E_{2g}$ frequency modes, respectively.[84-86] The long-range order ($I_{G'}/I_G$) and overall crystallinity ($I_{G'}/I_D$) (both listed in **Appendix 4A,** Table 4.13) of the materials was investigated using the area ratio of the *G'* band to *D* and *G* band[87-89]; the use of tri-isopropyl borate gave samples with no significant statistical difference in the long-range order, while it decreased with reaction time for those derived from trimethyl borate. A general decrease in overall crystallinity with an increase in reaction time was observed in both cases. Greater differences with reaction time were observed for samples produced using trimethyl borate. The trends in long range-order and overall crystallinity indicated that reaction time had a pronounced influence on the crystallinity (and maybe the incorporation of boron atoms) of MWCNTs when trimethyl borate was used as a boron source, larger than seen when

tri-isopropyl borate was used. The large extent of overlap and the comparable intensity of the *G'* and *D+G* bands for the pristine MWCNTs sample (**Appendix 4A, Figure 4.30**) relative to the samples indicated a presence of a higher number of layers relative to all the produced samples.[84-90] The number of layers is directly correlated to the diameter of the nanotubes, indicating that on average the prepared MWCNTs had smaller diameters than the pristine MWCNTs.

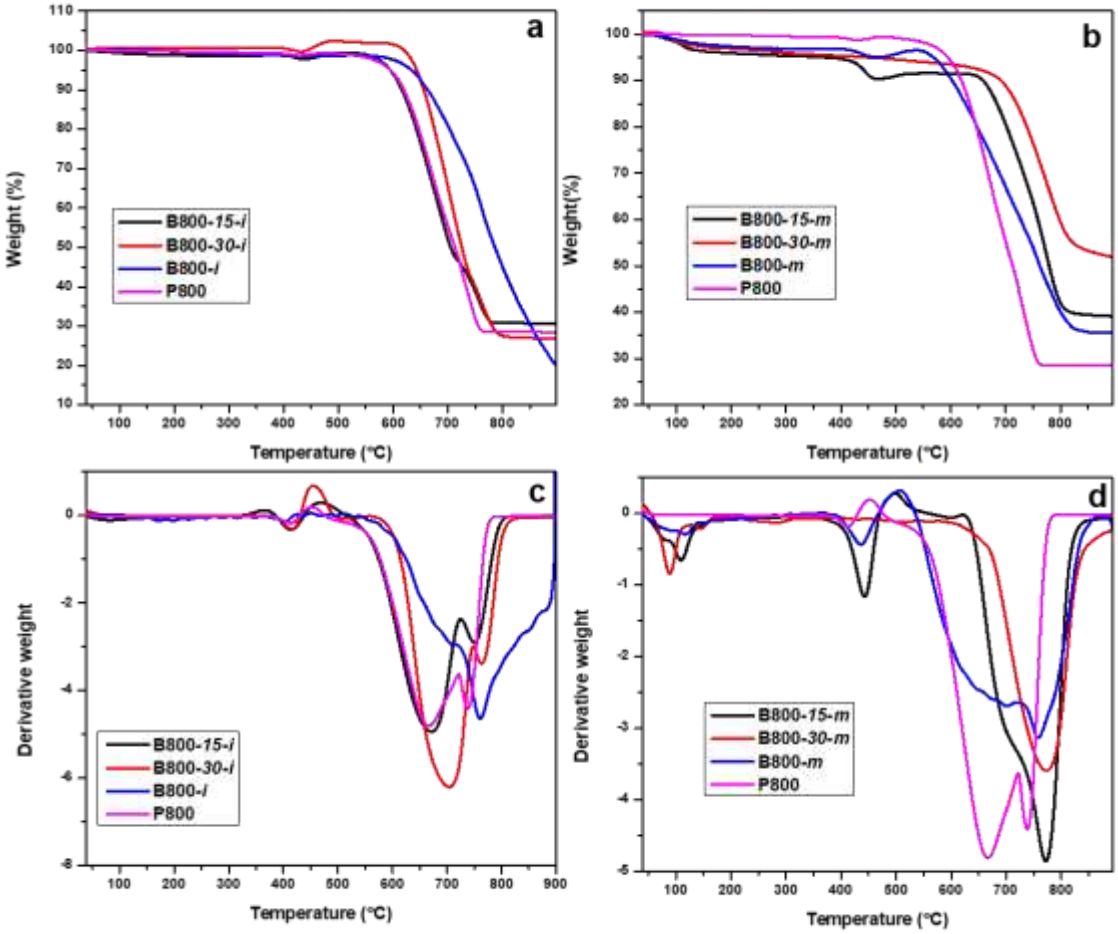


Figure 4.6: *a)* TGA analysis of as synthesized B-doped MWCNTs prepared from tri-isopropyl borate, *b)* TGA analysis of as synthesized B-doped trimethyl borate derived B-doped samples, *c)* derivative curve of as synthesized B-doped MWCNTs prepared from tri-isopropyl borate, *d)* derivative of as synthesized B-doped trimethyl borate derived B-doped samples.

Thermal analysis of the as synthesized MWCNTs (**Figure 4.6**) revealed that the thermal stability and carbon yield of the nanotubes increased with reaction time. Apart from sample B800-*15-i*, the first weight loss, attributed to a loss of adsorbed moisture, occurred at

approximately a 100℃ for all MWCNTs, including pristine MWNCTs (P800).[41] The second weight loss resulting from the oxidation of amorphous carbon was observed for all samples (except for B800-30-*m*) at 400℃. This was followed by an immediate weight gain at 450℃ due to the formation of metal oxides from the catalyst.[90-96] Sample B800-*30-m* did not report this mass gain, which suggested that the metals in the catalyst residue existed in their oxidized form. The weight derivative curve revealed that all samples, apart from B800-30-*m*, had more than one distinct type of carbon or MWCNTs (i.e., different morphologies) with different thermal properties.

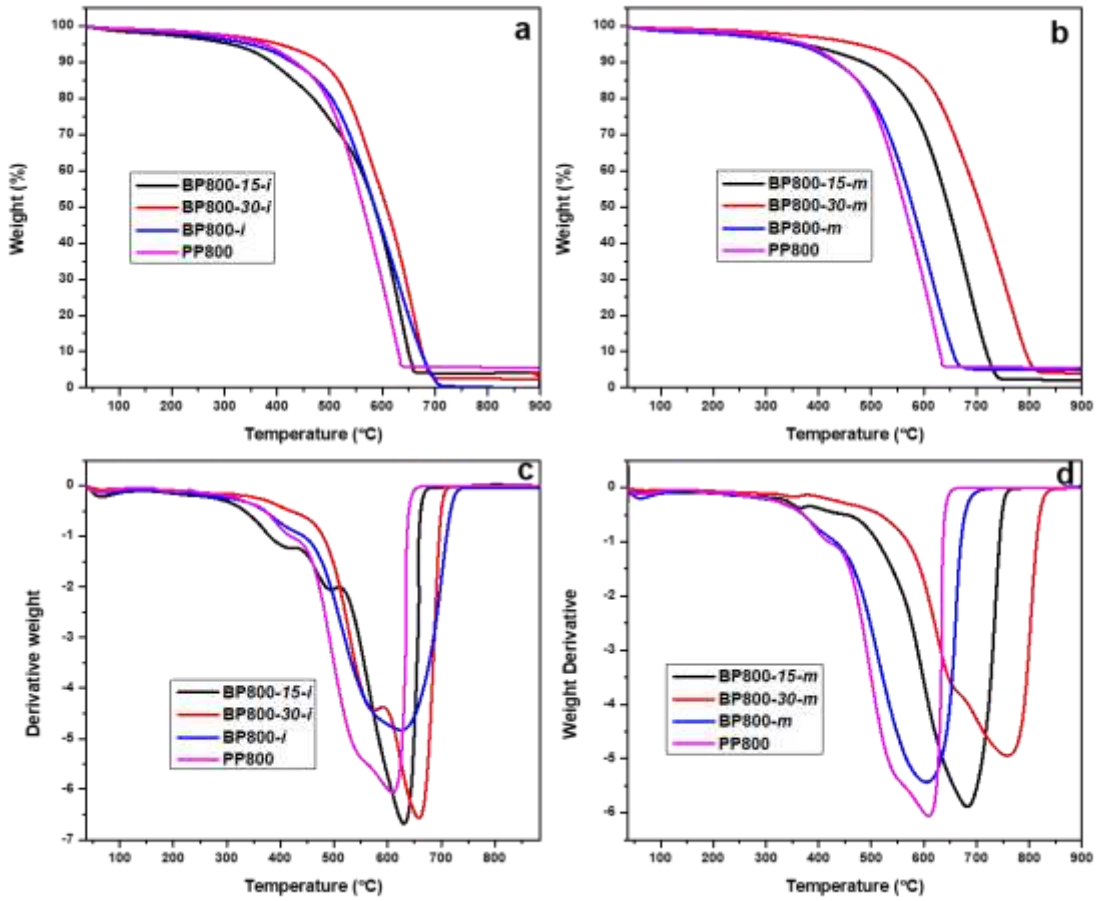


Figure 4.7: *a)* TGA analysis of as synthesized B-doped MWCNTs prepared from tri-isopropyl borate, *b)* TGA analysis of as synthesized B-doped trimethyl borate derived B-doped samples, *c)* derivative curve of as synthesized B-doped MWCNTs prepared from tri-isopropyl borate, *d)* derivative of as synthesized B-doped trimethyl borate derived B-doped samples

The as-synthesized samples were treated with HNO_3 to remove the catalyst residue and TGA analysis performed on the purified samples. A mass loss was attributed to the removal of moisture at < 100℃, and for the oxidation of amorphous carbon at 400℃ for all MWCNT samples (**Figure 4.7**).[41, 90-96] All the produced samples from both boron sources presented with better thermal stability than the pristine MWCNTs. The observed difference in thermal stability relative to pristine MWNCTs was smaller for MWCNTs prepared from tri-isopropyl borate, compared to those prepared from trimethyl borate (with the exception of sample BP800-*m*). Relative to the MWCNTs produced using trimethyl borate, the reaction time did not have a significant influence on the thermal stability of MWCNTs prepared from tri-isopropyl borate. On average, for both sets of samples a reaction time of 30 min produced the most thermally stable MWCNTs. The presence of MWCNTs with pronounced differences in morphology in one sample were only observed for BP800-15-*i*, BP800-30-*i*, and BP800-30-*m* samples as evidenced by the asymmetry in their derivative curves. Sample BP800-*i* presented with a broad thermal decomposition distribution that overlapped with BP800-15-*i* and BP800-30-*i* samples, which suggested a wide distribution in morphological properties (i.e., diameter, length, chirality) that encompassed both samples.

The concentration of sp^3 and sp^2 hybridized carbon relative to each other, estimated using the A_D/A_G ratio, can be used to evaluate the thermal properties of carbon materials. The density of defects (A_D/A_G) in carbon materials tends to be directly correlated to thermal stability, but the reported data had poor correlation between the two variables. Compared to all the other samples, BP800-*m* was the only one that reported thermal stability consistent with its A_D/A_G ratio relative to samples BP800-*15-m* and BP800-*30-m*. However, BP800-*15-m* reported a thermal stability lower than BP800-*30-m* despite having reported a lower density of defects (i.e., lower A_D/A_G), better long-range order and overall crystallinity. This was also observed for samples BP800-*15-i* and BP800-*30-i*. Graphitic indices tend to offer corroborating data to trends in thermal stability. However, a combination of two other factors, nanotube length and diameter, are also large contributors to thermal properties and consequently the poor correlation in thermal stability and crystallinity observed. Large diameter nanotubes have been reported to have high thermal stability relative to their counterparts, while nanotubes with small lengths (can be influenced by reaction time) reported low thermal stability.[94-100]

Table 4.3: Brunauer-Emmet-Teller surface area data

Sample	Surface area (m^2/g)	Pore volume (cm^3/g)	Pore size (nm)
BP800-*15*-*i*	27.6	0.117	25.7
BP800-*30*-*i*	36.1	0.227	25.1
BP800-*i*	23.9	0.154	28.4
BP800-*15*-*m*	37.4	0.224	23.9
BP800-*30*-*m*	40.2	0.224	22.2
BP800-*m*	71.7	0.351	23.5
PP800	15.0	0.111	29.3

Surface area studies were performed on the purified samples (Table 4.3), and all samples had small surface areas, but were larger than that of the pristine sample. The use of tri-isopropyl borate gave samples with surface area that increased with reaction time. Surface area of the MWCNTs synthesized using trimethyl borate was found to be directly proportional to reaction time, and a significant increase was observed between reaction times of 30 and 60 min. Additionally, the use of trimethyl borate produced MWCNTs with larger surface area than those produced from tri-isopropyl borate across all reaction times. In addition, the use of either boron source in the synthesis of MWCNTs led to a decrease in pore size and an increase in pore volume relative to the pristine sample.

XPS analysis (Table 4.4, **Appendix 4A, Figure 4.30**) of both sets of samples revealed that trimethyl borate produced MWCNTs with boron in the MWCNT structure. At a reaction time of 15 min and 60 min, trimethyl borate produced B-doped MWCNTs with an atomic % of 0.31% and 0.99%, respectively. However, no boron was detected for the sample produced at a reaction time of 30 min. Tri-isopropyl borate gave MWCNTs with no boron addition. It was also observed that compared to trimethyl borate derived samples, tri-isopropyl borate derived samples led to the addition of nitrogen to the lattice structure during the purification process. A decrease in the atom % of carbon was observed with an increase in reaction time, while the atomic % of oxygen was found to be directly correlated to the reaction time for both sets of

samples. This indicates that the addition of oxygen to MWCNTs becomes easier over longer reaction times.

Table 4.4a: XPS atomic % of heteroatom doped MWCNTs

Sample		C 1s	O 1s	N 1s	B 1s
BP800-15-*m*	Position (eV)	285.6	532.7	--	191.6
	Atomic %	89.07	10.63	--	0.31
BP800-30-*m*	Position (eV)	284.7	532.8	--	--
	Atomic %	87.07	12.93	--	--
BP800-*m*	Position (eV)	285.7	533.5	--	193.7
	Atomic %	84.30	15.70	--	0.99
BP800-30-*i*	Position (eV)	285.7	532.8	406.7	--
	Atomic %	89.18	10.11	0.71	--
BP800-*i*	Position (eV)	285.74	532.75	399.71	--
	Atomic %	85.50	14.34	0.16	--

See XPS spectra in **Appendix 4A, Figure 4.30 and 4.31**

The individual components of the B 1s and O 1s signals were isolated to identify the bonding configuration of each atom in the structure of the material (**Figure 4.8**). Sample BP800-15-*m* reported BCO_2 (190.8 eV) and B-O (192.2 eV) bonding configurations, while BP800-*m* reported only the B-O (192.6 eV) configuration. The B-O bonding configuration was also detected in the O 1s signal at 533.2 eV and 533.5 eV for the BP800-15-*m* and BP800-*m*, respectively. However, for BP800-15-*m* the BCO_2 could not be detected in the C 1s peak (expected at 282 eV). This could be due to the inability to resolve it from the background noise in the scan. This study also revealed that the reaction time determined the type of boron bonding configurations present in MWCNTs. Both samples showed the presence of B_2O_3 at 193.7 eV for BP800-15-*m* and 193.8 eV for BP800-*m*. This is consistent with what was reported in the XRD data (**Figure 4.2b**), which indicated that treatment with HNO_3 did not lead to the complete removal of the B_2O_3, but its phases were decreased to below the detection limit of XRD. Additionally, for both samples boron predominantly existed as B_2O_3.

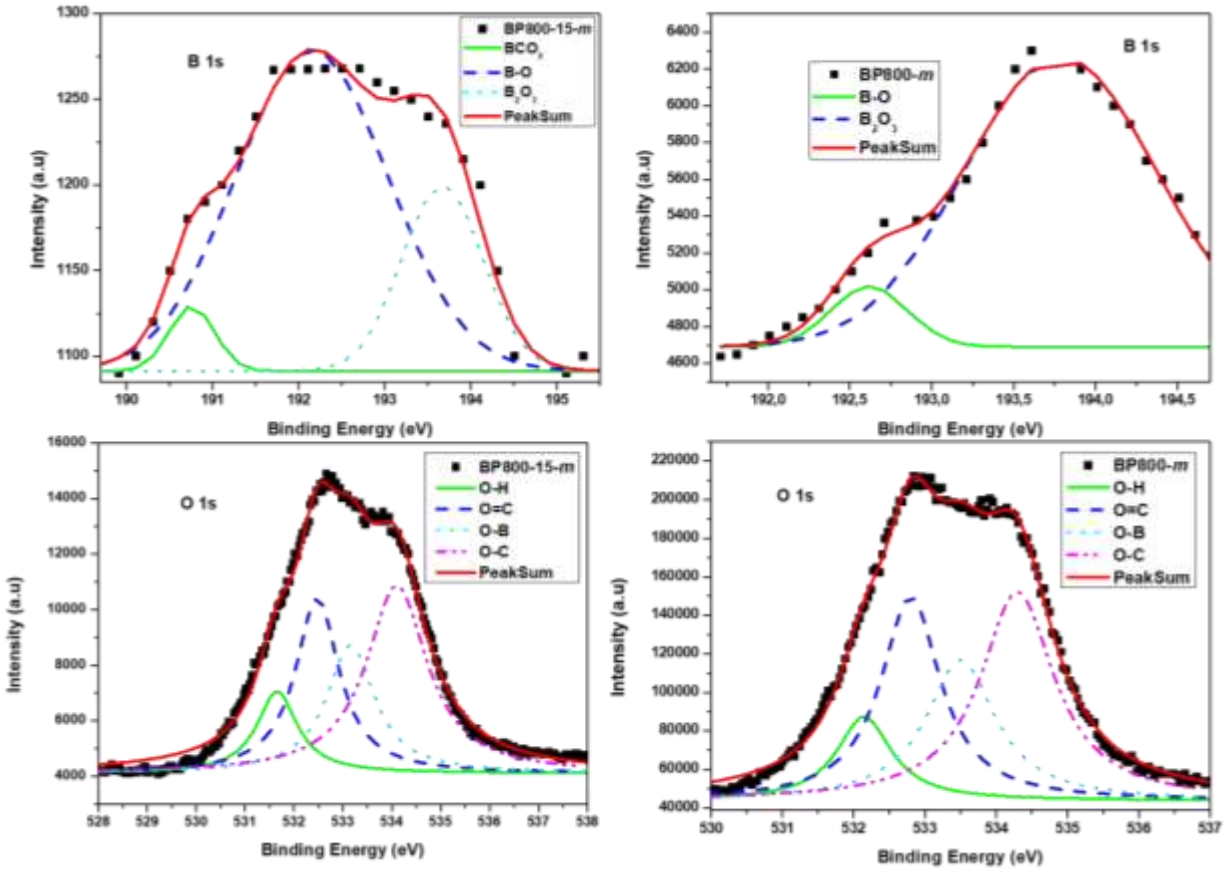


Figure 4.8: XPS fitted peaks for the B 1s and O 1s peaks of samples BP800-15-*m* and BP800-*m*.

The concentration (%) of the boron bonding configurations samples BP800-15-*m* and BP800-*m* were calculated (Table 4.4b). Sample BP800-*m* reported the highest concentration of B_2O_3 (92.37%) compared to BP800-15-*m*. This suggested that longer reaction time led to the formation of higher concentrations of B_2O_3. The B-O bonding configuration reported the highest concentration at a reaction time of 15 min (73.16%) and saw a massive decline at 60 min (7.63%). Thus, indicating that the B-O configuration is highly stable if it is not exposed to high temperatures for a prolonged time. Sample BP800-15-*m* had a low concentration of the BCO_2 (4.32%).

Table 4.4b: XPS % of boron bonding configurations

Sample	Bonding Configuration (%)		
	BCO_2	B-O	B_2O_3
BP800-15-*m*	4.32	73.16	22.52
BP800-*m*	--	7.63	92.37

A mechanism to explain the XPS data can be proposed. (i) Initially, B_2O_3 is formed at all 3 reaction times, but less is formed at lower concentrations for reaction times of 15 and 30 min. (ii) At 15 min the B-C (in a form of BCO_2) and B-O configurations are also formed from the trimethyl borate but increasing the reaction times to 30 and 60 min led to a loss of both the B-C and B-O configurations. However, this does not address why B_2O_3 is not detected in sample BP800-30-*m*. (iii) At 60 min, enough B_2O_3 is formed that it coated the surface of the formed nanotubes, and not only corrodes the surface of the nanotubes but it acted as a boron source, leading to the formation of the B-O bonding configuration. This was corroborated by the failure of tri-isopropyl borate to produce B-doped MWCNTs at a reaction time of 60 min. No B_2O_3 is formed during the reaction (consistent with XRD, see **Figure 4.1a**), thus no indirect boron source is available for the reaction.

XPS analysis has highlighted the shortcomings of using indirect methods of analysis such as XRD, Raman, and TGA in confirming or corroborating the addition of boron to the lattice structure. The indirect determinations about the success or failure of the incorporation of boron by XRD, Raman and TGA were found to be inconsistent with XPS analysis. In XRD analysis, a downward shift in the 002-peak and an increase in the d-spacing relative to pristine MWCNTs, which were attributed to the successful addition of boron to the lattice structure, was reported for samples BP800-*i*, BP800-15-*m*, BP800-30-*m*, and BP800-*m*. This was corroborated by XPS analysis for BP800-15-*m* and BP800-*m*, however, no boron was reported for samples BP800-*i* and BP800-30-*m*. This indicated that a downward shift in the 002-peak and larger d-spacing could not only be attributed to successful boron addition, but also the presence of oxygen in the lattice structure. However, despite containing oxygen the 002-peak shift and the d-spacing of sample BP800-30-*i* were found to be comparable to that of the pristine sample, suggesting that it may not simply be about the presence of the oxygen groups

but how they were added. Hence, it could be speculated that boron was added successfully during the reaction for samples BP800-30-*m* and BP800-*i* but it was lost before the reaction was completed, and thus potentially making it more susceptible to addition of oxygen during the purification process.

Raman analysis indicated that the I_D/I_G ratio of samples (BP800-15-*m*, BP800-30-*m* and BP800-*m*) derived from trimethyl borate increased with reaction time. This was initially attributed to the increased amounts of boron in the lattice structure with reaction time. However, XPS analysis revealed that the trend in density of defects was largely due to atomic % of oxygen that increased with reaction time. Additionally, it also showed that the incorporation of boron into the lattice structure, particularly for BP800-15-*m* and BP800-*m*, had minimal contribution to the concentration of defects in the material. However, they appeared to be significant in the thermal stability of the material. Sample BP800-30-*m* reported the highest thermal stability, and it did not report any boron in the lattice structure. On the other hand, sample BP800-15-*m* recorded the 2nd highest thermal stability followed by sample BP800-*m*, which was consistent with an increase in boron concentration (in particular B_2O_3) in each sample. Sample BP800-30-*i* reported larger density of defects (I_D/I_G) than BP800-*i*, this was despite the latter reporting a higher concentration of oxygen from the XPS analysis, and more amorphous carbon from TGA. Both samples had nitrogen incorporated in their lattice structure, with BP800-30-*i* having the higher concentration of nitrogen. In addition, the C 1s peak (**Appendix 4A, Figure 4.31**) of BP800-30-*i* was much wider than that of BP800-*i*, which suggested that more carbon bonding configurations existed within the structure. Thus, a combination of larger concentration of nitrogen and C 1s bonding configuration gave higher density of defects for BP800-15-*i* than for BP800-*i*.

4.3.1.1. Comparative analysis and summary.

The reaction time and boron source are significant factors in determining the type and quality of B-doped MWCNTs obtained.

i) In both studies the carbon yield (%) was found to be inversely correlated to the reaction time. The highest % yield was reported at a reaction time of 15 min for both sets of samples, while a reaction time of 30 min reported similar % yields. At a reaction time of 60 min, the use of tri-isopropyl borate produced the lowest % yield relative to the use of trimethyl borate. TEM analysis of the samples revealed the influence of boron sources and reaction time in the synthesis of MWCNTs. Higher reaction time of 60 min produced MWCNTs with the lowest average diameter despite the boron source used, with trimethyl borate leading to the production of MWCNTs with smaller average diameter and narrower diameter distribution. Additionally, except at a reaction time of 30 min, it also gave MWCNTs with smaller average diameters compared to when tri-isopropyl borate was used.

ii) XPS analysis revealed that trimethyl borate was successful in producing B-doped MWCNTs at different reaction times than tri-isopropyl borate. The use of trimethyl borate also revealed that changes in reaction time also determine boron bonding configuration. In addition, at higher reaction times, trimethyl borate may not serve as a direct boron source, but produces B_2O_3 during the reaction, which indirectly functions as a boron source.

iii) The XRD data revealed that the change in the reaction time yielded nanotubes with differences in morphologies and degrees of crystallinity. Samples derived from trimethyl borate all reported a downward shift of the 002 peaks, while the use of tri-isopropyl borate exhibited these characteristics for the sample produced at a higher reaction time (BP800-*i*) only. In both cases, it was found that the observed shifts could be ascribed to the presence of both oxygen and boron. The graphitization degree (i.e., arrangement of graphitic layers relative to each other) was generally much larger (> 80%) for tri-isopropyl borate derived samples at 15 and 30-min reaction times compared to trimethyl borate derived samples.

iv) Raman analysis of both sets of samples revealed that the use of both boron sources yielded materials that became increasingly disordered in their lattice structure at

higher reaction times. For reaction times 15- and 30-min, samples prepared from trimethyl borate presented with lower density of defects than those derived from tri-isopropyl borate. This was attributed to the presence of nitrogen and oxygen in the tri-isopropyl borate derived samples, which was absent in the trimethyl borate samples. A drop in the density of defects was observed at a reaction time of 60-min when tri-isopropyl borate was used, and this was ascribed to the higher concentration of nitrogen relative to the sample prepared at 30 min. An upward trend in density of defects was observed for the corresponding trimethyl borate sample, and this was correlated to an increase in oxygen concentration with reaction time. At a reaction time of 60 min, trimethyl borate produced a sample with more density of defects than when tri-isopropyl borate was used. This was attributed to the presence of boron, particularly B_2O_3, in the sample prepared from trimethyl borate. Changes in crystallinity with reaction time were pronounced when trimethyl borate was used as a boron source than tri-isopropyl borate.

v) The thermal stability of the purified MWCNTs derived from both boron sources revealed that in both cases, all the samples were more thermally stable than, and in some cases, comparable to the pristine sample. All the samples derived from trimethyl borate, except for the one prepared at a reation time of 60-min had better thermal stability than those derived from tri-isopropyl borate. This was ascribed to tri-isopropyl borate samples having nitrogen in their lattice structure. However, at a reaction time of 60 min, the tri-isopropyl derived sample reported better thermal stability because the trimethyl borate sample had relatively high concentration of B_2O_3, which could be corroding the surface of the sample. In both sets of samples, the most thermally stable MWCNTs was obtained at a reaction time of 30 min. Furthermore, the derivative curves of the most thermally stable samples for both sets revealed the presence of 2 types of carbon nanotubes with different thermal stabilities, suggesting the presence of two distinct morphologies within each sample.

vi) Surface area studies indicated that samples derived from tri-isopropyl borate had smaller surface area than those produced from tri-methyl borate, this difference became increasingly larger with an increase in reaction time. However, both set of samples presented with higher surface area than the pristine sample. The surface area was directly related to the reaction time but dropped at a reaction time of 60-

min for tri-isopropyl borate derived samples. All the tri-methyl borate derived samples had higher pore volume but slightly smaller pore sizes than the tri-isopropyl derived samples obtained at all reaction times, only samples prepared at a reaction time of 30-min presented with similar pore volumes.

4.3.2. Synthesis of boron doped MWCNTs (B-doped MWCNTs); temperature and boron source dependant study.

Samples produced at a reaction time of 60 min had a lower thermal stability and crystallinity. This suggested a higher concentration of defects in their structure. Hence, this section focused on whether a variation in reaction temperature at that reaction time would affect these properties (and possibly the concentration of boron), and how the prepared material would compare with their pristine counterparts (prepared in **chapter 3, section 3.3.2**). The influence of temperature (700, 750, 800℃) in the synthesis of B-doped MWCNTs using the CVD method with tri-isopropyl borate and trimethyl borate as boron sources over a Fe-Co/$CaCO_3$ was thus investigated. The carbon yield (%) (Table 4.5) samples prepared using tri-isopropyl borate (BP700-*i*, BP750-*i*, BP800-*i*) and trimethyl borate (BP700-*m*, BP750-*m*, BP800-*m*) reported an inverse correlation with the reaction temperature.

Table 4.5: Carbon yield (%) of B-doped MWCNTs.

Sample	Total Mass of purified samples (g)	Carbon yield (%)
BP700-*i*	2.4757	42.0
BP750-*i*	2.3470	39.8
BP800-*i*	1.5850	26.8
BP700-*m*	1.1304	19.2
BP750-*m*	2.9119	49.4
BP800-*m*	0.8530	14.5
*PP700	1.585	26.8
*PP750	0.935	15.8

*PP800	0.475	8.0

*See **chapter 3, section 3.3.2**

Temperatures of 700℃ (BP700-*i*) and 750℃ (BP750-*m*) produced the highest yields when tri-isopropyl borate and trimethyl borate were used, respectively. While the use of trimethyl borate at 750℃ (BP750-*m*) produced the highest carbon yield between both sets of samples. The use of either boron source across all temperatures, except for sample BP700-*m*, reported carbon yields higher than the corresponding pristine MWCNTs samples.

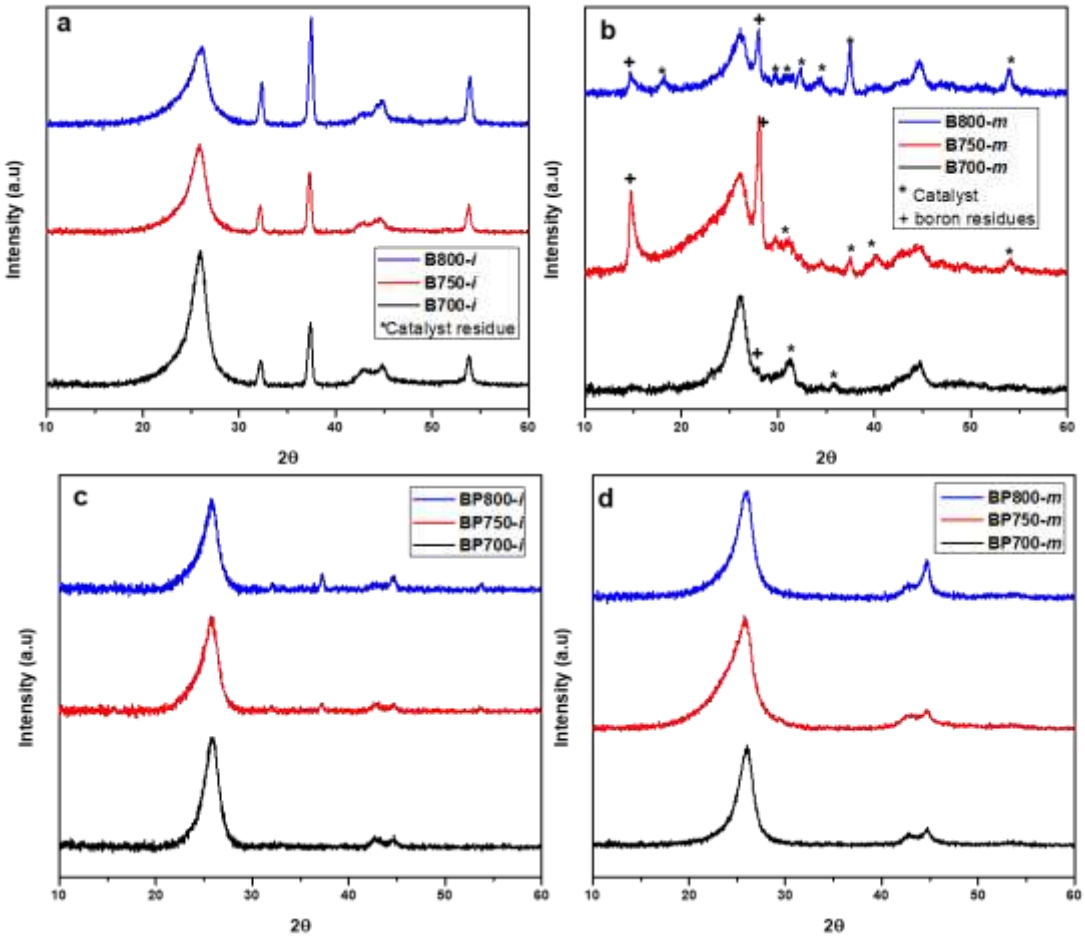


Figure 4.9: XRD analysis of *a)* as-synthesized tri-isopropyl borate derived B-doped MWCNTs, *b)* as-synthesized trimethyl borate derived B-doped MWCNTs *c)* purified tri-isopropyl borate derived B-doped MWCNTs, *d)* purified trimethyl borate derived B-doped MWCNTs.

The characteristic peaks arising from the 002 (26°), 100 (43°) and 101 (44-45°) planes, together with the peaks due to the catalyst residue were observed in the XRD data (**Figure**

4.9a-b) of the as-synthesized MWCNTs.[41, 63-66] All samples showed the presence of the catalyst residue. However, the XRD pattern of the as-synthesized samples prepared from trimethyl borate (**Figure 4.9b**) had the number of peaks arising from the catalyst residue and the boron source increase with an increase in temperature, with samples B750-*m* and B800-*m* showing the presence of boron oxide. XRD analysis (**Figure 4.9c-d**) corroborated the successful removal of the catalyst residue, and boron oxide in the case of trimethyl borate derived MWCNTs. However, despite multiple treatments of sample BP800-*i* with HNO_3, the catalyst residue was not totally removed.

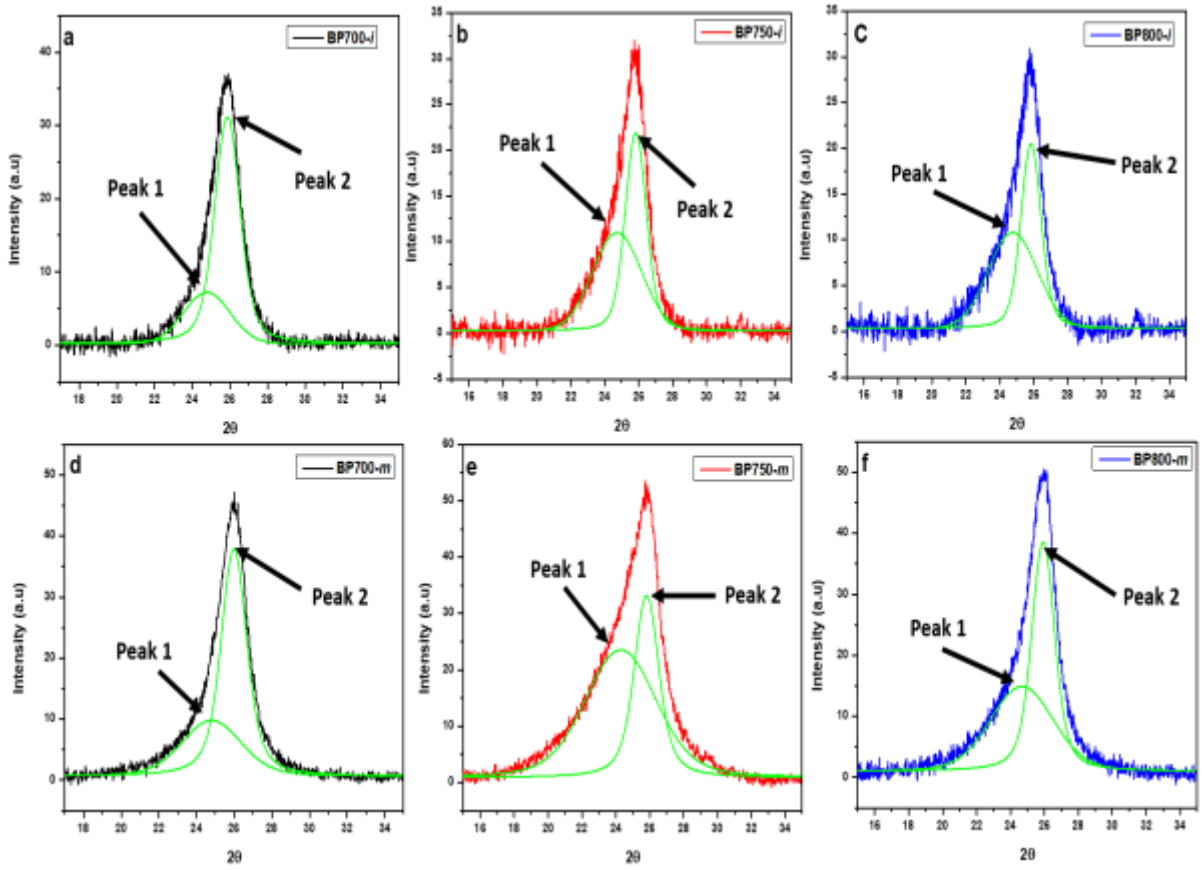


Figure 4.10: Deconvoluted 002 peaks of *a-c)* tri-isopropyl borate derived B-doped MWCNTs, and *d-f)* trimethyl borate derived B-doped MWCNTs using a Voigt function.

The d-spacing of the samples was determined from peak 2 of the deconvoluted 002 peaks (**Figure 4.10**), and the relatively large d-spacings for all samples were consistent with existing reports for MWCNTs with boron incorporated in their lattice structure.[41, 63, 65-66] The d-spacing of both sets of samples had a direct correlation with the reaction temperature compared to the pristine samples which reported an inverse correlation (**Figure 4.11**). Additionally, apart from sample BP700-*m*, all samples reported d-spacing larger than the pristine samples.

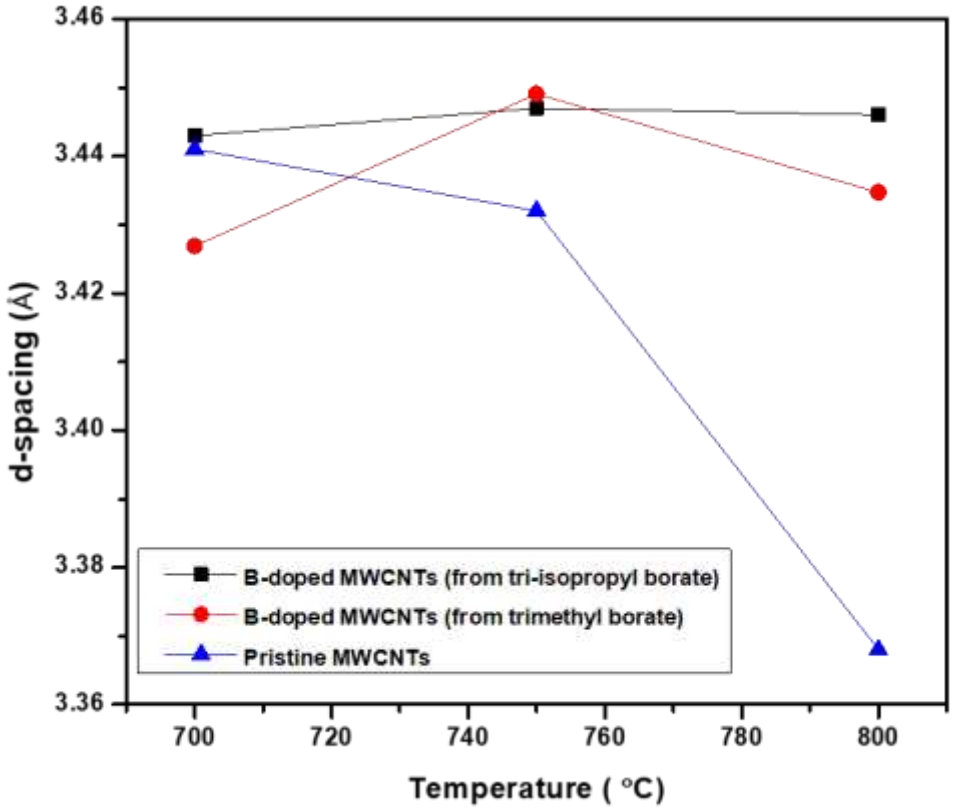


Figure 4.11: d-spacing comparison of B-doped and pristine MWNCTs.

Raman analysis of the purified B-doped samples showed the carbon *D* and *G* bands in the 1000-1800 cm^{-1} 1st order region (**Figure 4.12,** full data reported in **Appendix 4A** Table 4.15).[35, 39, 77-83] The ratio coefficient (I_D/I_G) for the tri-isopropyl borate derived samples was inversely correlated to temperature, with sample BP750-*i* reporting the lowest A_D/A_G. The intensity of the *D* and *D'* band followed the same trend. The trimethyl borate derived samples exhibited a direct correlation with the reaction temperature, with sample BP700-*m* reporting the lowest I_D/I_G. The intensity of *D* and *D'* bands were inversely and directly correlated to reaction temperature, respectively. Apart from the data of the 700℃ reaction temperature, samples prepared from trimethyl borate reported a higher density of defects than those prepared from tri-isopropyl borate.

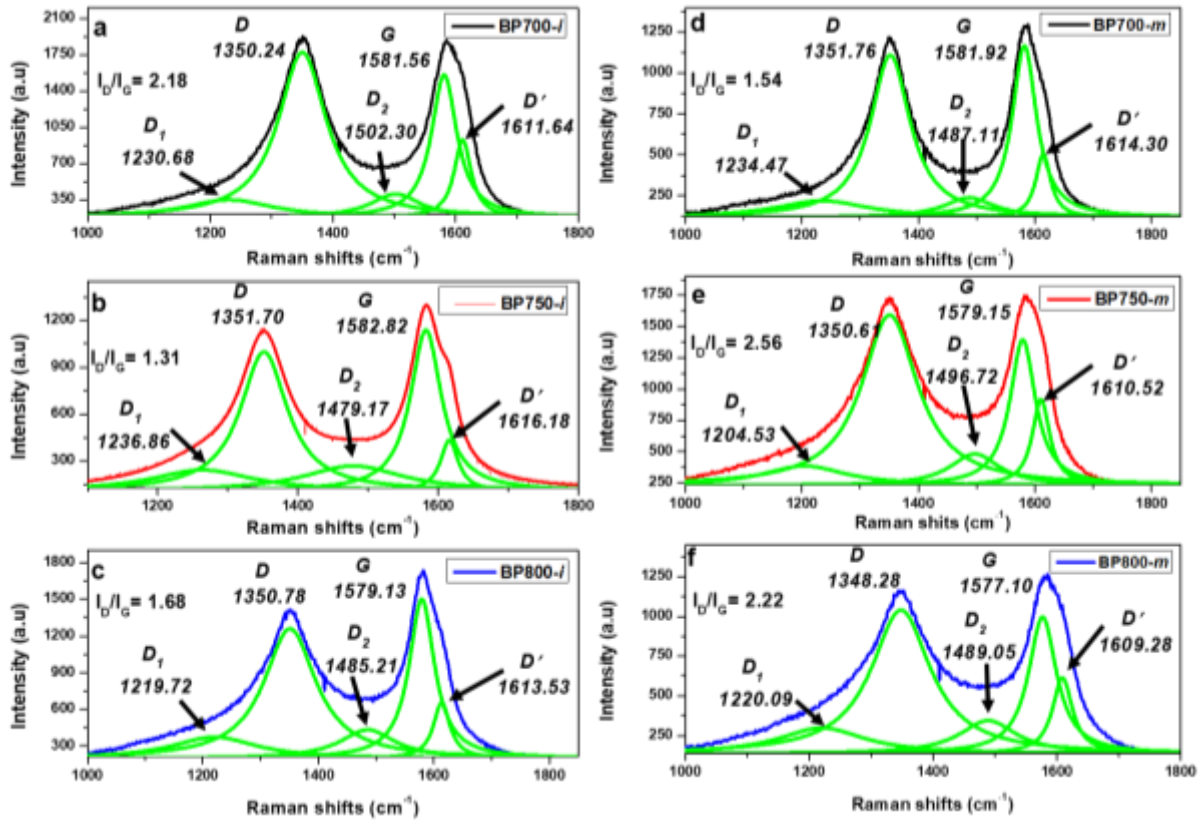


Figure 4.12: *a-c)* 1st order Raman Lorentzian fitted peaks for purified tri-isopropyl borate derived B-doped MWCNTs, *d-f)* 1st order Raman Lorentzian fitted peaks for purified trimethyl borate derived B-doped MWCNTs.

The crystallinity of the samples was investigated further by studying the intensity of *G'* band in the 2nd order region (**Figure 4.13**, full data reported in **Appendix 4A** Table 4.15) relative to the *D* and *G* band in the 1st order region.[83-86] The overall crystallinity ($I_{G'}/I_D$) of the materials was found to decrease with an increase in reaction temperature for the samples derived from trimethyl borate, i.e., BP700-*m* (0.52) > BP750-*m* (0.20) ≈ BP800-*m* (0.21). Samples prepared from tri-isopropyl borate had overall crystallinity increase with temperature i.e., BP750-*i* (0.57) > BP800-*i* (0.36) > BP700-*i* (0.28). Long range order ($I_{G'}/I_G$) for both sets of samples followed the same trend. Additionally, both trends for both sets of samples were consistent with the concentration of the density of defects deduced from the I_D/I_G ratio.[87-89]

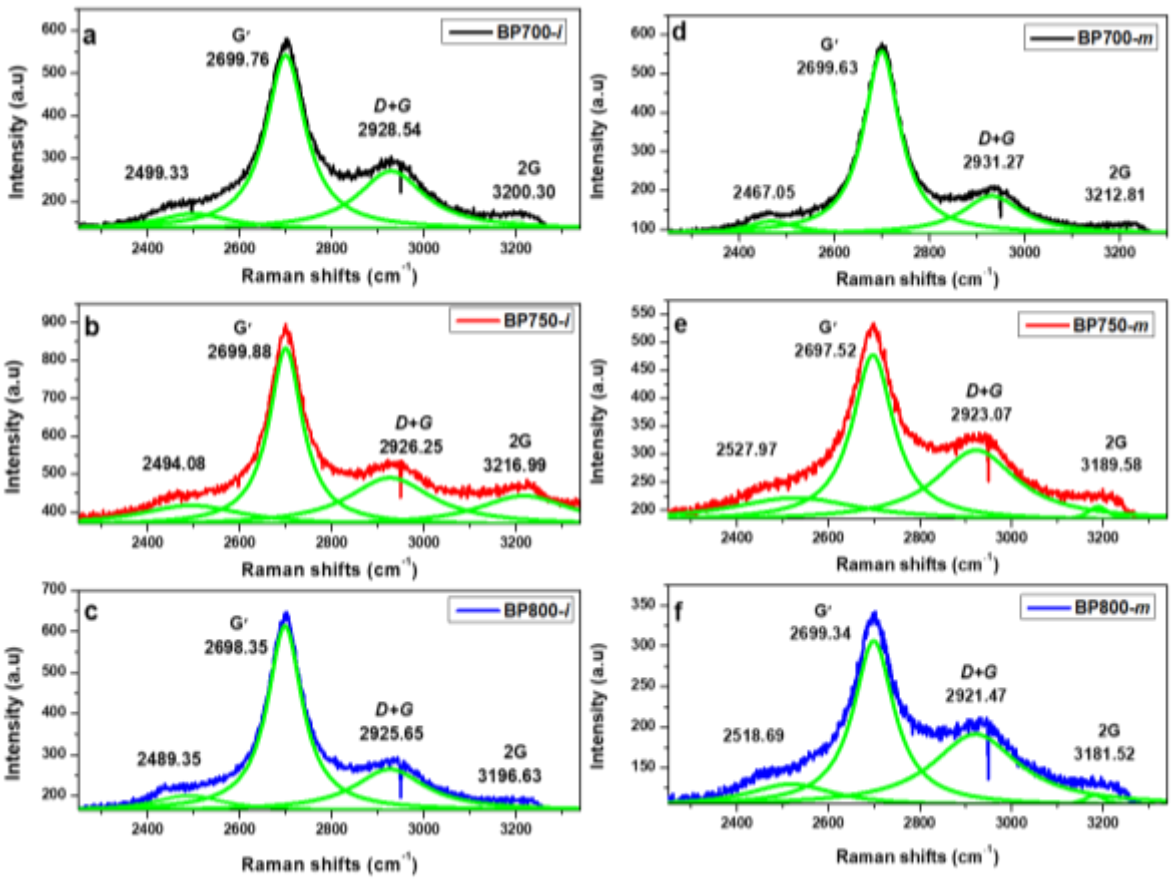


Figure 4.13: *a-c)* 2nd order Raman Lorentzian fitted peaks for purified tri-isopropyl borate derived B-doped MWCNTs, *d-f)* 2nd order Raman Lorentzian fitted peaks for purified trimethyl borate derived B-doped MWCNTs.

A comparison of I_D/I_G, $I_{G'}/I_G$ and $I_{G'}/I_D$ (**Figure 4.14**) ratios of each B-doped sample with the corresponding pristine MWCNTs (see Raman spectra in **Appendix 4A Figure 2.29**) samples was performed. All B-doped samples, except BP700-*i* had better crystallinity than the pristine counterparts.[41, 53, 64] The differences in crystallinity between the obtained samples and pristine MWCNTs became more prominent with an increase in temperatures.

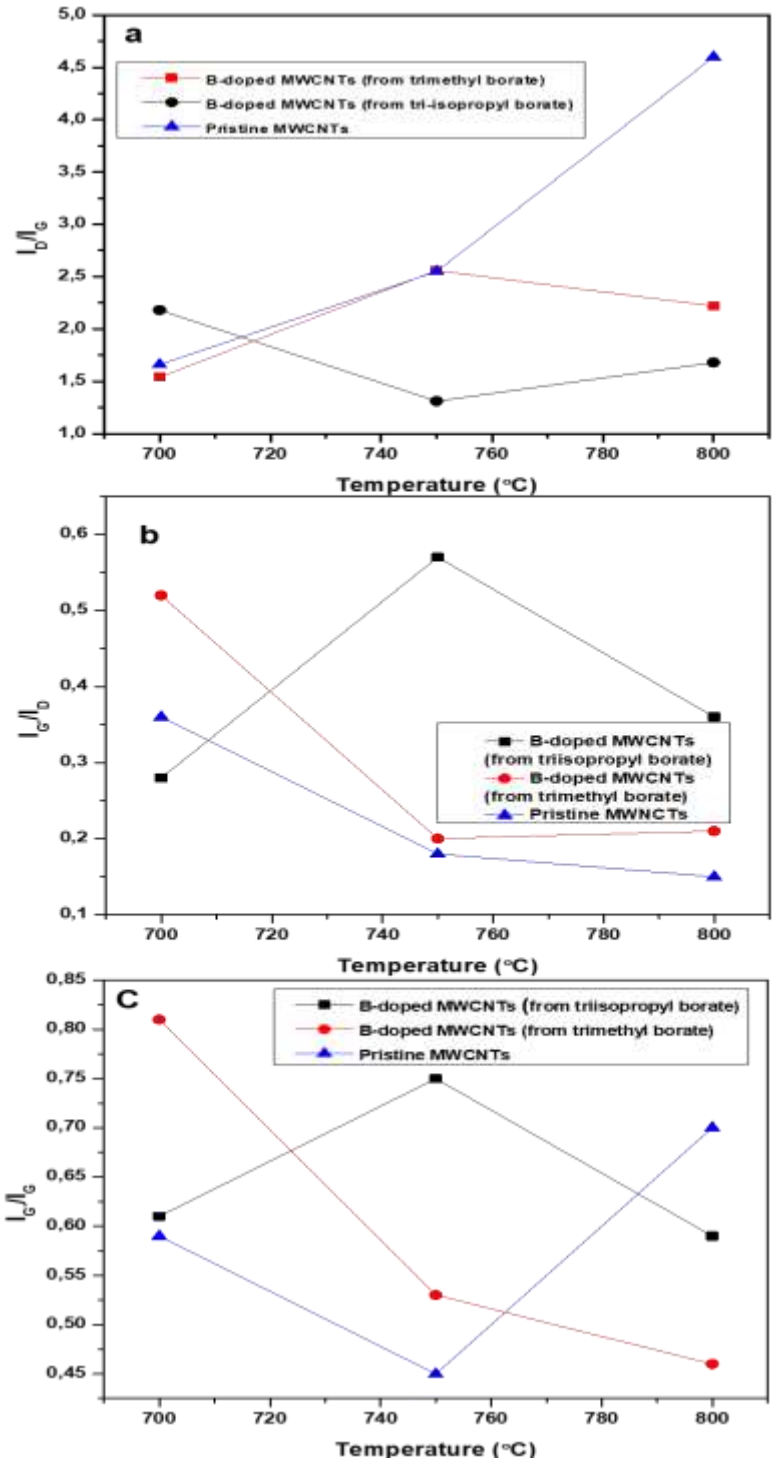


Figure 4.14: Comparative analysis of (*a*) the I_D/I_G ratio of B-doped and Pristine MWCNTs, (*b*) the $I_{G'}/I_D$ (overall crystallinity) of B-doped and Pristine MWCNTs, and *(c)* the $I_{G'}/I_G$ (long range-order) of B-doped and Pristine MWCNTs

The influence of reaction temperature on the thermal properties of the MWCNTs was investigated. The TGA of the as-synthesized samples (**Figure 4.15**) indicated that reaction temperatures of 700℃ (B700-*i*) and 750℃ (B750-*m*) produced the most thermally stable

material from tri-isopropyl borate and trimethyl borate, respectively. Samples prepared at 750℃ and 800℃ all showed two distinct morphologies with different decomposition temperatures. The oxidation of the amorphous carbon was observed at 400℃ for all samples prepared from tri-isopropyl borate, followed by a slight mass gain. In contrast, samples prepared from trimethyl borate reported an initial mass loss at 100℃, with sample B750-*m* reporting the largest mass loss. Additionally, the oxidation of amorphous carbon and subsequent mass gain at 400-500℃ was only observed for sample B750-*m*.[90-93]

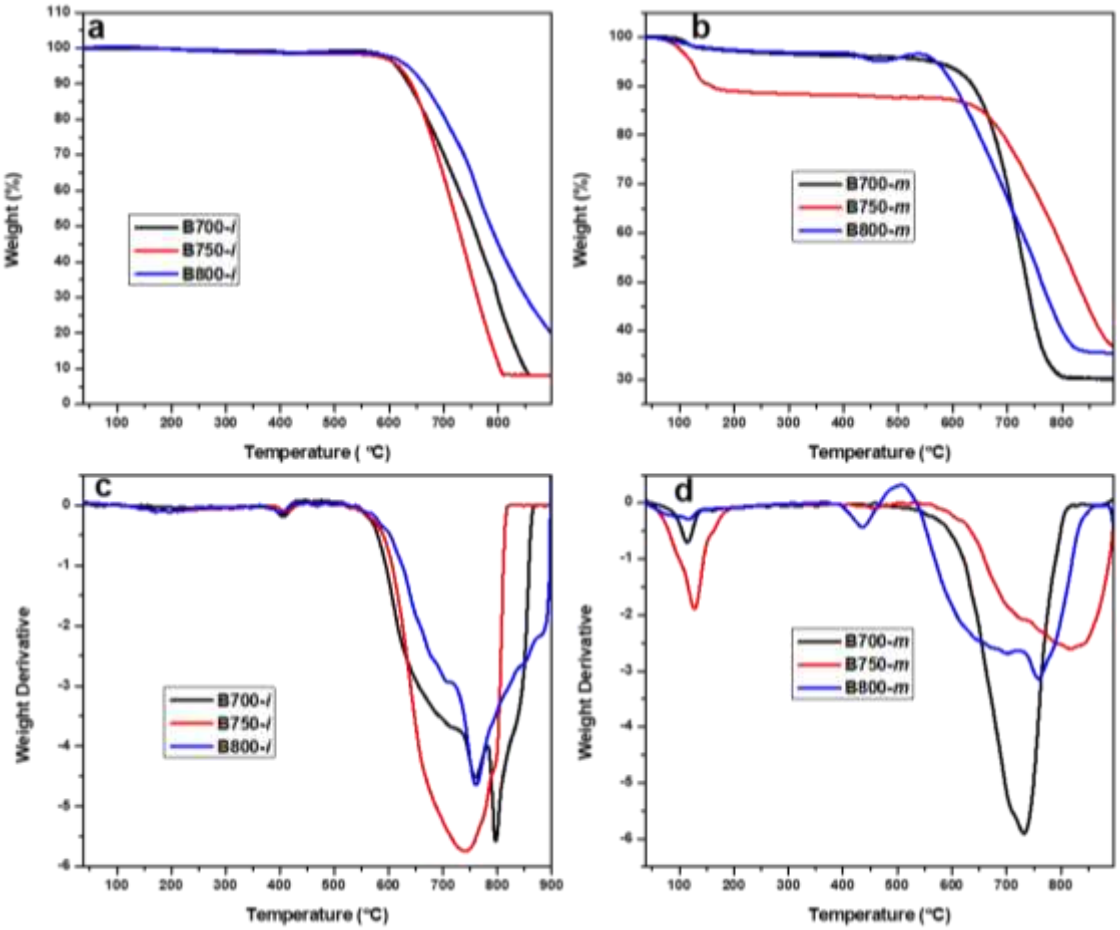


Figure 4.15: *a)* TGA analysis of as synthesized B-doped MWCNTs prepared from tri-isopropyl borate, *b)* TGA analysis of as synthesized B-doped trimethyl borate derived B-doped samples, *c)* derivative curve of as synthesized B-doped MWCNTs prepared from tri-isopropyl borate, *d)* derivative of as synthesized B-doped trimethyl borate derived B-doped samples

Treatment of the as-synthesized samples with HNO_3 gave purified samples with reduced thermal stability (**Figure 4.17**) and residual catalyst mass (< 5%). The thermal stability of both sets of samples was inversely proportional to the reaction temperature, with samples prepared

at 800℃ reporting the lowest thermal stability. The initial mass loss due to moisture was observed at 100℃ for all samples except BP700-*i*. This was followed by the decomposition of surface functional groups at 250℃, which was more prominent in sample BP750-*i*.[83] The oxidation of amorphous carbon at 400℃ was observed for samples prepared at 750℃ and 800℃ for both sets of samples.[90-93]

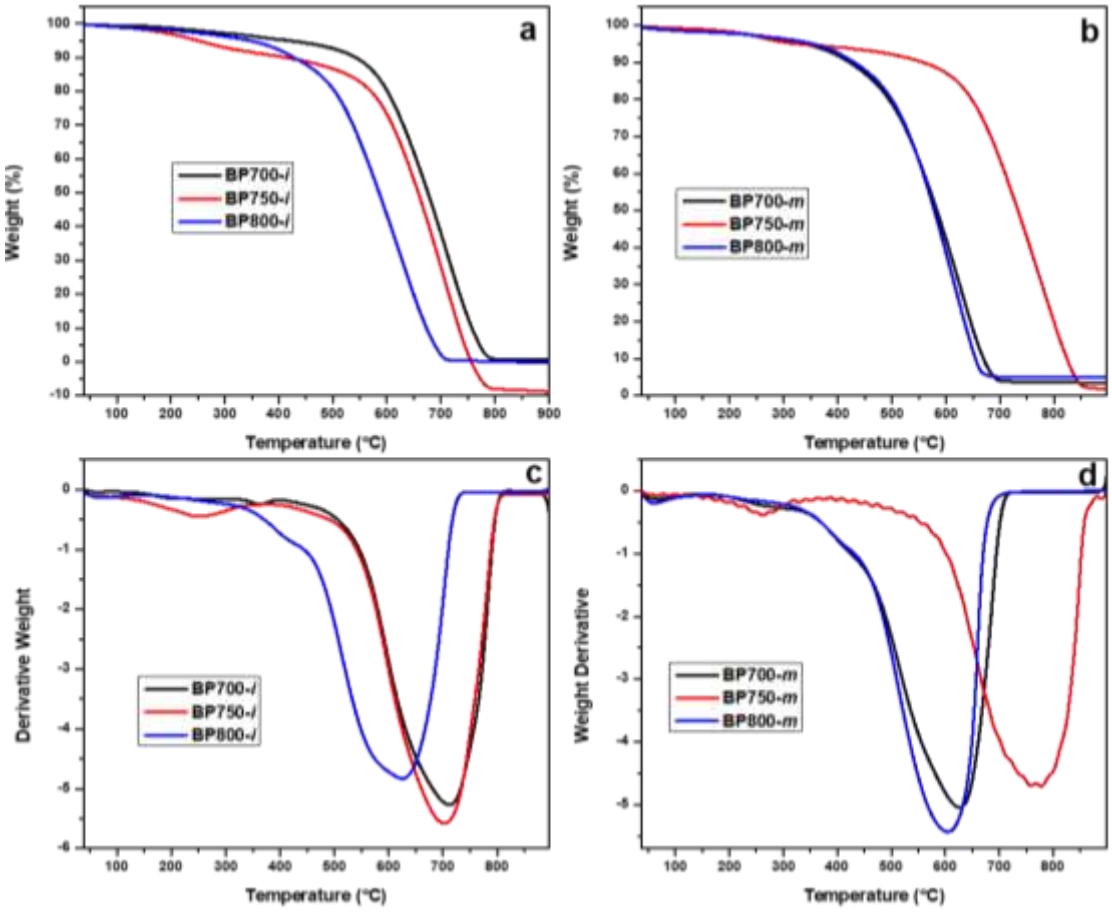


Figure 4.16: *a)* TGA analysis of as synthesized B-doped MWCNTs prepared from tri-isopropyl borate, *b)* TGA analysis of as synthesized B-doped trimethyl borate derived B-doped samples, *c)* derivative curve of as synthesized B-doped MWCNTs prepared from tri-isopropyl borate, *d)* derivative of as synthesized B-doped trimethyl borate derived B-doped samples

The thermal stability of the produced MWCNTs was compared to their corresponding pristine MWCNTs (**Figure 4.17**). Apart from sample BP700-*m*, all MWCNTs samples reported better thermal stability than their corresponding pristine MWCNTs. Relative to reaction temperatures

of 700℃ and 800℃, MWCNTs prepared at 750℃ for both sets had considerably better thermal stability than pristine MWCNTs obtained at the same temperature.

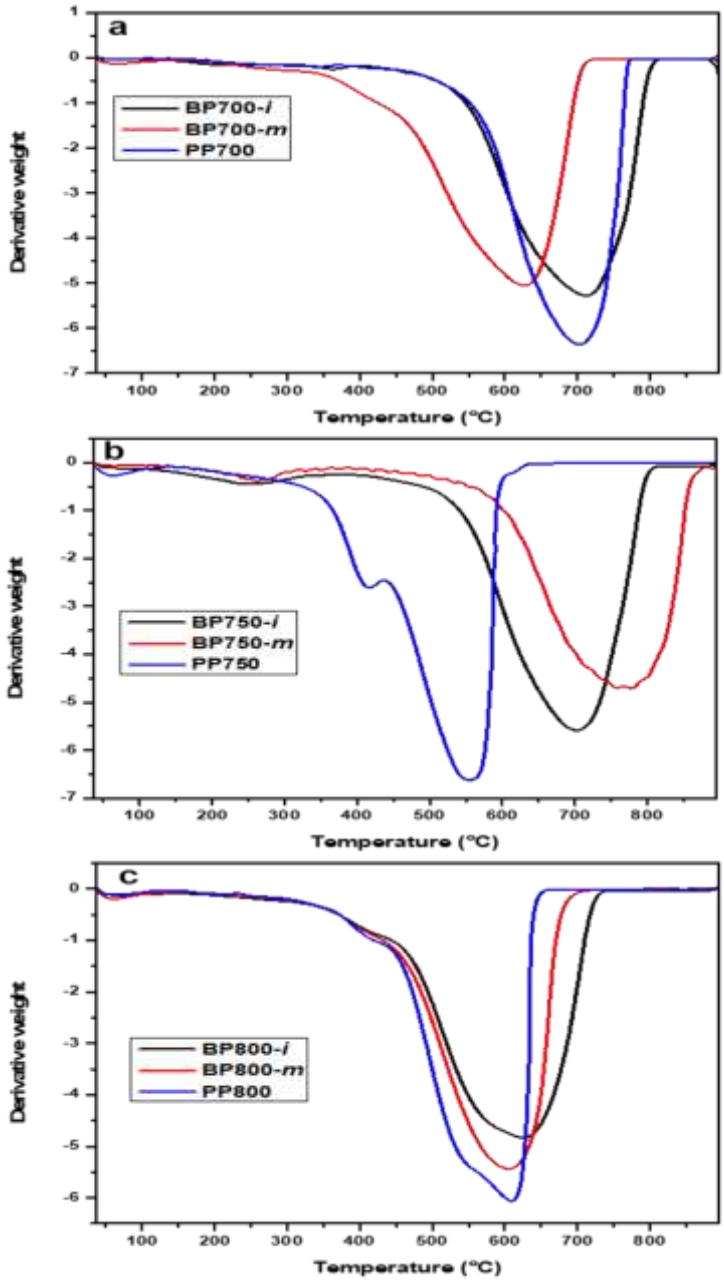


Figure 4.17: Comparison of TGA derivative curves of *a)* B-doped and pristine MWCNTs prepared at 700℃, *b)* B-doped and pristine MWCNTs prepared at 750℃, *c)* B-doped and pristine MWCNTs prepared at 800℃.

The BET data (Table 4.6) indicated that the surface area and pore volume decreased with reaction temperature for both sets of samples, but slightly increased at 800℃ (BP800-*i*) for samples prepared using tri-isopropyl borate. This correlation was also observed for pristine

MWCNTs. This indicated that the synthesis of high surface area pristine or doped MWCNTs requires lower reaction temperatures. All the samples had higher surface area and pore volume than their pristine counterparts. However, samples prepared at 700℃ and 800℃ reported surface area that was not considerably larger than that of the pristine samples. The pore sizes for both sets of samples and pristine MWCNTs were directly correlated to reaction temperatures.

Table 4.6: Brunauer-Emmet-Teller surface area data

Sample	Surface area (m^2/g)	Pore volume (cm^3/g)	Pore size (nm)
BP700-*i*	98.2	0.4122	16.79
BP750-*i*	63.3	0.2598	16.41
BP800-*i*	23.9	0.1539	28.38
BP700-*m*	108.7	0.4338	15.96
BP750-*m*	53.9	0.2478	18.39
BP800-*m*	71.7	0.3507	23.49
PP700	96.1	0.3674	15.29
PP750	35.9	0.1716	19.07
PP800	15.0	0.1106	29.32

XPS analysis (Table 4.7, **Appendix 4A, Figure 4.31**) of samples prepared at different temperatures with different sources indicated that trimethyl borate successfully produced B-doped MWCNTs at a higher temperature (800℃), compared to tri-isopropyl borate that was successful at lower temperatures of 700 ℃ and 750 ℃. Although, sample BP800-*m* reported higher atomic % of 0.99% compared to 0.39% in BP700-*i* and 0.29% in BP750-*i*, boron predominantly existed as B_2O_3. A general decrease in the atomic % of carbon was observed for both sets of samples, while a gradual increase was also observed in the concentration of oxygen.

Table 4.7a: XPS atomic % of heteroatom doped MWCNTs

Sample		C 1s	O 1s	N 1s	B 1s

BP700-*m*	Position (eV)	285.7	532.7	--	--
	Atomic %	85.44	14.56	--	--
BP750-*m*	Position (eV)	285.7	532.8	--	--
	Atomic %	84.14	15.86	--	--
BP800-*m*	Position (eV)	285.7	533.5	--	193.7
	Atomic %	83.31	15.70	--	0.99
BP700-*i*	Position (eV)	285.9	532.7	--	191.1
	Atomic %	86.97	12.65	--	0.39
BP750-*i*	Position (eV)	284.5	532.8	--	192.7
	Atomic %	84.14	12.80	--	0.29
BP800-*i*	Position (eV)	285.74	532.75	399.71	--
	Atomic %	85.50	14.34	0.16	--

See XPS spectra in **Appendix 4A, Figure 4.32 and 4.33**

The components of the B 1s and O 1s signals for all B-doped MWCNTs were isolated, and the bonding configurations identified (**Figure 4.18**). Excluding B_2O_3, BP800-*m* only reported the B-O (192.6 eV) bonding configuration. Sample BP700-*i* and BP750-*i* also reported the B-O bonding configuration at 192.7 eV and 192.4 eV, respectively. This was corroborated by the presence of the O-B bonding configuration in the O 1s peak of both samples at 533.4 eV (BP700-*i*) and 532.9 eV (BP750-*i*). Neither sample reported the presence of B_2O_3, but all revealed the presence of BC_2O and BCO_2 bonding configurations. The BC_2O and BCO_2 were observed at 191.0 eV and 191.9 eV for BP700-*i*, respectively, and at 190.9 eV (BC_2O) and 191.5 eV (BCO_2) for BP750-*i.* These bonding configurations could not be corroborated in the C 1s peaks of both samples, which was attributed to the inability to resolve them from the background noise.

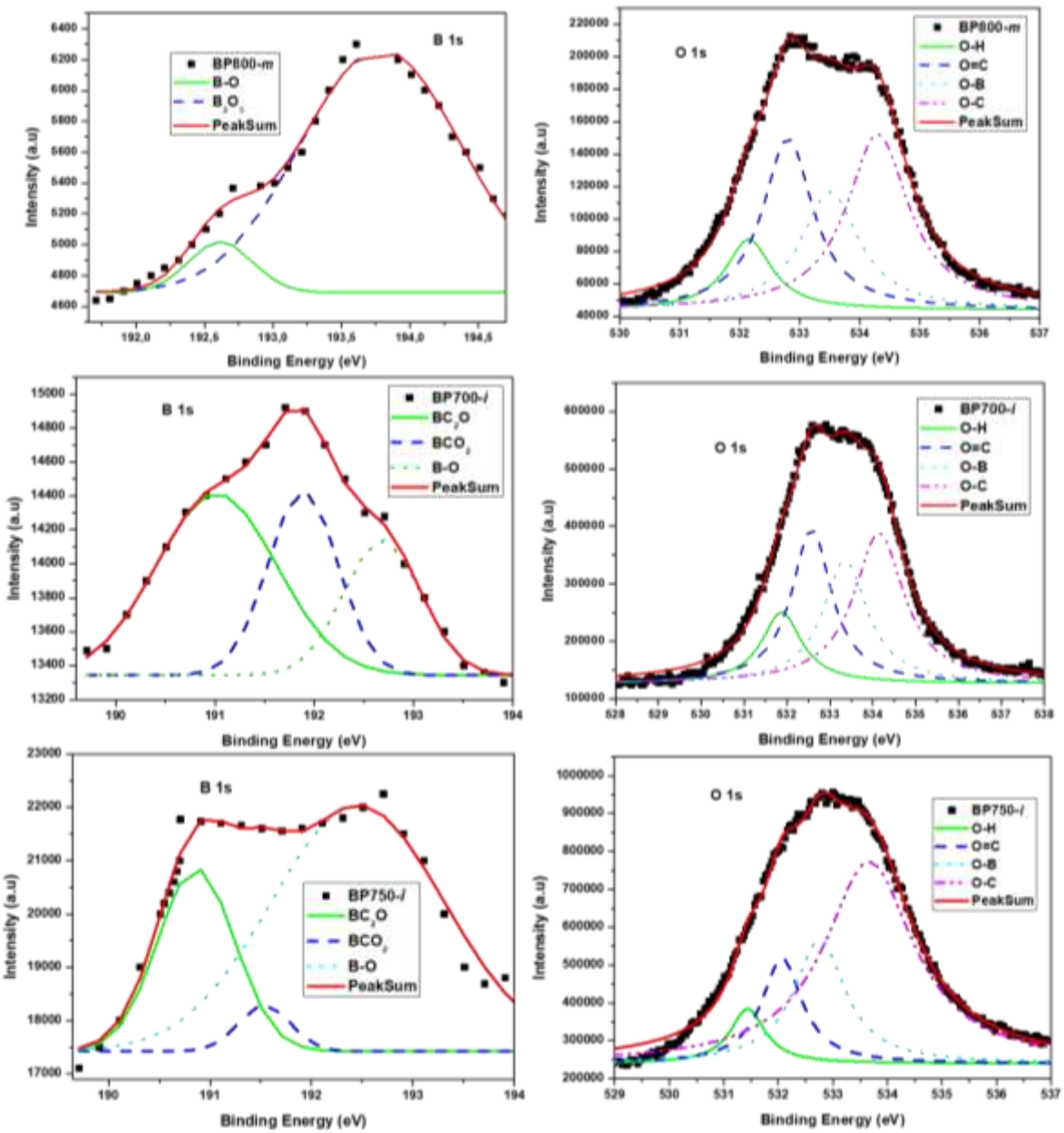


Figure 4.18: XPS fitted peaks for the B 1s and O 1s peaks for samples BP800-*m*, BP700-*i* and BP750-*i*.

The concentration of the boron doping configurations were calculated (Table 4.7b) and it was found that the BC_2O and BCO_2 decreased with an increase in temperature, and the B-O configuration increased with temperature. This suggested that the BC_2O and BCO_2 bonds were more stable and readily added at lower temperatures, while the opposite was observed for the B-O bond when tri-isopropyl borate was used. However, it was found that low concentration of the B-O bond was reported at higher temperatures when trimethyl borate was used.

Table 4.7b: XPS atomic % of boron bonding configurations.

Sample	Bonding Configuration (%)			
	BC_2O	BCO_2	B-O	B_2O_3
BP700-*i*	48.33	28.52	23.15	--
BP750-*i*	23.76	4.05	72.19	--
BP800-*m*	--	--	7.63	92.37

XRD analysis showed that the d-spacing of both sets of samples, except BP700-*m*, presented with d-spacing larger than their pristine MWCNTs counterparts. This was expected for samples that had boron successfully incorporated in their lattice structure (BP700-*i*, BP750-*i*, BP750-*m*, BP800-*m*). However, despite the absence of boron in their structure, sample BP800-*i* and BP750-*m* reported larger d-spacing than their pristine counterpart. There are two potential reasons for this; (i) the presence of oxygen in both samples, and the presence of nitrogen in the case of BP800-*i.* (ii) Boron was successfully added to the lattice structure but were lost as the reaction proceeded, thus creating defects by leaving atomic positions that would otherwise have atoms, empty. The latter could be a large contributor to both samples reporting more density of defects than samples containing boron in their lattice structure. Furthermore, should this mechanism be occurring, it suggests that in the synthesis of BP700-*m* no boron was incorporated in the lattice structure at any point in the reaction. Samples BP700-*i* was found to have a larger I_D/I_G ratio than BP750-*i*, which was attributed to the slightly higher concentration of boron and differences in the concentration of their boron bonding configurations. In addition, BP700-*i* was more thermally stable than BP750-*i*, this was ascribed to the larger concentration of the B-O bonding configuration in BP750-*i*. Thus, suggested that higher amount of B-O bonding reduces the thermal stability of the material.

4.3.2.1. Comparative analysis and summary.

The influence of temperature coupled with boron source on the synthesis of B-doped MWCNTs was investigated. Changes in temperature for both boron sources produced MWCNTs with different morphologies.

i) XPS analysis revealed that successful synthesis of B-doped MWCNTs using trimethyl borate required higher temperatures (800℃), while the use of tri-isopropyl borate required lower temperatures (700 ℃ and 750 ℃). In addition, the tri-isopropyl borate produced MWCNTs had more boron bonding configurations relative to trimethyl borate. Although trimethyl borate produced the highest boron concentration, it predominantly existed as B_2O_3 relative to tri-isopropyl borate that produced samples without B_2O_3.

ii) XRD analysis revealed that both boron sources at different reaction temperatures led to the production of MWCNTs presenting with large d-spacing, and that exhibited a downward shift in the Bragg reflections (except for sample BP700-*m*, prepared from trimethyl borate). MWCNTs produced from both boron sources exhibited an upward trend in d-spacing with an increase in temperature. The trend was attributed to successful addition of boron to the lattice structure for tri-isopropyl borate derived samples (excluding BP800-*i*), while it was ascribed to oxygen atoms and the reaction procedure for trimethyl borate derived samples. The crystallite size exhibited opposite trends with change in temperature; samples obtained from tri-isopropyl borate had an upward trend with increasing temperature, while samples derived from trimethyl borate exhibited a downward trend.

iii) Raman analysis highlighted the differences associated with the use of both different reaction temperatures and boron sources; the density of defects of samples obtained from the use of tri-isopropyl borate exhibited a direct correlation to the reaction temperature, while the use of trimethyl borate presented with the opposite trend. This correlation was consistent with the long-range order and overall crystallinity. Long-range order exhibited an inverse and direct correlation to reaction temperature for trimethyl and tri-isopropyl borate derived nanotubes, respectively. Overall crystallinity also reported the same trend with change in reaction temperature.

iv) The thermal analysis of each sample revealed that the use of tri-isopropyl borate and tri-methyl borate gave the most thermally stable samples at reaction temperatures of 700℃ and 750℃, respectively. This difference was due to different

factors, the former was ascribed to the addition of boron to the lattice structure, while the latter was attributed to the reaction process that led to the addition and subsequent removal of boron during the reaction. In addition, samples obtained at reaction temperatures of 700℃ and 800℃ using tri-isopropyl borate had the higher thermal stability than those produced from tri-methyl borate. The latter was due to the presence of B_2O_3 in the sample produced from trimethyl borate, while the former was ascribed to the successful addition of boron when tri-isopropyl borate was used as a boron source. The use of trimethyl borate at 750℃ produced a sample with better thermal stability than all the corresponding tri-isopropyl borate derived samples. All samples derived from both boron sources (apart from BP700-*m*) presented with better thermal stability than their corresponding pristine counterparts did.

v) Surface area studies indicated that reaction temperature was inversely proportional to the surface area and pore volumes of the produced nanotubes regardless of the boron source used. The use of tri-isopropyl saw a consistent decrease in surface area with temperature, while the use of tri-methyl borate gave the highest surface nanotubes area at 700℃, followed by 800℃ and 750℃, respectively. Both sets of samples presented with a surface area larger than the corresponding pristine sample derived under the same conditions.

4.3.3. Investigation of the effects of gas flow rate on the synthesis of B-doped MWCNTs.

4.3.3.1. Investigation of carrier and carbon source flow rates.

In this study, B-doped MWCNTs were produced using tri-isopropyl borate as a boron source, at the same total flow rate of 330 sccm, but at different flow rates of the carbon source and carrier gases. Three samples denoted BC800-*1* (110 sccm for C_2H_2 and 220 sccm for N_2), BC800-*2* (70 sccm for C_2H_2 and 260 sccm for N_2), BC800-*3* (50 sccm for C_2H_2 and 280 sccm for N_2) were produced. The data can be compared to the report by *Tetana et al.* which showed that the total flow rate of 330 sccm (i.e., carbon source gas flow rate of 90 sccm and carrier gas flow rate of 330 sccm) was the optimal condition. The impact of the simultaneous increase and decrease of the carrier and carbon source gases on the % yield (Table 4.8), respectively, was minimal. However, it led to the general increase of the carbon yield (%).

Table 4.8: Carbon yield (%) of B-doped MWCNTs derived from tri-isopropyl borate at different carbon source and carrier gas flow rates.

Sample	Flow rates of carbon source and carrier gas (sccm)	Total Mass (g)	Carbon yield (%)
BC800-*1*	C_2H_2 = 110 N_2 = 220	1.555	21.6
*BP800-*i*	C_2H_2 = 90 N_2 = 240	1.585	26.8
BC800-*2*	C_2H_2 = 70 N_2 = 260	1.006	21.9
BC800-*3*	C_2H_2 = 50 N_2 = 280	1.209	36.9

*Discussed in **section 4.3.1 and 4.3.2**

Given that the total flow rate of the system is constant, the amount (i.e., volume) of gas, in particular carbon source gas, becomes the significant factor in the % yield of the reaction. Lower volumes (i.e., low flow rates) of carbon source supplied to the reaction chamber gave higher yields than larger volumes (i.e., high flow rates) at the same total flow rate. Additionally, lower volumes of the carrier gas gave lower % yields compared to higher volumes. This could be attributed to two factors: (i) dilution of the carbon source gas (less molecules available per

total volume) (ii) rate of saturation on catalyst active sites. The latter is dependent on the former. An increase and decrease in carrier gas and carbon source gas flow rates (i.e., volume), respectively, led to an increase in dilution of the carbon source.

XRD analysis (**Figure 4.19**) of these samples revealed the characteristic peaks due to the 002 (26°), 100 (43°) and 101 (44-45°) graphitic planes, with sample BC800-*2* reporting more peaks due to the catalyst. The dominant 002 peaks exhibited varying degrees of asymmetry/broadening, with sample BCP800-*2* presenting with the sharpest peak, and thus the greatest degree of crystallinity. This is consistent with a higher graphitization degree (Table 4.7) observed for BCP800-*2*.[65, 73-76] All the samples presented with d-spacing (3.4 Å, Table 4.9) comparable to sample BP800-*i.*

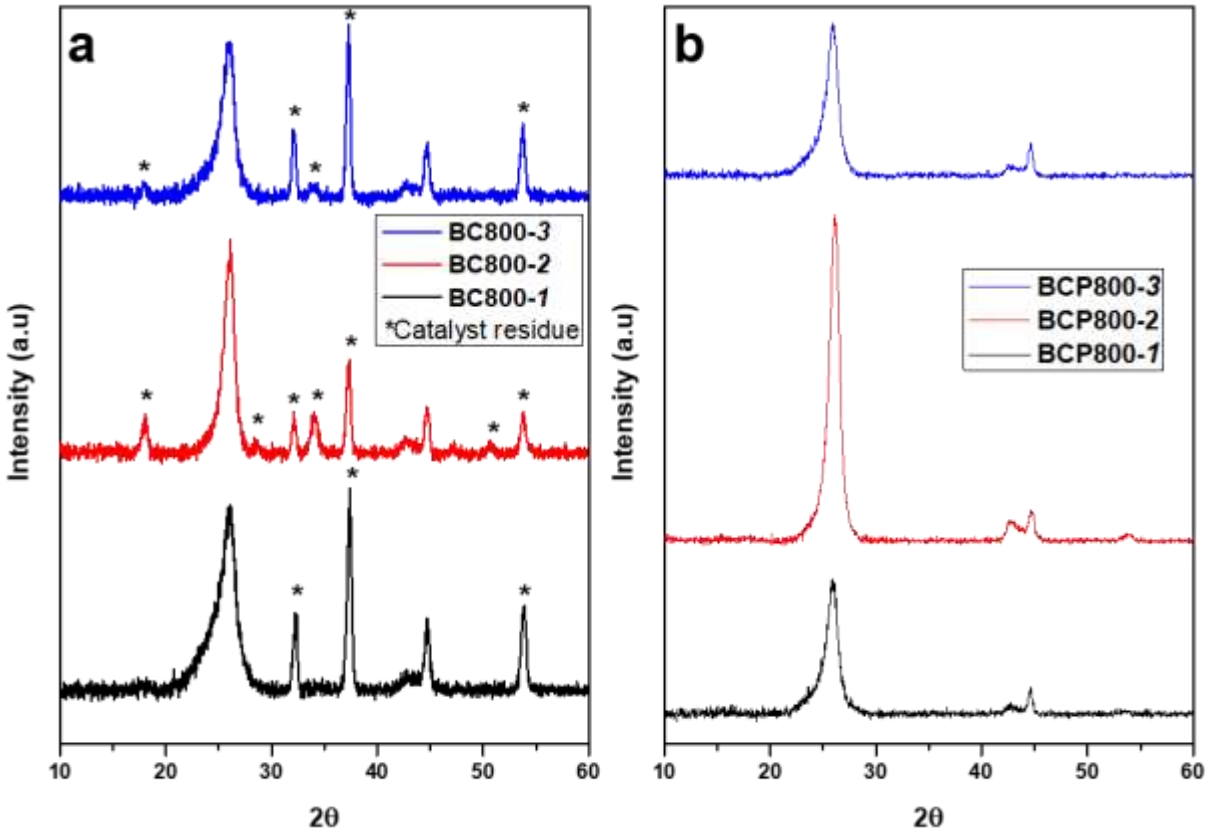


Figure 4.19: XRD analysis of *a*) as-synthesized MWCNTs, *b*) purified MWCNTs.

Table 4.9: The d-spacing and graphitization of the obtained MWCNTs.

Sample code	Flow rates of carbon source and carrier gas (sccm)	002 plane peak position (°)	d_{002} (Å)	g (%)
BCP800-*1*	C_2H_2 = 110 N_2 = 220	25.91	3.436	4.7
*BP800-*i*	C_2H_2 = 90 N_2 = 240	25.83	3.446	**(-7.0)
BCP800-*2*	C_2H_2 = 70 N_2 = 260	26.11	3.410	34.9
BCP800-*3*	C_2H_2 = 50 N_2 = 280	25.94	3.432	9.3

*Discussed in **section 4.3.1 and 4.3.2.** **Did obey the validity range.

Raman analysis (**Figure 4.20**, full data reported in **Appendix 4A** Table 4.16) of all purified samples presented with the carbon *D* and *G* bands at approximately 1350 and 1580 cm^{-1}.[35, 39, 77-83] The I_D/I_G ratio indicated that sample BCP800-*2* (i.e., 70 sccm-C_2H_2 and 260 sccm-N_2) presented with better crystallinity than all the other samples. This agrees with the XRD data, where sample BCP800-*2* presented with the sharpest and narrowest 002 peak. The small intensity of the *D* band was also consistent with a reduced density of defects within the material. Furthermore, the D_1 (arising from disordered graphitic lattice), D_2 (arising from amorphous carbon) and *D'* (arising from disordered graphitic lattice, i.e., graphene surface layers) bands are less prominent in sample BCP800-*2* compared to the other samples, which is consistent with better crystallinity.[102-104] This high crystallinity and in particular the shallow *D'* band is not consistent with a high density of defects (although this may only be confirmed by a technique such as XPS), and may suggest a low concentration of boron induced defects. The sample BCP800-*3* presented with the least crystallinity and more density of defects. The 2nd order region (**Figure 4.20d-f**, full data reported in **Appendix 4A** Table 4.15) presented with multiple bands (*G', D+G, 2G*), and the pattern of the signal indicated the presence of multiple graphitic layers.[84-86] The overall crystallinity ($I_{G'}/I_D$) ratio revealed similar trends of crystallinity as the I_D/I_G ratio, with the long-range order for sample BCP800-*2* (1.00) > BP800-*i* (0.36) > BCP800-*1* (0.35) > BCP800-*3* (0.20).[87-89] Similarly, the long-range order ($I_{G'}/I_G$)

exhibited this trend, BCP800-*2* (0.93) > BCP800-*1* (0.69) > *BP800-*i* (0.59) > BCP800-*3* (0.51).

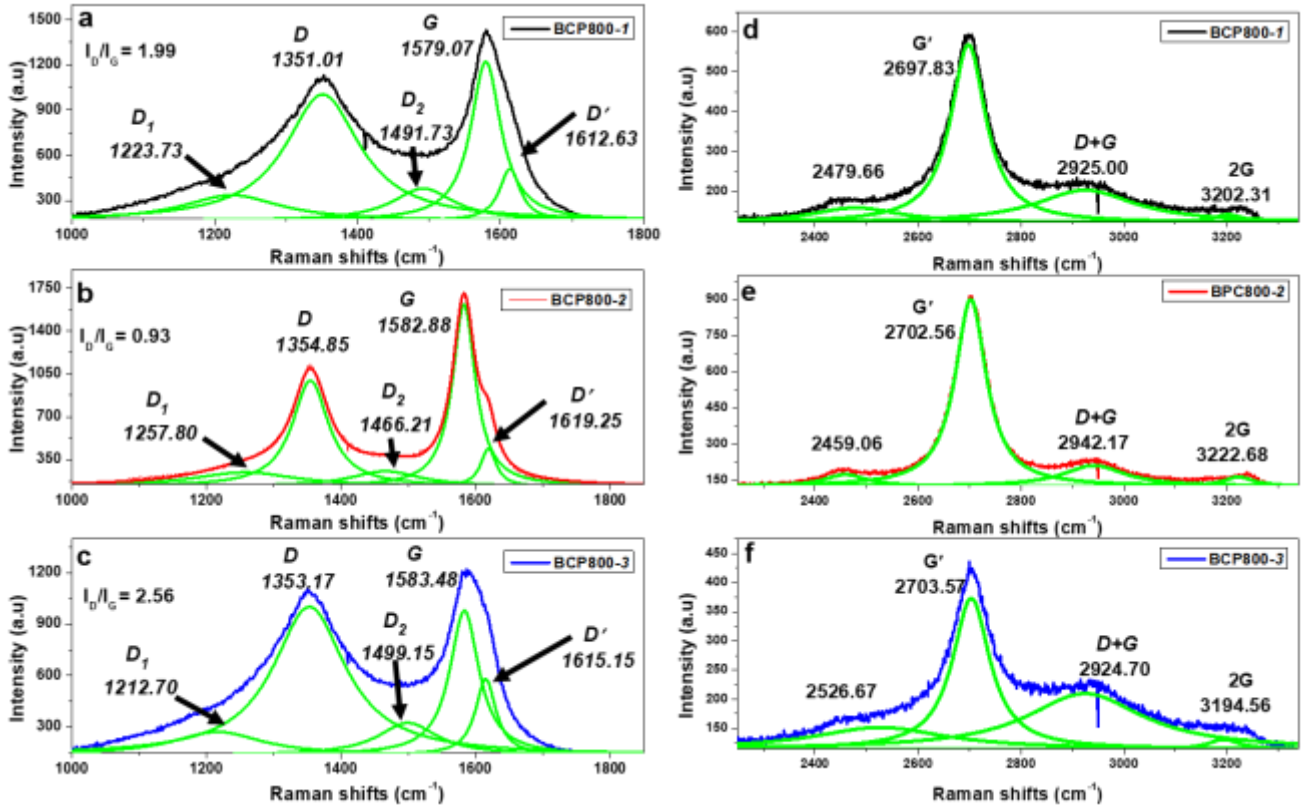


Figure 4.20: B-doped MWCNTs prepared at different carbon source and carrier gas flow rates using tri-isopropyl borate as boron source; (*a-c*) 1st order Raman Lorentzian fitted peaks, (*d-f*) 2nd order Raman Lorentzian fitted peaks.

The thermal analysis of the as-synthesized samples (**Figure 4.21**) indicated that their thermal stability was similar. The carbon yield for BC800-*1* > BC800-*2* > BC800-*3*, and the derivative curve revealed that the samples had two major morphologies of carbon present in them. The initial mass loss due to the oxidation of amorphous carbon for BC800-*3* and BC800-*2* were observed at 400℃ and 425℃, respectively. This mass loss was not observed for sample BC800-*1*. The initial mass loss was followed by a mass gain due to the formation of metal oxides in the temperature range of 400-500℃ for all samples.[90-93]

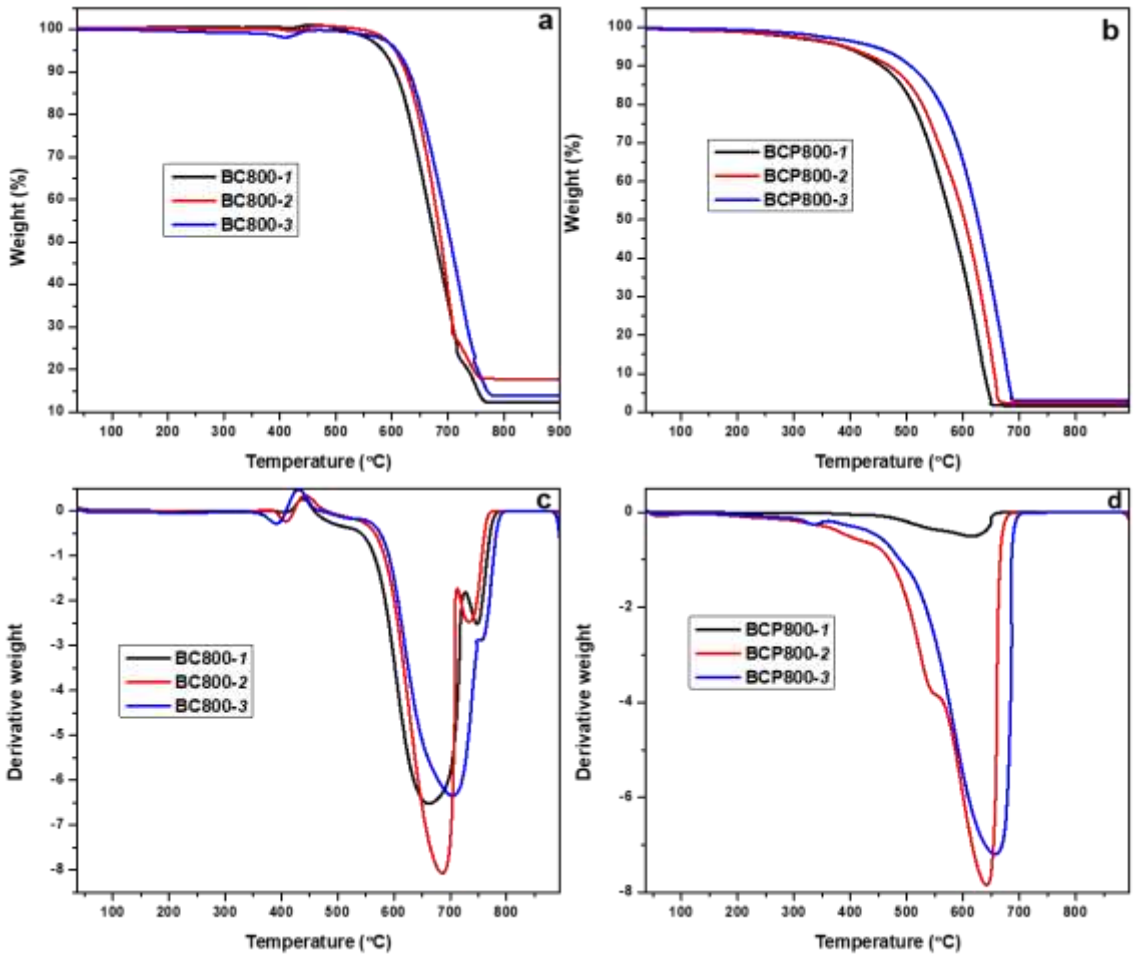


Figure 4.21: TGA analysis of *a)* as synthesized B-doped MWCNTs prepared from tri-isopropyl borate, *b)* purified B-doped tri-isopropyl borate derived B-doped samples, *c)* derivative curve of as synthesized B-doped MWCNTs prepared from tri-isopropyl borate, *d)* derivative curve of purified B-doped tri-isopropyl borate derived B-doped samples.

The thermal analysis of the purified samples revealed that despite the removal of the catalyst residue (< 5%), the difference in thermal stability between the samples was still small. The weight derivative curve for the BCP800-*2* sample indicated the presence of two major carbon morphologies, decomposing at 540℃ and 640℃. The thermal stability of BCP800-*3* (660℃) > BCP800-*2* (540 and 640℃) > *BP800-*i* (625℃) > BCP800-*1* (620℃). Sample BCP800-*2* and BCP800-*3* showed a first mass loss due to adsorbed moisture at ≅ 100℃, and the 2nd mass loss, arising from the oxidation of amorphous carbon at 350℃, was observed for BCP800-*3*.[90-93] The decrease of the carbon source gas and increase in the carrier gas flow rates relative to the flow rates determined by *Tetana et al.*[41, 90] gave material with better thermal stability. However, an increase in carbon source gas and a decrease in carrier gas flow rates reduced the thermal stability of the material.

The BET data (Table 4.10) showed that the surface area and pore volume increased with a reduction in the carbon source flow rate (110 to 50 sccm) and an increase in the carrier gas rate (220-280 sccm). Although sample BCP800-*3* (50 sccm C_2H_2 and 280 sccm-N_2) presented with a slightly larger pore size, the pore sizes were not significantly different from each other. Additionally, deviation from the flow rates reported by *Tetana et al.*[41, 90] led to the production of MWCNTs with lower surface area and pore volumes, but larger pore sizes.

Table 4.10: Brunauer-Emmet-Teller surface area data

Sample	Surface area (m^2/g)	Pore volume (cm^3/g)	Pore size (nm)
BCP800-*1*	25.1	0.1189	23.1
*BP800-*i*	108.7	0.4338	15.9
BCP800-*2*	39.3	0.1937	23.8
BCP800-*3*	41.2	0.2099	25.7

4.3.3.2. Investigation of the total flow rate in the synthesis of B-doped MWCNTs.

The significance of carbon source gas and carrier gas flow rates in the synthesis of boron doped MWCNTs while keeping the total flow rate constant was demonstrated in the previous section. The proceeding study was designed to investigate the significance of the total flow rate in the production of boron doped MWCNTs using tri-isopropyl borate as a boron source by varying the carbon source and carrier gas flow rates individually from 90 sccm and 240 sccm (as determined by *Tetana et al* [41,90]*)*, respectively.

Table 4.11: flow rates for the synthesis of B-doped MWCNTs and corresponding yields and % yields.

As-synthesized and purified sample codes.	Total flow rate (sccm)	Carbon source flow rate (sccm)	Carrier gas flow rate (sccm)	Total Mass (g)	Carbon yield (%)
BV800-*1 and* BVP800-*1*	290	50	240	0.6698	20.4
BV800-*2 and* BVP800-*2*	310	70	240	1.457	31.8
*BP800-*i*	330	90	240	1.585	26.8
BV800-*4 and* BVP800-*4*	350	90	260	1.963	33.3
BV800-*3 and* BVP800-*3*	370	90	280	1.664	28.2

*Optimal flow rates reported in **sections 4.3.1.1** and **4.3.2.1**

The carbon yield (%) (Table 4.11) had a direct correlation (not consistently) on the total flow rate of the system. Increasing the total flow rate relative to the reported optimal flow rate (330 sccm)[41, 90] led to an increase at 350 sccm but a decrease at 370 sccm. However, decreasing the total flow rate led to a general decrease in % yield, with an increase at 310 sccm, but a decrease at 290 sccm. Similar to the constant total flow rate study, the observed trend in % yield could be attributed to the dilution of the carbon source and rate of saturation of the active sites on the catalyst. However, in this case, the rate of saturation is also dependant on the total flow rate of the system. Consequently, a decrease in % yield was observed. On the other hand, even though dilution of the carbon source by decreasing the total flow rate to 310 sccm led to an increase in % yield, further dilution to a total flow rate of 290 sccm saw a significant decrease in yield.

This was attributed to the low total flow rate that potentially led to a relatively more rapid saturation of the catalyst active site (i.e., decreasing accessibility over time).

XRD analysis (**Figure 4.22**) of the as-synthesized samples exhibited the characteristic 002 (26°), 100 (43°) and 101 (44-45°) peaks resulting from the carbon graphitic planes. The broadness of the 002 peaks increased as the total flow rate increased, while the peaks due to the catalyst residue decreased at higher total flow rates. Sample BV800-*4* presented with peaks due to boron oxide, which was not observed for the other samples. The successful removal of the catalyst and boron residues using HNO_3 was confirmed by XRD analysis (**Figure 4.22b**).

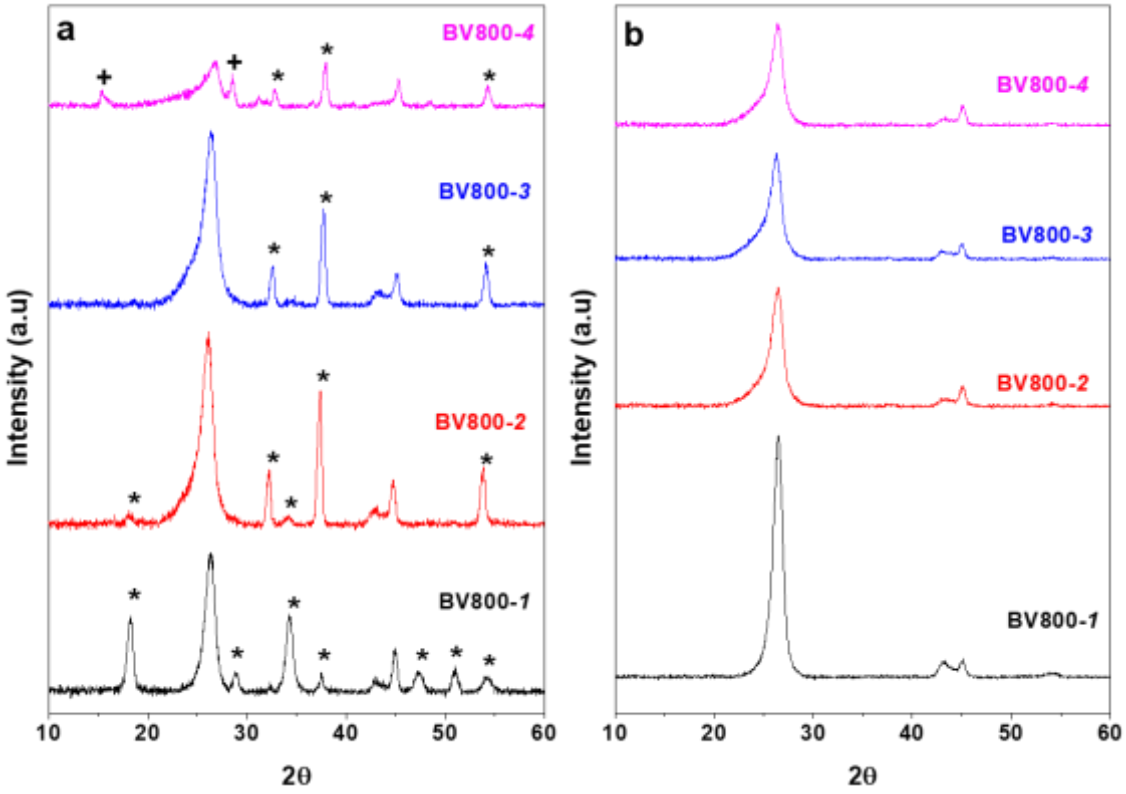


Figure 4.22: XRD analysis of *a)* as synthesized B-doped MWCNTs, *b)* purified B-doped MWCNTs.

The 2*θ* positions of the 002 peaks in the purified samples were found to be inversely proportional to the total flow rate. The crystallinity of the samples decreased at higher total flow rates as evidenced by the increase in asymmetry observed in the 002 peak. Sample BVP800-*1* presented with the highest degree of crystallinity as it exhibited the sharpest 002 peak. The d-spacings exhibited a direct correlation to the total flow rate (**Figure 4.23**). Relative to the optimal total flow rate reported in the production of good quality B-doped MWCNTs by

Tetana et al.[41] and *Mhlanga et al.*[111] (**Figure 4.23**, blue circle), either decreasing or increasing the total flow rates of the system resulted in smaller d-spacing.

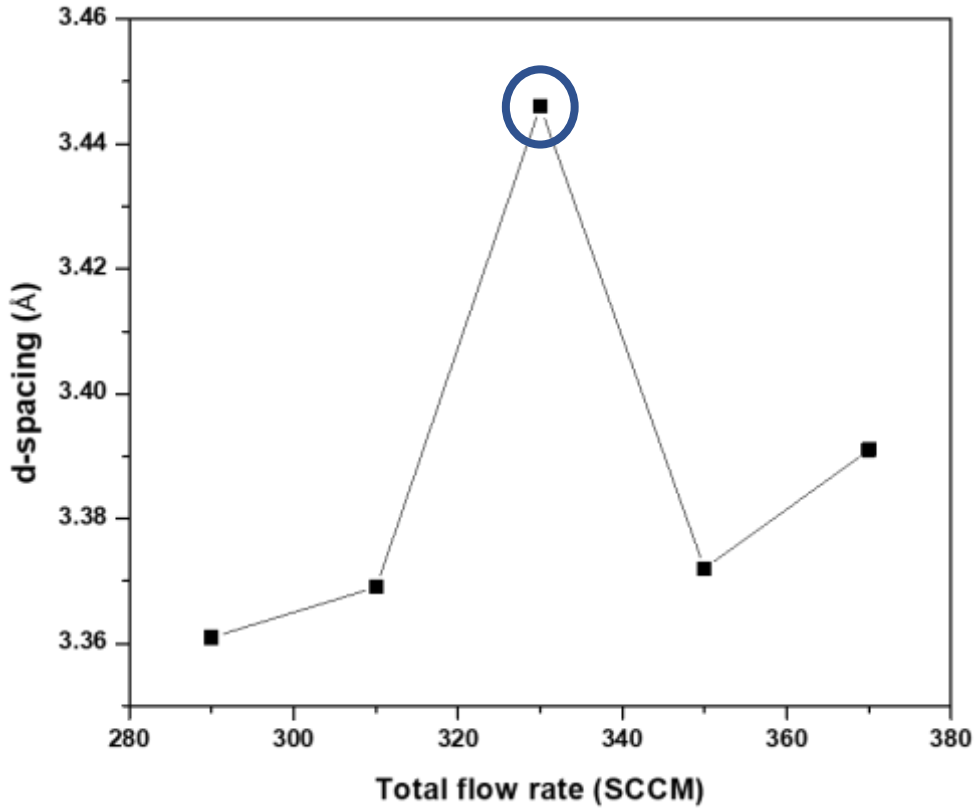


Figure 4.25: *a*) Total flow rate vs d spacing.

The characteristic Raman carbon *D* and *G* bands were observed for all samples at approximately 1350 and 1580 cm^{-1} (**Figure 4.24**, full data listed in **Appendix 4A** Table 4.16).[35, 39, 77-83] Using sample BP800-*i* (I_D/I_G = 1.69) as a reference point; it was revealed that lowering the total flow rate (330 to 290 sccm) by reducing the carbon source gas flow rate from 90 sccm to 50 sccm gave a highly crystalline sample (BVP800-*1*) at 50 sccm. While an increase in the total flow rate (330 to 370 sccm) by increasing the carrier gas flow rate (240 to 280 sccm) saw a general increase in the I_D/I_G ratio, which declined at a total flow rate of 370 sccm. The I_D/I_G ratio revealed that the density of defects of sample BVP800-*1* (0.79) < *BP800-*i* (1.69) < BVP800-*3* (1.79) < BVP800-*2* (2.52) < BVP800-*4* (3.31). The overall crystallinity deduced from the $I_{G'}/I_D$ ratio (listed in **Appendix 4A** Table 4.16)[87-89], BVP800-*1* (1.09) > BVP800-*3* (0.56) > *BP800-*i* (0.36) > BVP800-*2* (0.20) > BVP800-*4* (0.11), agreed with the trend in crystallinity deduced from the I_D/I_G ratio. The long-range order ($I_{G'}/I_G$) also exhibited the same trend, BVP800-*1* (0.86) > BVP800-*3* (0.62) > *BP800-*i* (0.59) >BVP800-*2* (0.49) > BVP800-*4* (0.36). The high crystallinity of sample BVP800-*1* also evidenced by the smaller intensity of

the *D*, *D'D1* and *D2* bands was consistent with its corresponding XRD data, which presented with the narrowest 002 peak.

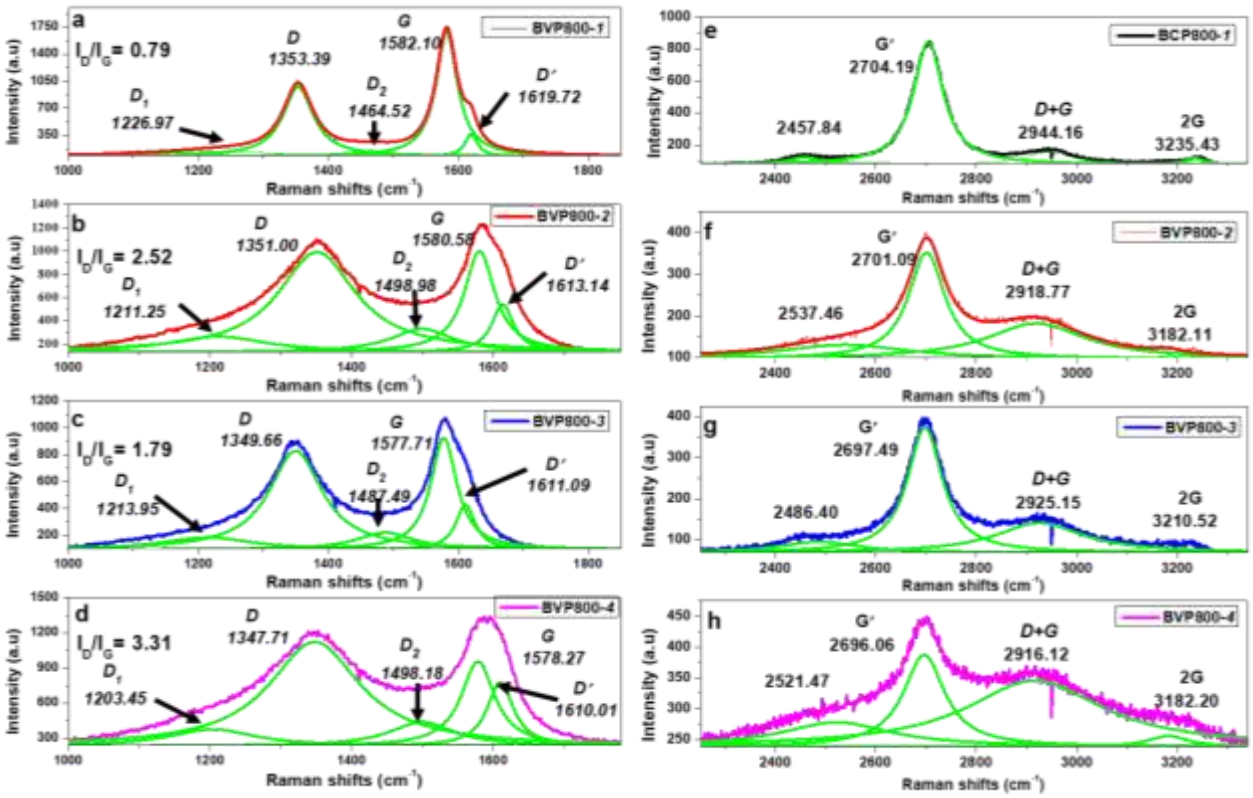


Figure 4.24: B-doped MWCNTs prepared at different carbon source and carrier gas flow rates using tri-isopropyl borate as boron source; (*a-c*) 1st order Raman Lorentzian fitted peaks, (*d-f*) 2nd order Raman Lorentzian fitted bands.

The presence of the 2nd order bands indicated the presence of multiple graphitic layers.[84-86] Decreasing the total flow rate (from 330 to 290 sccm) saw an increase in intensity of the *G'* band relative to the *G+D*. Thus, suggesting that a decrease in the total flow rate led to the production MWCNTs with a decrease in the number of layers, and consequently smaller average diameter. Increasing the total flow rate (330 to 370 sccm) only saw a decrease in the intensity of the *G'* band relative to the *D+G* band at 370 sccm, which indicated that higher total flow rates tend to give larger average diameter nanotubes.

The thermal stability of the as synthesized samples (**Figure 4.25a, c**) obtained at different total flow rates indicated that the total flow rate was directly proportional to the carbon yield. Sample BV800-*4* (350 sccm) was the only sample that had an initial mass loss at 200℃. All samples exhibited mass loss resulting from the oxidation of amorphous carbon between 400-450℃.[98-

[99] This was followed by a mass gain due to the formation of metal oxides between 400-500℃ for all samples, except BV800-*1* which exhibited the mass gain at 500-550℃. The 3rd mass loss due to carbon nanotubes in the derivative curve revealed the presence of two major morphologies of nanotube in samples BV800-*1* and BV800-*4*. Thermal analysis of the purified samples (**Figure 4.25b, d**) indicated a substantial removal of the residual catalyst. The thermal stability of the material was found to be directly proportional to the total flow rate of the reaction, i.e., BVP800-*1* (290 sccm) > BVP800-*2* (310 sccm) > BVP800-*4* (350 sccm) > BVP800-*3* (370 sccm). Sample BVP800-*4* was the only sample that presented with a mass loss at 200-300℃, which was attributed to the removal of functional groups and the oxidation of amorphous carbon.[98-99] In addition, the oxidation of amorphous carbon was observed at a higher temperature of 400℃ for the remaining samples. When compared to BP800-*i*, all the samples had enhanced thermal stability, samples prepared at higher total flow rates (350 and 370 sccm) reported higher but comparable decomposition temperatures to BP800-*i*, while the lower total flow rate (290 and 310 sccm) had noticeably better thermal stability than BP800-*i*.

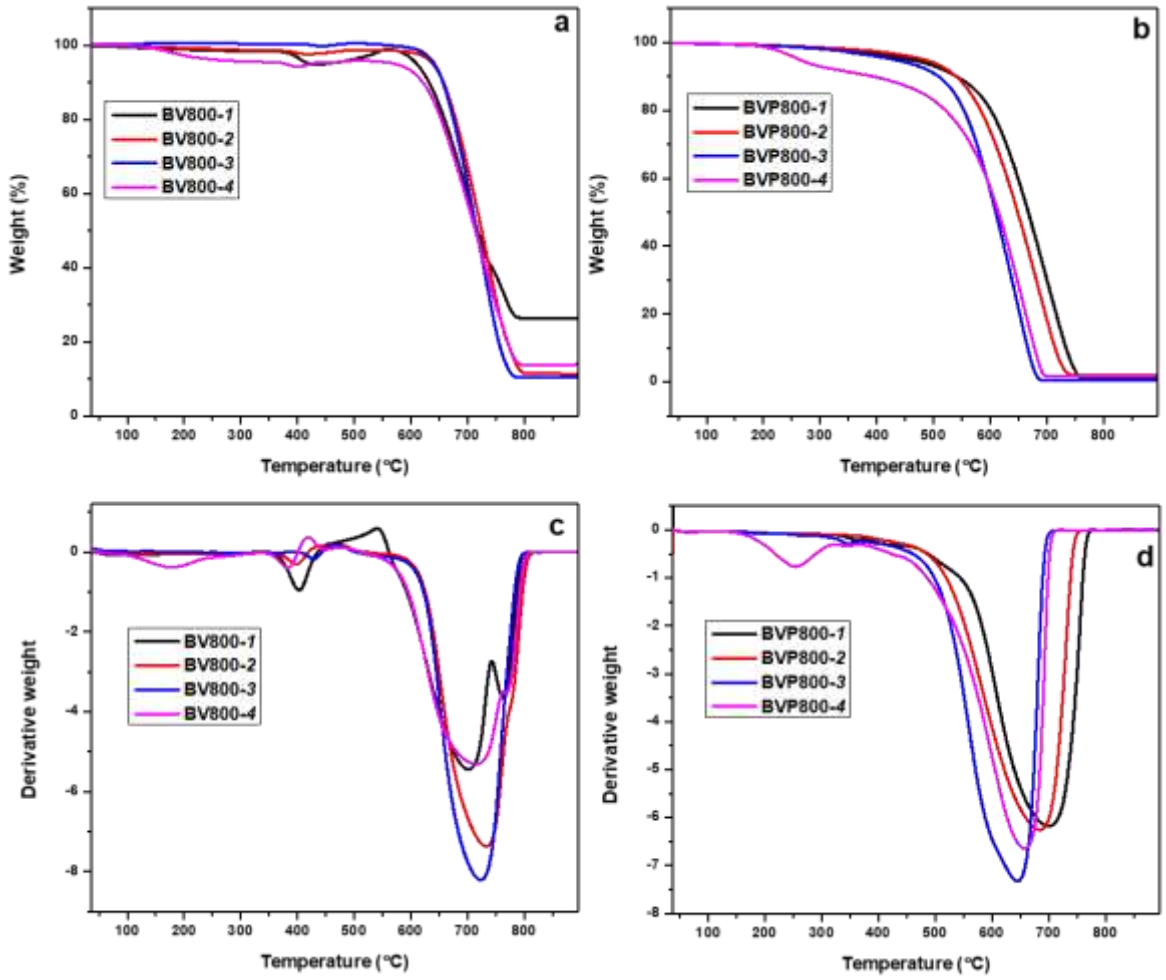


Figure 4.25: the thermogravimetric analysis (TGA) of *a)* as-synthesized B-doped samples prepared at different total flow rates using tri-isopropyl borate, *b)* purified B-doped samples prepared at different total flow rates using tri-isopropyl borate. *c)* derivative curve of as-synthesized B-doped samples prepared at different total flow rates using tri-isopropyl borate, *b)* derivative curve of purified B-doped samples prepared at different total flow rates using tri-isopropyl borate.

The BET data (Table 4.12) revealed that the lowest total flow rate produced nanotubes with the highest surface area, while the highest total flow rate produced nanotubes with the 2nd highest surface area. The surface area of the obtained samples was analysed relative to the BP800-*i* (330 sccm) sample; decreasing the total flow rate (330 to 290 sccm) led to an increase in surface area and pore volume increased, but a decrease in pore sizes. However, when the total flow rate was increased (330-370 sccm) the surface area and pore volume decreased at 350 sccm and increased at 370 sccm, and the pore size decreased with an increase in the total flow rate.

Table 4.12: Brunauer-Emmet-Teller surface area data

Sample	Surface area (m^2/g)	Pore volume (cm^3/g)	Pore size (nm)
BVP800-*1*	42.7	0.1895	17.7
BVP800-*2*	33.7	0.1722	20.5
BVP800-*3*	39.0	0.1919	19.7
BVP800-*4*	20.1	0.1127	24.9
*BP800-*i*	23.9	0.1539	28.4

4.3.3.3. Summary.

The flow rate of the carbon source and carrier gas has been shown to be an important factor in the production of MWCNTs. When the total flow rate of the system was kept constant, decreasing carbon source gas flow rate, while increasing the carrier gas flow rate led to an increase in % yield. Both the XRD and Raman analysis reported that the sample prepared at a carbon source and carrier gas flow rates of 70 sccm and 260 sccm, respectively, had the best crystallinity. While sample prepared at 50 sccm (carbon source) and 280 sccm (carrier gas)

reported the highest thermal stability and surface area. Altering the total flow rate of the system by keeping the flow rate of one the gases constant gave material with different characteristics, indicating the significance of not only the flow rate of each gas, but the total flow rate of the system. The d-spacing and graphitization degrees were found to be directly correlated to the total flow rate of the system. Variation of the total flow rate led to much more thermally stable material than when it was kept constant, with a decomposition temperature range of 600-750℃ compared to 550-660℃. Lower total flow rate of the system gave the most thermally stable material, with the highest surface area. Furthermore, the surface area was found to be inversely correlated to the total flow rate of the system.

Both studies have illustrated the significance of flow rate in the production of MWCNTs, indicating that not only is the choice of gases significant but the rate at which they are introduced into the system is also important.

4.4. Conclusion.

The modification of MWCNTs not only has the potential to impart and improve different characteristics, but also has the potential to improve versatility and scope of application. Boron doping of MWCNTs is one of the most broadly and extensively used modification techniques. In this chapter, boron doped MWCNTs were produced using the CVD method. The influence of reaction time (15, 30 and 60 min), temperature (700, 750 and 800℃), gas flow rate [constant total flow rate (330 sccm) vs different total flow rate (290, 310, 330, 350 and 370 sccm)] and boron source (tri-isopropyl borate vs trimethyl borate) were investigated, and variation in all these reaction conditions led to the production of different boron doped MWCNTs.

The influence of reaction time in the production of boron doped MWCNTs revealed that using either boron source gave the highest % yields at a reaction time of 15 min. However, the use of tri-isopropyl borate produced a lower % yield compared to trimethyl borate. Although both sets of samples reported a direct correlation of d-spacing with reaction time, this change in d-spacing with reaction time was more pronounced in the use of trimethyl borate than tri-isopropyl borate. At low reaction time, samples produced using trimethyl borate presented with better crystallinity than those prepared from tri-isopropyl borate. The use of either boron source gave the most thermally stable material at a reaction time of 30 min. Differences in thermal stability for samples produced using the same boron source were pronounced for those prepared from trimethyl borate compared to tri-isopropyl borate. Surface area for both sets of samples had a direct correlation to reaction time, and the use of tri-isopropyl borate produced samples

with smaller surface area compared to trimethyl borate. XPS analysis of both sets of samples revealed that trimethyl borate was successful at producing B-doped MWCNTs at 15- and 60-min reaction times, while tri-isopropyl borate failed across the board.

Reaction temperature also proved to be a significant factor in the production of boron doped MWCNTs. XPS analysis revealed that tri-isopropyl borate was successful at producing B-doped MWCNTs at lower temperatures of 700℃ and 750℃, while trimethyl borate was only successful at 800℃. The % yield of the material was directly correlated to the reaction temperature when tri-isopropyl borate was used as a boron source, while the use of trimethyl borate exhibited no clear relationship with temperature but produced the highest % yield at 750℃. All the material produced using either boron source (even those with no boron in the lattice structure), had larger % yield than the corresponding pristine MWCNTs. The d-spacing for both sets of samples had a direct correlation with reaction temperature. The density of defects/crystallinity was highly dependent on the boron source used, the use of tri-isopropyl borate had a direct correlation with temperature, while trimethyl borate produced the opposite trend. The most thermally stable material between both sets of samples was produced at 750℃ using trimethyl borate, followed by 700℃ using tri-isopropyl borate. All boron doped material reported higher thermal stability than their corresponding pristine MWCNTs. A direct correlation between surface area and reaction temperature were observed for both sets of samples, with the sample prepared at 700℃ using tri-isopropyl borate as a boron source.

The flow rate of individual gases and total flow rate are essential in the production of MWCNTs. The flow rate should allow for efficient interaction between the carbon source and active sites of the catalyst. High flow rates, whether for individual gases or for the total system, led to lower % yields. Furthermore, increase total flow rate led to a decrease in the surface area of obtained samples. Changing the total flow rate led to much more thermally stable material than when it was kept constant, with a decomposition temperature range of 600-750℃ compared to 550-660℃. Lower total flow rate of the system gave the most thermally stable material, Although the study produced different types of MWCNTs, the reaction time and temperature studies indicated that indirect methods (XRD, Raman etc) were not reliable in determining if boron was added successfully to the lattice structure of the material. Hence, discussions about the nature of the materials made no conclusions about the addition of boron, but restricted to their physical properties (i.e., crystallinity, thermal properties etc)

Despite the success reported in the reaction time and temperature studies in producing B-doped MWCNTs, it was clear that the methods employed are not proficient relative to other existing methods because they produced material with low concentrations of boron in the lattice structure.

Appendix 4A

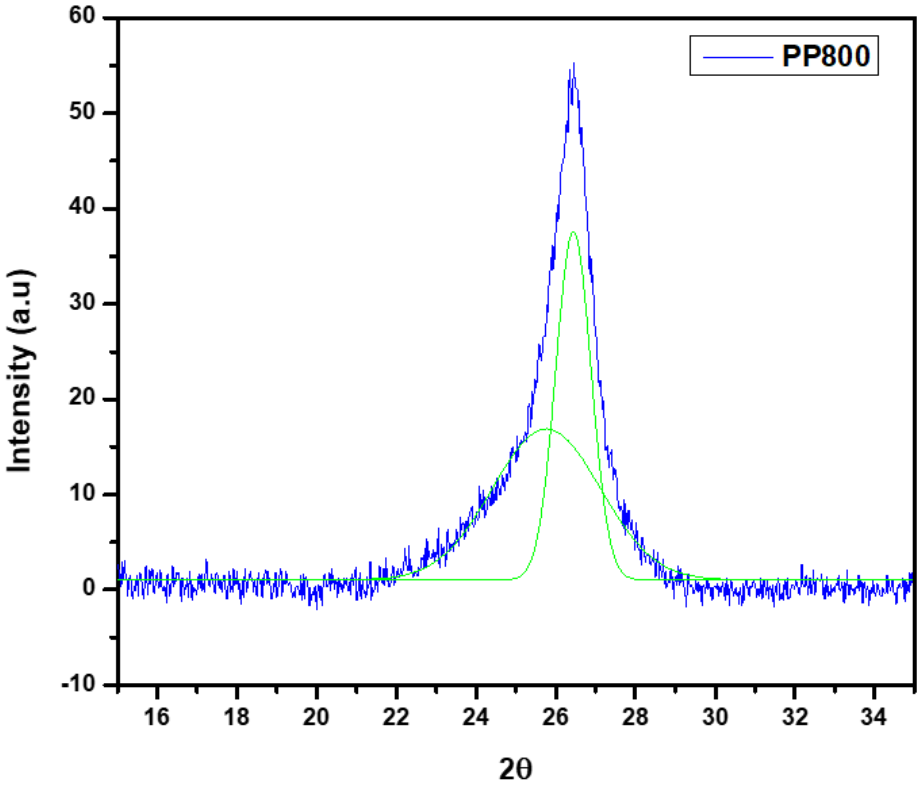


Figure 4.27: Deconvoluted XRD pattern of the 002 peak for pristine MWCNTs prepared at 800℃.

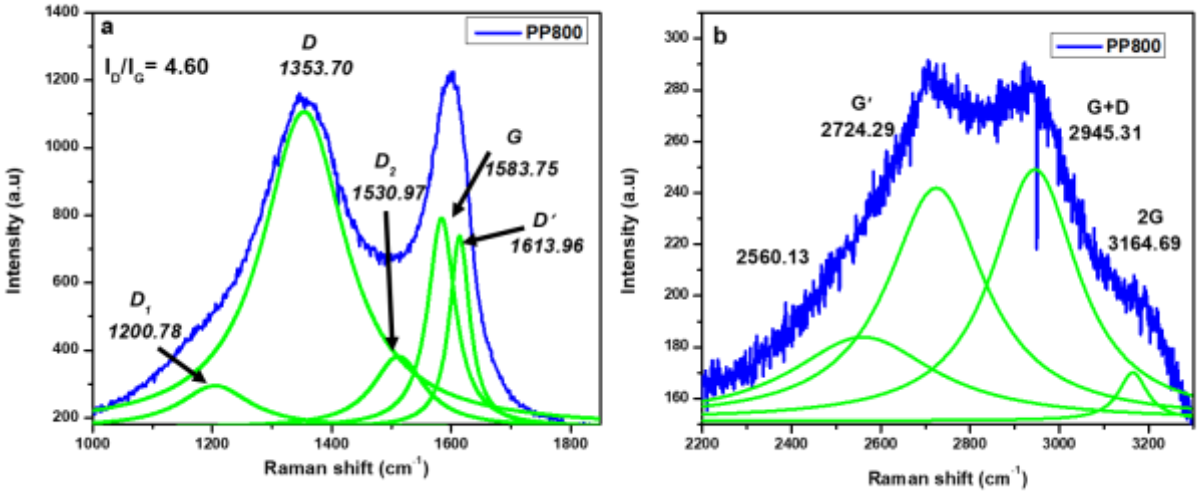


Figure 4.28: Deconvoluted XRD pattern of the Raman spectra for pristine MWCNTs prepared at 800℃.

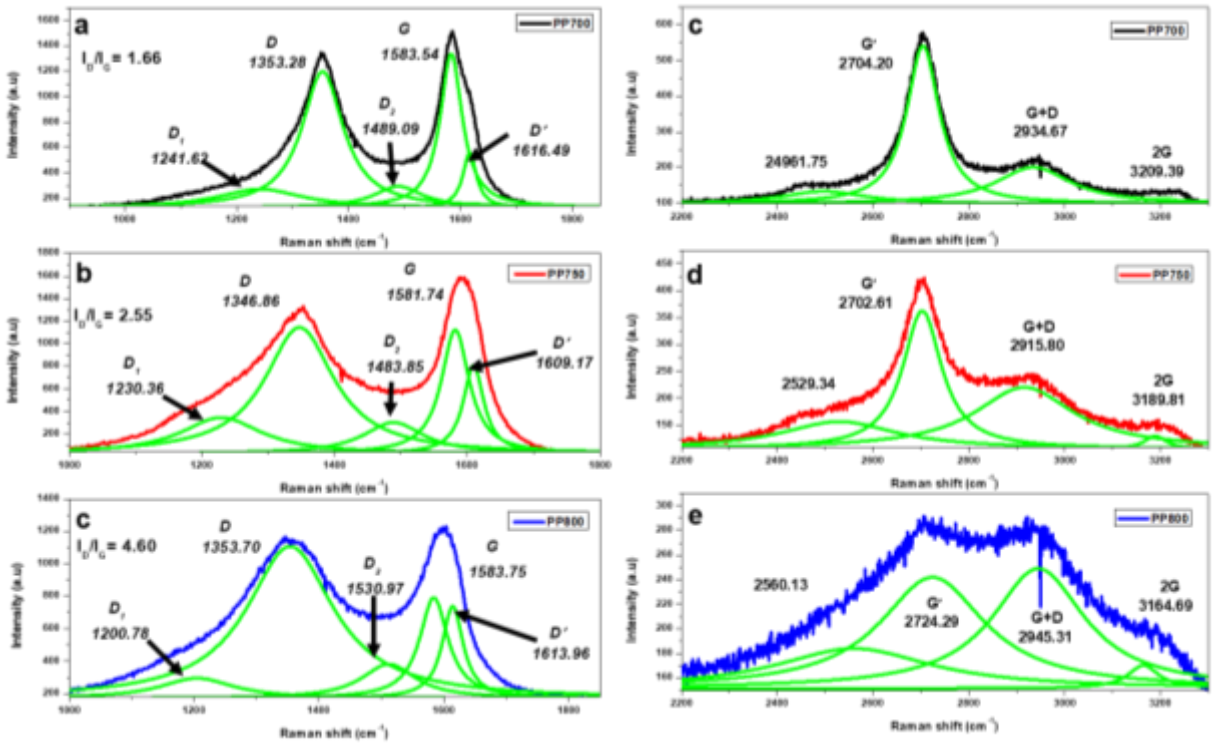


Figure 4.29: Deconvoluted Raman spectra for pristine MWCNTs prepared at 700, 750 and 800°C.

Table 4.13: Raman analysis summary of the Lorentzian fitted peaks for B-doped MWCNTs produced at different reaction times.

Sample	Area (D-peak)	Area (G-peak)	Intensity (D-peak)	Intensity (G-peak)	Area (G`-peak)	Ratio* I_D/I_G	Ratio $I_{G'}/I_G$	Ratio $I_{G'}/I_D$
BP800-15-*i*	169291.71	120773.83	1058.30	1544.78	74634.39	0.69	0.62	0.44
BP800-30-*i*	129391.33	64454.64	680.26	828.17	37366.50	0.82	0.58	0.29
BP800-60-*i*	182297.03	108601.06	1060.59	1301.24	64776.87	0.81	0.59	0.36
BP800-15-*m*	86128.15	103320.61	871.51	1559.58	102084.51	0.56	0.99	1.19
BP800-30-*m*	161673.79	86639.34	958.48	1088.34	50280.07	0.88	0.58	0.31
BP800-60-*m*	164593.77	74238.46	902.81	861.21	34475.52	1.05	0.46	0.21

*Calculated from intensity

Table 4.14: Raman analysis summary of the Lorentzian fitted peaks for B-doped MWCNTs produced from tri-isopropyl borate at different temperatures.

Sample	Area (D-peak)	Area (G-peak)	Intensity (D-peak)	Intensity (G-peak)	Area (G`-peak)	Ratio* I_D/I_G	Ratio $I_{G'}/I_G$	Ratio $I_{G'}/I_D$
BP700-*i*	238010.25	109327.32	1598.95	1381.69	66655.49	1.16	0.61	0.28
BP750-*i*	113878.14	86513.98	890.91	1030.86	64986.81	0.86	0.75	0.57
BP800-*i*	182297.03	108601.06	1060.59	1301.24	64776.87	0.81	0.59	0.36
BP700-*m*	128943.48	83611.74	994.60	1051.98	67605.09	0.95	0.81	0.52
BP750-*m*	249529.22	97136.18	1364.56	1165.33	51112.24	1.17	0.53	0.20
BP800-*m*	164593.77	74238.46	902.81	861.21	34475.52	1.05	0.46	0.21
PP700	247864.01	53855.24	936.17	620.52	53718.65	1.50	0.59	0.36
PP750	222484.91	87203.04	1117.01	1095.55	39722.01	1.01	0.23	0.18
PP800	247864.01	53855.24	936.17	620.52	37785.03	1.50	0.14	0.15

*Calculated from intensity

Table 4.15: Raman analysis summary of the Lorentzian fitted peaks for B-doped MWCNTs produced from tri-isopropyl borate at a constant total flow rate.

Sample	Area (D-peak)	Area (G-peak)	Intensity (D-peak)	Intensity (G-peak)	Area (G`-peak)	Ratio* I_D/I_G	Ratio $I_{G'}/I_G$	Ratio $I_{G'}/I_D$
BCP800-*1*	167618.62	84245.22	838.19	1056.35	58049.87	0.79	0.69	0.35
BCP800-*2*	89039.50	96238.77	866.66	1486.41	89524.85	0.58	0.93	1.00
BCP800-*3*	178591.23	69790.78	865.72	843.52	35875.63	1.03	0.51	0.20

*Calculated from intensity

Table 4.16: Raman analysis summary of the Lorentzian fitted peaks for B-doped MWCNTs produced from tri-isopropyl borate at varied total flow rate.

Sample	Area (D-peak)	Area (G-peak)	Intensity (D-peak)	Intensity (G-peak)	Area (G`-peak)	Ratio* I_D/I_G	Ratio $I_{G'}/I_G$	Ratio $I_{G'}/I_D$
BVP800-*1*	79998.31	101176.02	899.59	1615.24	86928.29	0.56	0.86	1.09
BVP800-*2*	180228.43	71471.34	861.57	869.17	35270.24	0.99	0.49	0.20
BVP800-*3*	114608.12	64151.69	736.96	833.15	40227.40	0.88	0.62	0.56
BVP800-*4*	218439.25	65890.45	892.72	725.35	23420.34	1.23	0.36	0.11

*Calculated from intensity

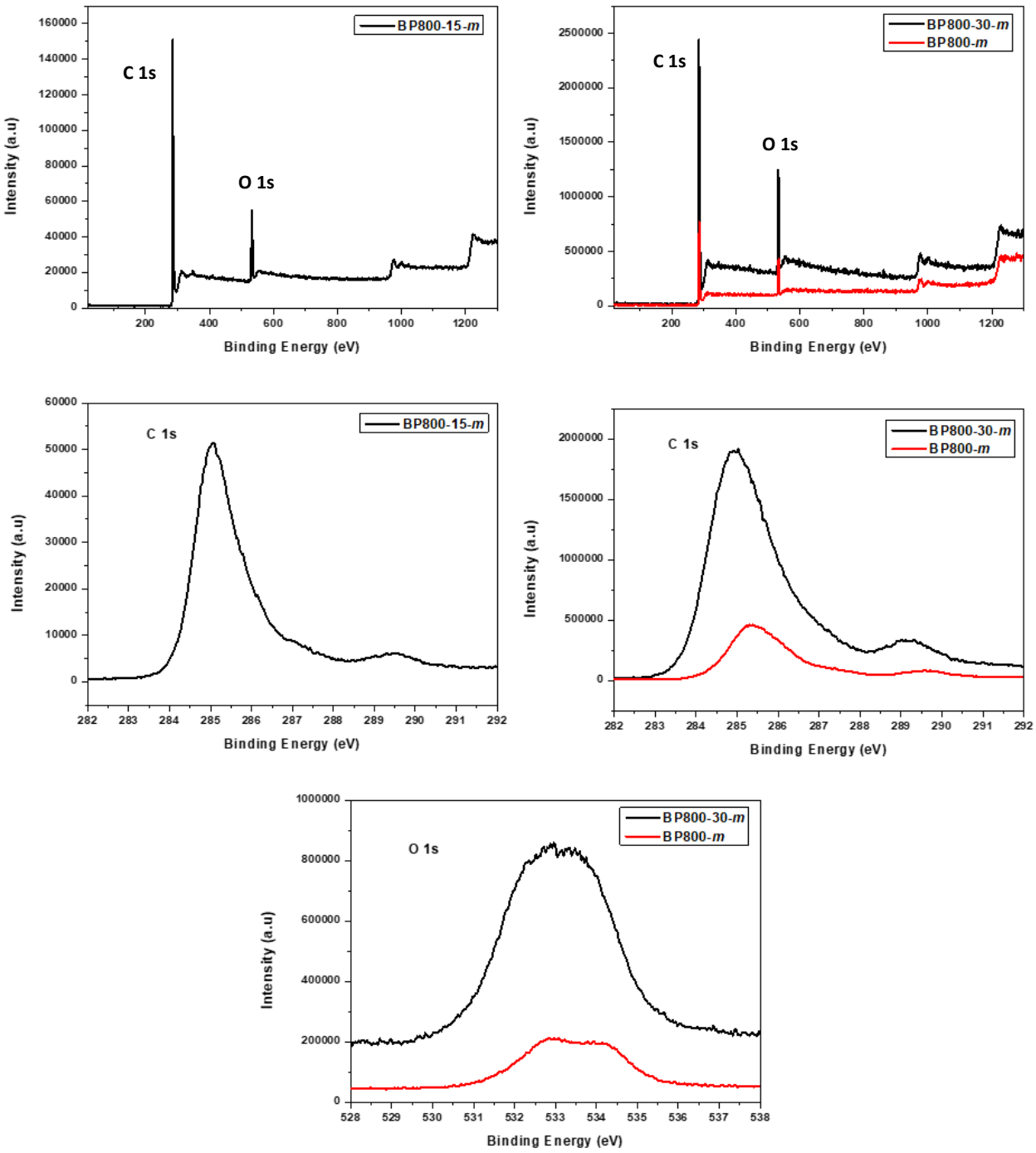


Figure 4.30: XPS analysis of heteroatom doped MWCNTs derived from trimethyl borate.

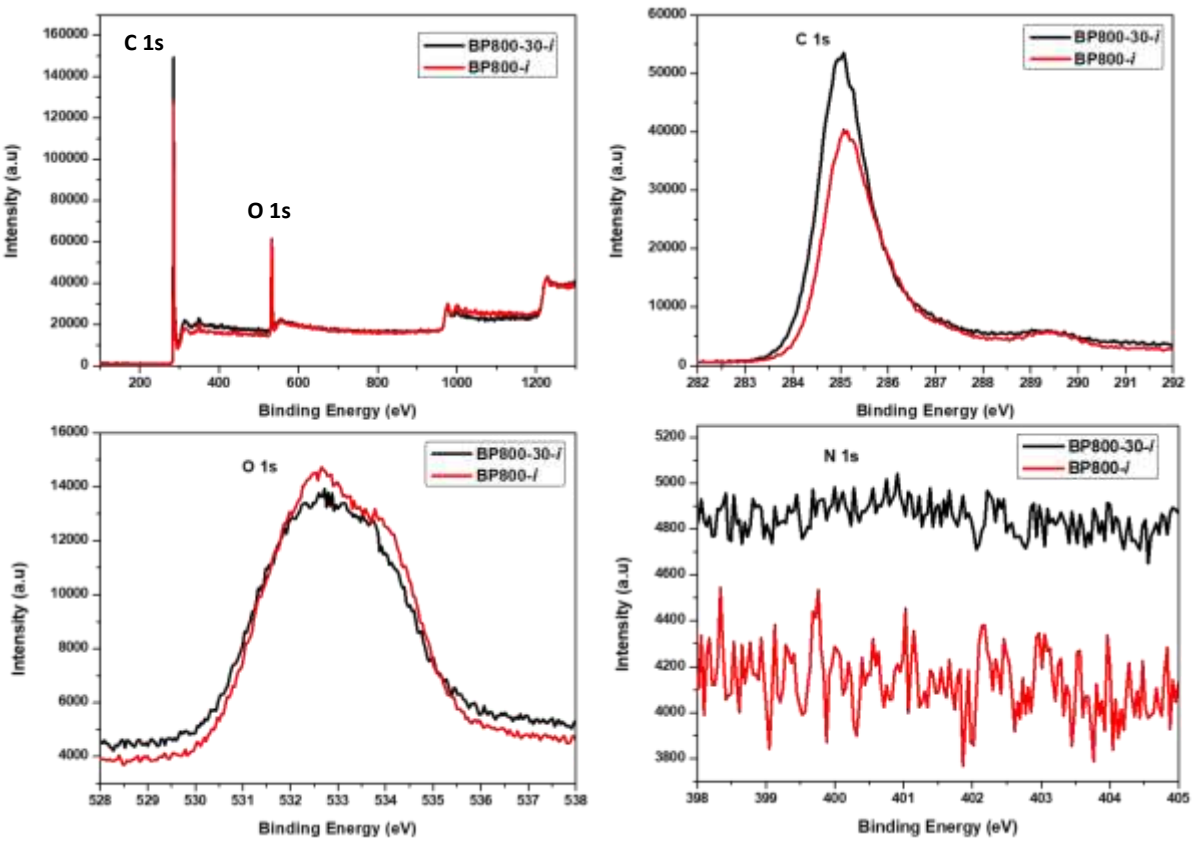


Figure 4.31: XPS analysis of heteroatom doped MWCNTs derived from tri-isopropyl borate.

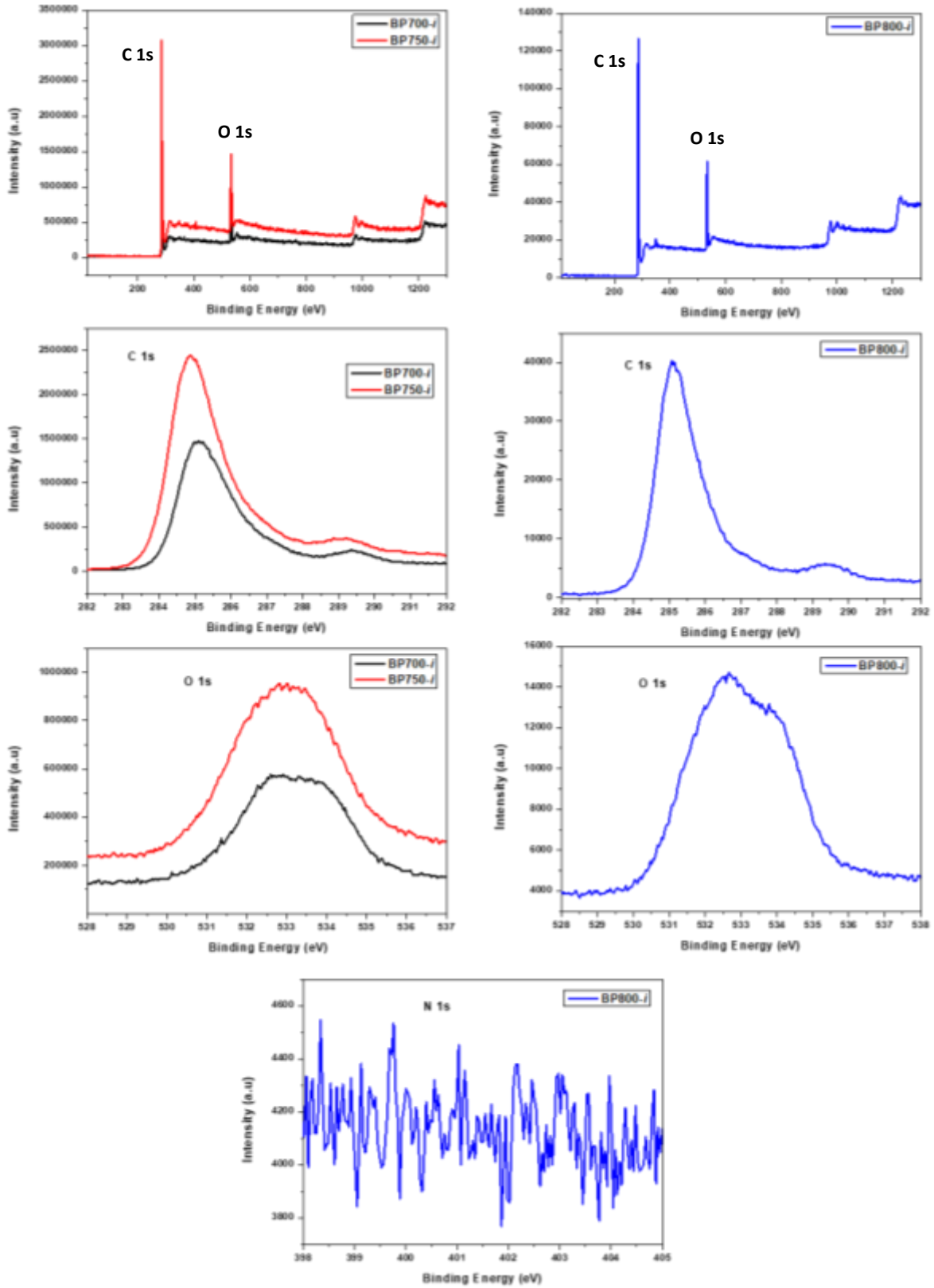


Figure 4.32: XPS analysis of heteroatom doped MWCNTs derived from tri-isopropyl borate.

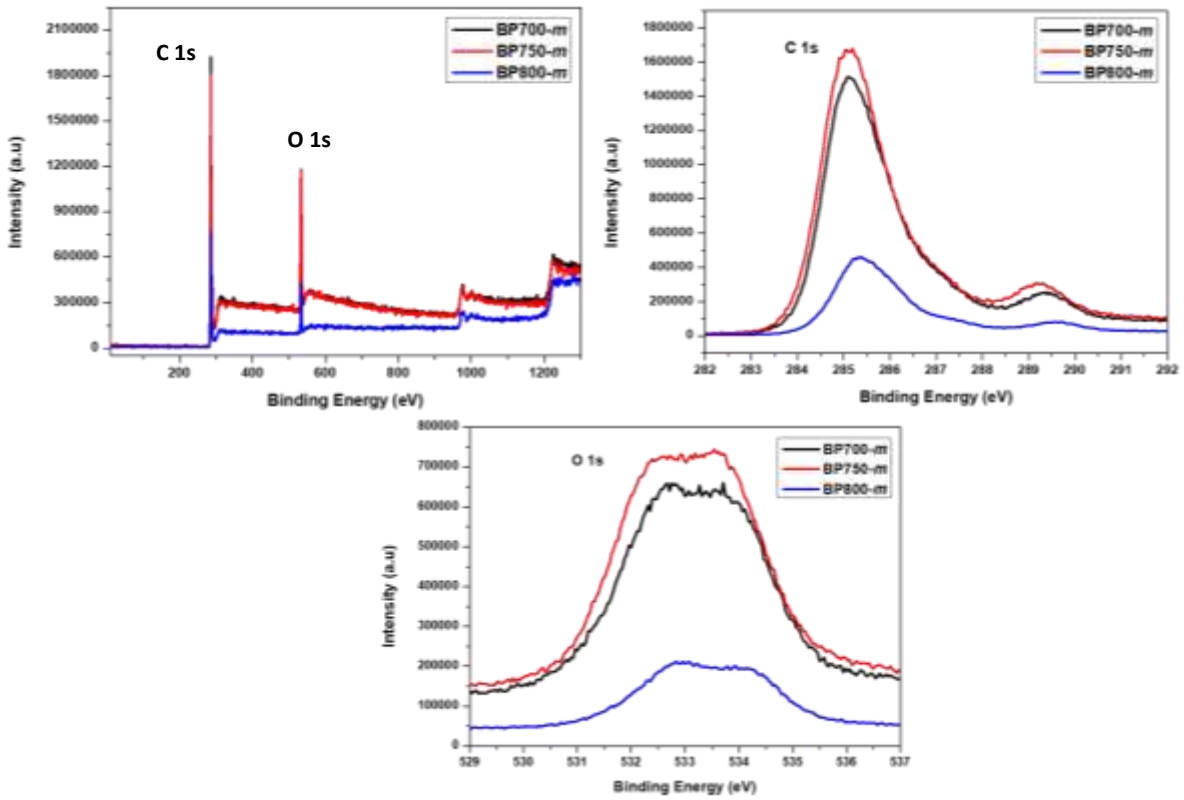


Figure 4.33: XPS analysis of heteroatom doped MWCNTs derived from trimethyl borate.

Chapter 4 References

1. X. Lu, Z. Chen. *Chemical Reviews*. 2005, **105**, 3643-3696.
2. S. Iijima, T. Ichihashi. *Nature*, 1993, **363**, 603-605.
3. E. Flahaut, R. Bacsa, A. Peigney, C. Laurent. *Chemical Communications*. 2003, 1442-1443.
4. K. P. Gong, F. Du, Z. H. Xia, M. Durstock, L. M. Dai. *Science*. 2009, **323**, 760-764.
5. H. Qi, C. Chian, J. Liu. *Chemistry of Materials*. 2006, **18**, 5691-5695.
6. S. Iijima. *Nature*. 1991, **354**, 56-58.
7. A. Szabó, C. Perri, A. Csató, G. Giordano, D. Vuono, J. B. Nagy. *Materials*. 2010, **3**, 3092-3140.
8. N. Anzar, R. Hasan, M. Tyagi, N. Yadav, J. Narang. *Sensors International.* 2020, **1**, 100003 (1-10).
9. K. Donaldson, R. Aitken, L. Tran, V. Stone, R. Duffin, G. Forrest, A. Alexander. *Toxicological Sciences.* 2006, **92**, 5-22.
10. N. Saifuddin, A. Z. Raziah, A. R. Junizah. *Journal of Chemistry.* 2012, **2013**, 676815 (1-18).
11. R. Kaur, P. Vatta, M. Kaur. *International Journal for Research in Applied Science and Engineering Technology.* 2018, **6**, 5075-5079.
12. Y. Leu, M.-H. Yeh, L.-Y. Lin, T.-J. Li, L.-Y. Chang, S.-Y. Shen, Y.-S. Li, G.-L. Chen, W.-H. Chiang, J.-J. Lin, K.-C. Ho. *ACS Sustainable Chemistry and Engineering.* 2017, **5**, 537-546.
13. M.-H. Yeh, Y.-A. Leu, W.-H. Chiang, Y.-S. Li, G.-L. Chen, T.-J. Li, L.-Y. Chang, L.-Y. Lin, J.-J. Lin, K.-C. Ho. *Journal of Power Sources.* 2018, **375**, 29-36.
14. J. Han, L. L. Zhang, S. Lee, J. Oh, K. S. Lee, J. R. Potts, J. Ji, X. Zhao, R. S. Ruoff, S. Park. *ACS Nano.* 2013, **7**, 19-26.
15. W.-H. Chiang, C.-Y. Hsieh, S.-C. Lo, Y.-C. Chang, T. Kawai, Y. Nonoguchi. *Carbon*. 2016, **109**, 49-56.
16. R. L. McCreery. *Chemical Reviews.* 2008, **108**, 2646-2687.
17. B. Wei, R. Spolenak, P. Kohler-Redlich, M. Rühle. E. Arzt. *Applied Physics Letters.* 1999, **74**, 3149-3151.
18. G. Gao, C. D. Vecitis. *ACS Applied Materials and Interfaces.* 2012, **4**, 1478-1489.

19. M. M. S. Fakhrabadi, A. Allahverdizadeh. V. Norouzifard. B. Badashzadeh. *Solid State Communications.* 2012, **152**, 1973-1979.
20. W. H. Chiang, G. L. Chen, C. Y. Hsieh, S. C. Lo. *RSC Advances.* 2015, **5**, 97579-97588.
21. G. Wang, W. Xing, S. Zhuo. *Electrochemica Acta.* 2013, **92**, 269-275.
22. O. Stephan, P. M. Ayajan, C. Colliex, P. Redlich, J. M. Lambert, P. Bernier, P. Lefin. *Science.* 1994, **266**, 1683-1685.
23. Z. Wengsieh, K. Cherrey, N. G. Chopra, X. Blaisé, Y. Miyamoto, A. Rubio, M. L. Cohen, S. G. Louie, A. Zettl, A. R. Gronsky. *Physical Review B.* 1995, **51**, 11229-11232.
24. J. Maultzsch, S. Reich, C. Thomsen, S. Webster, R. Czerw, D. L. Carroll, S. M. C. Vieira, P. R. Birkett, C. A. Rego. *Applied Physics Letters.* 2002, **81**, 2332-2335.
25. P. Redlich, M. J. Loeffler, P. M. Ajayan, J. Bill, F. Aldinger, M. Rühle. *Chemical Physics Letters.* 1996, **260**, 465-470.
26. M. Terrones, W. K. Hsu, S. Ramos, R. Castillo, H. Terrones. *Fullerene science and technology*. 1998, **6**, 787-800.
27. Y. Zhang, H. Gu, K. Suenega, S. Iijima. *Chemical Physics Letters.* 1997, **297**, 264-269.
28. K. McGuire, N. Gothard, P. L. Gai, M. S. Dresselhaus, G. Sumanesakara, A. M. Rao. *Carbon*. 2005, **43**, 219-227.
29. P. L. Gai, O. Stephan, K. McGuire, A. M. Rao, M. S. Dressselhaus. C. Colliex. *Journal of Materials Chemistry.* 2004, **14**, 669-675.
30. K. Hirahara, K. Suenaga, S. Bandow, S. Iijima. *Chemical Physics Letters.* 2000, **324**, 224-230.
31. S. Suzuki, H. Hinibo. *Carbon.* 2011, **49**, 2264-2272.
32. K. C. Mondal, N. J. Coville, M. J. Witcomb, G. Tejral, J. Havel. *Chemical Physics Letters.* 2007, **437**, 87-91.
33. P. Ayala, W. Plank, A. Grüneis, E. I. Kauppinen, M. H. Rümmeli, H. Kuzmany, T. Pichler. *Journal of Materials Chemistry.* 2008, **18**, 5676-5681.
34. S. Daothong, J. Parjanne, E. I. Kauppinen, M. Valkeapää, T. Pichler, P. Singjai, P. Alaya. *Physica Status Solidi B.* 2009, **246**, 2518-2522.
35. A. A. Koós, F. Dillon, E. A. Obraztsova, A. Crosseley, N. Grobert. *Carbon*. 2010, **48**, 3033-3041.
36. T. Watanabe, S. Tsuda, T. Yamaguchi, T. Takano. *Physica C: Superconductivity and its Applications.* 2010, **470**, S608-S609.

37. S. C. Lyu, J. H. Han, K. W. shin, J. H. Sok. *Carbon*. 2011, **49**, 1532-1541.
38. Z. Wang, C. H. Yu, D. C. Ba, J. Liang. *Vacuum.* 2007, **81**, 579-582.
39. K. C. Mondal, A. M. Strydom, R. M. Erasmus, J. M. Keartland, N. J. Coville. *Materials Chemistry and Physics.* 2008, **111**, 386-390.
40. W. Han, Y. Bando, K. Kurashima, T. Sato. *Chemical Physics Letters.* 1999, **299**, 368-373.
41. Z. N. Tetana. *Boron and nitrogen doped carbons for photochemical degradation reactions. University of the Witwatersrand.* PhD thesis; 2013.
42. S. V. Sawant, S. Banerjee, A. W. Patwardhan, J. B. Joshi, K. Dasgupta. *International Journal of Hydrogen Energy.* 2019, **44**, 18193-18204.
43. J. Zhou, P. Bai. *Asia-Pacific Journal of Chemical Engineering.* 2015, **10**, 325-338.
44. G. Parakhonskiy, N. Dubrovinskaia, E. Bykova, R. Wirth, L. Dubrovinsky. *Scientific Reports.* 2011, **1**, 96 (1-7).
45. B. C. Satishkumar, A. Govindaraj, K. R. Harikumar, J.-P. Zhang, A. K. Cheetham, C. N. R. Rao. *Chemical Physics Letters.* 1999, **300**, 473-477.
46. L. S. Panchakarla, A. Govindaraj, C. N. R. Rao. *ACS Nano.* 2007, **1**, 494-500.
47. X. Gao, W. Li, R. mei, C. Zhu, B. Zhou, L. Ma, Q. Wei, T. Liu. *Journal of Electroanalytical Chemistry.* 2019, **832**, 247-253.
48. M.-H. Yeh, L.-Y. Lin, J.-J. Li, Y.-A. Leu, G.-L. Chen, T.-C. Tien, C.-Y. Hsieh, S.-C. Lo, S.-J. Huang, W.-H. Chiang, K.-C. Ho. *Energy Procedia.* 2014, **61**, 1764-1767.
49. W. Han, Y. Bando, K. Kurashima, T. Sato. *Chemical Physics Letters.* 1999, **299**, 368-373.
50. E. Borowiak-Palen, T. Pichler, G. G. Fuentes, A. Graff, R. J. Kalenczuk, M. Knupfer. J. Fink. *Chemical Physics Letters.* 2003, **378**, 516-520.
51. W.-Q, Han, J. Cumings, X. Huang, K. Bradley, A. Zettl. *Chemical Physics Letters.* 2001, **346**, 368-372.
52. M. Bytrzejeweski, A. Bachmatiuk, J. Thomas, P. Alaya J. Serwatowski, H.-W. Hübers, T. Gemming, E. Borowiak-Palen, T. Pichler, R. J. Kaleńczuk, B. Büchner, M. H. Rümmeli. *Physica Status Solidi RRL.* 2009, **3**, 193-195.
53. D. P. Hashim, N. T. Narayan, J. M. Romo-Herrera, D. A. Cullen, M. G. Hahm, P. Lezzi, J. R. Suttle, D. Kellkhoff, E. Muñoz-Sandoval, S. Ganguli, A. K. Roy, D. J. Smith, R. Vajtai, B. G. Sumpter, V. Meunier, H. Terrones, M. Mauricio, P. M. Ajayan. *Scientific Reports.* 2012, **2**, 363 (1-8).

54. S. Wang, T. Cochell, A. Manthiram. *Physical Chemistry Chemical Physics.* 2012, **14**, 13910-13913.
55. S. Ishii, T. Watanabe, S. Ueda, S. Tsuda, T. Yamaguchi, Y. Takano. *Physica C.* 2008, **468**, 1210-1213.
56. P. Ai, M. Tan, N. Yamane, G. Liu, R. Fan, G, Yan, Y. Yoneyama, R. Yang, N. Tsubaki. *Chemistry a European Journal.* 2017, **23**, 8252-8261.
57. G. Keru, P. G. Ndungu, V. O. Nyamori. *Materials chemistry and physics.* 2015, **153**, 323-332.
58. L. Yang, S. Jiang, Y. Zhao, L. Zhu, S. Chen, X. Wang, Q. Wu, J. Ma, Z. Hu. *Angewandte Chemie International Edition.* 2011, **50**, 7132-7135.
59. Y. Xu, A. Tomita, T. Kyotani. *Journal of American society.* 2005, **127**, 8956-8957.
60. Y. Liu, L. Zhang, L. Cheng, W. Yang, Y. Xu. *Applied Surface Science.* 2009, **255**, 8761-8768.
61. E. Borowiak-Palen, T. Pichler, A. Graff, R. J. Kalenczuk, M. Knupfer, J. Fink. *Carbon.* 2004, **42**, 1123-1126.
62. Y. A. Kim, S. Aoki, K. Fujisawa, Y. I. Ko, K. S. Yang, C. M. Yang, Y. C. Jung, T. Hayashi, M. Endo, M. Terrones, M. S. Dresselhaus. *The Journal of Physical Chemistry C.* 2014, **118**, 4454-4459.
63. L. Wang, W. Guo, P. Lu, T. Zhang, F. Hou, J. Liang. *Frontiers in Chemistry.* 2019, **7**, 1-10.
64. M. Terrones, N. Grobert, H. Terrones. *Carbon.* 2002, **40**, 1665-1684.
65. M. Terrones, A. Jorio, M. Endo, A. M. Rao, Y. A. Kim, T. Hayashi, H. Terrones, J.-C. Charlier, G. Dresselhaus, M. S. Dresselhaus. *Materials Today.* 2004, 30-45.
66. S. Shiraishi, M. Kibe, T. Yokoyama, H. Kurihara, N. Patel, O. Oya, Y. Kaburagi, Y. Hishiyama. *Applied Physics A: Material Science and Processing*. 2006, **82**, 585-591.
67. D. Reznik, C. H. Olk, D. A. Neumann, J. R. D. Copley. *Physical Review B.* 1995, **52**, 116-124.
68. Ph. Lambin, A. Loiseau, C. Culot, L. P. Biŕo. *Carbon*. 2002, **40**, 1635-1648.
69. S. Amelinckx, D. Bernaerts. *Supercarbon, Synthesis, Properties and Application. Springer Series in Materials Science, Berlin: Springer.* 1998, 51-80.

70. D. K. Singh, P. K. Lyer, P. K. Giri. *Diamond and Related Materials.* 2010, **19**, 1281-1288.

71. R. Das, S. B. Abd Hamid, Md, Eaqub Ali, S. Ramakrishna, W. Yongzhi. *Current Nanoscience.* 2015, **11**, 1-14.

72. T. Vuković, M. Damnjanović, I. Milošević. *Physica E: Low Dimensional Systems and Nanostructures.* 2003, **16**, 259-268.

73. J. Majewska, B. Michalkiewicz. *Applied Physics A.* 2013, **111**, 1013-1016.

74. D. Hou, K. Li, R. Ma, Q. Liu. *Journal of Materiomics.* 2020, **6**, 628-641.

75. C. N. Barnakov, G. P. Khokhlova, A. N. Popova, S. A. Sozinov, Z. R. Ismagilov. *Eurasian Chemico-Technological Journal.* 2015, **17**, 87-93.

76. X. Mathebula. *Photocatalytic Degradation of Methyl Violet in Water using TiO_2/Cellulos-N-MWCNTs. University of the Witwatersrand.* MSc dissertation; 2018.

77. N. G. Tsierkezos, U. Ritter, Y. N. Thaha, C. Downing, P. Szroeder, P. Scharff. *Microchima*. 2016, **183**, 35-47.

78. A. Sadezky. H. Muckenhuber, H. Grothe, R. Niessner, U. Pöschl. *Carbon*. 2005, **43**, 1731-1742.

79. A. Jorio, M. A. Pimenta, A. G. S. Filho, R. Saito, G. Dresselhaus. M. S. Dresselhaus. *New Journal of Physics.* 2003, **5**, 139.1-139.17.

80. A. C. Ferrari, J. Robertson. *Physical Review B.* 2001, **64**, 075414 (1-13).

81. A. C. Ferrari, J. Robertson. *Physical Review B.* 1999, **61**, 14095-14107.

82. Z. Xing, Y. Qi, Z. Tian, J. Xu, Y. Yuan, C. Bommier, J. Lu, W. Tong, D. Jiang, X. Ji. *Chemistry of Materials.* 2017, **29**, 7288-7295.

83. S. O. Ibrahim, K. U. Isah, A. S. Abdulkareem, U. Ahmadu, J. O. Tijani, W. D. Ross. *Journal of Material Science: Materials in Electronics.* 2020. DOI: https://doi.org/10.1007/s10854-020-03550-0

84. M. S. Dresselhaus, A. Jorio, M. Hofmann, G. Dresselhaus, R. Saito. *Nano Letters.* 2010, **10**, 751-758.

85. M. S. Dresselhaus, G. Dresselhaus, M. Hofmann. *Philosophical Transactions of the Royal Society.* 2008, **366**, 231-236.

86. L. M. Malard, M. A. Pimenta, G. Dresslhaus, M. S. Dresselhaus. *Physics Reports.* 2009, **473**, 51-87.

87. S. Santangelo, G. Messina, G. Faggio, M. Lanza, C. Milone. *Journal of Raman Spectroscopy.* 2011, **42**, 593-602.

88. R. A. Dileo, B. J. Landi, R. P. Raffaelle. *Journal of Applied Physics.* 2007, **101**, 064307 (1-5).

89. S. Santangelo, M. Dhanagopal, G. Faggio, G. Messina, A. Pistone, M. Lanza, C. Milone. *Diamond and Related Materials.* 2010, **19**, 599-603.

90. Z. N. Tetana, S. D. Mhlanga, G. Bepete, R. W. M. Krause, N. J. Coville. *South African Journal of Chemistry.* 2012, **56**, 39-49.

91. B. J. Landi, C. D. Cress, C. M. Evans, R. P. Raffaelle. *Chemistry of Materials*. 2005, **17**, 6819-6834.

92. Z. J. Shi, Y. F. Lian, F. H. Liao, X. H. Zhou, Z. N. Gu, Y. Zhang, S. Iijima, H. D. Li, K. T. Yue, S. L. Zhang. *Journal of Physics and Chemistry of Solids.* 2000, **61**, 1031-1036.

93. J. W. Chiang, B. E. Brinson, A. Y. Huang, P. A. Willis, M. J. Bronikowski, J. L. Margrave, R. E. Smalley, R. H. Hauge. *Journal of Physical Chemistry B.* 2001, **105**, 8297-8301.

94. J. H. Lehman M. Terrones, E. Mansfield, K. E. Hurst, V. Meunier. *Carbon.* 2011, **49**, 2581-2602.

95. H. Li, N. Zhao, C. He, C. Shi, X. Du, J. Li. *Materials science and Engineering A.* 2008, **473**, 355-359.

96. G. S. B. McKee, C. P. Deck, K. S. Vecchio. *Carbon.* 2009, **47**, 2085-2094.

97. A. Peigney, Ch, Laurent, E. Flahaut, R. R. Bacsa, A. Rousset. *Carbon.* 2001, **39**, 507-514.

98. Z. Li, E. Dervishi, Y. Xu, V. Saini, M. Mahmood, O. D. Oshin, A. R. Biris. A. S. Biris. *Catalysis Letters.* 2009, **131**, 356-363.

99. D. Y. Kim, C. M. Yang, Y. S. Park, K. Kim, S. Y. Jeong, J. H. Han, Y. H. Lee. *Chemical Physics Letters.* 2005, **413**, 135-141.

100. P. Ruz, S. Banerjee, M. Pandey, V. Sudarsan, P. U. Sastry, R. J. Kshirsagar. *Solid State Sciences.* 2016, **62**, 105-111.

101. S. D. Mhlanga, K. C. Mondal, R. Carter, M. J. Witcomb, N. J. Coville. *South African Journal of Chemistry.* 2009, **62**, 67-76.

102. T. P. Mofokeng, Z. N. Tetana, K. I. Ozoemena. *Carbon.* 2020, **169**, 312-326.

103. R. Al-Jishi, G. Dresselhaus. *Physical Review B.* 1982, **26**, 4514-4522.

104. T. Jawhiri, A. Roid, J. Casado. *Physical Review B.* 2000, **61**, 14095

Chapter 5: The synthesis of Boron-Nitrogen Co-doped MWCNTs.

5.1. Introduction

The utility and significance of CNTs in nanotechnology has been studied at length since their discovery. This has in part being driven by their physicochemical modification leading significant alteration of their structural, chemical, and electronic properties i.e., imparts them with novel properties. It followed that their modification led to an expansion and diversification of their application in diverse technologies. Heteroatom doping using nitrogen and boron has been at the centre of this work.[1-15] The substitution of carbon atoms with nitrogen can produce n-type CNT based semiconductors with enhanced electrical conductivity. This is attributed to the shifting of the Fermi level of the pristine carbon nanomaterial closer to the conduction band following N-incorporation. This effect reduces the work function of the CNT.[16-20] The incorporation of boron may produce p-type CNT conductors that possess improved conductivity resulting from either a creation of an acceptor level by the boron atoms below the Fermi-level,[21] the shift of the Fermi-level with varying boron concentration,[22] or multi-mode conduction[23] (i.e., ballistic, ohmic conduction) across the material. However, after boron doping the opposite effect on conductivity has also been observed.[24] The incorporation of either heteroatom affects other properties such as thermal stability[25-26], stiffness[27-28], biocompatibility[29-30], efficiency in oxidation reduction reactions[31-32] e.t.c.

Since individual heteroatom doping with nitrogen and boron offer such great versatility in tuning the electron states within the forbidden band, it is essential to consider what their simultaneous incorporation into the CNT structure might yield. To the best of our knowledge not much research has gone into simultaneous B and N doping (i.e., substitution of C), but existing research has indicated synergistic effects from boron and nitrogen co-doped carbon materials.[33-39] Zhou and co-workers produced boron and nitrogen co-doped CNTs that were used as a support for Pt in the oxidation of methanol. They reported high electrocatalytic activity coupled with improved durability. Furthermore, a high CO anti-poisoning ability was observed relative to Pt/C. These effects were attributed to the combination of the fast electron transfer from the carbon to nitrogen atoms, and the increased number of adsorption sites provided by boron in the material. Boron also provides superior promoting abilities for the electrochemical reactions.[40-46]

Additionally, Zhang *et al* synthesized highly porous and large pore volume boron nitrogen co-doped CNTs with high boron (15.05%) and nitrogen (6.71%) content. They tested the material for use in lithium-ion batteries as an anode; the material was found to have high capacity, good capacity retention, high coulombic efficiency, and cyclic performance. Their work also suggests that their high porosity and large pore volume of the carbon made them a viable candidate for other applications such as hydrogen storage.[47] This was corroborated by work reported by Sawant *et al* using a material with much lower nitrogen (1.34%) and boron (1.5%) content for hydrogen storage.[48] He *et al* investigated the use of boron nitrogen co-doped CNTs for the reduction of oxygen. The material registered better catalytic activity than pristine, nitrogen doped, and boron doped CNTs by promoting a 4-electron oxygen reduction reaction and resulting in a high current exchange density.[49] However, the use of this technique has also been shown to convert some CNTs with metallic behaviour to semiconductors.[50]

The addition of nitrogen and boron independently into the structure of CNTs induces varying behaviour, the dual incorporation clearly offers an opportunity to combine both behaviours to produce a material with superior qualities. However, there are still challenges associated with the production of boron and nitrogen co-doped CNTs. This include the addition of nitrogen and boron onto sites that minimize or eliminate the formation of boron-nitrogen bonds, as these tend to reduce the ability of the atoms to activate the carbon -system.[51-52] In some cases, this leads to negative effects such as loss in electrocatalytic activity.[53-57] The boron and nitrogen tend to co-exist in two ways in the sp^2 carbon structure; bonded together (B-N) or separately (B-C-N). Both cases are reported to yield different electronic structures, and in particular, different conjugation effects in the π-system. When they co-exist in their bonded state, the vacant boron orbitals neutralize the lone pair of electrons on the nitrogen. Consequently, this leaves fewer lone pairs of electrons and vacant orbitals to activate or conjugate with the π-system. Thus, the material's behaviour closely resembles the inert undoped CNTs, particularly when the concentrations of both nitrogen and boron content increases in the material. This indicates that it is not only the position of the nitrogen and boron atoms that is significant, but also the distance between them in the carbon π-system. When the atoms co-exist in their separated configuration, their ability to conjugate with the carbon π-system is not impeded by the neutralization, thus they are able to initiate electron transport in the material.[25, 58-64]

As a result, the synthetic methods for boron nitrogen co-doped CNTs require careful consideration. There are two general approaches that have been utilized for their production, each provides varying control in the type of boron nitrogen configuration that will result in the

material. (i) A two-step process that involves synthesizing either pristine CNTs, boron doped CNTs and nitrogen doped CNTs, followed by doping with nitrogen and/or boron. This may involve the use of a precursor with the dual function as a source of nitrogen and boron dopants in pristine CNTs. This precursor may be prepared from independent boron and nitrogen sources or may 'naturally' contain both nitrogen and boron in their chemical structure. For example, Ma *et al* used $B_4N_3O_2H$ powder for the co-doping of MWCNTs at 1700℃ using the CVD method.[65] While Iyyamperumal *et al* prepared boron nitrogen co-doped MWCNTs using melamine diborate prepared from melamine and boric acid, as a boron-nitrogen source in the CVD method at 1000℃.[66] However, it may also involve treating nitrogen doped CNTs with a boron source or vice versa. Han and co-workers produced boron nitrogen co-doped MWCNTs by treating nitrogen doped MWCNTs with B_2O_3 at 1260℃ under Ar/N_2 atmosphere using the CVD method.[67] (ii) The second approach involves a direct one step synthesis. Aerosol based CVD method (900-1100℃) was utilized by Koós *et al* in the fabrication of boron nitrogen co-doped MWCNTs using a solution of triphenyl borane and benzyl amine in toluene.[68] While Zhang and co-workers used a single source for boron and nitrogen, the versatile and non-toxic NH_3BH_3 to produce boron-nitrogen co-doped MWCNTs in a single step.[47]

In order to leverage the potential benefits of incorporating both nitrogen and boron to the lattice structure, our work utilized the first approach to produce boron-nitrogen co-doped MWCNTs. Boron doped MWCNTs were produced in a one-step CVD method and then were doped with nitrogen. Furthermore, nitrogen doped MWCNTs were also synthesized and then treated with boron precursors to obtain the desired material. This approach was chosen to be able to compare samples doped with one element with the co-doped samples. This approach was chosen for comparison of two step single element doped CNTs to those co-doped with boron and nitrogen.

5.2. Materials and Methods

5.2.1. Starting material.

Acetonitrile (99.9 %), trimethyl borate (98%), tri-isopropyl borate (98%), and 55% nitric acid (HNO_3) were purchased at Sigma Aldrich South Africa and used as purchased. Distilled water was used for all the experiments and washings. The gases ethylene (C_2H_2) and nitrogen (N_2) were supplied by Afrox South Africa.

5.2.2. Synthesis of boron nitrogen co-doped MWCNTs.

All the material in this chapter were produced using the *post doping* method. Two general methods were developed; (i) boron doped MWCNTs with the highest thermal stability reported in **chapter 4** from the temperature and source dependant studies were treated with acetonitrile to incorporate nitrogen into the material. (ii) Nitrogen doped MWCNTs were initially produced using acetonitrile as a nitrogen source, and the obtained N-doped MWCNTs were treated with either trimethyl borate or tri-isopropyl borate.

Method A:

The two boron-doped material prepared at 750℃ and 700℃ using trimethyl borate and tri-isopropyl borate, respectively, were each (100 mg) placed on a quartz boat in a tubular quartz tube that was inserted into a horizontal furnace and connected to a N_2 (240 sccm) gas line. The B-N-doped MWCNTs were obtained by increasing the temperature of the furnace (10℃/min) to the desired temperature of 800℃ under a N_2 atmosphere. The N_2 gas was bubbled through a boron source into to the reaction chamber for 1 h once the required temperature was reached. The reaction was cooled down to room temperature using compressed air, and the boat containing a black solid of MWCNTs was retrieved and placed into a sample vial.

Method B:

10 % Fe-Co/$CaCO_3$ (300 mg) [*Catalyst A* **chapter 3, Section 3.2.1 method B**] was placed on a quartz boat in a tubular quartz tube that was inserted into a horizontal furnace. The quartz tube was connected to N_2 and C_2H_2 gas lines. The N_2 gas (240 sccm) and C_2H_2 (90 sccm) gases were bubbled through acetonitrile into the reaction chamber for 1 h, at the set point temperature (800℃). The reaction was cooled down to room temperature using compressed air. The boat containing a black solid of MWCNTs was retrieved and the product collected. The obtained N-doped sample and an excess of HNO_3 (55%) were added to a round bottom flask and left stirring under reflux at 110℃ for 4 h. The resulting solution was left to cool to room temperature. The cooled solution was diluted with water, filtered, and washed until the filtrate had a neutral pH. The obtained black solid was left to dry in an oven at 100℃ for 12 h in an oven.

The obtained nitrogen doped MWCNTs (100 mg) were placed in a quartz boat in a tubular quartz tube inserted into a horizontal furnace and connected to a N_2 (240 sccm) gas line. The N_2 gas was bubbled through a boron source into the reaction chamber for 1 h once the required

temperature of 800℃ was reached with a heating rate of 10 ℃/min. The reaction was cooled down to room temperature using compressed air after an hour. The boat containing a black solid of MWCNTs was retrieved and the product collected.

5.2.3. Characterization techniques

The morphology of the materials was investigated using the scanning electron microscope (SEM, ZEISS SIGMA 03-30 FESEM instrument). The structural characteristics were studied by Raman spectroscopy using a 514.5 nm laser line generated from an argon ion laser. The powder x-ray diffraction (PXRD) analysis performed on a Bruker D2 phaser with a nickel filtered copper radiation = 0.15406 nm was also used for structural determinations and assessing the purity of the samples. The Brunauer, Emmet, and Teller (BET) method via N_2 adsorption under isothermal conditions (-196℃, using liquid nitrogen) on a Micromeritics TriSta 3000 instrument was used to determine the surface area, pore volumes and sizes of the material. The thermal properties of the materials were investigated over a temperature range 35-900 under an atmosphere of air (20 ml/min) using the PerkinElmer TGA4000 instrument.

5.3. Results and discussions

5.3.1. Synthesis of boron-nitrogen co-doped MWCNTs from nitrogen doped MWCNTs using tri-isopropyl borate as a boron source.

Nitrogen doped (N-doped) MWCNTs were prepared using acetonitrile as a nitrogen source via the CVD method over a Fe-Co/$CaCO_3$ at 800℃. Boron doped MWCNTs (BP800-*i*) were also produced under the same conditions using tri-isopropyl borate as a boron source. Both samples were treated with HNO_3 for the removal of catalyst residue, and functionalization of the nanotubes, respectively. 100 mg of the N-doped sample was treated further with tri-isopropyl borate at 800℃ (using a CVD set up) for the addition of boron to the nanotube lattice. The yields (Table 5.1) of the N-doped and B-doped samples were calculated using equation 5.1:

$$\text{Carbon yield (\%)} = \frac{\text{M}_{\text{obtained from reaction}}}{density\ of\ carbon\ source \times flow\ rate \times reaction\ time} \times 100 \quad \text{..... (5.1)}$$

The yield of the B- and N-co-doped (BN800) was determined using the equation below:

$$\text{Yield (\%)} = \frac{M_{final}}{M_{initial}} \quad \text{..... (5.2)}$$

where $M_{initial}$ is the mass of the MWNCTs used in the reaction (100 mg) and M_{final} the mass of sample collected after the reaction.

Table 5.1: Yield (%) of N-doped, B-doped and B-N co-doped MWNCNTs

Sample	Total mass (g)	Yield (%)
NP800	3.867	65.6
*BP800-*i*	1.585	26.9

XRD analysis (**Figure 5.1**) of the N-doped (NP800) and B-doped (BP800-*i*) materials revealed the characteristic peaks resulting from the 002 (~26°), 100 (~43°) and 101 (~44-45°) carbon graphitic planes. However, the XRD data also revealed that the complete removal of the catalyst residue was unsuccessful, and only a decrease in its concentration was observed. The XRD pattern (**Figure 5.1**) of the obtained material (NB800) exhibited the characteristic carbon graphitic peaks, a minute downward shift in the 002-peak relative to the nitrogen doped MWCNTs was observed.

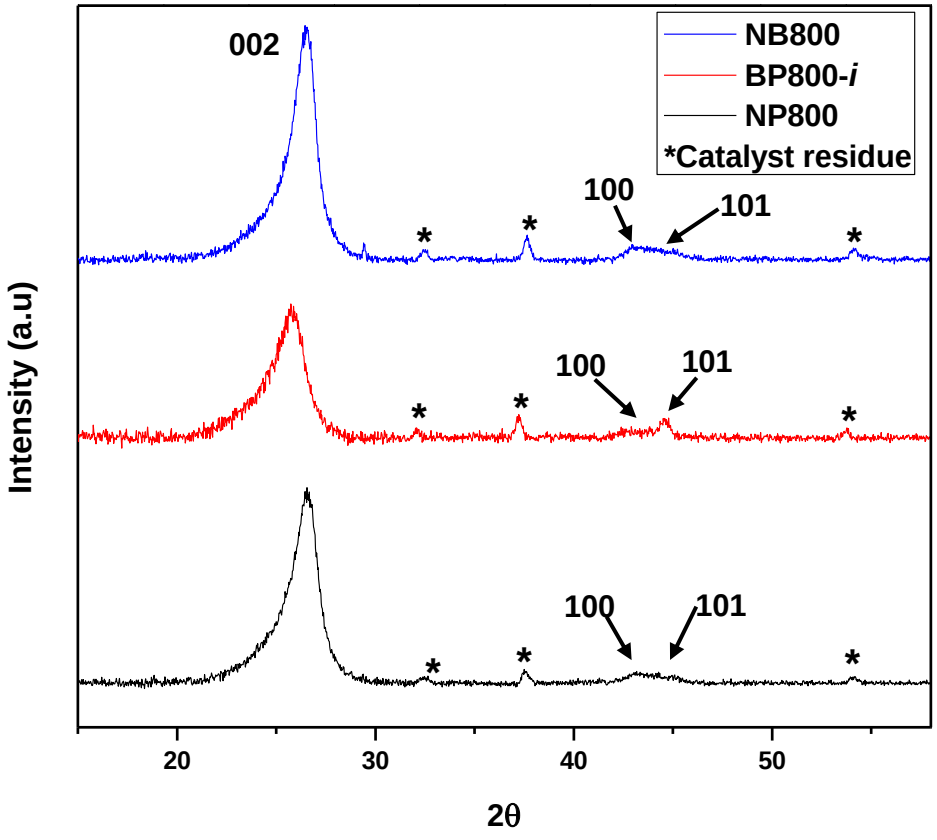


Figure 5.1: XRD pattern of N-doped, B-doped and B-N co-doped MWCNTs

The asymmetry/broadening of the 002-peaks was more prominent for BP800-*i* than NP800 and NB800 (consistent with the broadening factor FWHM, see Table 5.2), but NB800 presented with a slightly narrower peak (i.e., better crystallinity) than NP800. This may have been due to the graphitizing effect of boron,[69-71] however, given that the NP800 sample was heated to 800℃, an unintentional annealing process which led to better crystallinity through the removal of functional groups and amorphous carbon might have occurred. The 002 peaks were deconvoluted using a Voigt spectral function (**Figure 5.2**). Peak 2 was used to determine the interlayer spacing (d-spacing) using the Bragg equation (Table 5.2). A slight increase in the d-spacing was observed after the N-doped sample was treated with tri-isopropyl borate, .[69, 70, 72-74]

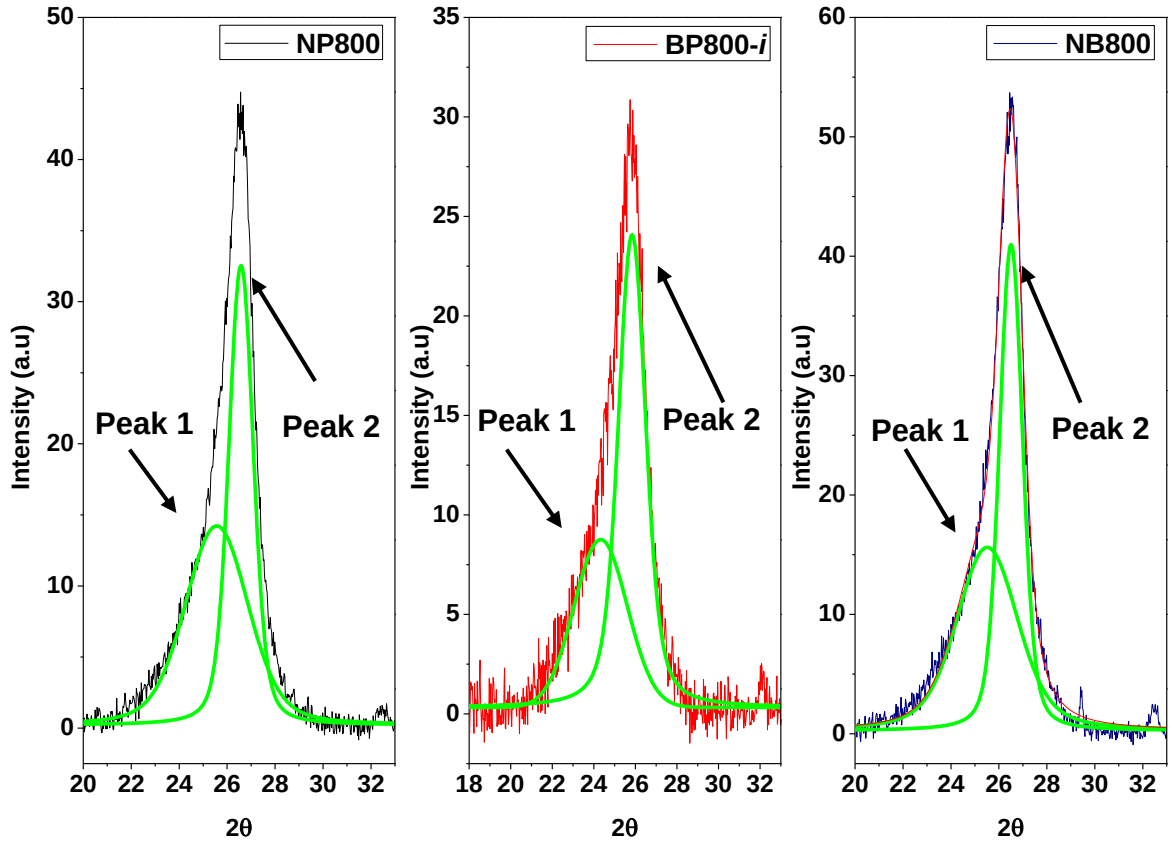


Figure 5.2: XRD spectra of purified N-doped, B-doped, co-doped MWCNTs deconvoluted 002 peaks using Voigt spectral function.

Table 5.2: The crystallite size and d-spacing of MWCNTs.

Sample code	002 plane peak position (°)	FHWM (°)	d_{002} (Å)
NP800	26.58	0.9998	3.351
BP800-*i*	25.83	1.145	3.446
NB800	26.50	0.9404	3.361

The structural features and crystallinity of the material were investigated using Raman analysis (**Figure 5.3**, full data listed in **Appendix 5A** Table 5.8), all three samples exhibited the *D* and *G* bands resulting from the presence of graphitic carbonaceous material. The characteristic *D* and *G* bands arise from the A_{1g} symmetry forbidden breathing mode (results from disorder in the material) and E_{2g} from vibrations of sp^2 hybridized carbon atoms, respectively.[47-48, 75-78] The bands had multiple components that could be isolated by using different spectral fitting models, four peak or 5 peak models have been used to fit and isolate components in these bands.[79-81] Samples BP800-*i* and NB800 were deconvoluted using a 5-peak model and a Lorentzian function, however, with NP800 neither the 5 nor 4 peak models were successful in isolating (i.e., produce a good fit of the data) the components. This is because the asymmetry observed in the *G* band appeared to have more than 2 components, so a 6-peak model (Lorentzian function) was adopted from the work reported by Singh *et al.*, where they isolated an additional band (M band) attributed to the presence of material exhibiting metallic behaviour.[82] The presence of the M band is consistent with literature reports indicating that N-doped CNTs can exhibit metallic behaviour.[76, 83-85] The other isolated components D_1, D_2 and D' arise from disordered graphitic lattice of the A_{1g} symmetry, amorphous carbon and disorder on the surface graphene layers from the E_{2g} vibrational mode, respectively.[77-78, 82] A downward shift in the *D* band of NP800 from 1355 cm^{-1} to 1351 cm^{-1} (NB800) was observed after treatment with tri-isopropyl borate, the resulting Raman shift was comparable to that of BP800-*i* (1350 cm^{-1}). A similar trend was observed for the Raman shift of the *G* band, a downward shift from 1587 cm^{-1} to 1576 cm^{-1}.

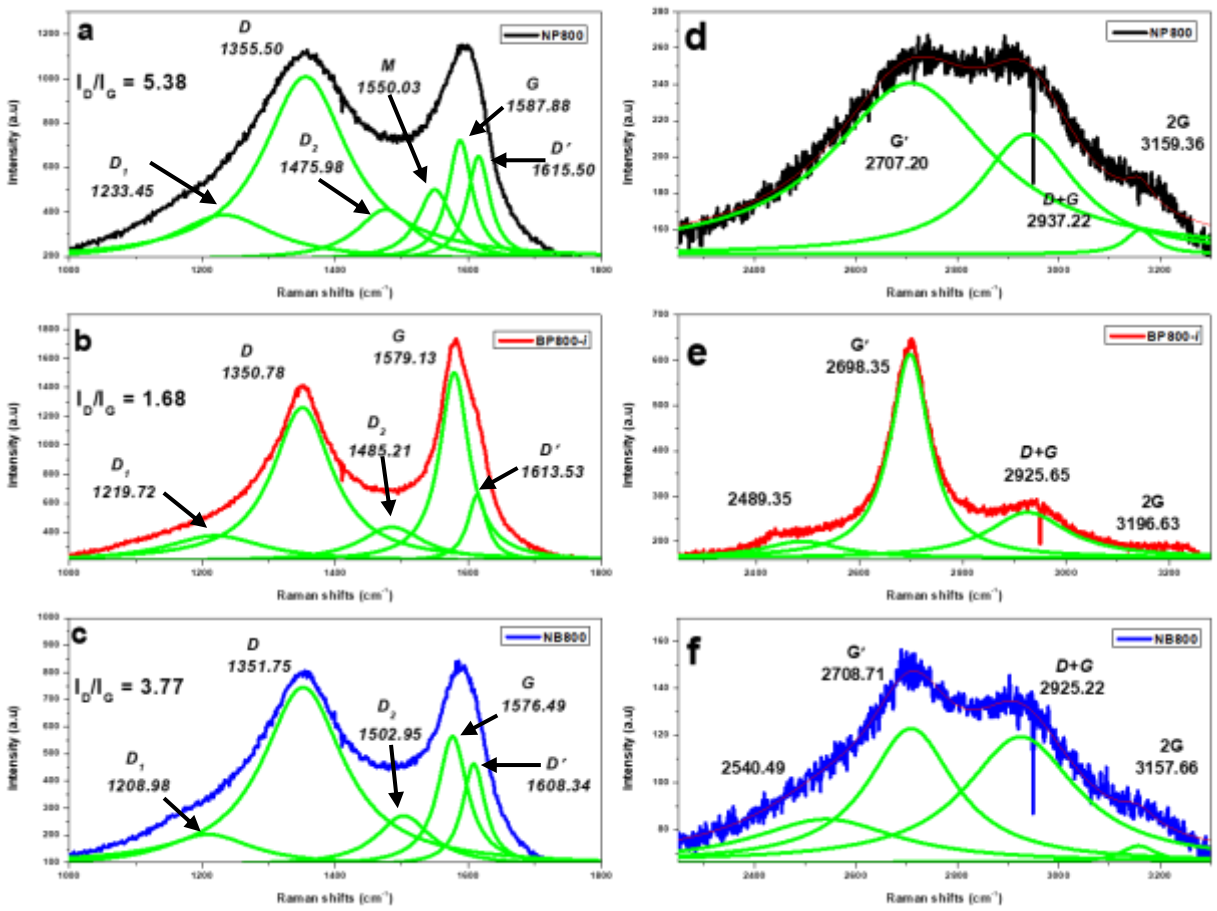


Figure 5.3: Spectra of N-doped, B-doped and B-N co-doped MWCNTs (*a-c*) 1st order Raman Lorentzian fitted peaks, (*d-f*) 2nd order Raman Lorentzian fitted peaks.

The R-coefficient (I_D/I_G) was determined from the area of the *D* and *G* bands (R-coefficient calculated from the intensity also listed in **Appendix 5A Table 5.8**), NP800 reported a high I_D/I_G ratio indicating a high concentration of defects resulting from the functionalization process and addition of nitrogen to the lattice structure. Treatment with the boron source resulted in the reduction of the I_D/I_G ratio. The observed graphitization can be attributed to two factors; the removal of functional groups due to the unintended annealing process the material underwent prior to exposure to the boron source. It may also signal the successful addition of boron to the lattice structure, as boron is known to have a graphitization effect on CNT material.[69-71] In addition, a downward shift in the *D* band was observed relative to the N-doped MWCNTs. The absence of the M band in NB800 also suggested a successful incorporation of boron in the lattice structure, leading to a loss on metallic behaviour of MWCNTs in the sample. The 2nd order region of the spectra (**Figure 5.3e-g**) presented with 4 bands resulting from the overtone of the D-band which arises from a double resonance process. The *G´*, *D+G* and *2G* bands are attributed to the *2D*, $2E_{2g}$ and $D+E_{2g}$ frequency modes, respectively, these bands

were fitted using a Lorentzian function.[47-48, 77-78, 82] The ratio of the area of the *G'* to the *D* band ($I_{G'}/I_D$, listed in **Appendix 5A** Table 5.8) gives information about the overall crystallinity of the material, and the ratio of the *G'* to the *G* band ($I_{G'}/I_G$, listed in **Appendix 5A** Table 5.8) gives information about the long-range order of the material .[86-88] The $I_{G'}/I_D$ and $I_{G'}/I_G$ of the NP800 sample increased from 0.29 to 0.12 and 1.44 to 0.47, respectively, after treatment with tri-isopropyl borate. This could be attributed to a combination of the annealing during the reaction and a successful incorporation of boron in the lattice structure of the N-doped MWCNTs.

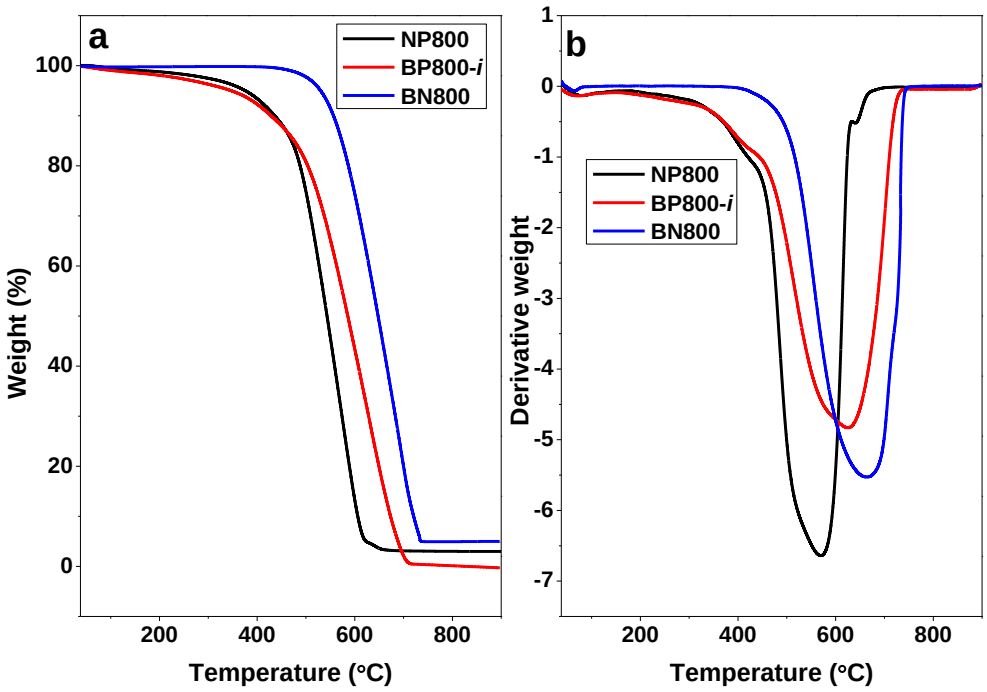


Figure 5.4: a) TG analysis of N-doped (black), B-doped (red) and B-N co-doped (blue) MWCNTs, b) derivative curve of N-doped, B-doped and B-N co-doped MWCNTs.

The thermal properties of the samples were investigated using TG analysis (**Figure 5.4**), NP800 had the lowest thermal stability, followed by BP800-*i*. The treatment of NP800 with tri-isopropyl borate resulted in material (NB800) with higher thermal stability than both samples. The oxidation of the MWCNTs was observed at 575℃ and 625℃ for NP800 and BP800-*i*, respectively. While the co-doped sample presented with the highest oxidation temperature of 675℃. The first weight loss from 200-450℃ attributed to the removal of functional groups and oxidation of amorphous carbon was observed only for the N-doped and B-doped samples.[76, 89-90] This corroborated that NP800 was annealed before being exposed to the boron source, which

indicated that the graphitizing effect of boron may have not been the only contributing factor to the improved thermal stability and consequently the crystallinity of the material.

Table 5.3: BET Surface area data of N-doped, B-doped and nitrogen-boron co-doped MWCNTs.

Sample	Surface area (m^2/g)	Pore volume (cm^3/g)	Pore size (nm)
NP800	21.1	0.0872	21.65
BP800-*i*	23.9	0.1539	28.36
NB800	2.6	0.0421	79.66

A substantial decrease in the surface area and pore volume for the N-doped MWCNTs were reported after treatment with tr-isopropyl borate obtained, but the pore size increased by 3-folds. The surface area, pore volume, and pore size of NP800 was found to be comparable to those reported by Tetana *et al.*[76]

Table 5.4: Atomic % of heteroatom doped MWCNTs

Sample		C 1s	O 1s	N 1s	B 1s
NP800	Position (eV)	284.20	532.76	401.07	--
	Atomic %	80.45	18.54	0.97	--
BP800-*i*	Position (eV)	285.74	532.75	399.71	--
	Atomic %	85.50	14.34	0.16	--
NB800	Position (eV)	285.68	532.71	400.76	192.77
	Atomic %	92.28	5.98	0.25	0.79

XPS analysis (**Figure 5.5,** Table 4.4) was used to assess the atomic composition of each sample. The successful synthesis of N-doped MWCNTs (NP800) was corroborated by the presence of nitrogen at 0.97%. A decrease in the atomic % of nitrogen to 0.25% prior to treatment with tri-isopropyl borate was observed. In addition, a successful incorporation of boron at 0.79% was also reported for the resulting sample (NB800). The decrease in nitrogen could be attributed to the loss of nitrogen at the high reaction temperatures or through its substitution by boron.

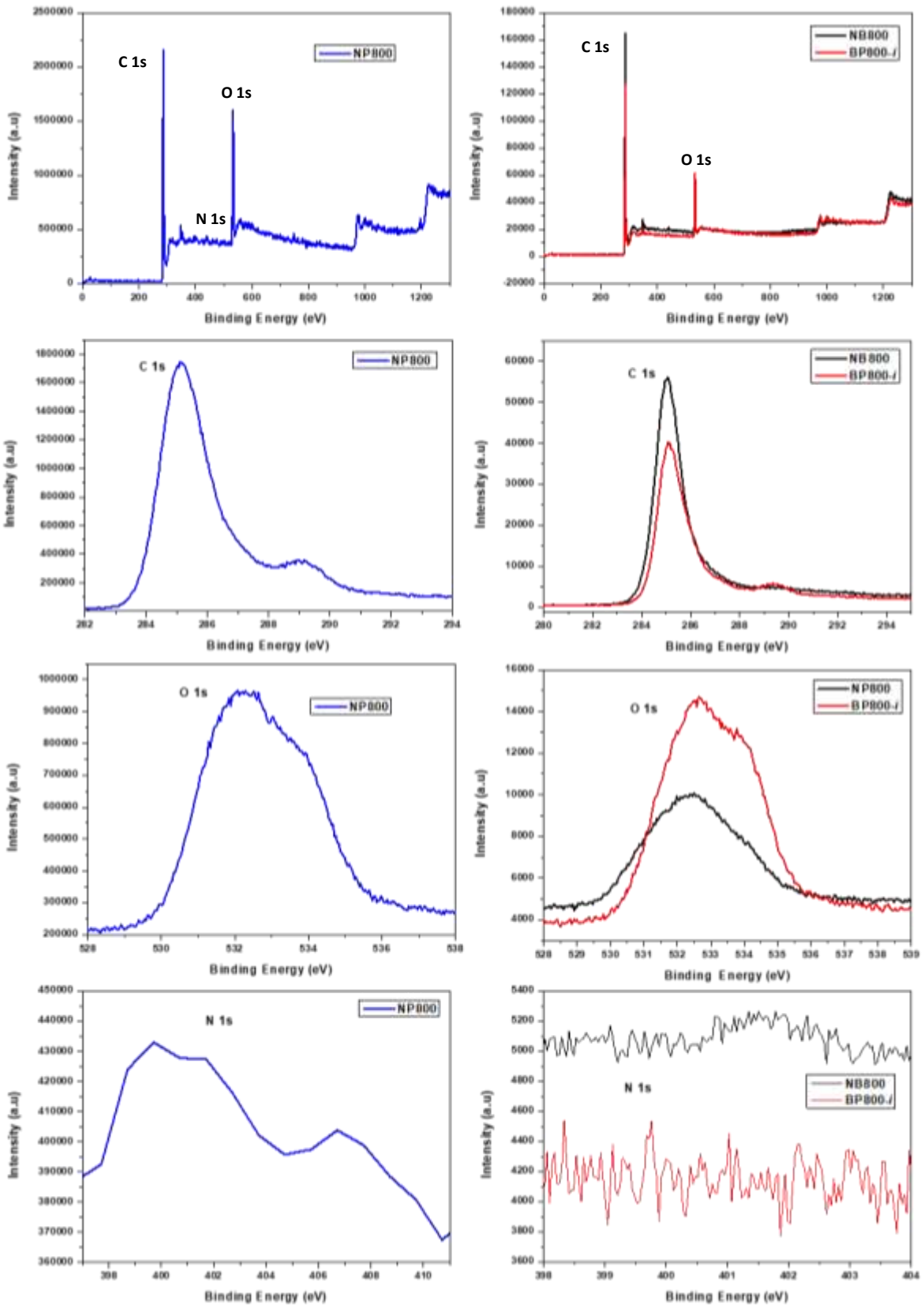


Figure 5.5: XPS analysis of samples NP800, BP800-*i*, and NB800.

The use of tri-isopropyl borate in the synthesis of B-doped MWCNTs was found to produce pristine MWCNTs, as evidenced by the absence of boron in the XPS profile of sample BP800-*i*. Each signal in the XPS spectra of the NB800 sample were investigated more closely by isolating components associated with the different bonding modes of each atom (**Figure 5.6**). Peak fitting performed on the B 1s signal revealed that boron was present in two bonding modes, B-N (191.6 eV) and B-O-C (192,5 eV), it was also found to exist as B_2O_3 (193.5 eV). Although the B-N bonding mode is reported in the same region as the BCO_2, the absence of B-C bonding configuration in the C 1s peak (expected at 282 eV) suggests that the peak at 191.6 eV was due to B-N bonding (Left hand side of the shoulder of the major peak). In addition, peak fitting of the N 1s and O 1s signal corroborated the presence of the B-N (398.2 eV) and B-O (532.4 eV) bonding configurations, respectively.

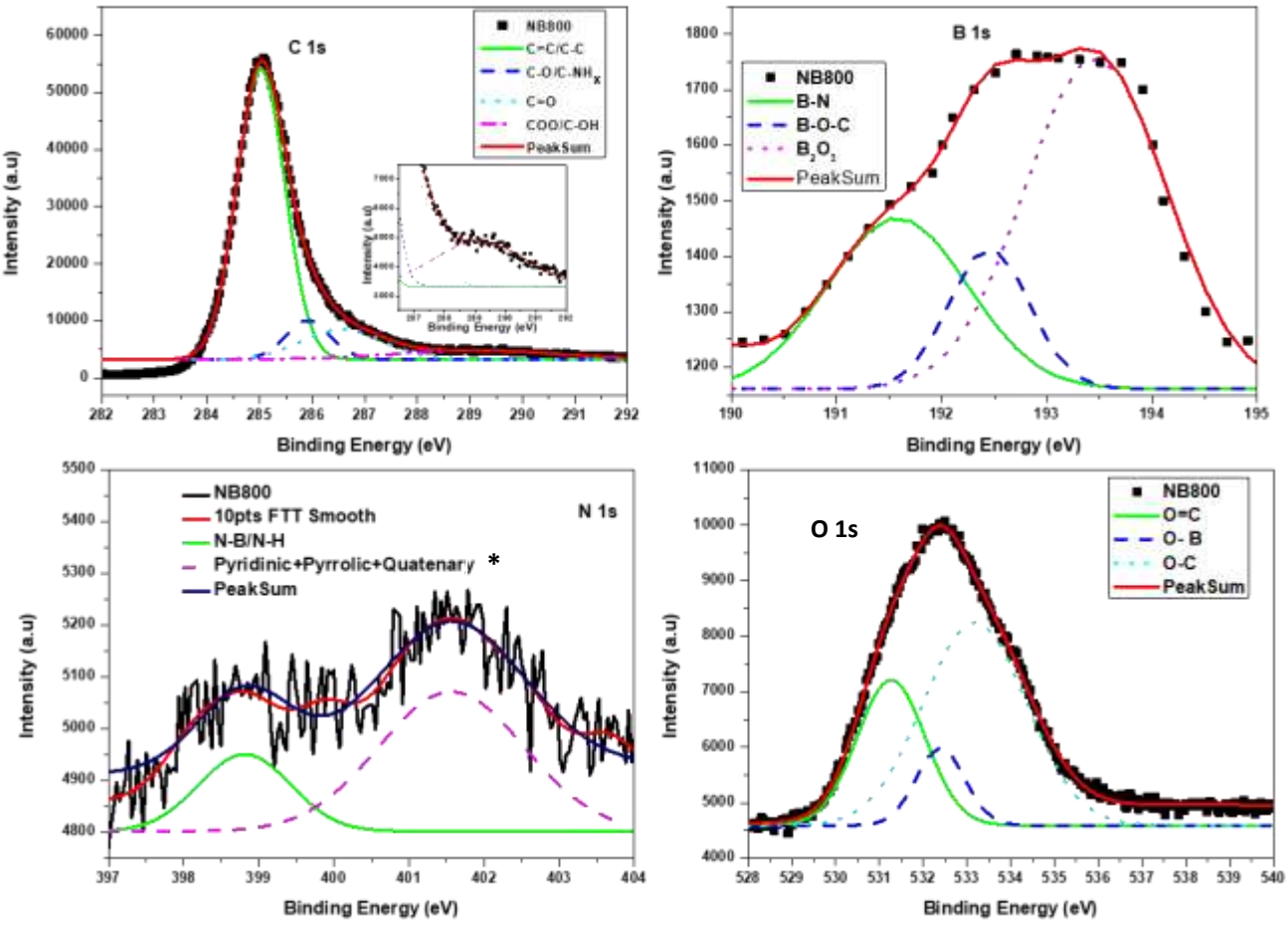


Figure 5.6: XPS fitted peaks of boron-nitrogen co-doped MWCNT (NB800). *See bonding configuration in **Appendix 5A, Figure 5.14**.

5.3.2. Synthesis of boron-nitrogen co-doped MWCNTs from tri-isopropyl borate and trimethyl derived B-doped MWCNTs.

The boron doped samples used in this study were selected from the reaction temperature (700 and 750℃) and boron source study from **chapter 4**. A post doping process was chosen to incorporate nitrogen into the lattice structure of the B-doped MWCNTs at 800℃. Thus, it was essential to consider the thermal stability of the B-doped samples used in this study to mitigate any significant loses of the B-doped material due to thermal degradation in the process of the reaction. Hence, B-doped MWCNTs with the highest thermal stability, synthesized at 700℃ (BP700-*i*) and 750℃ (BP750-*m*) using tri-isopropyl borate and trimethyl borate, respectively, were used in this study. The chosen samples BP700-*i* and BP750-*m* (100 mg) were treated with acetonitrile at 800℃ to give samples BN800-*i* and BP800-*m*, respectively.

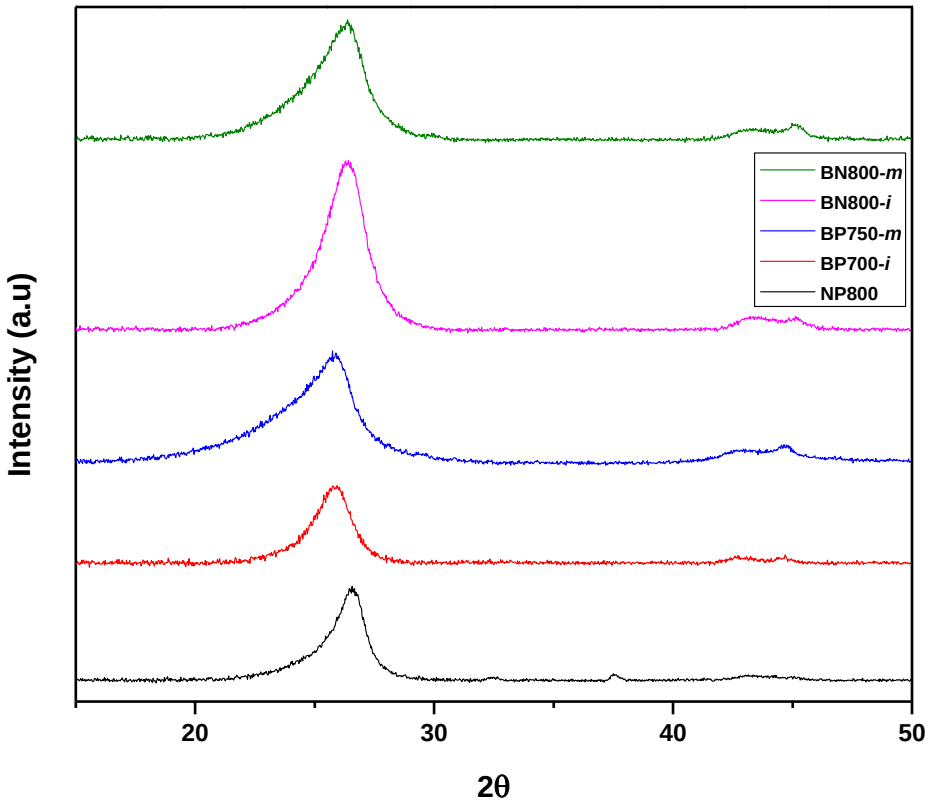


Figure 5.7: XRD spectrum of N-doped, B-doped and B-N co-doped MWCNTs.

The XRD pattern (**Figure 5.7**) of the obtained samples presented with 002, 100 and 101 peaks due to the carbon graphitic planes. The 2θ values of the 002 peaks for the BN800-*i* (26.39°) and BN800-*m* (26.27°) samples were both higher than the 2θ value than the corresponding B-doped samples. These values were comparable to the 2θ value of the N-doped MWCNTs. The

002 peaks were deconvoluted using a Voigt spectral function (**Figure 5.8**), and the d-spacing of each material was determined from peak 2 of the deconvoluted 002 peaks. The d-spacing for sample BN800-*i* (3.375 Å) was smaller than the B-doped MWCNTs (3.443 Å) but close to the value reported for the NP800 sample (3.351 Å). BN800-*m* (3.391 Å) also presented with d-spacing comparable to that of the NP800 sample (3.351 Å), which was smaller than that of the BP750-*m* (3.449 Å). This was a potential indicator of the successful addition of nitrogen to the lattice structure of the B-doped MWCNTs.

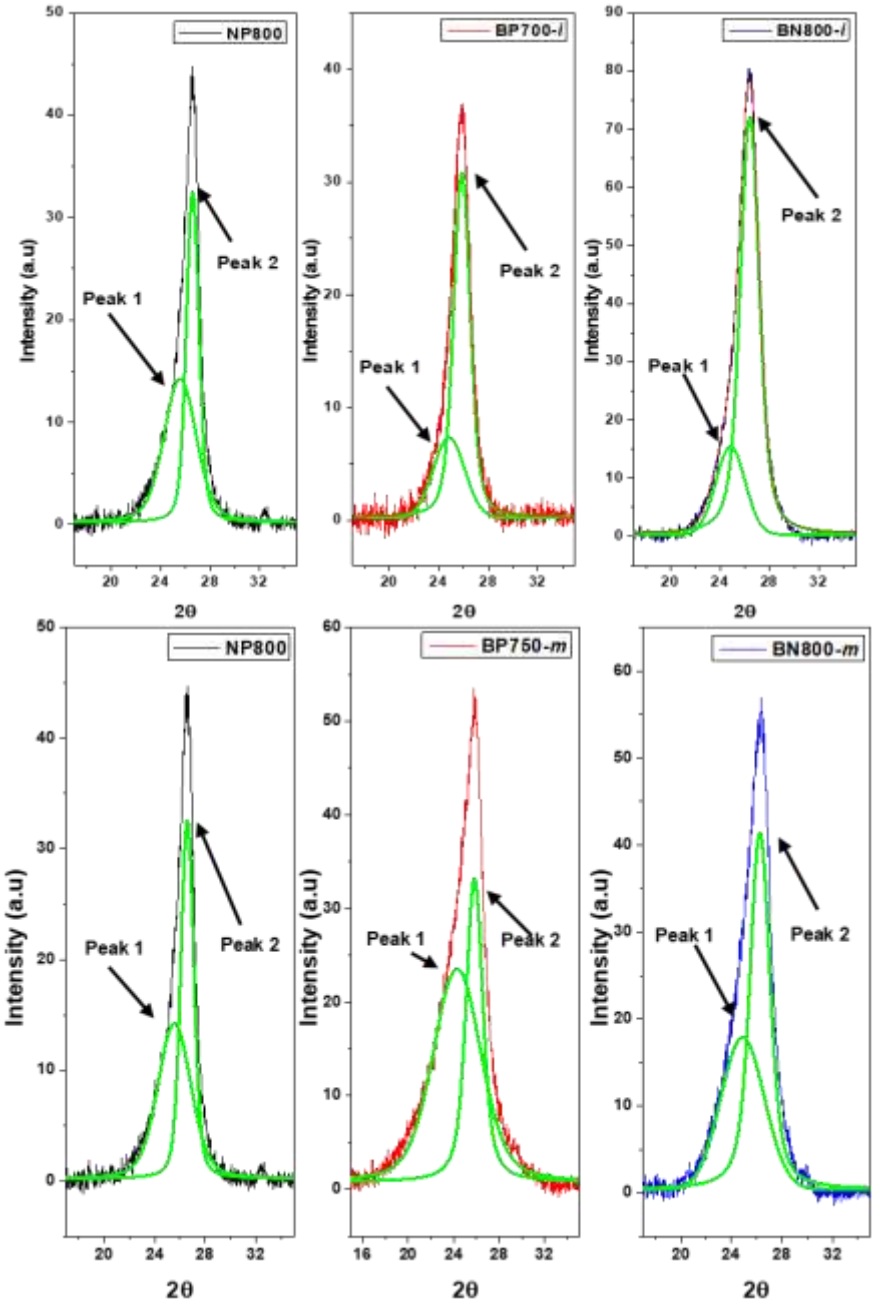


Figure 5.8: XRD spectra of N-doped, B-doped, co-doped MWCNTs deconvoluted 002 peaks using Voigt spectral function.

The Raman analysis of the N-doped, B-doped and nitrogen-boron co-doped samples presented with the characteristic *D* (~1350 cm^{-1}) and *G* (1580 cm^{-1}) bands in the first order region (**Figure 5.9a-c** and **Figure 5.10a-c**). The I_D/I_G ratio of the BN800-*i* was found to be lower than BP700-*i*, suggesting the presence of fewer defects in the carbon or graphitic lattice. This is inconsistent with the concentration of the incorporated nitrogen to the lattice structure. However, if nitrogen was successfully added to the lattice structure, the lower ratio (fewer defects) might be attributed to the annihilation of B-type bonding configuration (bond enthalpy B-C/B-O (356/536 kJ/mol) versus N-C/C=N (305/615 kJ/mol)) in B-doped MWCNTs during the annealing. The treatment of the BP750-*m* sample with acetonitrile led to an increase in the I_D/I_G ratio from 2.56 to 2.95. This indicates an increase in defects in the structure, suggesting a successful incorporation of nitrogen in the lattice structure.

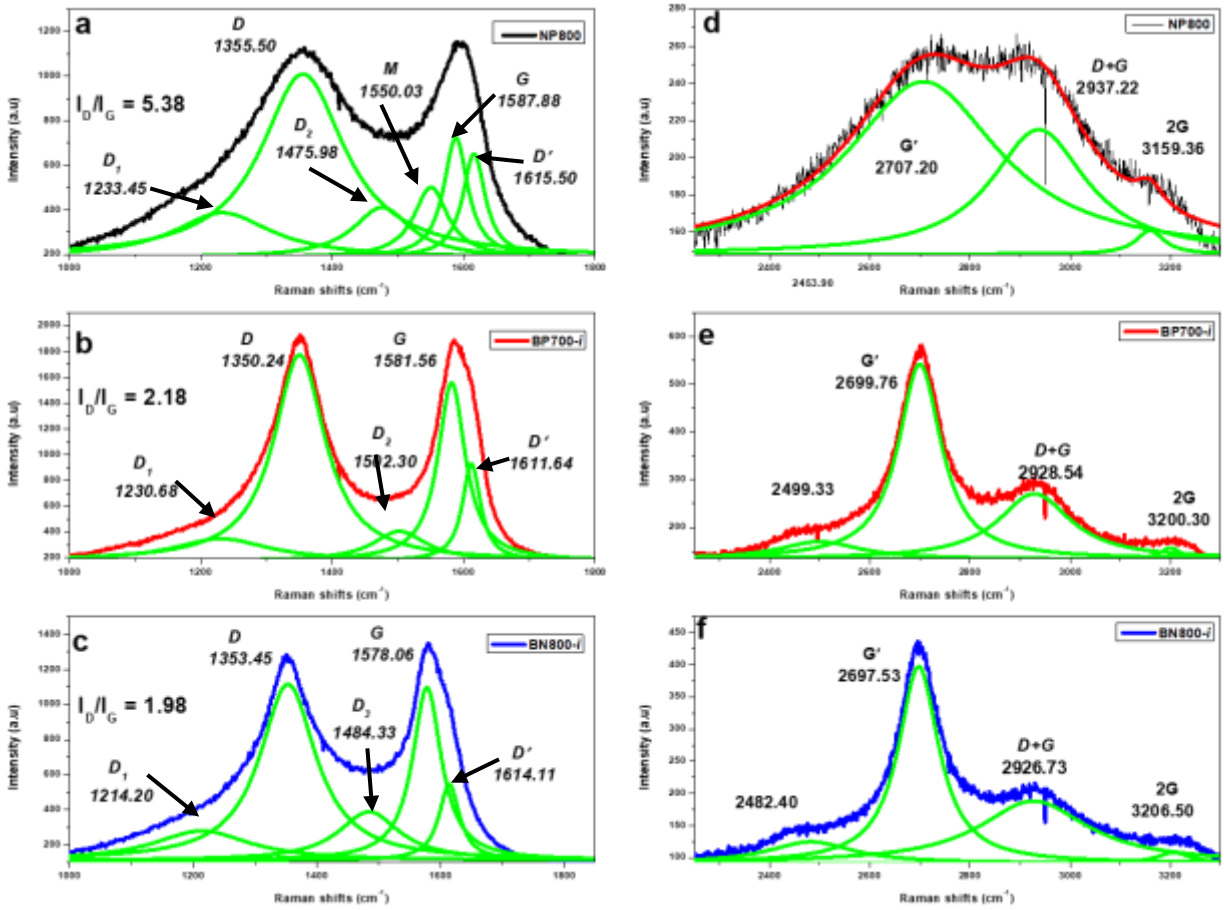


Figure 5.9: Raman spectra of N-doped, B-doped and B-N co-doped; (*a-c*) 1st order Raman Lorentzian fitted peaks (*d-f*) 2nd order Raman Lorentzian fitted peaks.

A band (~2700 cm^{-1}) in the 2nd order region (**Figure 5.9d-f** and **Figure 5.10d-f**) resulting from the overtone of the D-band had a multiplicity that indicated the presence of multiple graphitic

layers. The $I_{G'}/I_D$ ratio (listed in **Appendix 5A** Table 5.10) of BP700-*i* (0.28) and BP750-*m* (0.20) were slightly higher than that of BN800-*i* (0.27) and BN800-*m* (0.15), respectively, which indicated that the treatment of the B-doped MWCNTs with acetonitrile led to a decrease in the overall crystallinity of the material. In addition, the long-range order decreased from 0.61 (BP700-*i*) and 0.53 (BP750-*m*) to 0.54 (BN800-*i*) and 0.43 (BN800-*m*), respectively.[86-88] Long-range order indicates the sequential arrangement of sp^2 hybridized bonds, so its reduction suggests a disruption of this arrangement, and thus corroborating the addition of nitrogen to the lattice structure.[86-88]

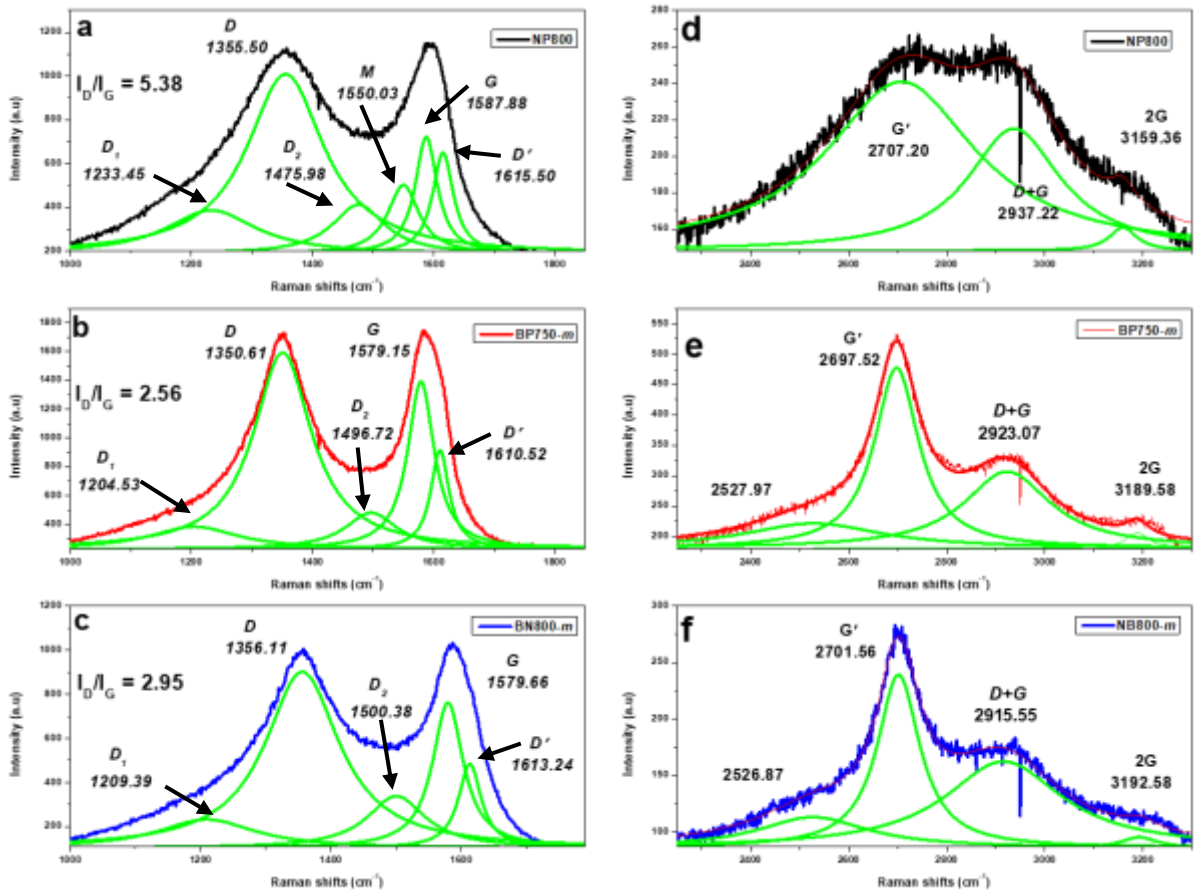


Figure 5.10: Raman spectra of N-doped, B-doped and B-N co-doped (*a-c*) 1st order Raman Lorentzian fitted peaks (*d-f*) 2nd order Raman Lorentzian fitted peaks.

The thermal analysis (**Figure 5.11**) of the co-doped samples revealed that both samples had lower thermal stability than the B-doped MWCNTs from which they were prepared. Given that N-doped MWCNTs generally report thermal stability less than B-doped MWCNTs, the reduction in thermal stability of the B-doped MWCNTs after treatment with acetonitrile suggested a successful incorporation of nitrogen into the lattice structure. The 1st mass loss due to the removal of functional groups was observed from 200℃ for the boron and nitrogen

doped MWCNTs, but not for the co-doped samples. Thus, corroborating that the B-doped samples underwent an annealing process prior to treatment with acetonitrile. The 2nd mass loss due to the oxidation of amorphous carbon was not observed for sample BN800-*m*. However, it was observed at ~ 400℃ and 375℃ for NP800 and BP700-*i*, respectively, but was observed at slightly lower temperature for BN800-*i* (350℃).[75-76, 89-90]

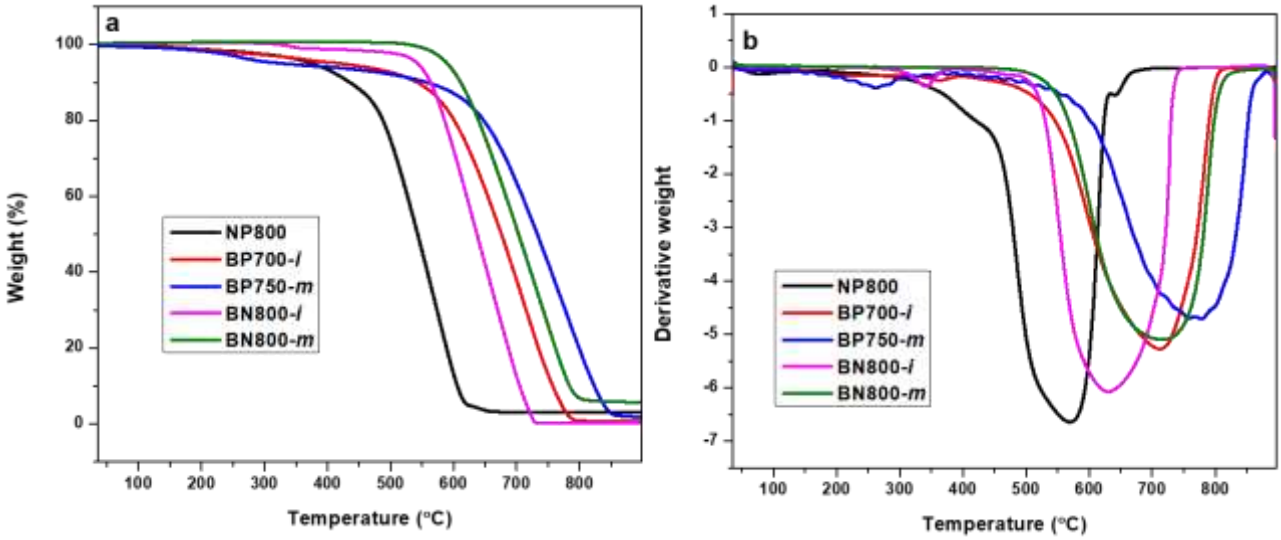


Figure 5.11: TG analysis of N-doped, B-doped and B-N co-doped MWCNTs.

The N-doped MWCNTs had a lower surface area (Table 5.5) than both B-doped MWCNTs, the reduced surface area suggested the addition of nitrogen to MWCNTs is preceded by a decrease in surface area. Given that N-doped MWCNTs tend to report lower surface areas than their corresponding pristine and boron doped MWCNTs counterpart, the reported surface area for the co-doped samples suggest a successful incorporation of nitrogen to the lattice structure of the B-doped MWCNTs. The decrease of the surface area of the BN-800-*i* and BN800-*m* is consistent with their decrease in thermal stability relative to their parent MWCNTs.

Table 5.5: BET Surface area data of doped MWCNTs

Sample	Surface area (m^2/g)	Pore volume (cm^3/g)	Pore size (nm)
NP800	21.1	0.0872	21.65
BP700-*i*	98.2	0.4122	15.29
BN800-*i*	78.7	0.4394	23.79
BP750-*m*	53.9	0.2478	19.07
BN800-*m*	40.1	0.2358	25.08

Table 5.6: XPS atomic % of heteroatom doped MWCNTs

Sample		C 1s	O 1s	N 1s	B 1s
NP800	Position (eV)	284.20	532.76	401.07	--
	Atomic %	80.45	18.54	0.97	--
BP700-*i*	Position (eV)	285.85	532.73	--	191.81
	Atomic %	86.97	12.65	--	0.39
BN800-*i*	Position (eV)	285.68	532.71	400.76	--
	Atomic %	92.28	5.98	0.25	--
BP750-*m*	Position (eV)	285.67	532.77	--	--
	Atomic %	84.14	15.86	--	--
BN800-*m*	Position (eV)	285.68	533.71	401.69	--
	Atomic %	89.69	7.85	2.47	--

XPS analysis (**Figure 5.12,** Table 5.6) revealed that tri-isopropyl borate (BP700-*i*) was successful in the production of B-doped MWCNTs, while trimethyl borate was unsuccessful. A boron atomic % of 0.39 was reported for sample BP700-*i*, but it did not report any amount of nitrogen. The fitted B 1s signal reported 3 bonding configurations: BCO_2 (191.0 eV), BC_2O (191.9 eV), and B-O (192.7 eV). Nitrogen (0.29%) was successfully incorporated into the structure of BP700-*i* after treatment with acetonitrile to produce sample BN800-*i*. However, the sample reported the absence of boron with the incorporation of nitrogen; this was ascribed to the substitution of boron by nitrogen and the loss of boron at the high reaction temperature (800℃). The removal of boron was corroborated not only by the absence of the B 1s signal, but by the comparison of the O 1s fitted peaks of both samples. Sample BN800-*i* did not report the B-O bonding configuration that was found at 533.4 eV in sample BP700-*i*. Although trimethyl borate failed to produce B-doped MWCNTs (BP750-*m*, see XPS in **Appendix 5A, Figure 5.13**), it was found that treating the sample with acetonitrile led to the addition of higher concentrations of nitrogen than when the *in-situ* method was used (NP800). Thus, indicating that incorporating trimethyl borate in the production of pristine MWCNTs, followed by treatment with acetonitrile results in material with relatively high concentrations of nitrogen.

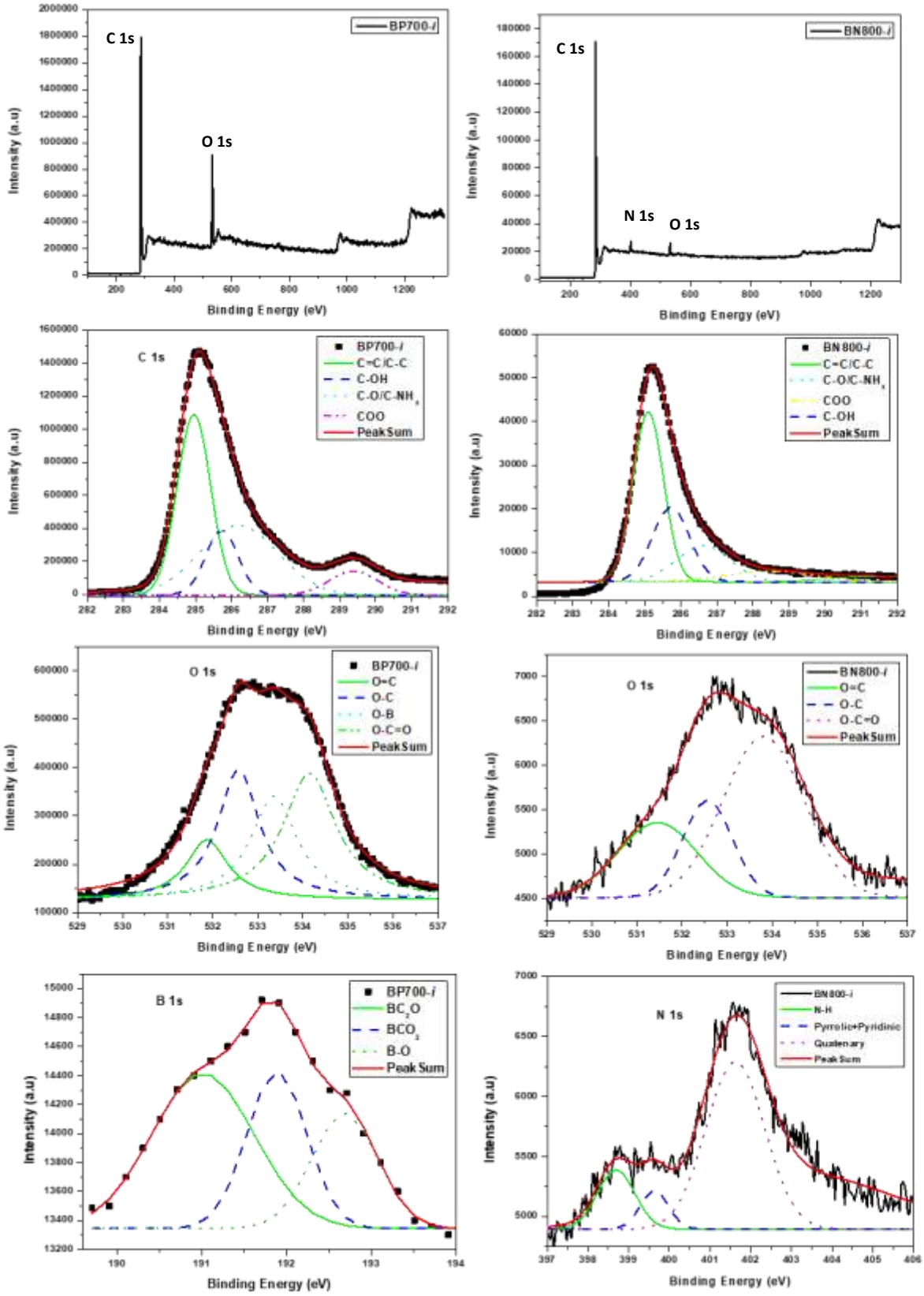


Figure 5.13: XPS analysis of heteroatom doped MWCNTs. *See nitrogen bonding configuration in **Appendix 5A, Figure 5.14**.

5.4. Conclusion.

Heteroatom doped MWCNTs were synthesized using a two-step synthesis method that employed a combination of the *in situ* and *post* doping strategies. In the XRD analysis of the co-doped sample (NB800) derived from nitrogen doped MWCNTs (NP800), it exhibited a downward shift in its Bragg reflection, an observation consistent with boron addition to CNT lattice structure. Samples BN800-*i* and BN800-*m* derived from B-doped MWCNTs BP700-*i* and BP750-*m*, respectively, an upward shift was observed after doping with nitrogen. Which was also consistent with the addition of nitrogen to the lattice structure of MWCNTs. The Raman analysis of NB800 revealed a reduction in the density of defects relative to NP800, this was attributed to two factors; (i) the removal of functional groups from NP800 prior to being doped with boron and this was confirmed by TG analysis, (ii) the graphitization effect that boron has been reported to have on MWCNTs. However, the reduction in the overall crystallinity of the produced material relative to the N-doped sample corroborated the substitution of carbon with nitrogen. A similar observation was made for BN800-*i*, but BN800-*m* presented with larger density of defects than the boron sample from which it was derived. And this was despite TG analysis revealing the removal of surface functional groups from the material. The TG analysis of the co-doped samples revealed that the addition of boron to the N-doped MWCNTs increased their thermal stability. However, the addition of nitrogen to B-doped MWCNTs reduced the thermal stability of the material. It appeared that the surface area of all the co-doped samples was independent of the synthetic route as it reduced for all samples relative to the MWCNTs samples they were derived from. XPS analysis indicated that boron was incorporated successfully to nitrogen doped MWCNTs, and nitrogen was incorporated successfully to boron doped MWCNTs. However, the addition of nitrogen was accompanied by the removal of boron from the structure of the material. The work in this chapter indicated that N-doped MWCNTs are suitable for the production of nitrogen co-doped MWCNTs than B-doped MWCNTs.

Appendix 5A

Table 5.7: The crystallite size and d-spacing of the obtained MWCNTs.

Sample code	002 plane peak position ()	L_a (nm)	FHWM ()	d_{002} (Å)
NP800	26.58	7.328	0.9998	3.351
BP700-*i*	25.86	6.277	1.233	3.443
BN800-*i*	26.39	6.188	1.249	3.375
BP750-*m*	25.81	6.511	1.189	3.449
BN800-*m*	26.27	5.925	1.306	3.391

Table 5.8: Raman analysis summary of the Lorentzian fitted peaks for B-doped MWCNTs produced from tri-isopropyl borate at different temperatures. *Calculated from intensity

Sample	Area (D-peak)	Area (G-peak)	Intensity (D-peak)	Intensity (G-peak)	Area (G`-peak)	Ratio* I_D/I_G	Ratio $I_{G'}/I_G$	Ratio $I_{G'}/I_D$
NP800	200653.32	37315.06	822.88	536.92	53920.23	1.53	1.44	0.29
BP800-*i*	182297.03	108601.06	1060.59	1301.24	64776.87	0.81	0.59	0.36
BP700-*i*	238010.25	109327.32	1598.95	1381.69	66655.49	1.16	0.61	0.28
BP750-*m*	249529.22	97136.18	1364.56	1165.33	51112.24	1.17	0.53	0.20
BN800-*i*	174132.31	87776.87	1005.31	986.72	47125.06	1.02	0.54	0.27
NB800	152139.78	40378.43	654.73	474.04	18848.33	1.38	0.47	0.12
BN800-*m*	174453.73	59149.22	789.75	659.67	25345.25	1.19	0.43	0.15

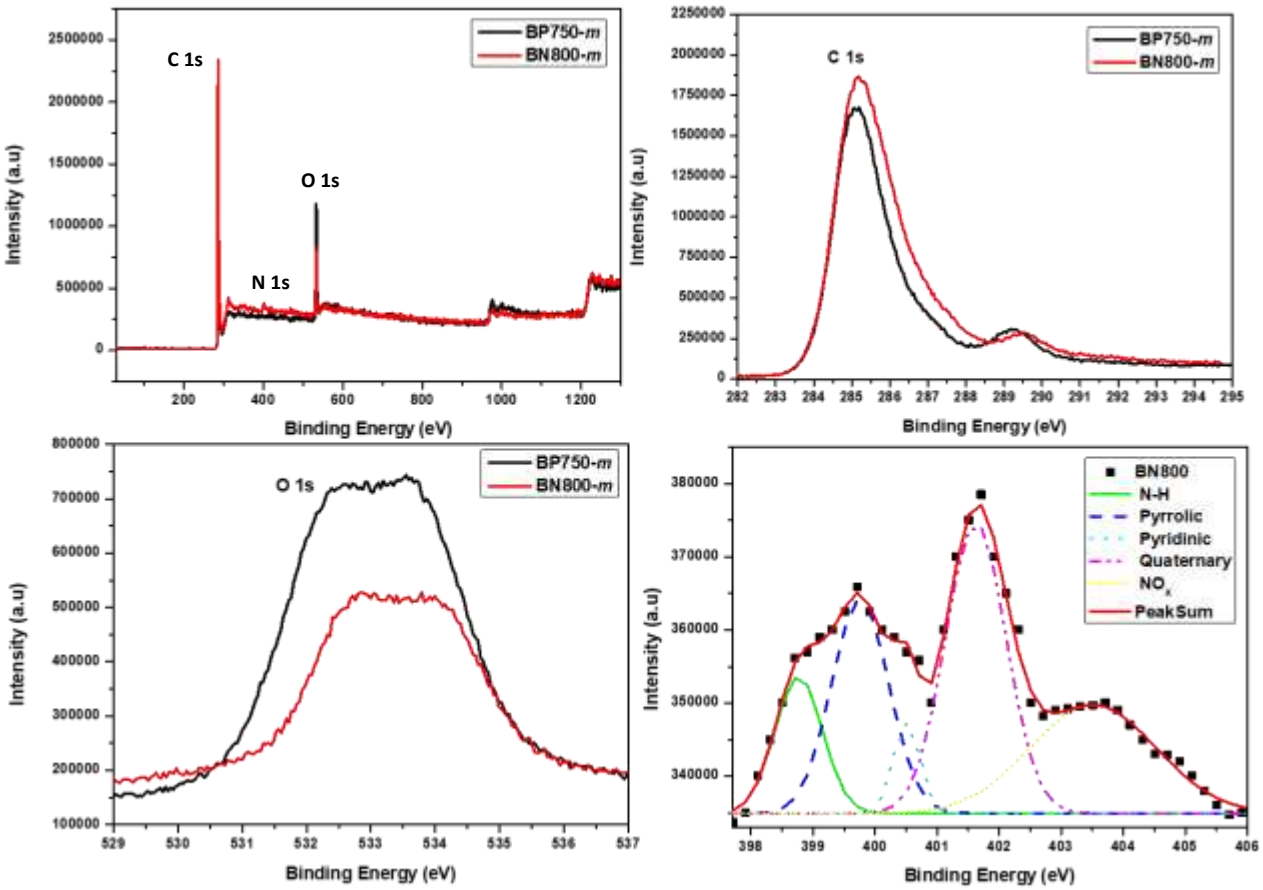


Figure 5.13: XPS analysis of heteroatom doped MWCNTs.

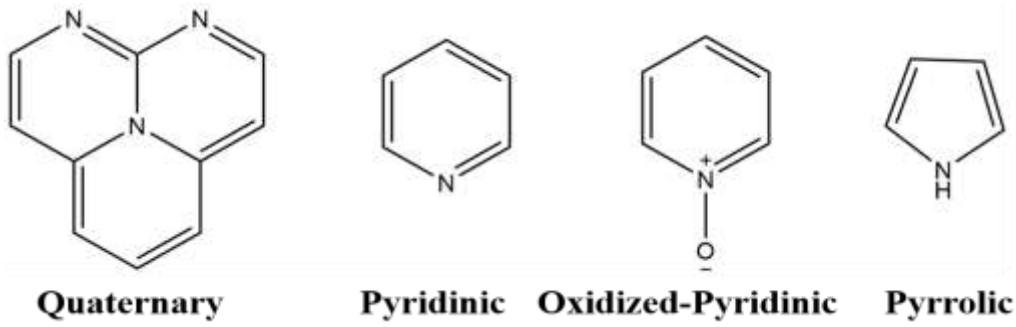


Figure 5.14: Bonding configurations for nitrogen in CNTs

Chapter 5 References

1. S. Iijima. *Nature*. 1991, **354**, 56-58.
2. S. Iijima. T. Ichihashi. *Nature*. 1993, **363**, 603-605.
3. J. Y. Lao, W. Z. Li, J. G. Wen, Z. F. Ren. *Applied Physics Letters.* 2002, **80**, 500-502.
4. J. W. Jang, C. E. Lee, S. C. Lyu, T. J. Lee, C. J. Lee. *Applied Physics Letters.* 2004, **84**, 2877-2879.
5. D. Golberg, Y. Bando, W. Han, K. Kurashima, T. Sato. *Chemical Physics Letters.* 1999, **308**, 337-342.
6. C. P. Ewels, M. Glerup. *Journal of Nanoscience and Nanotechnology.* 2005, **5**, 1345-1363.
7. M. Terrones, A. Jorio, M. Endo, A. M. Rao, Y. A. Kim, T. Hayashi, H. Terrones, J.-C. Charlier, G. Dresselhaus, M. S. Dresselhaus. *Materials Today.* 2004, 30-45.
8. W. H. Moon, H. J. Hwang. *Physica E.* 2005, **28**, 419-422.
9. J. L. Blackburn, Y. Yan, C. Engtrakul, P. A. Parilla, K. Jones, T. Gennett, A. C. Dillion, M. J. Hebben. *Chemistry of Materials.* 2006, **18**, 2558-2566.
10. D. Golberg, Y. Bando, K. Kurashima, T. Sato. *Diamond and Related Materials.* 2001, **10**, 63-67.
11. W. K. Hsu, S. Y. Chu, E. Munoz-Picone, J. L. Boldu, S. Firth, P. Franchi, B. Roberts, A. Schilder, H. Terrones, N. Grobert, Y. Q. Zhu, M. Terrones, M. E. McHenry, H. W. Kroto, D. R. M. Walton. *Chemical Physics Letters.* 2000, **323**, 572-579.
12. M. Yudasaka, R. Kikuchi. Y. Ohki, S. Yoshimura. *Carbon*. 1997, **35**, 671-676.
13. O. Y. Podyacheva, S. V. Cherepanova, A. I. Romanenko, L. S. Kibis, D. A. Svintsitskiy. A. I. Boronin, O. A. Stonkus, A. N. Suboch. A. V. Puzynin, Z. R. Ismagilov. *Carbon.* 2017, **122**, 475-483.
14. R. B. Sharma, D. J. Late, D. S. Joag, A. Govindaraj, C. N. R. Rao. *Chemical Physics Letters.* 2006, **428**, 102-108.
15. K. C. Mondal, A. M. Strydom, R. M. Erasmus, J. M. Keartland, N. J. Coville. *Materials Chemistry and Physics.* 2008, **111**, 386-390.

16. R. Czerw, M. Terrones, J.-C. Charlier, X. Blasé, B. Foley, R. Kamalakaran, N. Grobert, H. Terrones, D. Tekleab, P. M. Ajayan, W. Blau, M. Ruhle, D. L. Carroll. *Nano Letters.* 2001, **9**, 457-460.

17. M. Terrones, P. M. Ajayan, F. Banhart, X. Blasé, D. L. Carroll, J.-C. Charlier, R. Czerw, B. Foley, N. Grobert, R. Kamalakaran, P. Kohler-Redlich, M. Ruhle, T. Seeger, H. Terrones. *Applied Physics A.* 2002, **74**, 355-361.

18. O. Stephan, P. Ajayan. *Science.* 2004, **266**, 1863-1865.

19. J. D. Wiggins-Camacho, K. L. Stevenson. *The Journal of Physical Chemistry C.* 2009, **113**, 19082-19090.

20. K. Fujisawa, T. Tojo, H. Muramatsu, A. L. Elías, A. M. Vega-Díaz, F. Tristán-López, J. H. Kim, T. Hayashi, Y. A. Kim, M. Endo, M. Terrones. *Nanoscale.* 2011, **3**, 4359-4364.

21. D. L. Carroll, Ph. Redlich, X. Blasé, J.-C. Charlier, S. Curran, P. M. Ajayan, S. Roth, M. Ruhle. *Physical Review Letters.* 1998, **81**, 2332-2335.

22. H. Mousavi, R. Moradian. *Solid State Sciences.* 2011, **13**, 1459-1464.

23. K. Liu, Ph, Avouris, R. Martel. *Physical Review B.* 2001, **63**, 1611404 (1-4).

24. K. Fujisawa, T. Hayashi, M. Endo, M. Terrones, J. H. Kim, Y. A. Kim. *Nanoscale.* 2018, **10**, 12723-12733.

25. K. Gong, F. Du, Z. Xia, M. Durstock, L. Dai. *Science.* 2009, **323**, 760-764.

26. Y.-A. Leu, M.-H. Yeh, L.-Y. Lin, T.-J. Li, L.-Y. Chang, S.-Y. Shen, Y.-S. Li, G.-L. Chen, W.-H. Chiang, J.-J. Lin, K.-C. Ho. *ACS Sustainable Chemistry and Engineering.* 2017, **5**, 537-546.

27. A. Agarwal, H. Yinnon, D. R, Uhlmann, R. T. Pepper, C. R. Desper. *Journal of Material Science.* 1986, **21**, 3455-3466.

28. Y. Ganesan, C. Peng, Y. Lu, L. Ci, A. Srivastava, P. M. Ajayan, J. Lou. *ACS Nano.* 2010, **4**, 7637-7643.

29. C. Deng, J. Chen, X. Chen, C. Xiao, L. Nie, S. Yao. *Biosensers and Bioelectronics.* 2008, **23**, 1272-1277.

30. J. C. Carrero-Sánchez, A. L. Elías, R. Mancilla, G. Arrellín, H. Terrones, J. P. Laclette, M. Terrones. *Nano Letters*. 2006, **6**, 1609-1616.

31. P. M. Gíslason, E. Skúlason. *Nanoscale*. 2019, **11**, 18683-18690.

32. Y. Cao, H. Yu, J. Tan, F. Peng, H. Wang, J. Li, W. Zheng, N.-B. Wong. *Carbon*. 2013, **57**, 433-442.

33. I. T. Kim, M. J. Song, Y. B. Kim, M. W. Shin. *International Journal of Hydrogen Energy*. 2016, **41**, 22026-22033.

34. W. He, P. Xue, H. Du, L. Xu, M. Pang, X. GaoJ. Yu, Z. Zhang, T. Huang. *International Journal of Hydrogen Energy.* 2017, **42**, 4123-4132.

35. T. Ishii, T. Maie, N. Kimura, Y. Korobi, Y. Imashiro, J. Ozaki. *International Journal of Hydrogen Energy.* 2017, **42**, 15849-15496.

36. S. S. Samantaray, V. Sangeetha, S. Abinaya, S. Ramaprabhu. *International Journal of Hydrogen Storage.* 2018, **43**, 8018-8025.

37. W. Wang, P. Wang, Y. Kang, J. Zhao, P. Tao, Z. Lei. *International Journal of Hydrogen Storage.* 2019, **44**, 4771-4779.

38. X.-H. Li. M. Antonietti. *Angewandnte Chemie-International Edition.* 2013, **52**, 4572-4576.

39. Z.-S. Wu, A. Winter, L. Chen, Y. Sun, A. Turchanin, X. Feng, K. Müllen. *Advanced Materials.* 2012, **24**, 5130-5135.

40. Q. Zhou, J. Wu, Z. Pan, X. Kong, Z. Kui, D. Wu, G. Hu. *International Journal of Hydrogen Energy*. 2020, **45**, 33634-33640.

41. Y. Guo, P. Yuan, J. Zhang, H. Xia, F. Cheng, M. Zhou, J. Lin, Y. Qiao, S. Mu, Q. Xu. *Advanced Functional Materials.* 2018, **28**, 1805641 (1-9).

42. R. Li, X. Wang, Y. Dong, X. Pan, X. Liu, Z. Zhao, J. Qui. *Carbon*. 2018**, 132**, 580-588.

43. H. N. Yang, W. J. Kim. *Electrochimica Acta.* 2016, **209**, 430-439.

44. Y. Sun, C. Du, M. An, L. Du, Q. Tan, Y. Gao, G. Yin. *Journal of Power Sources.* 2015, **300**, 245-253.

45. S. Gosh, S. Ramaprabhu. *Carbon*. 2019, **141**, 692-703.

46. T. Liu, M. Li, X. Bo, M. Zhou. *Journal of Colloid and Interface Science.* 2019, **533**, 709-722.

47. L. Zhang, G. Xia, Z. Guo, X. Li, D. Sun, X. Yu. *International Journal of Hydrogen Energy.* 2016, **41**, 14252-14260.

48. S. V. Sawant, S. Banerjee, A. W. Patwardhan, J. B. Joshi, K. Dasgupta. *International Journal of Hydrogen Storage.* 2020, **45**, 13406-13413.

49. W. He, P. Xue, H. Du, L. Xu, M. Pang, X. Gao, J. Yu, Z. Zhang, T. Huang. *International Journal of Hydrogen Energy.* 2017, **42**, 4123-4132.

50. Z. Xu, W. Lu, W. Wang, C. Gu, K. Liu, X. Bai, E. Wang, H. Dai. *Advanced Materials.* 2008, **20**, 3615-3619.

51. Y. Zhou, Y. Sun, H. Wang, C. Zhu, J. Gao, D. Wu, H. Huang, Y. Liu, Z. Khang. *Inorganic Chemistry Frontiers.* 2018, **5**, 2958-2991.

52. J. Jin, F. Pan, L. Jiang, X. Fu, A. Liang, Z. Wei, J. Zhang, G. Sun. *ACS Nano.* 2014, **8**, 3313-3321.

53. Z.-H Sheng, H.-L. Gao, W.-J. Bao, F.-B. Wang, X.-H. Xia. *Journal of Materials Chemistry.* 2012, **22**, 390-395.

54. Y. Liu, S. Chen, X. Quan, H. Yu, H. Zhao, Y. Zhang, G. Chen. *Journal of Physical Chemistry C.* 2013, **117**, 14992-14998.

55. Y. Qian, Z. Hu, X. Ge, S. Yang, Y. Peng, Z. Kang, Z. Liu, J. Y. Lee, D. Zhao. *Carbon.* 2017, **111**, 641-650.

56. J. Ozaki, T. Anahara, N. Kimura, A. Oya. *Carbon*. 2006, **44**, 3358-3361.

57. H. Fei, R. ye, G. Ye, Y. Gong, Z. Peng, X. Fan. E. L. G. Samuel, P. M. Ajayan, J. M. Tour. *ACS Nano.* 2014, **8**, 10837-10843.

58. Y. Zhao, L. Yang, S. Chen, X. Wang, Y. Ma, Q. Wu, Y. Jiang, W. Qian, Z. Hu. *Journal of American society.* 2013, **135**, 1201-1204.

59. L. Yang, S. Jiang, Y. Jao, L. Zhu, S. Chen, X. Wang, Q. Wu, J. Ma, Z. Hu. *Angewandte Chemie International Edition.* 2011, **50**, 7312-7315.

60. S. Wang, E. Iyyamperumal, A. Roy, Y. Xue, D. Yu, L. Dai. *Angewandte Chemie International Edition.* 2011, **50**, 11756-11760.

61. S. Wang, L. Zhang, Z. Xia, A. Roy, D. W. Chang, J.-B. Baek, L. Dai. *Angewandte Chemie International Edition*. 2012, **51**, 4209-4212.

62. M. Grundmann. *The Physics of Semiconductors: An Introduction Including Nanophysics and Application; Springer-Verlag: Berlin*. 2010, page 206.

63. E. D. Glendening, C. R. Lendis, F. Weinhold. *Wiley Interdisciplinary Reviews: Computational Molecular Science.* 2012, **2**, 1-42.

64. H. Khalfoun, P. HErmet, L. Henrard, S. Latil. *Physical Review B.* 2010, **81**, 193411 (1-4).

65. R. Z. Ma, Y. Bando, T. Sato. *Chemical Physics Letters.* 2001, **337**, 61-64.

66. E. Iyyamperumal, S. Wang, L. Dai. *ACS Nano.* 2012, **6**, 5259-5265.

67. W.-Q. Han, J. Cumings, X. Huang, K. Bradley, A. Zettl, *Chemical Physics Letters.* 2001, **346**, 368-372.

68. A. A. Koós, F. Dillon, E. A. Obraztsova, A. Crossely, N. Grobert. *Carbon*. 2010, **48**, 3033-3041.

69. Z. N. Tetana. *Boron and nitrogen doped carbons for photochemical degradation reactions. University of the Witwatersrand.* PhD thesis; 2013.

70. D. P. Hashim, N. T. Narayan, J. M. Romo-Herrera, D. A. Cullen, M. G. Hahm, P. Lezzi, J. R. Suttle, D. Kellkhoff, E. Muñoz-Sandoval, S. Ganguli, A. K. Roy, D. J. Smith, R. Vajtai, B. G. Sumpter, V. Meunier, H. Terrones, M. Mauricio, P. M. Ajayan. *Scientific Reports.* 2012, **2**, 363 (1-8).

71. M. Terrones, N. Grobert, H. Terrones. *Carbon.* 2002, **40**, 1665-1684.

72. S. Shiraishi, M. Kibe, T. Yokoyama, H. Kurihara, N. Patel, O. Oya, Y. Kaburagi, Y. Hishiyama. *Applied Physics A: Material Science and Processing*. 2006, **82**, 585-591.

73. D. K. Singh, P. K. Lyer, P. K. Giri. *Diamond and Related Materials.* 2010, **19**, 1281-1288.

74. M. Terrones, A. Jorio, M. Endo, A. M. Rao, Y. A. Kim, T. Hayashi, H. Terrones, J.-C. Charlier, G. Dresselhaus, M. S. Dresselhaus. *Materials Today.* 2004, 30-45.

75. S. O. Ibrahim, K. U. Isah, A. S. Abdulkareem, U. Ahmadu, J. O. Tijani, W. D. Ross. *Journal of Material Science: Materials in Electronics.* 2020. DOI: https://doi.org/10.1007/s10854-020-03550-0

76. Z. N. Tetana, S. D. Mhlanga, G. Bepete, R. W. M. Krause, N. J. Coville. *South African Journal of Chemistry.* 2012, **56**, 39-49.

77. R. Al-Jishi, G. Dresselhaus. *Physical Review B.* 1982, **26**, 4514-4522.

78. Y. Wang, D. C. Alsmeyer, R. I. McCreery. *Chemistry of Materials.* 1990, **2**, 557-563.

79. S. L. H. Rebelo, A. Guedes, M. E. Szefcyk, A. M. Pereira, J. P. Araújo, C. Freire. *Physical Chemistry Chemical Physics.* 2016, **18**, 12784-12796.

80. X. Li, J.-I. Hayashi, C.-Z. Li. *Fuel.* 2006, **85**, 1509-1517.

81. A. Sadezky, H. Muckenhuber, H. Grothe, R. Niessner, U. Pöschl. *Carbon*. 2005, **43**, 1732-1742.

82. D. K. Singh, P. K. Lyer, P. K. Giri. *Diamond and Related Materials.* 2010, **19**, 1281-1288.

83. X. Wang, Y. Li, G. Yu, C. Xu, J. Zhang. *Journal of Physical Chemistry B.* 2001, **105**, 9422-9425.

84. L. F. Mabena, S. S. Ray, S. D. Mhlanga, N. J. Coville. *Applied Nanoscience.* 2011, **1**, 67-77.

85. J. Amadou, K. Chizari, M. Houllé, I. Janawoska, O. Ersen, D. Bégin, C. Pham-Huu. *Catalysis Today.* 2008, **138**, 62-68.

86. S. Santangelo, G. Messina, G. Faggio, M. Lanza, C. Milone. *Journal of Raman Spectroscopy.* 2011, **42**, 593-602.

87. R. A. Dileo, B. J. Landi, R. P. Raffaelle. *Journal of Applied Physics.* 2007, **101**, 064307 (1-5).

88. S. Santangelo, M. Dhanagopal, G. Faggio, G. Messina, A. Pistone, M. Lanza, C. Milone. *Diamond and Related Materials.* 2010, **19**, 599-603.

89. B. J. Landi, C. D. Cress, C. M. Evans, R. P. Raffaelle. *Chemistry of Materials*. 2005, **17**, 6819-6834.

90. Z. J. Shi, Y. F. Lian, F. H. Liao, X. H. Zhou, Z. N. Gu, Y. Zhang, S. Iijima, H. D. Li, K. T. Yue, S. L. Zhang. *Journal of Physics and Chemistry of Solids.* 2000, **61**, 1031-1036.

Chapter 6: The synthesis of phosphorous doped MWCNTs.

6.1. Introduction.

Heteroatom doping of carbon nanomaterials is a chemical process that involves a 'controlled' modification of the intrinsic properties of the material. The substitution of carbon in carbon nanomaterials with nitrogen and boron has been reported on extensively.[1-21] Another element that has not been investigated and reported as extensively is the group V counterpart, phosphorous, but existing work has demonstrated its potential in resulting in material with properties that possess greater utility than their parent material. The substitution of carbon is achieved despite phosphorous atoms being much larger than carbon atoms in size. [22-27]

P-doped carbon nanostructures have been used extensively and some examples are described below. Wang *et al.* demonstrated the use of phosphorous doped carbon dots decorated on graphene for the reduction of oxygen, and reported a performance comparable to that of Pt/C. The use of the composite as a cathode in the liquid aluminium-air battery yielded a power density of 157.3 mW/cm^2 compared to 151.5 mW/cm^2 for Pt/C.[25] Phosphorous was also incorporated successfully into a three dimensional carbon nanofiber network by Chen and co-workers, which showed good supercapacitor performance.[22] The work by Yi *et al* has also demonstrated the successful use of phosphorous doped carbon as a cathode in supercapacitors.[23] Some phosphorous doped carbon nanomaterials have also been used in biological applications. For example, Kumar *et al* investigated cell labelling, and differentiation and outgrowth of neuronal cells using fluorescent phosphorous doped carbon dots. The carbon dots demonstrated excellent photostability, biocompatibility, cell viability and cellular uptake.[28]

Phosphorous doped CNTs have continued to draw attention and have been studied by different research groups.[29-32] The resulting CNTs may exhibit n-type behaviour because phosphorous contains more electrons than carbon and so can function as a current carrier, electron acceptor, and modulate the CNT electronic properties.[33-34] An increase in phosphorous concentration in the CNT network modifies the surface chemical properties of CNTs and creates localized charge sites on the phosphorous dopant.[35-36] This modification in surface properties (i.e. charge distribution) makes them viable for application in the development of sensors and fuel cells.[37-39] P-doped CNTs served as excellent supports for platinum in the oxidation of methanol

compared to their pristine counterparts. They were found to give higher electrocatalytic activity coupled with long term stability. This was attributed to the ability of phosphorous doped CNTs to encourage excellent dispersion of platinum by lowering its surface potential energy.[38] The incorporation of phosphorous into the CNT structure, even at small concentrations, has also given improved electrochemical properties in different oxidation reduction reactions (ORR) in different electrochemical applications[39-42], such as lithium sulphur type batteries[43]. Additionally, phosphorous has been used successfully as a co-dopant to nitrogen in the modification of the properties of MWCNTs.[27, 36, 44]

The rarity of studies associated with P-CNTs had previously created a gap in knowledge around the mechanism of phosphorous incorporation into the lattice structure, and the bonding of P in the carbon network framework. Some initial studies have resorted to confirming or corroborating the modification of CNTs using phosphorous through indirect methods (at times coupled with first principle theoretical calculations from Density Field Theory (DFT) calculations) such as energy dispersive X-ray (EDX) studies, electron energy loss spectroscopy (EELS), and thermogravimetric and Raman analysis.[27, 44-48] However, the use of a technique such as EELS can be limited by the phosphorous content being below the detection threshold.[46] Additionally, the use of Raman spectroscopy does not give sufficient and precise information about the type of bonding that may exist, this is even inherent in low dimension materials with Raman inactive localized modes.[45] The use of X-ray photoelectron spectroscopy (XPS) has been found to be an appropriate approach to address both questions of concentration and bonding.[32,40, 43-45] For example, Larrude and co-workers demonstrated this by reporting a concentration of 0.11-0.32 % phosphorous content and the presence of P-C (~129.5 eV) and P-O (~133.3 eV) bonding in their P-CNT samples.[45]

The successful substitution of carbon by phosphorous, and its resulting concentration in the lattice structure depends on factors such as the synthetic method used. These include the spray pyrolysis[45], hydrothermal synthesis[42-43] and chemical vapor deposition (CVD) methods[32, 41, 44, 49]. The type of phosphorous precursor also plays a central role in the synthesis method used and the concentration of the phosphorous to be incorporated. PPh_3 appears to be the most used precursor. It has been utilized in two ways when producing CNTs in the CVD method viz. by *in-situ* or post doping methods. Since it is a solid powder, an *in-situ* approach that involves dissolving it in a solvent may be applied; Liu *et al*. prepared phosphorous-doped MWCNTs using a toluene-based solution containing ferrocene and PPh_3 over a $FeMo/Al_2O_3$ catalyst. The *post doping* method is a two-step process that first requires the synthesis of the CNTs, and then

in the second step their modification; Yuan *et al.* functionalized MWCNTs that were mixed with PPh_3 through grinding, and then by heating to 800℃.[50] Apart from PPh_3, other phosphorous precursors include H_3PO_4[42-43], NaH_2PO_2[40], trimethyl-phosphine[32], triethyl-phosphine[51] etc. Despite some reported success in incorporating phosphorous into the lattice structure of CNTs, several challenges are associated with this process: The atomic radius of phosphorus (atomic radius = 100 pm/1.00 Å[52], covalent atomic radius = 107 pm/1.07 Å[53]) is much larger than that of carbon (atomic radius = 70 pm/0.070 Å[52], covalent atomic radius = 76 pm/0.076 Å[53]), and thus its incorporation introduces pronounced localized bond length distortions and subsequently induce strain to the lattice that are more pronounced than heteroatoms with similar atomic radius to carbon such as boron and nitrogen. The P-C bond (264 kJ/mol at 298 K)[54-56] is weak and phosphorous is highly oxyphilic, thus exposure of the resulting material to oxygen or air may result in a reaction that forms the much stronger single P-O (335 kJ/mol at 298 K) or double P=O (544 kJ/mol at 298 K)[56-58] bonds. Formation of either bond is dependent on the oxidation of the phosphorous in the lattice structure. As a consequence, the phosphorous atoms tend to predominantly add to the edges of a carbon plane.[57]

The work in this chapter describes the production of P-doped MWCNTs using PPh_3 as a source of phosphorous in the CVD method. Both the *in-situ* and *post doping* approaches were utilized to draw comparisons between the methods.

6.2. Materials and Methods.

6.2.1. Starting materials.

The reagents used were all analytical grade and were utilized as obtained; triphenyl phosphine ($\geq$ 99%) and 55% nitric acid (HNO_3) were purchased from Sigma Aldrich. The ethylene (C_2H_2) and nitrogen (N_2) gases were supplied by Afrox South Africa. Distilled water was used for all experiments and washings where required.

6.2.2. Synthesis of phosphorous doped MWCNTs.

Method A:

Two phosphorous doped MWCNTs Ph(1:1)800 and Ph(1:2)800 were prepared from 250 mg of pristine MWCNTs (PP700-2) that were milled with 250 mg and 500 mg of triphenyl phosphine, respectively. The resulting mixture was placed in a quartz boat in a tubular quartz tube which was connected to a N_2 gas line (flow rate 240 sccm) in a horizontal furnace. The temperature of the furnace was raised at a rate of 10℃/min, and kept at 800℃ for 1 h. The reaction was cooled down to room temperature using compressed air; the boat containing a black solid mass of MWCNTs was collected. Ph(1:1)800 (90%) and Ph(1:2)800 (94%).

Method B:

Pristine MWCNTs (250 mg) were placed in quartz boat in a tubular quartz tube. The temperature of the furnace was raised at a rate of 10℃/min and kept at 800℃ for 1 h. Once the desired temperature was obtained, N_2 gas (240 sccm) was bubbled through a solution of triphenyl phosphine (5 g) dissolved in toluene (400 ml) for 1h in a horizontal furnace. The reaction was then cooled down to room temperature using compressed air, the boat containing a black solid of MWCNTs was retrieved and the product (PhPo800) collected.

Method C:

300 mg of 10% Fe-Co/$CaCO_3$ [*Catalyst B* **chapter 3, Section 3.2.1 method B**] catalyst was placed in a quartz boat in a quartz tube in a horizontal furnace. The tube was connected to two gas lines supplying C_2H_2 (90 sccm) and N_2 (240 sccm) gases that functioned as a source of carbon and as a carrier gas, respectively. The temperature of the furnace was raised at 10℃/min to 800℃ in a N_2 atmosphere. Once the desired temperature was reached, C_2H_2 and N_2 were bubbled through a solution of triphenyl phosphine (5 g) dissolved in toluene (400 ml) for 1h. The reaction was cooled down to room temperature using compressed air, and the boat

containing a black solid of MWCNTs was collected. The obtained P-doped sample and an excess of HNO_3 (55%) were added to a round bottom flask and left stirring under reflux at 110℃ for 4h. The resulting solution was left to cool to room temperature. The cooled solution was diluted with water, filtered, and washed until the filtrate had a neutral pH. The obtained black solid (PhP800) was left to dry at 100℃ for 12h in an oven (Yield 24%).

6.2.3. Characterization techniques.

The powder X-ray diffraction (PXRD) technique was used to study the structural characteristics of the samples and for assessing their purity (Bruker D2 phaser with a nickel filtered copper radiation λ_{K_α} = 0.15406 nm). Additionally, Raman spectroscopy, using a 514.5 nm laser line, generated from an argon ion laser was utilized for structural analysis. The morphology of the material was determined using scanning electron microscopy (SEM, ZEISS SIGMA 03-30 FESEM instrument). A PerkinElmer TGA4000 instrument was used to study the thermal properties of the material under an atmosphere of air (20 ml/min) over a temperature range of 35-900℃. The surface area, pore volumes and sizes of the material were determined via N_2 adsorption under isothermal conditions (-196℃, using liquid nitrogen) on a Micromeritics TriStar 3000 instrument using the Brunauer, Emmet, and Teller (BET) method

6.3. Results and discussion

6.3.1. The synthesis of phosphorous doped MWCNTs.

Pristine MWCNTs (PP700-2) were produced over an Fe-Co/$CaCO_3$ catalyst using the CVD method, and the obtained sample was purified and functionalized under reflux using HNO_3. PXRD analysis (**Figure 6.1a: Table 6.1**) of the sample not only confirmed that there were no structural phases attributed to the catalyst residue, but also revealed the three MWCNT characteristic peaks due to the 002(~26°), 100(~43°) and 101(~44-45°) graphitic planes. Phosphorous doped MWCNTs were prepared using two post-doping methods (*Method A and B*). The PXRD data of the resulting samples Ph(1:1)800 and Ph(1:2)800 (prepared using *Method A*) revealed a downward shift in the 2theta position of the 002 peak (Table 6.1) relative to the pristine P700-2 (Table 6.1). Sample Ph(1:2)800 reported the lowest Bragg reflection. The PXRD analysis of the PhPo800 sample (prepared using *Method B*) also revealed a downward shift in the 002-peak position.

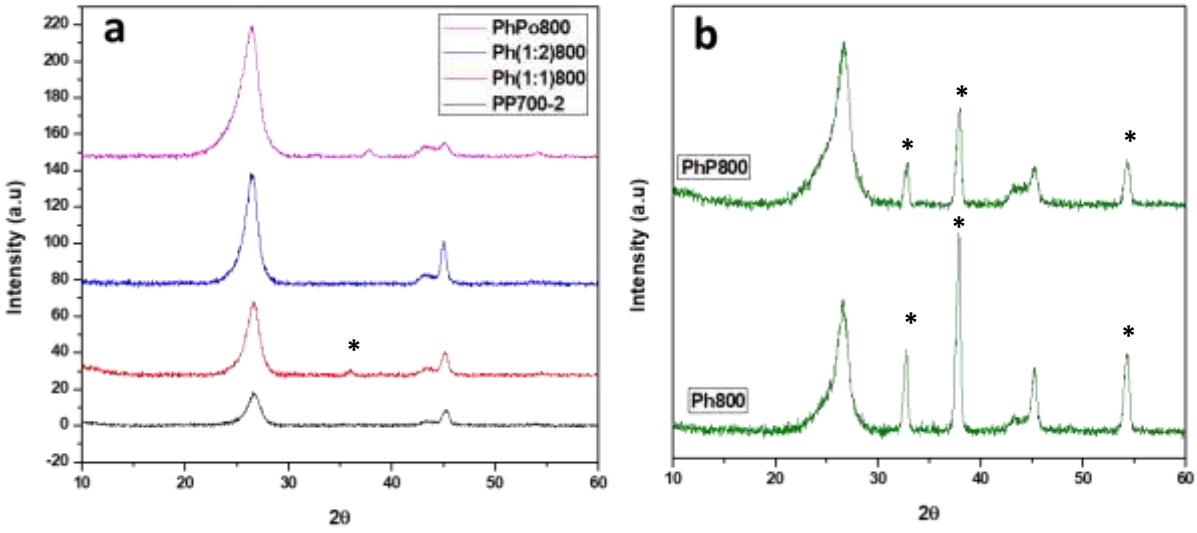


Figure 6.1: PXRD pattern of *a)* phosphorous doped MWCNTs prepared using the post doping method *b)* phosphorous doped MWCNTs prepared using the *in-situ* doping method. *Catalyst residue

PXRD analysis (**Figure 6.1b**) of the Ph800 (un-purified) and PhP800 (purified) sample prepared using the *in-situ* method (*Method C*) revealed three peaks ascribed to graphitic carbon at (002) for 2θ = 26.70°, (100) for 2θ = 43.39° and (101) 2θ = 45.72° planes. However, the removal of the catalyst residue was unsuccessful. Multiple acid treatments and longer treatment times were also explored, but none of the methods led to the successful removal of the residue. Given that acid treatment also damages the nanotubes via oxidation, only the data for the sample treated once for four hours under reflux are presented here.

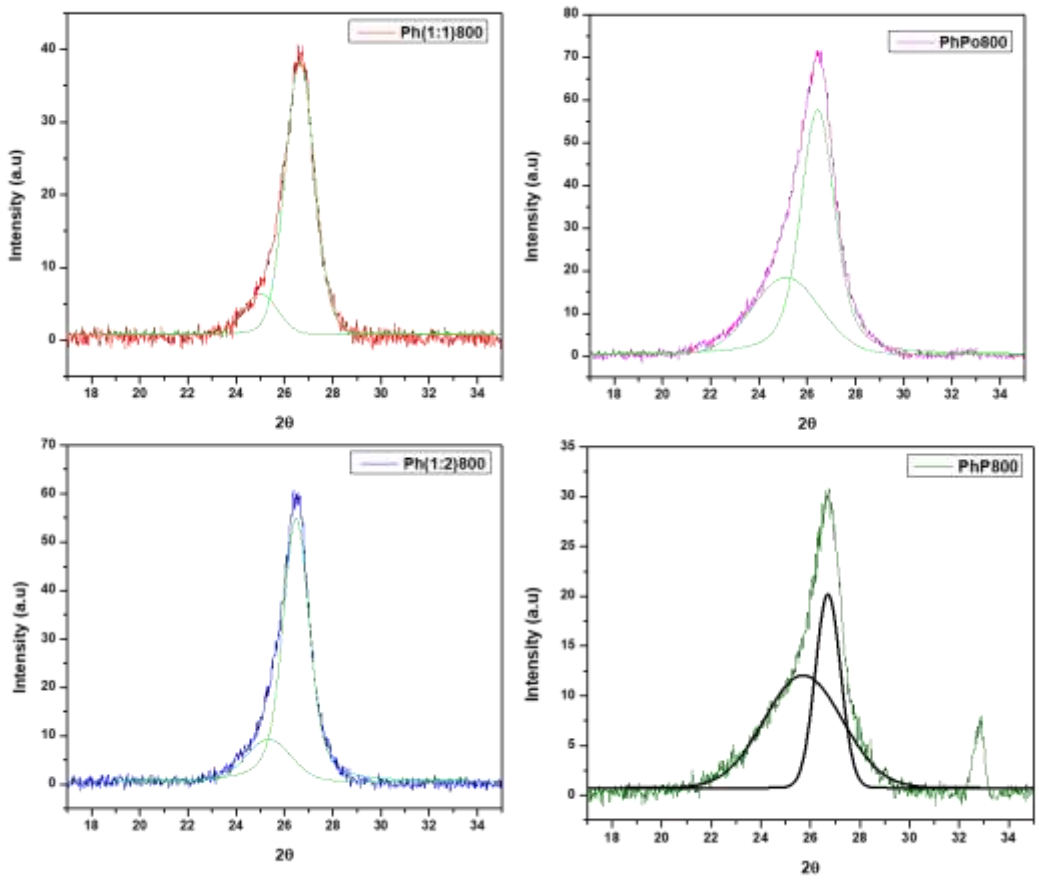


Figure 6.2 PXRD pattern of the deconvoluted (002) peaks for pristine and phosphorous doped MWCNTs using the Voigt function.

The crystallite size and interlayer spacing (d_{002}) (Table 6.1) were determined from the dominant (002) peak (**Figure 6.2**). No significant difference was observed in the interlayer spacing of the phosphorous doped MWCNTs, and all samples reported a very small increase in the interlayer spacing relative to the pristine MWCNTs. All three phosphorous doped MWCNTs prepared from the post doping method gave broader (002) peaks relative to the PP700-2 sample. This suggests a reduction in crystallinity after treatment with triphenyl phosphine, due to the creation of defects within the material. However, it was not clear from this data if these defects were a consequence of a successful incorporation of phosphorous to the lattice structure of the material or due to other factors.

Table 6.1: The crystallite size and d-spacing of the obtained MWCNTs.

Sample code	002 plane peak position (°)	L_a (nm)	d_{002} (Å)
Ph(1:1)800	26.67	6.195	3.339
Ph(1:2)800	26.47	6.727	3.337
PhPo800	26.43	6.197	3.369
PhP800	26.70	6.428	3.336
PP700-2 (pristine)	26.72	6.095	3.333

SEM analysis (**Figure 6.3**) of the obtained samples revealed the presence of intertwined and entangled CNTs with varying diameters and lengths. The MWCNTs in samples Ph(1:1)800 (A) and PhPo800 (C) had smoother surfaces compared to the Ph(1:2)800 (B) and PhP800 (D) samples which showed a combination of rough and smooth surfaces.

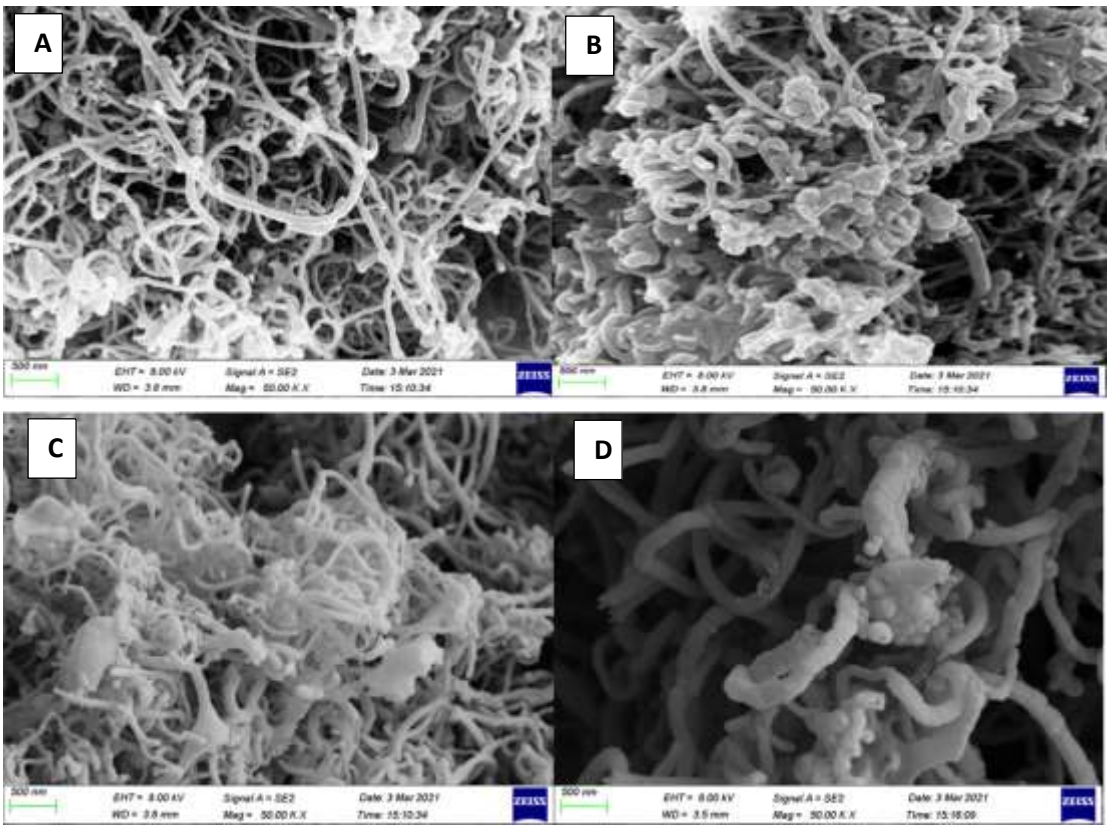


Figure 6.3: SEM images of phosphorous doped MWCNTs, *a)* Ph(1:1)800, *b*) Ph(1:2)800, *c*) PhPo800, *d)* PhP800.

Raman analysis of all the samples showed the carbon *D* and *G* bands (**Figure 4.5a-e,** Table 6.2), and a band with peak(s) in the 2nd order region (**Figure 6.4f-j)**.[59-60] The graphitisation indexes I_D/I_G (area under the peaks used), $I_{G'}/I_D$ (overall crystallinity indicator, see Table 6.2) and $I_{G'}/I_G$ (long range order, see Table 6.2) of the pristine MWCNTs increased after treatment with PPh_3. The changes observed in the $I_{G'}/I_G$ ratio after treatment with PPh_3 for samples Ph(1:1)800 and Ph(1:2)800 are not consistent with the introduction of defects in the lattice structure of the pristine MWCNTs (PP700-2). However, sample PhPo800 showed a 50% reduction in long range order relative to the pristine MWCNTs. The overall crystallinity ($I_{G'}/I_G$) of all three products obtained from the post doping method decreased relative to the pristine MWCNTs, suggesting the successful introduction of defects to the structure.

Sample PhPo800 reported the highest I_D/I_G ratio and lowest $I_{G'}/I_D$ and $I_{G'}/I_G$ ratios compared to the other P-doped samples produced from the post doping method. This indicates that the material had a larger density of defects and potentially a higher concentration of phosphorous in the lattice structure relative to all the other P-doped samples. This difference can be attributed to the contrasting characteristics of the synthetic methods used. Since PPh_3 has a low melting (79-81℃) and boiling point (377 ℃)[61], a considerable amount of PPh_3 could have been vaporized and lost at a reaction temperature of 800℃ in the production of Ph(1:1)800 and Ph(1:2)800. However, in the production of PhPo800 the PPh_3 is introduced to the reaction at 800℃.

Table 6.2: The graphitization indexes of phosphorous doped MWCNTs.

Sample	I_D/I_G	$I_{G'}/I_G$	$I_{G'}/I_D$
Ph(1:1)800	1.52	0.74	0.49
Ph(1:2)800	1.89	0.69	0.37
PhPo800	2.09	0.21	0.19
PhP800	3.48	0.38	0.11
PP700-2 (Pristine)	1.48	0.66	0.69

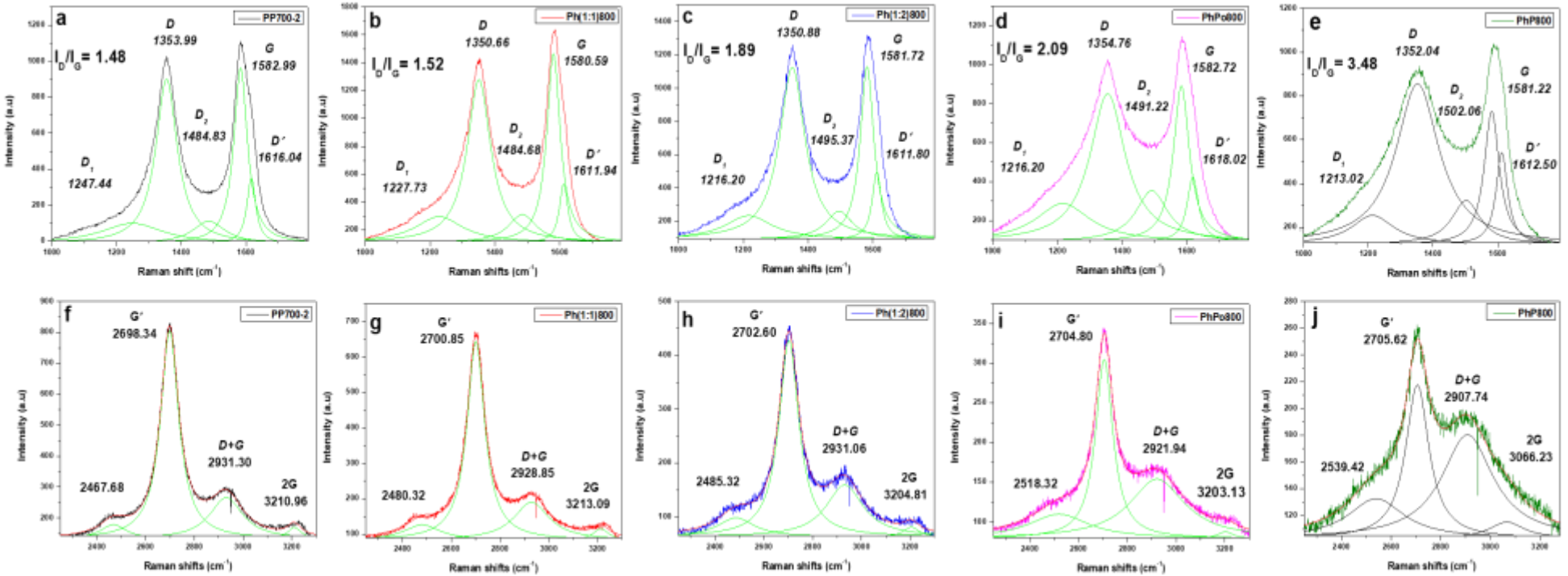


Figure 6.4: Raman spectra of pristine and phosphorous doped MWCNTs *(a-e)* 1st order Lorentzian fitted bands, *(f-j)* 2nd order Lorentzian fitted bands.

Sample Ph(1:2)800 had more defects (i.e., higher concentration of phosphorous incorporated into the lattice structure from I_D/I_G ratios), lower long-range order ($I_{G'}/I_G$) and overall crystallinity ($I_{G'}/I_D$) when compared to Ph(1:1)800. This indicated that despite the loss of PPh_3 during the production of both samples, the use of increased amounts of PPh_3 (250 mg vs 500 mg) might have compensated for its loss at high temperature. The sample prepared using the *in-situ* method (PhP800) reported the highest density of defects (I_D/I_G) and lowest overall crystallinity ($I_{G'}/I_D$) compared to those produced from the post doping method.

The thermal properties (**Figure 6.5**) of the host material indicate that the treatment of pristine MWCNTs with PPh_3 via mixing prior to heat treatment i.e., samples Ph(1:1)800 and Ph(1:2)800, gave materials with slightly improved thermal stability relative to the pristine sample PP700-2. The treatment of the pristine MWCNTs with PPh_3 solution led to a slight reduction in thermal stability (PhPo800) compared to the pristine material. All the obtained samples reported narrow and more symmetrical derivative weight curves (**Figure 6.5b**) relative to the pristine MWCNTs, indicating that the method yielded MWNCTs with a narrower distribution in morphology. All the three MWNCTs prepared from the post doping method had higher thermal stability at lower temperatures (< 500 ℃) compared to the pristine sample. The improved thermal stability (at < 500℃) and purity could be attributed to the removal of amorphous carbon during the reaction.

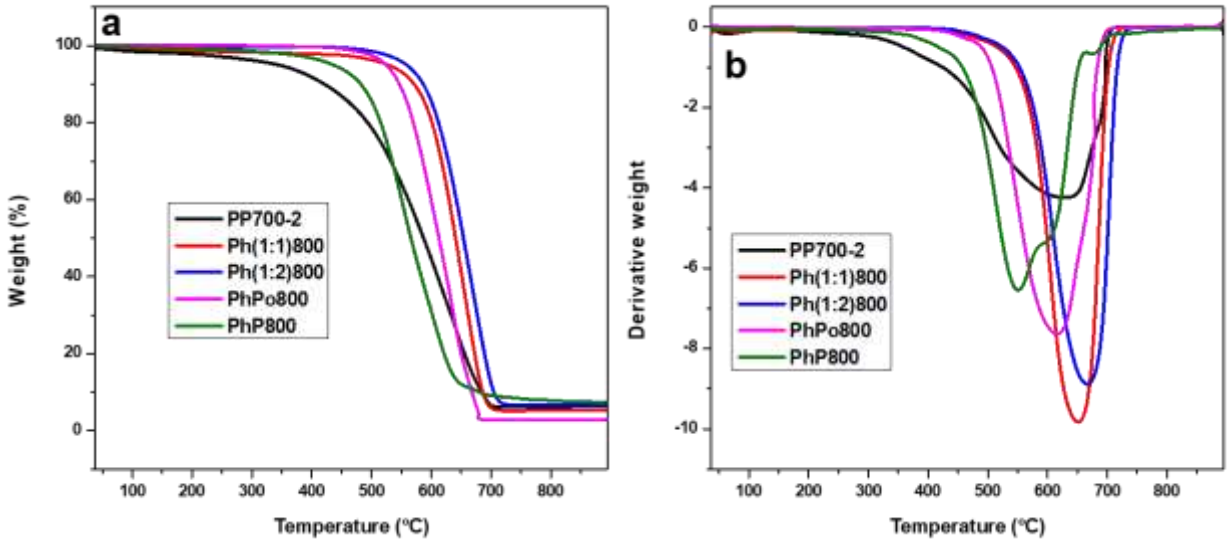


Figure 6.5: TG analysis of pristine and phosphorous doped MWCNTs

This was corroborated by the substantial weight loss due to removal of surface functional groups and amorphous carbon observed at ~ 200℃ for the pristine sample but was absent for

all phosphorous doped MWCNTs. The 2nd major weight loss due to the oxidation of the graphitic carbon indicated the thermal stability sequence, Ph(1:2)800 (668 ℃) > Ph(1:1)800 (650 ℃) > PP700-2 (640 ℃) > PhPo800 (615 ℃). The low thermal stability of PhPo800 relative to the other samples treated with PPh_3 was consistent with its higher I_D/I_G, and lower $I_{G'}/I_G$ and $I_{G'}/I_D$ graphitic indexes relative to the other phosphorous doped and pristine MWCNTs. The higher thermal stability of Ph(1:2)800 and Ph(1:1)800 could be as a consequence of the larger long range order and overall crystallinity relative to PhPo800, and not necessarily the absence of phosphorous in the lattice structure. The *in-situ* method produced MWCNTs (PhP800) with two types of morphologies compared to the post doping method. One had the lowest thermal stability compared to those produced using the post doping method. The 2nd type had thermal stability comparable to PhPo800, but was lower than that of Ph(1:1)800 and Ph(1:2)800. Unlike the other obtained MWCNTs, PhP800 reported a weight loss due to the amorphous carbon at lower temperatures (300-450℃), thus corroborating that the post doping method unintentionally led to the removal of amorphous carbon during the reaction.

Treatment of the pristine MWCNTs with PPh_3, using two different post doping methods led to a general increase in the surface areas and pore volumes and with a reduction in the pore sizes (Table 6.3). The samples (Ph(1:1)800 and Ph(1:2)800) obtained from pre-mixing of the pristine MWCNTs with PPh_3 prior to heat treatment under an inert atmosphere, presented with larger surface areas and pore volumes than PhPo800. Additionally, it was observed that the increase in the mass (1:2) of PPh_3 relative to the pristine MWCNTs led to surface area values that were not significantly different from each other. The sample prepared using the *in-situ* method gave the lowest surface area and pore volume, relative to the other obtained MWCNTs.

Table 6.3: Surface area data of phosphorous doped MWCNTs

Sample	Surface area (m^2/g)	Pore volume (cm^3/g)	Pore size (nm)
Ph(1:1)800	87.7	0.4361	22.84
Ph(1:2)800	82.5	0.4270	22.79
PhPo800	77.6	0.4125	22.56
PhP800	11.6	0.0595	24.70
PP700-2 (Pristine)	63.8	0.3489	26.66

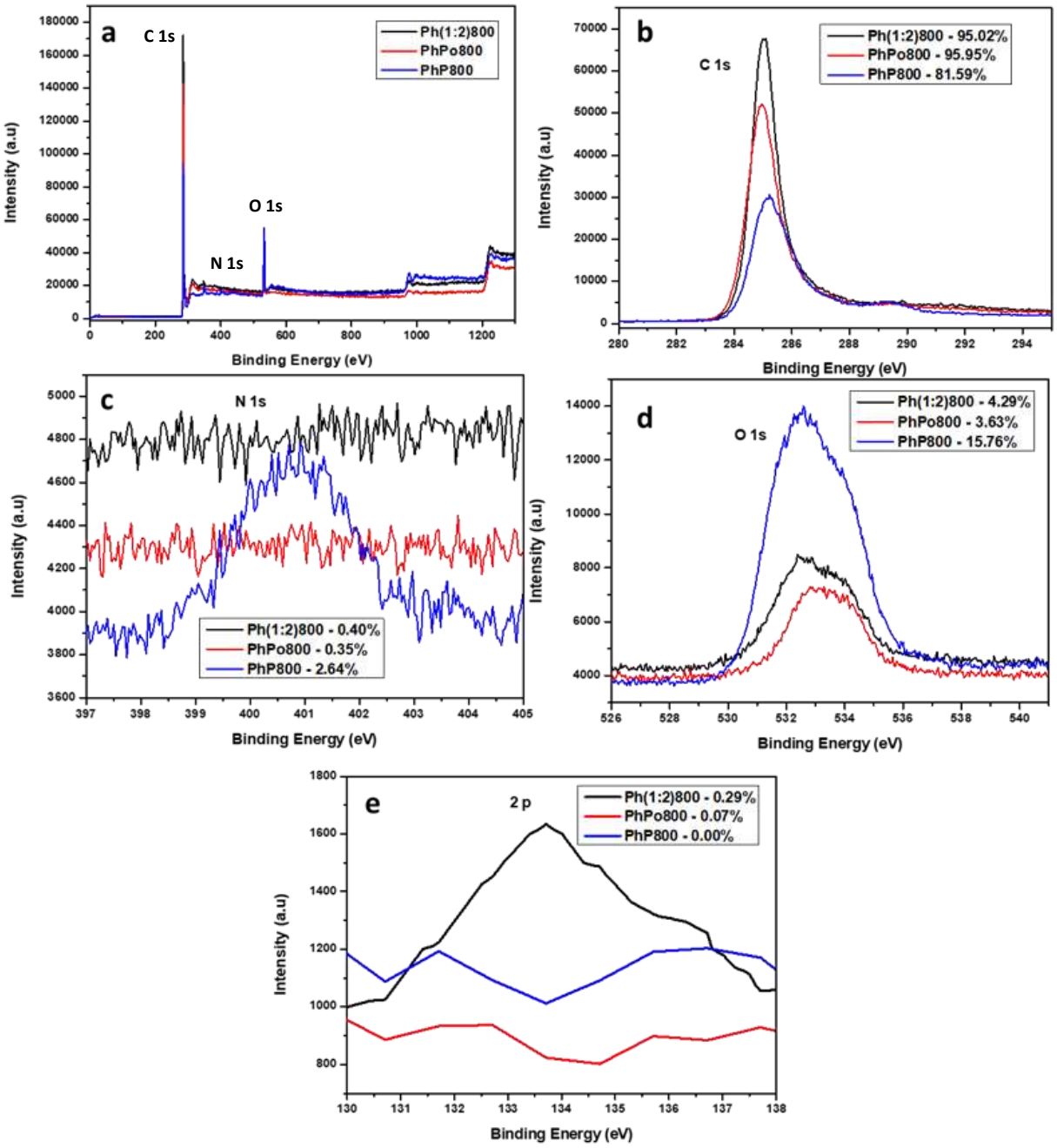


Figure 6.6: XPS analysis of phosphorous doped MWCNTs: *a)* complete XPS scan, *b)* C 1s, *c)* N 1s, *d)* O 1s, *e)* P 2p.

XPS analysis (**Figure 6.6,** Table 6.4) of the phosphorous doped MWCNTs showed the presence of phosphorous in Ph(1:2)800 and PhPo800. Sample Ph(1:2)800 reported the highest atomic % of phosphorous of 0.29% relative to the 0.07% for PhPo800 (**Figure 6.6e**). The observed difference can be attributed to the difference in the synthesis methods, in particular the "delivery" system (i.e., how, and when the PPh_3 was added to the reaction). Using a solution of phosphorous in toluene addressed the problems associated with the low boiling and

melting points of PPh_3. However, a small amount (~ 70-80 ml out of the initial 400 ml) of the solution was delivered into the reaction chamber. As a result, smaller amounts of phosphorous took part in the synthesis of PhPo800 compared to Ph(1:2)800. Additionally, the loss of PPh_3 could have been minimized by mixing it with the pristine MWCNTs through milling prior to heating. Which might have forced and trapped PPh_3 in the layer and cavities of the MWCNTs.

Table 6.4: XPS data of P-doped MWCNTs

Sample		C 1s	O 1s	N 1s	P 2p
Ph(1:2)800	Position (eV)	285.71	532.98	400.73	133.71
	Atomic %	95.02	4.29	0.40	0.29
PhPo800	Position (eV)	285.67	533.71	399.69	131.71
	Atomic %	95.95	3.63	0.35	0.07
PhP800	Position (eV)	285.82	532.71	400.64	--
	Atomic %	81.59	15.76	2.64	0.00

The P 2p signal for sample Ph(1:2)800 reported the two components resulting from the P-O (133.64 and 134.87 eV) and P-C/C-P=O (131.86 eV) bonds (**Figure 6.7b**), and these were consistent with work reported in literature.[32, 44-45, 62-63] Additionally, the P-C bond component was observed in the C 1s signal of the material at 286.51 eV (**Figure 6.7a**).[62] In the case of sample PhPo800, despite reporting the presence of phosphorous, components due to the P-C bond could not be isolated because of the inability to resolve it from the background noise in the spectra. It is also important to consider that given the high reaction temperature used, the weak P-C bond may have not survived these conditions. Thus, a sample with disordered surfaces and some P-O species may have been obtained. However, although some of the literature work quoted above as corroborating evidence to the successful synthesis of P-doped MWCNTs used different synthetic methods, they also used high reaction temperatures from 700-850 ℃. [44-45, 63] This suggests that the P-C bond in CNTs may be able to survive such harsh reaction conditions during the synthesis. As far as we know, studies that investigate this claim in MWCNT or CNTs are not available. However, a study by Wang and co-workers demonstrated the evolution of phosphorous containing groups (C-O-P, C-P=O, C-P) with heat treatment (400-900℃) under nitrogen and hydrogen atmosphere on 'graphite like' activated carbons. They found that under nitrogen atmosphere, the C-P bond was only stable as the C-P=O (at 132.2 eV in XPS, in the lattice and edges graphite like crystallites) linkage at

temperatures up to and above 800°C.[64] Assuming that this is consistent across carbon graphite like material, it suggests that the formation of C-P bonding in the P-doped MWCNTs was not only successful, but stable at high temperatures.

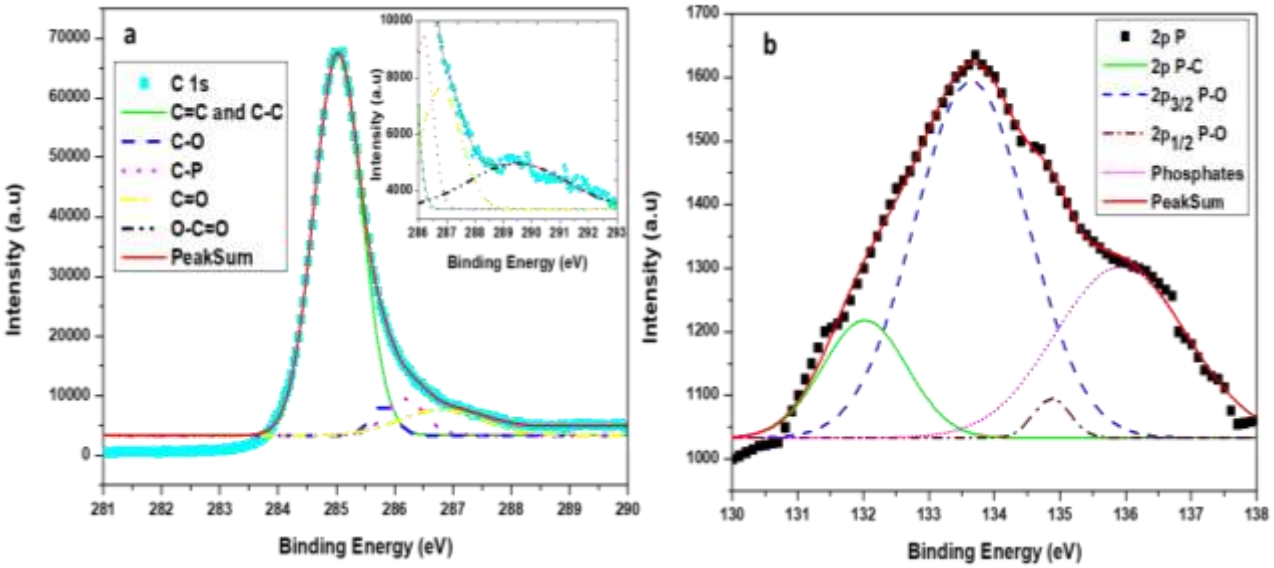
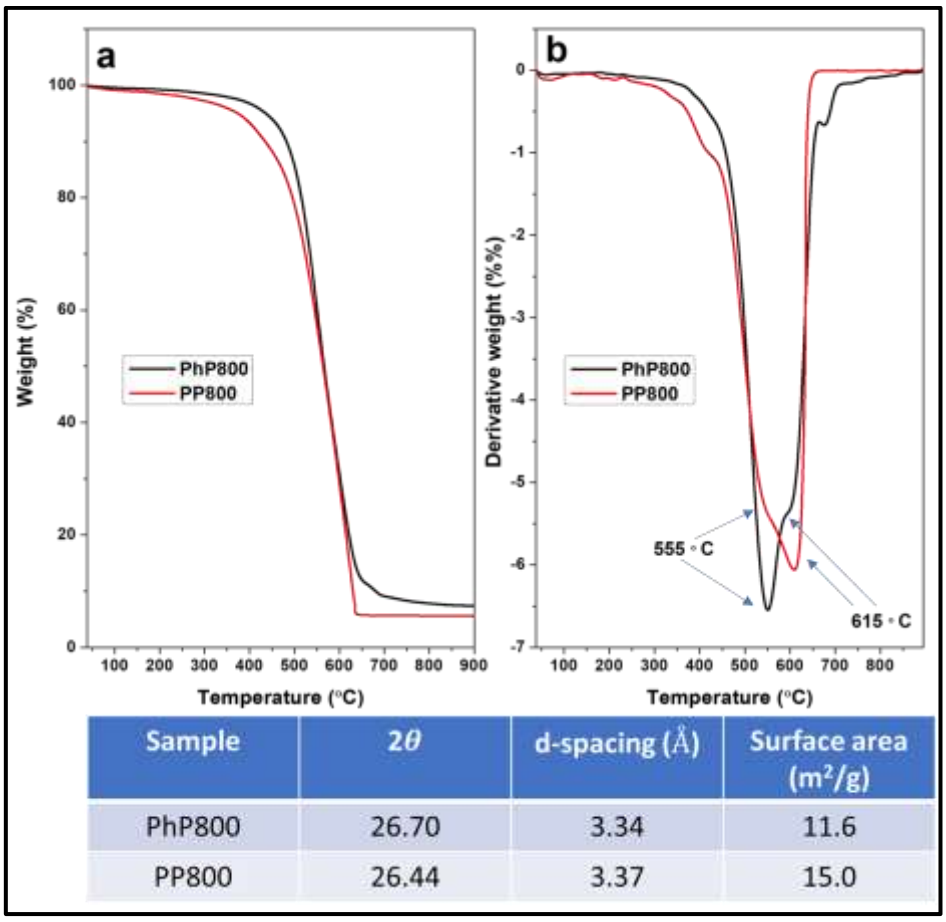


Figure 6.7: Fitted XPS peaks *a)* C 1s Ph(1:2)800 *b)* P 2p Ph(1:2)800.

The *in-situ* method did not add phosphorous to the lattice structure of the material as evidenced by the absence of the P 2p XPS signal (**Figure 6.6e**). The failure of the method can also be ascribed to the low amount of PPh_3 solution (100-110 ml out of the initial 440 ml) delivered into the reaction chamber during the reaction. Although it reported the largest density of defects relative to the samples produced from the post doping methods, this was attributed to the high atomic % of oxygen (15.76%) and nitrogen (2.64%) compared to samples Ph(1:2)800 {N (%) = 0.40, O (%) = 4.29%} and PhPo800{N (%) = 0.35%, O (%) = 3.63%}. The high concentrations of N and O can be attributed to the use of HNO_3 in the attempted purification of PhP800, which resulted in the functionalization of the material. Additionally, it is possible that the reaction was successful, but treatment with HNO_3 may have resulted in the removal of phosphorus from the material (no data available for sample obtained in between production) through an oxidation process: $P + 5HNO_3 \rightarrow H_3PO_4 + 5NO_2 + H_2O$.

The failure of the reaction was corroborated through the comparison of the thermal, XRD and surface area data (**Figure 6.8**) of a pristine sample prepared under the same conditions as sample PhP800. The reported differences between the two samples are insignificant: a difference of 0.30 for 2theta, 0.03 for d-spacing, and 1.6 for surface area. Furthermore, the XPS

data highlighted the shortcomings associated with the use of indirect methods of analysis for determining the substitution of carbon.



Sample	2θ	d-spacing (Å)	Surface area (m^2/g)
PhP800	26.70	3.34	11.6
PP800	26.44	3.37	15.0

Figure 6.8: Thermal, XRD and surface area comparison of samples PhP800 and PP800.

6.4. Conclusion.

PPh_3 was used in three different methods to prepare phosphorous doped MWCNTs. The *post doping* method produced material that exhibited different crystallographic, thermal, and surface area properties relative to the parent pristine MWCNTs. The samples (Ph(1:1)800 and Ph(1:2)800) that were prepared from the simultaneous heat treatment of a premix of triphenyl-phosphine and pristine MWCNTs showed improvements in thermal stability, overall crystallinity ($I_{G'}/I_D$) and long-range order ($I_{G'}/I_G$). However, thermal analysis and the higher I_D/I_G ratio relative to the pristine sample indicated that these improvements were predominantly due to the removal of amorphous carbon and not the presence of phosphorous atoms in the lattice structure. XPS analysis corroborated the successful addition of phosphorous to the lattice structure of sample Ph(1:2)800 at 0.29%. Sample PhPo800 reported the lowest thermal stability relative to the pristine, Ph(1:1)800 and Ph(1:2)800 samples. Additionally, it also showed a higher density of defects, low long-range order, and low overall crystallinity. However, XPS analysis of sample PhPo800 reported the lowest phosphorous atomic % of 0.07%. Additionally, the lower crystallinity and thermal stability were due largely to the presence of oxygen and nitrogen than phosphorous. The *post doping* methods produced material that had higher surface area than the pristine sample. The *in-situ* method gave a product (PhP800) with the highest density of defects and lowest overall crystallinity. However, XPS analysis revealed that this was due to the high atomic % of oxygen in the lattice structure at 15% and not the presence of phosphorous. A comparison of the sample with a pristine sample prepared under the same conditions corroborated the failure of the *in-situ* method. It was revealed that the post doping method was better suited for the addition of phosphorous to the lattice structure and edges of MWCNTs.

Appendix 6A.

Table 6.5: Raman analysis summary of the Lorentzian fitted peaks for P-doped and pristine MWCNTs.

Sample	Area (D-peak)	Area (G-peak)	Intensity (D-peak)	Intensity (G-peak)	Area (G`-peak)	Ratio $I_{G'}/I_G$	Ratio $I_{G'}/I_D$
PhP800	186237.11	53475.78	735.05	608.93	20567.00	0.38	0.11
Ph(1:1)800	161012.11	106113.19	1169.91	1356.12	78391.26	0.74	0.49
Ph(1:2)800	154155.43	82156.64	1035.09	1039.26	56900.61	0.69	0.37
PhPo800	157139.43	74892.38	761.63	801.73	30942.60	0.21	0.19
PP800	247864.01	53855.24	936.17	620.52	37785.03	0.70	0.15
PP700-2	364995.46	144594.02	1903.63	1680.50	82528.95	1.06	0.69

Chapter 6 References.

1. C. Hu, D. Liu, Y. Xiao, L. Dai. *Progress in Natural Science: Materials International.* 2018, **28**, 121-132.
2. D. Jana, A. Bandyopadhyay. *Carbon-Science and Technology.* 2018, **10**, 35-80.
3. R. Czerw, M. Terrones, J.-C. Charlier, X. Blasé, B. Foley, R. Kamalakaran, N. Grobert, H. Terrones, D. Tekleab, P. M. Ajayan, W. Blau, M. Ruhle, D. L. Carroll. *Nano Letters.* 2001, **9**, 457-460.
4. M. Terrones, P. M. Ajayan, F. Banhart, X. Blasé, D. L. Carroll, J.-C. Charlier, R. Czerw, B. Foley, N. Grobert, R. Kamalakaran, P. Kohler-Redlich, M. Ruhle, T. Seeger, H. Terrones. *Applied Physics A.* 2002, **74**, 355-361.
5. O. Stephan, P. Ajayan. *Science.* 2004, **266**, 1863-1865.
6. J. D. Wiggins-Camacho, K. L. Stevenson. *The Journal of Physical Chemistry C.* 2009, **113**, 19082-19090.
7. K. Fujisawa, T. Tojo, H. Muramatsu, A. L. Elías, A. M. Vega-Díaz, F. Tristán-López, J. H. Kim, T. Hayashi, Y. A. Kim, M. Endo, M. Terrones. *Nanoscale.* 2011, **3**, 4359-4364.
8. D. L. Carroll, Ph. Redlich, X. Blasé, J.-C. Charlier, S. Curran, P. M. Ajayan, S. Roth, M. Ruhle. *Physical Review Letters.* 1998, **81**, 2332-2335.
9. H. Mousavi, R. Moradian. *Solid State Sciences.* 2011, **13**, 1459-1464.
10. K. Liu, Ph, Avouris, R. Martel. *Physical Review B.* 2001, **63**, 1611404 (1-4).
11. K. Fujisawa, T. Hayashi, M. Endo, M. Terrones, J. H. Kim, Y. A. Kim. *Nanoscale.* 2018, **10**, 12723-12733.
12. S. Ali, T. liu, Z. lian, B. Lo, D. S. Su. *Journal of Materials Chemistry A.* 2017, **5**, 16653-16662.
13. Z.-W. Tian, X.-Q. Cui, J.-K. Tian, M.-C. Cui, L. Jin, R. Jia, R. I. Eglitis. *Journal of Saudi Chemical Society.* 2020, **24**, 857-864.
14. D. Golberg, Y. Bando, W. Han, K. Kurashima, T. Sato. *Chemical Physics Letters.* 1999, **308**, 337-342.
15. C. P. Ewels, M. Glerup. *Journal of Nanoscience and Nanotechnology.* 2005, **5**, 1345-1363.
16. M. Yudasaka, R. Kikuchi. Y. Ohki, S. Yoshimura. *Carbon.* 1997, **35**, 671-676.
17. R. B. Sharma, D. J. Late, D. S. Joag, A. Govindaraj, C. N. R. Rao. *Chemical Physics Letters.* 2006, **428**, 102-108.

18. J. Zhao, R. Luque, M. R. H. S. Gilani, J. Lai, A. Nsabimana, G. Xu. *Journal of Materials Chemistry A.* 2018, **6**, 23780-23786.
19. Z. Yang, H. Nie, X. Chen, X. Chen, S. Huang. *Journal of Power Sources.* 2013, **236**, 238-249.
20. N. E. Benti, G. A. Tiruye, Y. S. Mekonnen. *RSC Advances.* 2020, **10**, 21387-21398.
21. S. Majeed, J. Zhao, L. Zhang, S. Anjum, Z. Liu, G. Xu. *Nanotechnology Reviews.* 2013, **2**, 615-635.
22. L. Chen, Z.-H. Huang, H.-W. Liang, H.-L. Gao, S.-H. Yu. *Advanced Functional Materials.* 2014, **24**, 5104-5111.
23. J. Yi, Y. Qing, C. T. Wu, Y. Zeng, Y. Wu. X. Lu, Y. Tong. *Journal of Power Sources.* 2017,**351**, 130-137.
24. J. Zhou, X. Shan, J. Ma, Y. Gu, Z. Qian, J. Chen, H. Feng. *RSC Advances*. 2014, **4**, 5465-5468.
25. M. Wang, Y. Li, J. Fang, C. J. Villa, Y. Xu, S. Hao, J. Li, Y. Liu, C. Wolverton, X. Chen, V. P. Dravid, Y. Lai. *Advanced Energy Materials.* 2020, **10**, 1902736 (1-8).
26. A. R. Maclntosh, G. Jiang, P. Zamani, Z. Song, A. Riese, K. J. Harris, X. Fu, Z. Chen, X. Sun, G. R, Goward. *The Journal of Physical Chemistry C.* 2018, **12**, 6593-6601.
27. E. Cruz-Silva, D. A. Cullen, L. Gu, J. M. Romo-Herrera, E. Muñoz-Sandoval, F. López-Urías, B. G. Sumpter, V. Meunier, J.-C. Charlier, D. J. Smith, H. Terrones, M. Terrones. *ACS Nano.* 2008, **2**, 441-448.
28. B. V. Kumar, R. Kumar, O. Friedman, Y. Golan, A. Gedanken, O. Shefi. *Chemistry Select.* 2019, **4**, 4222-4232.
29. J. Song, Z. Yu, M. Gordin, X, Li, H. Peng, D. Wang. *ACS Nano.* 2015, **9**, 11933-11941.
30. X. Chen, Q. Shen, Z. Li, W. Wan, J. Chen, J. Zhang. *Applied Materials and Interfaces.* 2020, **12**, 654-666.
31. I. O. Maciel, J. Campos-Degaldo, M. A. Pimenta, M. Terrones, H. Terrones, A. M. Rao, A. Jorio. *Physica Status Solidi B.* 2009, **246**, 11-12.
32. G. Ruiz-Soria, T. Susi, M. Sauer, K. Yanagi, T. Pichler, P. Ayala. *Carbon*. 2015, **81**, 91-95.
33. V. Griadun. *InTech: Carbon nanotubes.* J. M. Marulanda (Editor), 2010, Chapter 8, 147-168.
34. H. Sternschulte, K. Thonke, R. Sauer, S. Koizumi. *Physical Review B.* 1999, **59**, 12924-12927.

35. E. Cruz-Silva, F. Lopez-Urias, E. Munoz-Sandoval, B. G. Sumpter, H. Terrones, J.-C. Chrlier, V. Meunier, M. Terrones. *ACS Nano.* 2009, **3**, 1913-1921.
36. E. Cruz-Silva, F. Lopez-Urias, E. Munoz-Sandoval, B. G. Sumpter, H. Terrones, J-C. Charlier, V. Meunier, M. Terrones. *Nanoscale.* 2011, **3**, 1008-1013.
37. S. Wang, D. Yu, L. Dai. *Journal of the American Chemistry Society.* 2011, **133**, 5182-5185.
38. Z. Liu, Q. Shi, F. Peng, H. Wang, R. Zhang, H. Yu. *Electrochemistry Communication.* 2012, **16**, 73-76.
39. M. Borghei, N. Laocharoen, E. Kibena-Põldsepp, L.-S. Johansson, J. Campbell, E. Kauppinen, K. Tammeveski, O. J. Rojas. *Applied Catalysis B: Environmental.* 2017, **204**, 394-402.
40. Z. Xin, S. Wang, J. Wang, X. Huang, X. Ji, Y. Yao, L. Shao. *Electrochemistry Communications.* 2016, **67**, 26-30.
41. Z. Liu, Q. Shi, R. Zhang, Q. Wang, G. Kang, F. Peng. *Journal of Power Sources.* 2014, **268**, 171-175.
42. Y. Xia, H. Shang, Q. Zhang, Y. Zhou, X. Hu. *Journal of Electroanalytical Chemistry.* 2019, **840**, 400-408.
43. M.-Q. Guo, J.-Q. Huang, X.-Y. Kong, H.-J. Peng, F.-Y. Qian, L. Zhu, W.-C. Zhu, Q. Zhang. *New Carbon Materials.* 2016, **31**, 352-362.
44. J. Liu, H. Liu, Y. Zhang, R. Li, G. Liang, M. Gauthier, X. Sun. *Carbon*. 2011, **49**, 5014-5021.
45. D. Larrude, M. E. H. Maia da Costa, F. H. Monteiro, A. L. Pinto, F. L. Freire Jr. *Journal of Applied Physics.* 2012, **111**, 064315 (1-6).
46. O. Maciel, J. Campos-Delgado, E. Cruz-Silva, M. A, Pimenta, B. G. Sumpter, V. Meunier, F. Lopez-Urias, E. Munoz-Sandoval, H. Terrones, M. Terrones, A. Jorio. *Nano Letters.* 2009, **9**, 2267-2272.
47. F. Mohammadi, H. Tovakol. *Fullerenes, Nanotubes and Carbon Nanostructures.* 2018, **26**, 218-225.
48. Y. Tong, X.-Y. Zhang, Q. Wang, X. Xu. *Computational and Theoretical Chemistry.* 2015, **1059**, 1-6.
49. Z. Liu, F. Peng, H. Wang, H. Yu, J. Tan, L. Zhu. *Catalysis Communication.* 2011, **16**, 35-38.
50. L.-P. Yuan, Z.-Y. Wu. W.-J. Jiang, T. Tang, S. Niu, J.-S. Hu. *Nano Research.* 2020, **13**, 1376-1382.

51. J. Patiño, N. López-Salas, M. C. Gutiérrez, D. Carriazo, M. L. Ferrer. F. del Monte. *Journal of Materials Chemistry A.* 2016, **4**, 1251-1263.
52. J. C. Slater. *Journal of Chemical Physics.* 1964. **41**, 3199-3205
53. B. Cordero, V. Gómez, A. E. Platero-Prats, M. Revés, J. Echeverria, E. Cremades, F. Barragán, S. Alvares. *Dalton Transactions.* 2008, **21**, 2832-2838.
54. T. L. Cottrell. *The strength of chemical bonds. 2nd edition*. 1958, Butterworths, London.
55. B. deB. Darwent. *National Standard Reference Data Series. National Bureau Standards.* 1970, No. 31, Washington DC.
56. S. W. Benson. *Journal of Chemical Education.* 1965, **42**, 502-518.
57. S. Santangelo, G. Messina, G. Faggio, M. Lanza, C. Milone. *Journal of Raman Spectroscopy*. 2011, **42**, 593-602.
58. R. A. Dileo, B. J. Landi, R. P. Raffaelle. *Journal of Applied Physics.* 2007, **101**, 064307 (1-5).
59. M. S. Dresselhaus, G. Dresselhaus, M. Hofmann. *Philosophical Transactions of the Royal Society.* 2008, **366**, 231-236.
60. L. M. Malard, M. A. Pimenta, G. Dresslhaus, M. S. Dresselhaus. *Physics Reports.* 2009, **473**, 51-87.
61. https://www.chemicalbook.com/ChemicalProductProperty_EN_CB8771461.html Date accessed: 27/06/2021.
62. X. Wu, K. Gong, G. Zhao, W. Lou, X. Wang, W. Liu. *RSC Advances.*2018, **8**, 4595-4603.
63. D. Yu, Y. Xue, L. Dai. *Journal of Physical Chemistry Letters.* 2012, **3**, 2863-2870.
64. Y. Wang, S. Zuo, J. Yang, S.-H. Yoon. *Langmuir.* 2017, **33**, 3112-3122.

Chapter 7: The dispersion of pristine MWCNTs in aqueous and organic solvents.

7.1. Introduction.

CNTs have exceptional conductivity, high mechanical, and thermal stability, and they also possess a high aspect ratio. This is due to their micro-meter length versus their nano-meter diameter. The high aspect ratio coupled with strong inter-tubal Van de Waals forces leaves them entangled and bundled, with high cohesive strength, and high hydrophobicity, which exacerbates their tendency to agglomerate and makes them insoluble in water and various organic solvents.[1-10] The use of CNTs in many devices has been extensively reported, however, this agglomeration issue has an impact on the pre-processing of the CNTs needed for making any device, making it a nontrivial issue. A lot of research has gone into overcoming this limitation, as it has impact on the development of CNT applications in varying fields.[1-2, 9-17]

A critical question that arises from investigations meant to improve the solubilization of CNTs is: do CNTs dissolve in solvents, and should the resulting CNT-solvent mixtures be described as a solution? The answer is no. However, it is noted that in the literature many authors describe CNTs as being soluble in a solvent. Solution and solubility describe a process of individualizing CNTs completely and creating a thermodynamically stable system. CNTs are found to form thermodynamically metastable systems that are kinetically stable but form colloids or suspensions, but not homogenous solutions. So, despite reports of uniform "solutions" being obtained, CNTs in any solvent should be described as dispersed rather than dissolved. Dispersion describes a process the separation of the smallest dispersible unit of agglomerate from its bulk into its host matrix system resulting in the formation of a colloid or suspension. [1, 10, 18-21]

This differentiation was illustrated by Sun *et al* using the Tyndall effect. Solutions do not scatter or reflect light, but colloids and suspensions do.[1] By shining a laser through prepared CNT dispersions, they were able to observe the Tyndall effect (i.e., reflection and scattering) in all their prepared dispersions. This corroborates that CNTs tend to form colloids and suspensions, and whether a colloid or suspension forms depends on the concentration of the dispersion.[1]

Obtaining a significantly de-bundled and homogenous dispersion of CNTs is dependent on several factors. A dispersion may be obtained using physical techniques such as conventional stirring, ultrasonication[22-24], centrifugation[25-27], plasma and irradiation[28-31], and electrophoresis[32-33], or a combination of these methods may also be employed. Even though techniques such as ultrasonication, plasma and irradiation are of a physical nature, they tend to affect the structural integrity and consequently the morphology of the CNTs. Sonication has been reported to be able to reduce the CNT length and to strip off graphitic layers.[34-36] In contrast, some plasma techniques such as those based on oxygen, tend to add hydrophilic groups to the CNT structure[37]. Dispersion is also reliant on the type of solvent that is used, and more precisely on the solvent polarity and structure. The dispersive ability of solvents such as water[38-40], ethanol[41-43], DCM[44-45], nematic liquid crystals[46], isopropyl alcohol[47-48], DMF[49] have been investigated. Different pressure and temperature conditions can also be used to aid in the dispersion of CNTs. Jagadish *et al.* reported improved dispersion of MWCNTs using hydrothermal supercritical conditions in an autoclave at the supercritical temperatures of four different solvents.[2]

In addition to these factors, there exists strategies such as functionalization for aiding in obtaining sufficiently de-bundled and homogenized dispersions. This process may be physical or chemical in nature.[50-55] Chemical functionalization of CNTs involves the addition of functional groups to the structure of the CNTs, largely on the surface of the outer layers, and tips. This process leads to a loss in the conjugated π-electron system as hybridization changes from sp^2 to sp^3 in the structure.[50-60] Different chemical reactions such as oxidation[61-62], ozonolysis[63-64], Diels-Alder[65-66], and fluoronation[67-68], have been utilized to functionalize and give variants of CNTs (**Figure 7.1**).

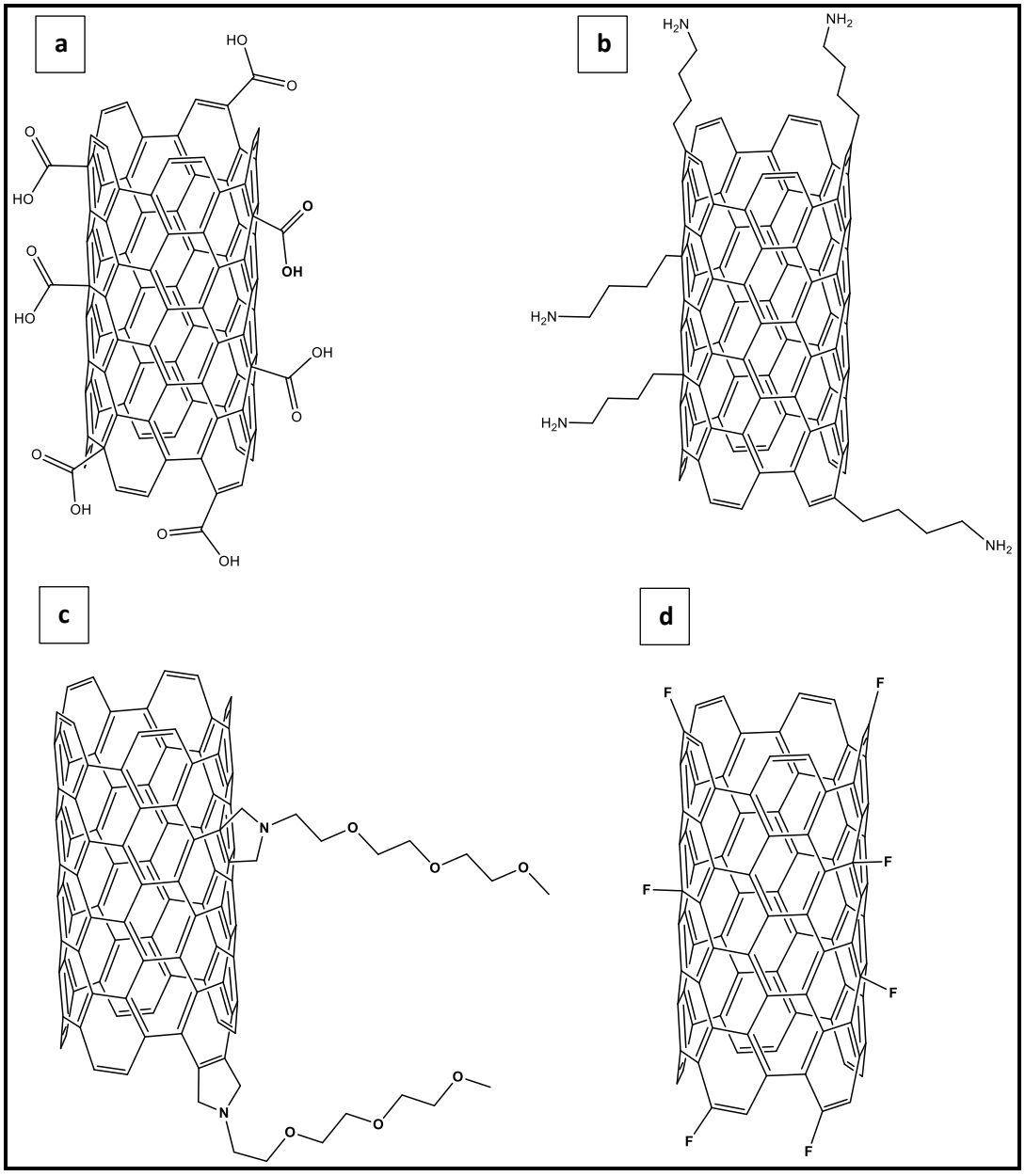


Figure 7.1: Functionalization of CNTs. Reaction conditions: a) H_2SO_4/HNO_3,[69] b) *(i)*HNO_3, *(ii)* $SOCl_3$, 65℃, 24 h. *(iii)* poly(ethylene glycol) bis(3-aminopropyl), 60℃, 24 h.[70] c) R-$NHCH_2CO_2H(CH_2O)_n$ in DMF, 130℃ .[71] d) F_2, 50-200℃ , 5 days.[72]

Depending on the types of groups that are added, and solvents used, improvement in dispersibility can be developed. In the case of polar solvents like water or solvents with polar groups such as ethanol and acetone, this improvement is attributed to the presence of the COOH, C-OH, C-NH_2 functional groups that participate in hydrogen bonding. Additionally, the functional groups on the surface of the CNTs tend to discourage inter-tubal interaction (i.e., agglomeration).[61-72] This technique has been successfully utilized in improving the dispersibility of CNTs. Additionally, this methodology can also modify the CNT chemistry,

for example, fluorinated CNTs are more reactive than pristine CNTs due to the weak C-F bonds present.[73] Moreover, functionalization of CNTs tend to improve the properties (mechanical, thermal) of polymer composites due to their improved interaction and ability to disperse within the polymer matrix.[74-75] Due to their improved dispersibility in different solvents, functionalized CNTs can produce 'smooth' CNT based films, an essential property for excellent electro-catalytic activity and electron transport.[76-77] However, the damage that this technique does to the structure of the CNTs leads to a deterioration in their electrical conductivity, thermal and mechanical properties.[78-79]

Consequently, techniques for the dispersion of CNTs that are non-covalent (i.e., do not damage the structure of the CNTs) have been developed. Polymer[80-85] and surfactant[86-95] assisted dispersion have become of great interest. Polymer assisted dispersion techniques that are covalent in nature have been used[96-97] e.g., covalent functionalization of CNTs produced from the arc discharge method using polyethylene glycol terminated with tetrahydrofurfuryl. The resulting dispersion not only led to improved dispersion but gave a highly viscous dispersion.[98] Non-covalent polymer functionalization has had a great deal of success and offers the advantage of not altering the structure of the CNTs. The groups can attach themselves to the surface of the CNTs using Van der Waals interactions such as hydrogen bonding, CH-π, and $\pi - \pi$ interactions. Furthermore, depending on the chain length of the polymer, they tend to wrap themselves around the surface of the tubes. These factors, coupled together prevent extensive agglomeration of CNTs by reducing inter-tubal interactions, thus improving dispersion homogeneity and stability.[80-85, 99-102] Additionally, when pH sensitive polymers are used, altering the pH of the solution influences the extent of dispersion.[103] Several studies that involve the use of different solvents, dispersion aids and techniques, including some of the key findings are listed in Table 7.1.

Table 7.1: Reported dispersion studies of MWCNTs

Dispersion medium	Dispersion technique	Key findings	References
Polymer matrix: Elastomer poly(dimethylsiloxane) (PDMS) in Chloroform or THF	10-minute sonication of CNT-solvent mixture, addition of PDMS followed by 14 minutes mechanical stirring and 1 minute.	Both THF and chloroform suspensions were stable for 27 h and 42 h, respectively.	103
Polymer matrix: Linear low-density polyethylene (LLDP) with a polyethylene glycol additive.	Melt mixing at 200℃, 200 rpm, for 5 minutes using a twin-screw micro-compounder.	Composite nearly free of MWCNTs agglomerates, which led to a decrease in electrical volume resistivity of the composite.	104
Solvent matrix: N-methyl-2-pyrrolidone (NMP), N, N-dimethylformamide (DMF), Tetrahydrofuran (THF).	Sonication and left to stand for a week.	NMP resulted in the most stable dispersion, while DMF and THF showed separation after 7 days.	105
Solvent matrix: benzyl alcohol, 1,2 dirchloro-benzene, chloroform, DMF.	Tip sonication for 15 minutes in an ice bath, followed by ultracentrifugation at 10k rpm for 1h.	DMF gave better dispersion of MWCNTs with oxygen containing functional groups, while chloroform and benzyl alcohol gave better dispersions of MWCNTs with nitrogen containing functional groups.	106
Solvent matrix: chloroform, acetone, toluene.	Dispersed using ultrasound for 4h.	The MWCNTs were successfully dispersed in all solvents without aid, and remained stable for 10 days	107

Solvent matrix: Water	Sonicated at different time intervals: 10, 20, 30, 40 minutes.	Concentration of suspended MWCNTs increased with sonication time. The mechanical property of MWCNTs-cement composite improved with an increase in sonication time of the MWCNTs dispersion.	108
Surfactant matrix: aqueous TX100, aqueous SDS, aqueous TX100-SDS solutions.	Vials were shaken at 150 rpm at 25℃ for 7 days, followed by centrifugation at 3000 rpm for 30 minutes.	TX100 presented with better dispersive ability than SDS, while SDS resulted in more stable dispersions. The combination of both surfactants reduces the concentration of suspended MWCNTs.	109
Surfactant matrix: ethanol-SDS, ethanol-TX100, ethanol-pluronic F-127, ethanol-CTAB, ethanol-span-60	Ultrasonication for 3 h.	The following trend in dispersability was observed; CTAB < pluronic F127 < TX100 < span-60 < SDS.	110
Surfactant matrix: aqueous-SDS, aqueous-DTAB, aqueous-SDS-DTAB.	Mechanical stirring for 6 h, followed by sonication for a 100 min, and the resulting dispersions were centrifuged for 30 min at 3000 rpm.	SDS and DTAB exhibited poor dispersive ability than the SDS-DTAB mixture.	111
Surfactant matrix: aqueous-SDS, aqueous-SDBS, aqueous-Dichlorobenzene (DB).	Ultrasonication for 40 min.	Surfactant containing dispersions had good stability. DB presented with the better dispersability, but SDBS and SDS resulted in dispersions with better stability. The dispersions	112

		containing SDS reported the best thermal conductivity.	

The ability of surfactants to produce stable and homogenous dispersions is largely attributed to their chemical structure; they have both hydrophilic (i.e polar functional groups, cationic or anionic) and hydrophobic components, and their basic chemical structure consists of a head and tail. The head is generally hydrophilic, while the tail is hydrophobic.[113-114] The different polarities in the structure are central to the surface functionalization mechanism of the CNTs, and how they behave in a solvent. There exist four general types of surfactants, non-ionic, cationic, anionic, and zwitterionic, and examples of each are shown in **Figure 7.2**. [115]

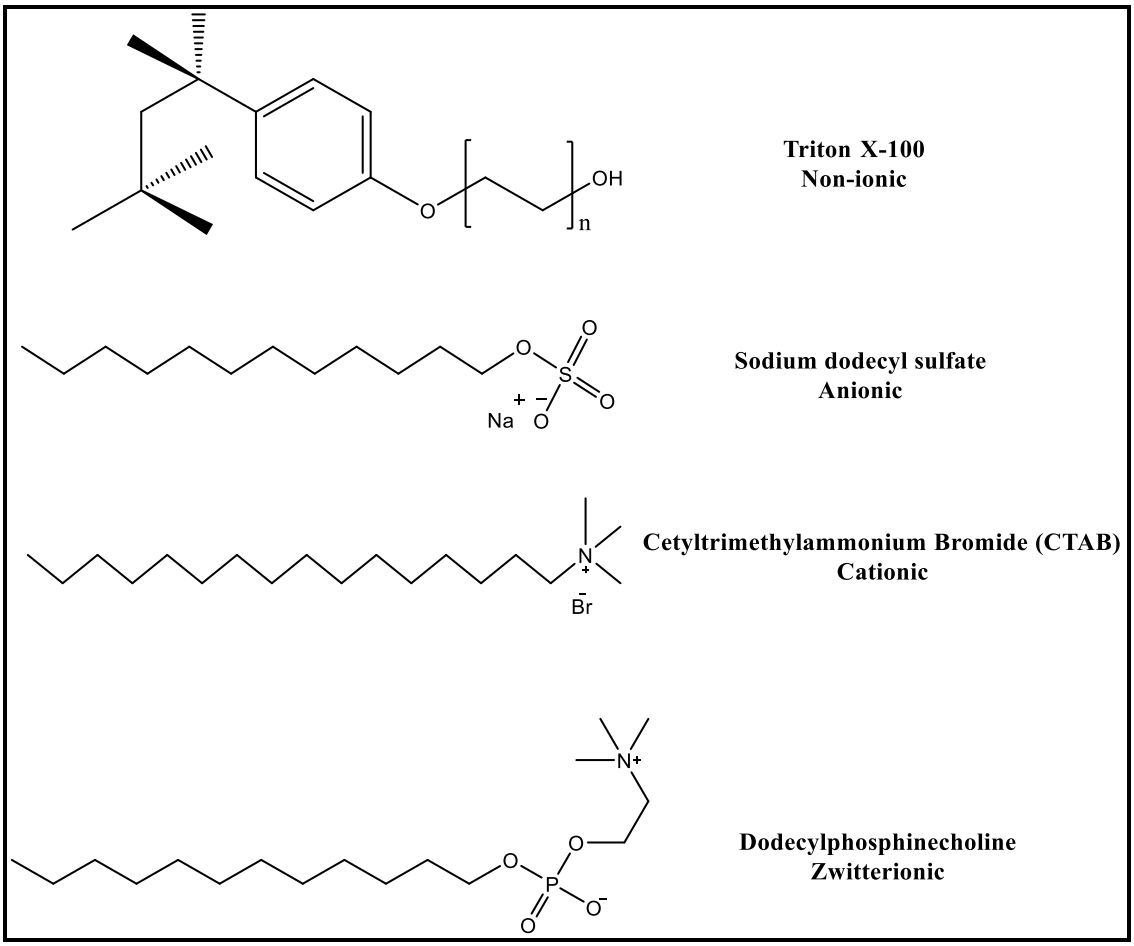


Figure 7.2: Types of surfactants and their corresponding example

In a simple dispersion, obtained without aid, the interactions are between CNTs and the solvent. A homogenous and stable dispersion is obtained when on average the physical interactions between the CNTs and solvent are stronger than the CNT-CNT or solvent-solvent interactions.

The addition of a surfactant introduces more interactions within the dispersion. Given the existence of both hydrophilic and hydrophobic groups in the structure, the surfactant interacts with both the CNTs and the solvent. Hence, when poor dispersion in observed (CNT-CNT interaction > solvent-solvent interaction), the addition of a surfactant tends to lead to improved dispersion and stability by interacting with both the solute (i.e., CNTs) and solvents. The hydrophobic component of the surfactant interacts with the CNTs while the hydrophilic component interacts with the solvent.[109, 114]

Depending on the combination of the solvent and surfactant, the concentration of the surfactant in the dispersion is critical. There exists a concentration level at which it begins to self-assemble and form polymerized supramolecular aggregates called micelles, thus leading to the reduced dispersion of the solute. This is referred to as the critical micelle concentration (CMC), and it is different for the same surfactant in varying solvents.[116-118]

Apart from polymers and surfactants, other chemicals such as inorganic salts[119-120], organic acids[121-122], sugars[123] and biomolecules[124], and natural products[125] have been utilized to aid in the dispersion of CNTs. Given the diversity of dispersants available, the choice of dispersant is also influenced by the application in which the CNTs are to be utilized. For example, Leu *et al* used a non-conductive dispersant poly(oxyethylene)-segmented imine (POEM) to aid in the dispersion of pristine and boron doped CNTs for the fabrication of thin films. However, they found that despite the improved dispersion, the conductivity and electrocatalytic activity of the resulting films had deteriorated due to the presence of the POEM. The subsequent removal of the dispersant saw an increase in both properties. Additionally, their work indicated that should removal of a dispersant be necessary, the method of removal is important, and it should be one that minimizes damage to the material.[76]

As summarized in Table 7.1, various methods have been used to successfully disperse MWCNTs. Additionally, UV-vis analysis has been used quantitatively and qualitatively to determine and compare the dispersive ability of different mediums. The dispersive ability of a medium is directly correlated to the concentration of MWCNTs in the resulting dispersion. The concentration can be deduced from the Beer Lambart's law: $A = \varepsilon bc$, where A is the absorbance of the sample, ε is the molar absorbivity, b the path length of light, and c is the concentration of the sample.[103-112, 126-129] *Sharma et al.* reported how covalent functionalization of MWCNTs using acids (HNO_3 and H_2SO_4) and combinations thereof, affected their dispersability in an SDS solution. HNO_3 treated MWCNTs gave the largest absorbance and

more readily dispersed in the solution.[126] Li *et al* determined that MWCNTs dispersed in an SDS solution reported lower absorbance than those dispersed in a TX100 solution, indicating that TX100 is better at aiding MWCNTs dispersion than SDS.[109] In addition, Sabri *et al.* reported NMP to be a better dispersive medium than DMF and THF, because their dispersions recorded the lowest absorbance.[105]

In this study, the dispersion of HNO_3 treated MWCNTs in several dispersion mediums with different polarities has been determined. The CNTs were dispersed in different volumes of water and some commonly used organic solvents (EtOH, ethyl acetate, toluene, hexane, and dichloromethane (DCM)), using a combination of conventional stirring and ultrasonication at room temperature. These solvents were chosen due to differences in their chemical and physical properties such as polarity, viscosity, and structure (aliphatic, aromatic, halogenated).

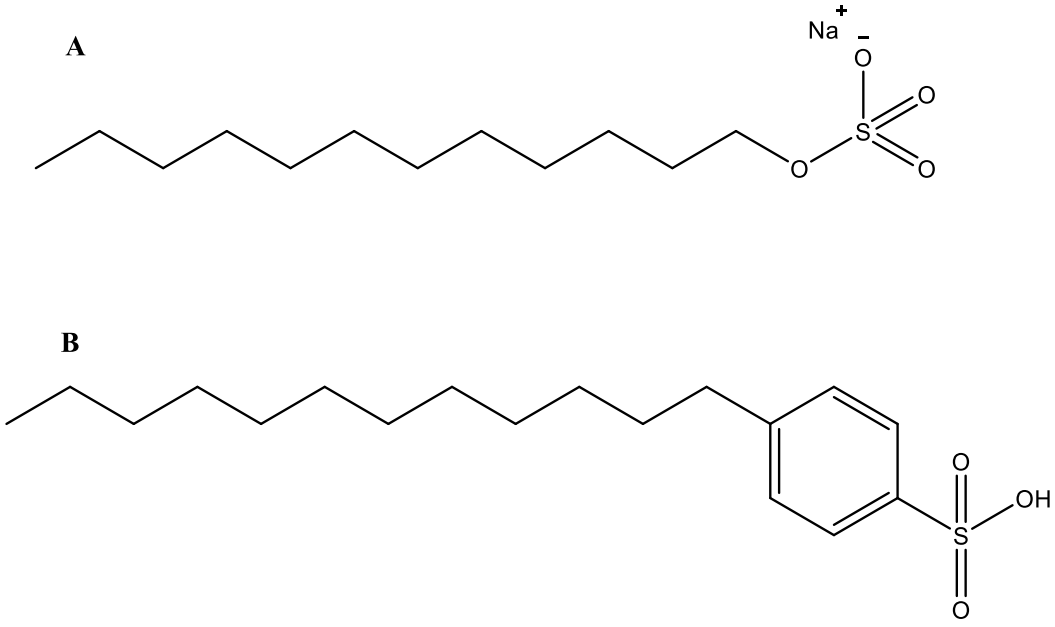


Figure 7.3: Structure of surfactants. a) SDS, b) dodecylbenzenesulfonic acid (DBSA)

Additionally, the influence of surfactants SDS and DBSA (**Figure 7.3**), and their combination thereof at different concentrations (by weight) in water and ethyl acetate were also investigated. The dispersive ability of each solvent and surfactant was studied qualitatively using UV-vis spectroscopy. In addition to the challenges associated with the processability (i.e., dispersion) of MWCNTs, one sample of MWCNTs tends to contain nanotubes with different morphologies. As a result, the sample has a distribution of properties such as conductivity and aspect ratio. This means that the thin films fabricated from such a sample exhibits the average behaviour of these different properties and depending on the application this could be

detrimental to the performance of the thin film. Hence, it is essential to explore methods of separating nanotubes of different properties to exploit them separately. Successful separation will allow for improvement in the tailoring the nanotubes for different application. So, this work also aimed at leveraging the differences in aspect ratios, and consequently diameter of the nanotubes to separate them using different solvents. Given that diameter is proportional to the optical band gaps of nanotubes, the optical band gap of the MWCNTs in each dispersion was determined using their UV-vis data to corroborate the successful separation of the nanotubes according to diameter.

7.2. Materials and Methods.

7.2.1. Starting material.

Ethanol (EtOH), dichloromethane (DCM), hexane, toluene, and ethyl acetate were of analytical grade and used as obtained from Merck and Sigma Aldrich. In all experiments that required water, distilled water was utilized. Sodium dodecyl sulphate (SDS) and dodecylbenzenesulfonic acid (DBSA) were of reagent grade (Sigma Aldrich) and were used as received.

7.2.2. Dispersion of MWCNTs

7.2.2.1. Dispersion of MWCNTs in water and organic solvents.

Pristine MWCNTs (40 mg, sample PP700) were added to different solvents (water, ethyl acetate, EtOH, hexane, toluene, DCM, and chloroform). Three different concentrations of each solvent were prepared by varying the volume (10.0 ml, 15.0 ml, and 20.0 ml) used. These were then stirred for 5 h and then ultra-sonicated (37℃) for 1 h and the resulting solutions were left to stand for 24 h. The supernatant solutions (5.0 ml) were collected, with minimal disturbances to the solution, using a syringe, and were analysed by UV-vis spectroscopy. Dispersions that were too concentrated (i.e., opaque) to analyse using the UV-vis instrument were diluted until they were transparent; 5.0 ml of the supernatant dispersion was collected and then diluted to 20.0 ml. If the dispersion was still too concentrated, a 2nd dilution was performed; 2.5 ml from the 1st dilution was diluted to 10.0 ml. The resulting dispersions were added to a quartz cuvette and the UV-vis spectra were recorded between 300 nm to 800 nm. The absorbance of the supernatant portions of the dispersions were correlated to the concentration of the MWCNTs in each dispersion using the relationship expressed by the Beer Lambart law ($A = \varepsilon bc$).

7.2.2.2. Surfactant aided dispersion of MWCNTs in water and ethyl acetate.

Method A:

Four surfactant (SDS and DBSA) solutions with concentrations of 0.4 mg/ml, 0.8 mg/ml, 1.6 mg/ml, and 2.5 mg/ml were prepared in 10.0 ml of water and ethyl acetate. Pristine MWCNTs (40 mg) were added to all the solutions. These were stirred for 5 h and ultra-sonicated (37℃) for 1 h. The resulting dispersions were left to stand for 24 h. The supernatant dispersions (5.0 ml) were collected with minimal disturbances to the dispersion using a syringe and analysed (3 ml) by UV-vis spectroscopy. Dilutions, if needed, were achieved by the procedure reported in 7.2.2.1. The resulting dispersions were added to a quartz cuvette and the UV-vis spectra recorded from 300 nm to 800 nm.

Method B:

The mass of surfactants that produced the best dispersion in ethyl acetate and water from *Method A* were used to produce two solutions. A mixture of SDS (8 mg) and DBSA (25 mg) in 10.0 ml ethyl acetate and a second mixture of SDS (4 mg) and DBSA (25 mg) in 10 ml water were prepared. Pristine MWCNTs (40 mg) were added to both solutions and stirred for 5 h and ultra-sonicated (37℃) for 1 h, and the resulting dispersions were left to stand for 24 h. The supernatant dispersions (5.0 ml) were collected with minimal disturbances to the solution using a syringe and analysed by UV-vis spectroscopy. Dilutions, if needed, were achieved by the procedure reported in 7.2.2.1. The resulting dispersions were added to a quartz cuvette and the UV-vis spectra recorded from 300 nm to 800 nm.

7.2.2. Characterization techniques.

The optical properties and concentrations of the prepared dispersions were investigated at a wavelength range between 300-800 nm using a Analytikjena specord210 plus UV-vis instrument. To obtain the absorbance of only the MWCNTs in each dispersion, the solvents were used in the reference cell and in cases where the surfactants were used the mixture of the solvent and surfactant were used in the reference cell. An FEI Tecnai T12 Transmission Electron Microscope was used to obtain images of the pristine MWCNTs.

7.3. Results and Discussion

7.3.1. The dispersion of pristine MWCNTs in water and organic solvents.

The water and the organic solvents used exhibited different dispersive abilities, although UV-vis analysis was the primary characterization technique used to qualitatively assess this, the investigation highlighted physical observations that can be used to deduce the extent of the dispersive ability of each solvent.

(i) The obtained dispersions were either clear, transparent, or opaque. These physical observations are an indicator of how well dispersed the MWCNTs were in each solvent. Opaque dispersions had a higher concentration of MWCNTs suspended in the solvent, while clear dispersions are an indicator of a lower concentration of suspended MWCNTs.

(ii) When left to stand without agitation, the dispersions exhibited varying degrees and rates of MWNCTs agglomeration in different solvents (i.e., varying metastability-amount of time it takes for a large concentration of MWCNTs to agglomerate and collect at the bottom of the dispersion[127, 130-131]). Clear dispersions had low meta-stability (large concentration of MWCNTs rapidly agglomerated), and opaque dispersions had a higher metastability (small concentrations of MWCNTs remained agglomerated).

UV-vis analysis of the supernatant portion of the dispersions offered corroborating evidence for these physical observations. It is important to note that since the dispersions are suspensions and not solutions, the recorded spectra are not corrected for light scattering by the solution. Consequently, the reported absorbances are a combination of the absorbance by the solution and potential multiple light scattering induced absorbance by the sample. However, the margin of error reduces significantly as the dispersions are diluted, and recorded absorbance spectra become less accurate with an increase in opacity. Given that the analysed samples are clear or transparent, the recorded spectra are predominantly a consequence of light absorption by the sample (MWCNTs) instead of the scattering.[132]

All the three sets of dispersions per solvent (10, 15, 20 ml) for ethyl acetate and H_2O were opaque, while the EtOH dispersions were clear. These physical observations were consistent across all the different volumes of the solvents. Although ethyl acetate and H_2O dispersions were opaque, H_2O dispersions had the higher absorbance (**Figure 7.4a**) and consequently

constituted a larger concentration of suspended MWCNTs than ethyl acetate (**Figure 7.4b**) and ethanol. Ethanol dispersions reported the lowest absorbance (**Figure 7.4c**) relative to both solvents. Additional dispersions of MWCNTs were obtained using DCM, toluene, and hexane, and in all cases the MWCNTs/solvent mixtures gave clear solutions. DCM recorded the highest absorbance (**Figure 7.4d**), followed by toluene (**Figure 7.4e**), and hexane (**Figure 7.4f**).

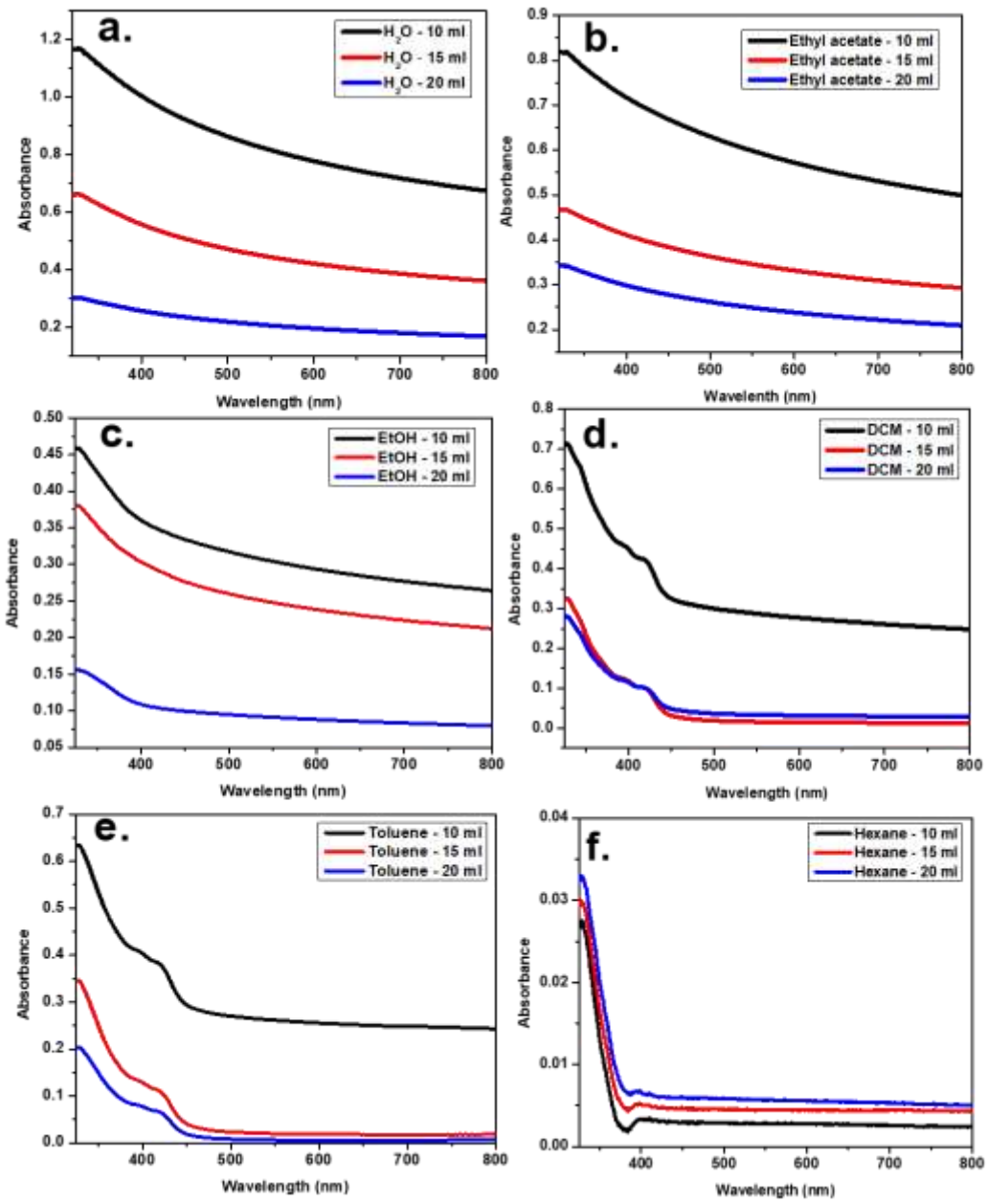


Figure 7.4a-f: UV-Vis spectra of pristine MWCNTs after dispersion in, a) ethyl acetate, b) water, c) EtOH, d) DCM, e) toluene, f) hexane.

The absorbance spectra (i.e., pattern/shape) of the dispersions were different across some solvents. For example, H_2O and ethyl acetate dispersions reported similar absorption patterns, but they were different to all the other dispersions. In addition, hexane dispersions had different absorbance patterns to DCM and toluene dispersions, which had similar absorbance patterns to each other. This suggested that dispersions with similar absorbance patterns had MWCNTs with similar configurational characteristics suspended in the solvent, while dispersions with differing patterns suspended MWCNTs with different characteristics. TEM analysis of the whole sample of MWCNTs (**Figure 7.5**) revealed that it contained MWCNTs with different diameters and length, indicating that they also had different aspect ratios (length to diameter ratio) that can result in unique dispersive properties in different dispersion mediums. As the sample contained MWCNTs with different aspect ratios, some dispersions obtained from different solvents reported different physical properties (opaque vs clear), and consequently different UV-vis spectra patterns. This indicated that different solvents could suspend MWCNTs with certain characteristics (i.e., aspect ratio), while other MWCNTs in the dispersion would collect at the bottom of the solution.

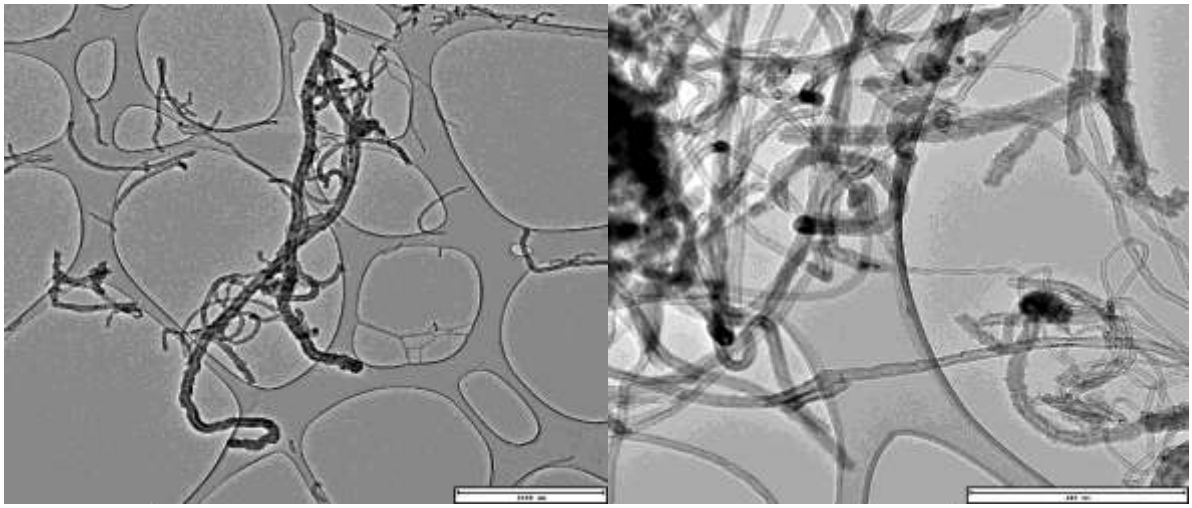


Figure 7.5: TEM images of pristine MWCNTs

To provide corroborating data that the MWCNTs in each solvent not only had different dispersive properties, but aspect ratios and consequently diameter in different dispersive mediums, the UV-vis data was used to determine the direct and indirect band gap energies (E_g) of the MWCNTs in each dispersion. The band gap of the CNTs is proportional to the diameter of the CNTs, direct band gap $(E_g) \approx \frac{1}{d}$.[133-136] These can be estimated from Tauc plots using the expression derived from Fermi Golden rules for an electronic transition (equation 1):

$$(\alpha h\nu)^{1/\gamma} = B(h\nu - E_g) \quad \text{(1)}$$

where α is the energy absorption coefficient, h is Planck's constant, B is a constant, and E_g is the band gap energy. The γ term is defined by the nature of the electronic transition; for direct allowed transition $1/\gamma$ is equal to ½, while for allowed indirect transitions $1/\gamma$ is equal to 2. A plot of $(\alpha h\nu)^{1/\gamma}$ (y-axis) and energy ($h\nu$, in eV) gives the Tauc plot. A linear extrapolation of the region that has a steep linear increase with light absorption (energy) onto the x-axis gives an estimation of the direct and indirect band gaps (**Figure 7.6a-c**).[126, 137-138] The application of this method requires an adherence to several 'rules'; one of which being that the absorbance of the material in question should not absorb or should have negligible absorbance at energies below the band gap energy (for an indirect bang gap, this includes the phonon required to complete the electron transition). Failure to observe this rule has been found to lead to distorted readings of the band gap energy, and this incorrect reading of the band gap has been found to be more pronounced in semiconducting materials, and those that have been chemically modified (i.e., doped, or covalent functionalization).[137] Consequently, given that the MWCNTs in question have been modified and all the dispersions (except for those derived from hexane) showed a noticeable absorbance below the band gap energy, an estimation of their band gaps from the Tauc plot will be accompanied by the abovementioned distorted reading (**Figure 7.6a-c**). The observed absorbance below the band gap energy can be attributed to several factors.

(i) The modification to the material (i.e., functionalization of MWCNTs) by the presence of localized intra-band gap states, these show up in the absorbance spectrum as an Urbach tail.[137]

(ii) The presence of MWCNTs with near metallic behaviour arising from high strain and torsion in the tubes, and thus absorb light with higher wavelengths.[33, 139-143]

(iii) The presence of MWCNTs with different chirality, and diameters.[133, 139-143]

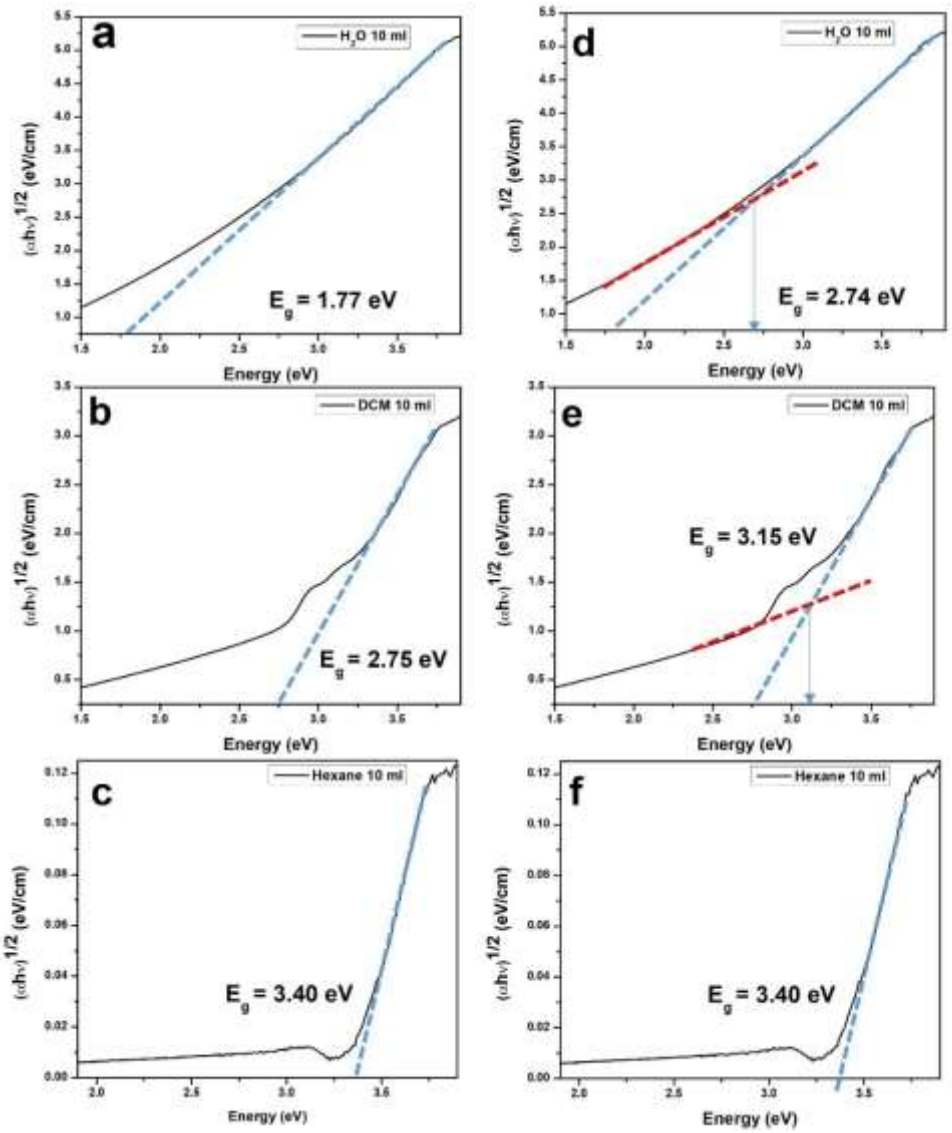


Figure 7.6a-c: Estimation of direct band gap energy: (a-c) without considering absorbance below the band gap energy (i.e., the Urbach tail), (d-f) considering the Urbach tail.

A study by Makaula *et al*. reported a method that addresses the aforementioned error in the method by combining the linear extrapolation onto the x-axis from the Tauc plot method with a linear fit extrapolation (also referred to as an abscissa) for the slope of the lower energy absorbance. The band gap estimations are read from where the two linear fits meet and has been reported to give a much more accurate estimation of the band gap energies (**Figure 7.6d-f**).[137] The method used in **Figure 7.6a-c** illustrated that ignoring the absorbance below the band gap leads to an underestimation of the band gap energies, which was corrected in **Figure 7.6d-f**. However, for samples that produce insignificant absorbance below the band gap estimation line (i.e., **Figure 7.6c** versus **Figure 7.6f**), little to no difference in band gap estimation was observed.

The direct and indirect band gap energies for the water and organic solvent-based dispersions are listed in Table 7.2. The dispersions from ethyl acetate and H_2O at different volumes presented have direct band gap energies of 2.76 eV and 2.74-2.75 eV, respectively. The table below shows indirect band gap energies of 2.99-3.01 eV (ethyl acetate) and 2.99-3.03 eV (H_2O). The differences in the band gap energies are insignificant and suggest that ethyl acetate and H_2O led to the suspension of the same type (i.e., morphology) of MWCNTs from the sample. The EtOH dispersions reported larger direct (3.01-3.03 eV) and indirect (3.24-3.26 eV) band gap energies relative to the MWCNTs in ethyl acetate and H_2O dispersions. The 10 ml DCM and toluene dispersions reported comparable direct band gap energies of 3.15 and 3.17 eV, respectively. Their diluted dispersions (15- and 20-ml) gave slightly higher direct band gap energies of 3.27 eV (DCM) and 3.27-3.29 eV (toluene) and indirect band gap energies of 3.40 eV (DCM) and 3.40-3.43 eV (toluene). The highest direct (3.35-3.40eV) and indirect (3.49-3.50 eV) band gap energies were observed in hexane dispersions. The similarities and differences in the band gap energies of MWCNTs in these dispersions corroborated those different solvents led to the suspension of MWCNTs with different properties, in their particular aspect ratio and diameter. Additionally, the smallest diameter MWCNTs (largest band gaps, > 3.0 eV) are better dispersed in hexane, DCM, and toluene while the larger diameter MWCNTs (lowest band gaps, 2.7 eV) are better dispersed in water and ethyl acetate.

Table 7.2: Direct and Indirect band gap energies of MWCNTs in different solvents.

	Direct band gap energy (eV)			Indirect band gap energy (eV)		
Dispersions	10 ml	15 ml	20 ml	10 ml	15 ml	20 ml
Water	2.74	2.75	2.75	2.99	3.03	3.00
Ethyl-acetate	2.76	2.76	2.76	2.99	3.00	3.01
EtOH	3.00	3.01	3.01	3.24	3.26	3.24
DCM	3.20	3.27	3.27	3.40	3.40	3.40
Toluene	3.20	3.27	3.29	3.40	3.43	3.43
Hexane	3.40	3.35	3.35	3.50	3.49	3.49

Tauc plots for the listed band gap energies are found in **Appendix 7A**.

7.3.2. The dispersion of MWCNTs in water and ethyl acetate using surfactants.

The study was extended to the use of surfactants to examine their effects on dispersions that had the highest concentration of suspended MWCNTs (i.e., highest absorbance). The dispersions with the highest absorbance, 10 ml of water and ethyl acetate dispersions, had different amounts (4 mg, 8 mg, 16 mg, and 24 mg) of SDS and DBSA added to them. The use of surfactants in the dispersion of MWCNTs introduces more interactions in addition to the MWCNTs-solvent, MWCNTs-MWCNTs and solvent-solvent interactions. These may include the MWCNTs-surfactant interactions, solvent-surfactant interactions, MWCNTs-surfactant-solvent interactions, surfactant-surfactant interactions, and surfactant-surfactant-solvent, surfactant-surfactant-MWCNTs, surfactant-surfactant-solvent-MWCNTs interactions. The nature of the dispersion obtained, opaque or transparent, and consequently the concentration of suspended MWCNTs is primarily determined by the relative strength of the MWCNTs-solvent and MWCNTs-surfactant-solvent interactions. A reduction or disruption of either interaction by either of the competing interactions can lead to a reduction in the amount of suspended MWCNTs.[127, 132] Three major interactions can cause this; (i) Solvent-solvent interactions, the energy barrier of which neither the MWCNTs nor surfactant can break, resulting in a lack of suspension of MWCNTs in the solvent. (ii) Strong MWCNTs-MWCNTs interactions, the energy barrier of which neither the solvent or surfactant can overcome, and thus lead to the agglomeration of MWCNTs. (iii) Surfactant-surfactant interactions, the tails of the surfactants are non-polar and have the potential to interact with each other more strongly than the MWCNTs, which leads to a formation of micelles. The structure of micelles is such that the hydrophilic tails are encapsulated by the hydrophilic head, so given that CNTs are predominantly hydrophobic, the MWCNTs-surfactant portion of the MWCNTs-surfactant-solvent interaction is disrupted. The formation of micelles is reported to occur at the critical mass concentration (CMC), that depends on the type of surfactant, and the solvent in which the surfactant is used.[118, 127-131, 140-143]

The SDS-ethyl acetate dispersions (**Figure 7.7a**) were all opaque, but the DBSA-ethyl acetate dispersions were transparent with absorbance values ranging from 0.063-0.12 (**Figure 7.7b**) compared to an absorbance of 0.81 for the 10 ml surfactant free dispersion. The use of DBSA at all amounts led to a general reduction in suspended MWCNTs. However, a more significant increase in absorbance of suspended MWCNTs is observed for the dispersion with 25 mg of DBSA. Additionally, the absorbance pattern of the DBSA-ethyl-acetate dispersions were

different from that of the surfactant free dispersions. Indicating that DBSA also influenced the type of MWCNTs that remained suspended in the solvent.

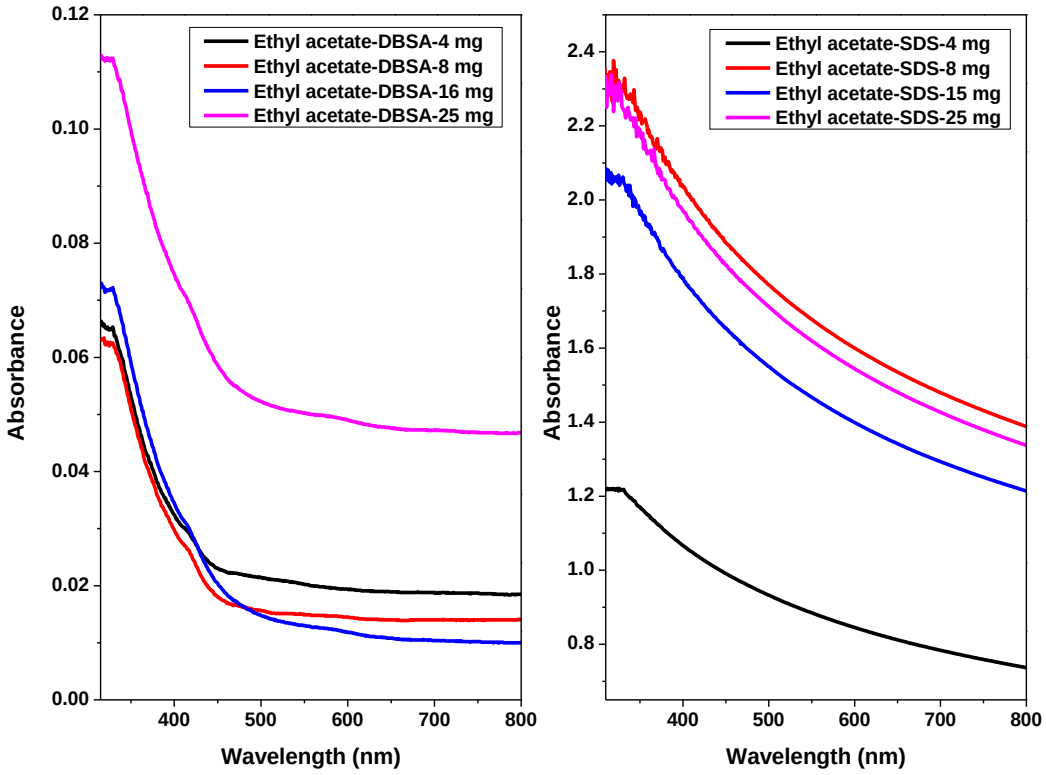


Figure 7.7a-b: UV-Vis spectra of pristine MWCNTs surfactant assisted dispersion in ethyl acetate: a) DBSA in ethyl acetate, b) SDS in ethyl acetate.

The SDS surfactant had a different effect on the concentration of suspended MWCNTs. The SDS-ethyl acetate dispersions with the same amount of MWCNTs used reported higher absorbance ranging from 1.22-2.38 (**Figure 7.8b**) compared to the 10 ml surfactant free dispersion (0.81). Additionally, the dispersions presented with similar absorbance patterns as the surfactant free dispersion, indicating that SDS did not influence the types of MWCNTs that remained suspended in the solvent matrix. A clear relationship between the mass of the SDS and suspended MWCNTs could not be established; 4 mg of SDS gave the lowest absorbance, which increased at 8 mg, but reduced at higher masses of 16 and 25 mg.

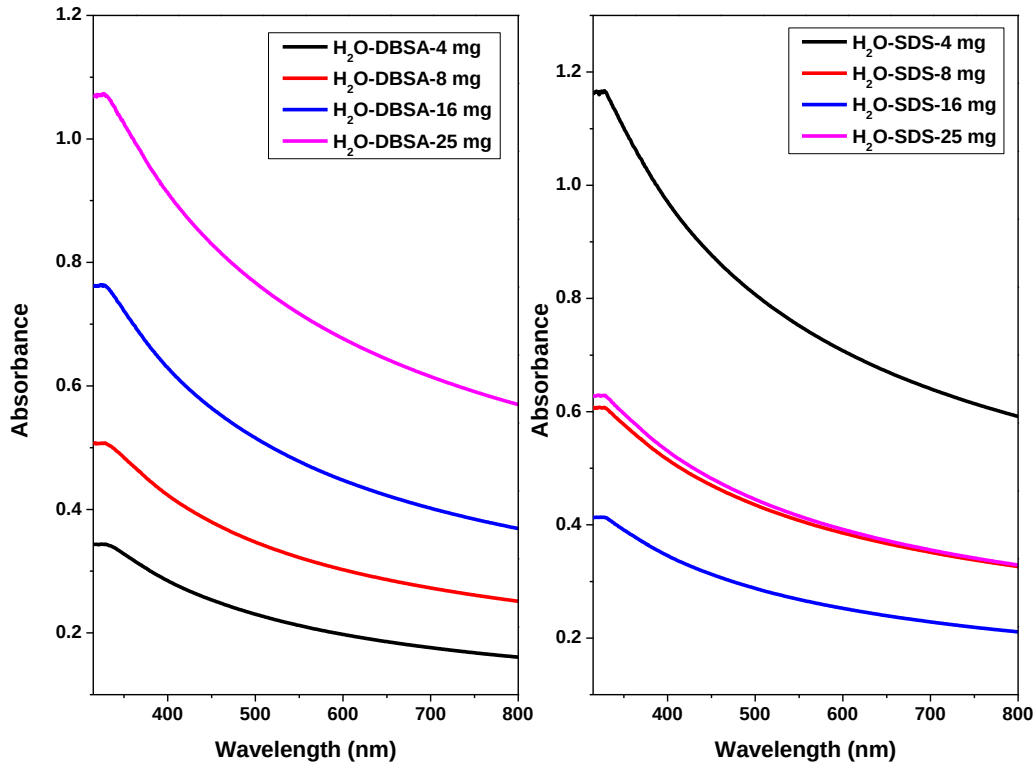


Figure 7.8a-b: UV-vis spectra of surfactant assisted pristine MWCNTs dispersions in water: a) DBSA in water, b) SDS in water.

The use of SDS and DBSA in H_2O both led to the production of opaque dispersions and the opacity was found to increase with DBSA mass but decreased with an increase in SDS mass. The observation was consistent with the UV-Vis data (**Figure 7.8a-b**); both surfactants with suspended MWCNTs gave dispersions with lower absorbance relative to the surfactant free H_2O dispersion. The 10 ml surfactant free dispersions gave an absorbance of 1.19, while DBSA-H_2O and SDS-H_2O dispersions reported absorbance ranging from 0.35-1.18 and 0.41-1.17, respectively. The DBSA mass was directly proportional to the suspended MWCNTs concentration, while the SDS mass was inversely proportional to the suspended MWCNTs concentration. For the SDS-H_2O dispersions, the absorbance at 25 mg increased to a value comparable to that of the dispersion with 8 mg of SDS. The use of SDS and DBSA in H_2O does not appear to influence the types of MWCNTs that get suspended in water as they presented with similar absorbance patterns to each other and the surfactant free dispersion.

The study was expanded to determine if the use of a mixture of the two surfactants would affect the concentration and type of dispersed MWCNTs. The mass of SDS and DBSA that produced dispersions with the highest absorbance were used as the mixture for the dispersion of MWCNTs in both H_2O and ethyl acetate.

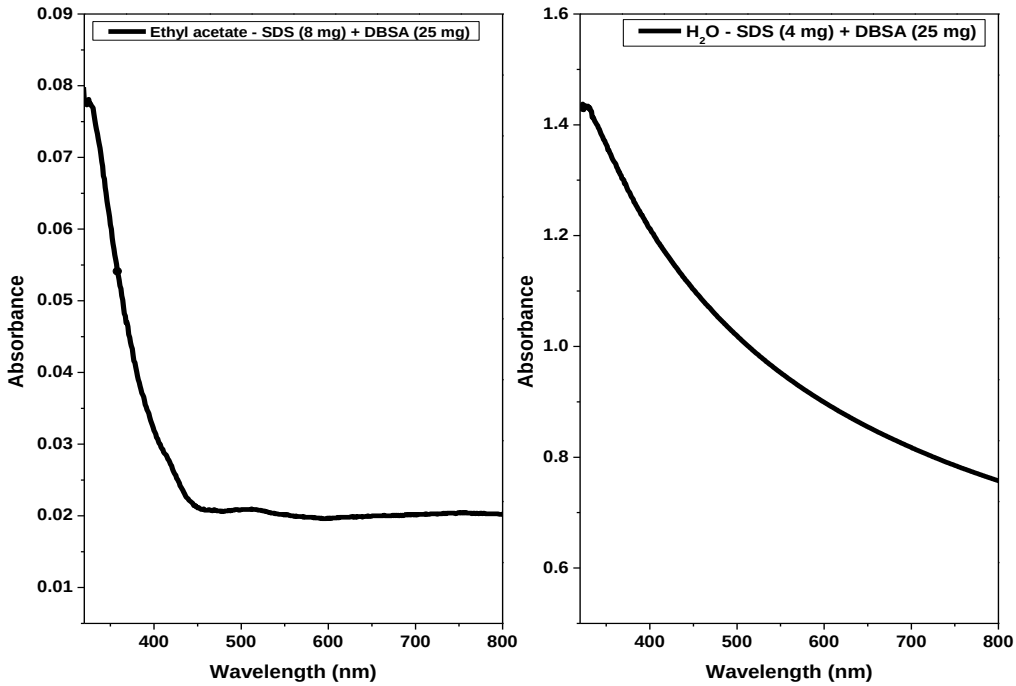


Figure 7.9: UV-vis spectra of pristine MWCNTs dispersions in ethyl acetate and water aided by a mixture of surfactants; a) SDS and DBSA in ethyl acetate, b) SDS and DBSA is water.

A mixture of 8 mg SDS and 25 mg DBSA in 10 ml ethyl acetate were used for the dispersion of MWCNTs. The resulting dispersion was clear with an absorbance of 0.08 (**Figure 7.9**), indicating a drop in concentration of suspended MWCNTs compared to the use 25 mg DBSA-ethyl acetate (2.38), 8 mg SDS-ethyl acetate (0.12) and ethyl acetate (0.81) dispersions. Additionally, the dispersion also showed a different absorbance pattern, indicating that the mixture had an influence on both the concentration and type of MWCNTs suspended in the matrix. The mixture of SDS (4 mg) and DBSA (25 mg) in 10 ml of H_2O resulted in an opaque dispersion. UV-vis analysis of the diluted dispersion indicated an increase in absorbance (1.43) relative to the DBSA-H_2O (1.08), SDS-H_2O (1.29) and H_2O (1.18) dispersions. The absorbance pattern and band gaps of all four dispersions were similar, which indicated that the use of surfactants in H_2O, either individually or simultaneously only influenced the concentration of suspended MWCNTs in H_2O, but not the type (all had the same characteristics) of suspended MWCNTs.

It is conceivable that the interaction between surfactant and MWCNTs altered the electronic properties of MWCNTs, thus leading to the difference in absorbance patterns and band gaps observed. However, a study by Bystrezjewski *et al.* where they used SDS and sodium dodecyl benzenesulfonate (SDBS) in H_2O for the dispersion of MWCNTs reported an influence of

surfactants on the diameter distribution of MWCNTs in the dispersion. They found that SDS had an adsorption affinity for CNTs with larger diameter compared to SDBS which preferred adsorbing onto smaller diameter CNTs.[144] Given that the band gap of MWCNTs is dependent on their diameter, the influence of SDS and DBSA on the diameter distribution was illustrated through the estimation of the direct and indirect band gap energies (Table 7.3) of the MWCNTs in the different dispersions. It is essential to note that only the supernatant portion of the dispersion was analysed without incorporating through any form of agitation of the dispersion the MWCNTs that had collected at the bottom. Thus, the recorded band gaps represent only the MWCNTs that remained suspended in the solvent.

Table 7.3: Direct and indirect band gaps of surfactant aided dispersions.

	Direct band gap energy (eV)				Indirect band gap energy (eV)			
	4 mg	8 mg	16 mg	25 mg	4 mg	8 mg	16 mg	25 mg
SDS-ethyl-acetate	2.74	2.74	2.73	2.76	2.99	3.01	2.98	2.99
DBSA-ethyl-acetate	3.25	3.26	3.25	3.10	3.40	3.41	3.41	3.25
SDS-water	2.75	2.76	2.75	2.75	3.02	3.00	3.02	2.99
DBSA-water	2.74	2.73	2.76	2.75	3.02	3.00	3.02	3.00
	Mixture of surfactants							
SDS+DBSA-water	2.73				3.03			
SDS+DBSA-ethyl-acetate	3.25				3.40			

Tauc plots for the listed band gap energies are found in **Appendix 7A**.

The SDS-H_2O and DBSA-H_2O dispersions reported similar direct band gap energies ranging from 2.75-2.76 eV and 2.73-2.76 eV, respectively. The indirect band gap energies for both sets of dispersion ranged from 3.00-3.02 eV. The band gap energies of these dispersions are similar to the recorded direct and indirect band gaps for the H_2O dispersions (2.74-2.275 eV and 2.99-3.03 eV). The SDS-ethyl acetate also reported similar direct (2.73-2.76 eV) and indirect (2.98-3.01 eV) band energies as found for the ethyl acetate dispersions (2.76 eV and 2.99-3.01 eV). The DBSA-ethyl acetate dispersion reported different direct (3.00, 3.25-3.26 eV) and indirect (3.25, 3.40-3.41 eV) band gap energies relative to the ethyl-acetate dispersions. The dispersions

derived from a mixture of DBSA and SDS in ethyl acetate gave direct and indirect band gap energies different from the surfactant free dispersions. On the other hand, the use of the mixture in H_2O recorded similar band gap energies to that of H_2O surfactant free dispersions

The band gap energy values corroborated the deduction made from the UV-vis spectra and revealed that the use of SDS in water and ethyl acetate only affects the concentration and not the type of suspended MWCNTs by reporting similar band gap energies. The use of DBSA in ethyl acetate influenced both the concentration and type of suspended MWCNTs, while its use in water affected both the concentration and type of suspended MWCNTs. The low band gap energies reported for SDS containing dispersions corroborates the study by Bytrezjewski *et al* that SDS has affinity for wider MWCNTs.[144] DBSA was found to have affinity for wider MWCNTs (lower band gap energies) only when used in water compared to when added to ethyl acetate-dispersions. Even when it was used concurrently with SDS in ethyl acetate, the dispersion exhibited preference for narrower diameter MWCNTs (higher band gap energies).

7.4. Conclusion.

The hydrophobicity and high aspect ratio of MWCNTs makes them difficult to utilize in applications that require their dissolution in different solvents. Various methods have been employed to varying degrees and success to address this challenge. Our study investigated their dispersion in different volumes of aqueous and organic solvents; ethyl acetate, EtOH, DCM, toluene, and hexane. Water and ethyl acetate gave the largest concentration of suspended MWCNTs and exhibited the highest meta-stability, while the organic solvents DCM, toluene and hexane reported dispersions with the lowest concentration and meta-stability. Variation of the volume of each solvent revealed that all dispersions except hexane, had an increase in volume leading to a decrease in suspended MWCNTs concentration. The influence of the surfactants SDS and DBSA on dispersions revealed that the use of DBSA in ethyl acetate, and both their use in water generally lead to a decrease in the concentration of suspended MWCNTs. However, the use of SDS in ethyl acetate led to an increase in the concentration of suspended MWCNTs across all surfactant concentrations.

All solvents had suspended MWCNTs in their matrix, however, the UV-vis pattern of the suspended MWCNTs differed with each type of dispersion. This suggested that some solvents like DCM and H_2O did not suspend MWCNTs with the same properties. Consequently, a significant observation was made, dispersibility is not only a measure of concentration but was significantly influenced by the structural properties, particularly the diameter of MWCNTs.

This observation was also made for the surfactant-based dispersions. Solvent based and surfactant-based dispersions had an influence on the diameter distribution of the suspended MWCNTs. Water and ethyl acetate exhibited affinity for MWCNTs with smaller band gaps, indicating that they are a better medium for the dispersion of wide MWCNTs. Toluene, hexane and DCM exhibited affinity for MWCNTs with narrow diameters. SDS exhibited affinity for wide MWCNTs, as all SDS based dispersion apart for the mixture with DBSA in ethyl acetate reported smaller band gap energies. The type of MWCNTs that DBSA had preferred affinity for dependent on the solvent used; when used in water it preferred wide MWCNTs, but preferred narrower MWCNTs when used in ethyl acetate.

Overall, this study not only corroborated the significance of solvent and surfactant, or combination thereof in the dispersion of MWCNTs, but also revealed that for a sample that contains MWCNTs with different physical properties e.g., aspect ratio, these can potentially be separated, according to their diameter by dispersing the sample in different solvents and solvent-surfactant mediums.

Appendix 7A.

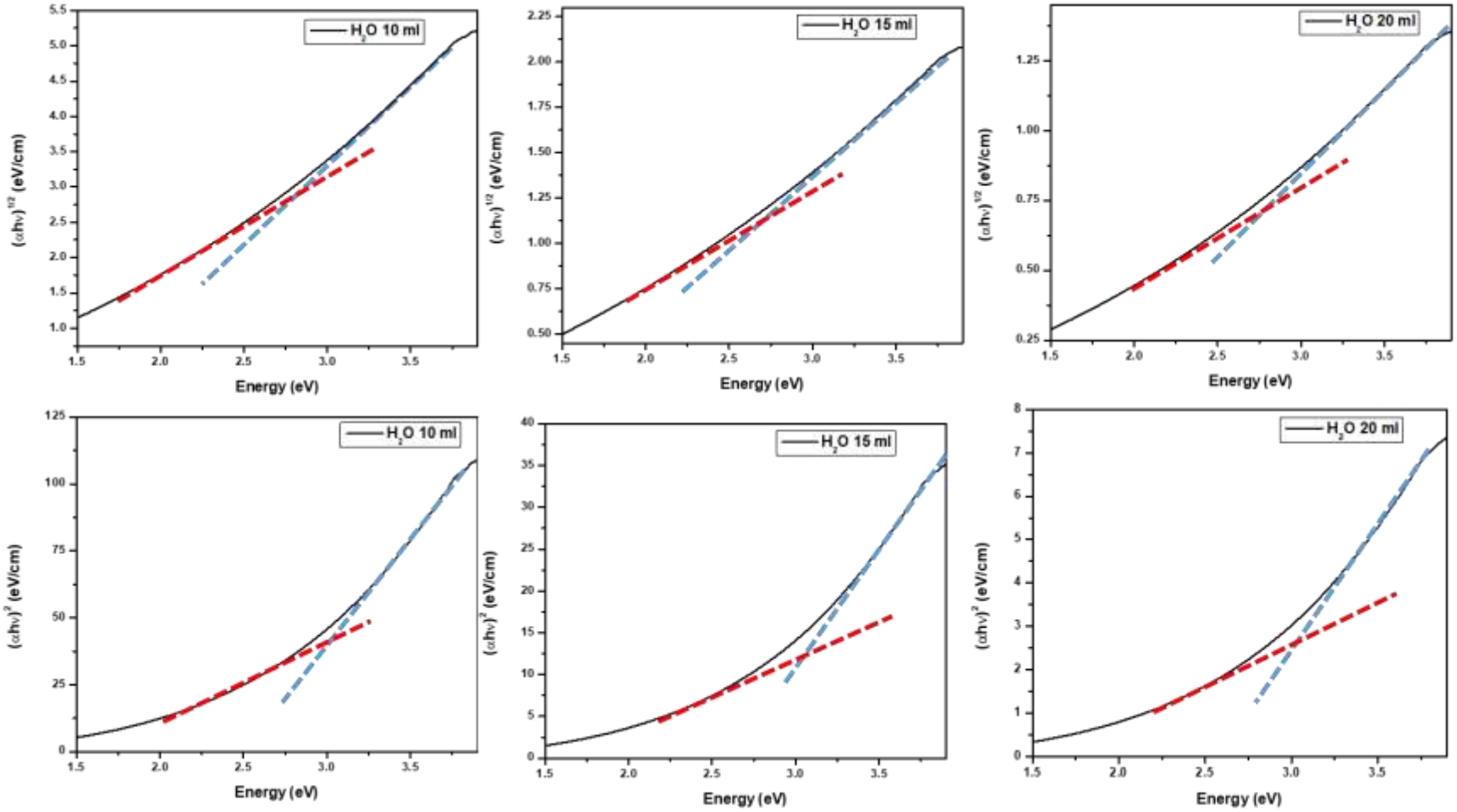


Figure 7.10: Tauc plots for direct and indirect band gaps of MWCNTs in water.

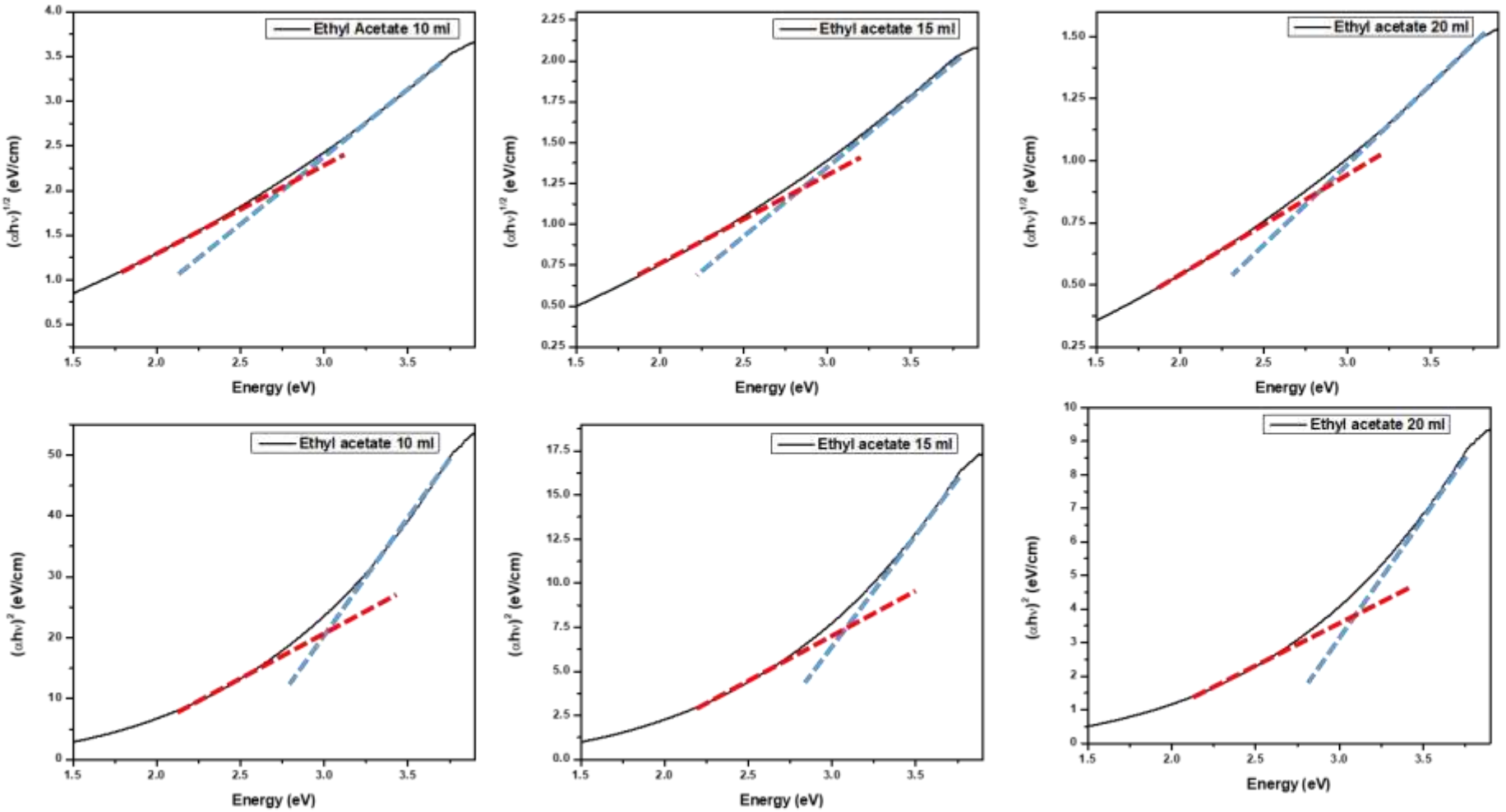


Figure 7.11: Tauc plots for direct and indirect band gaps of MWCNTs in ethyl acetate.

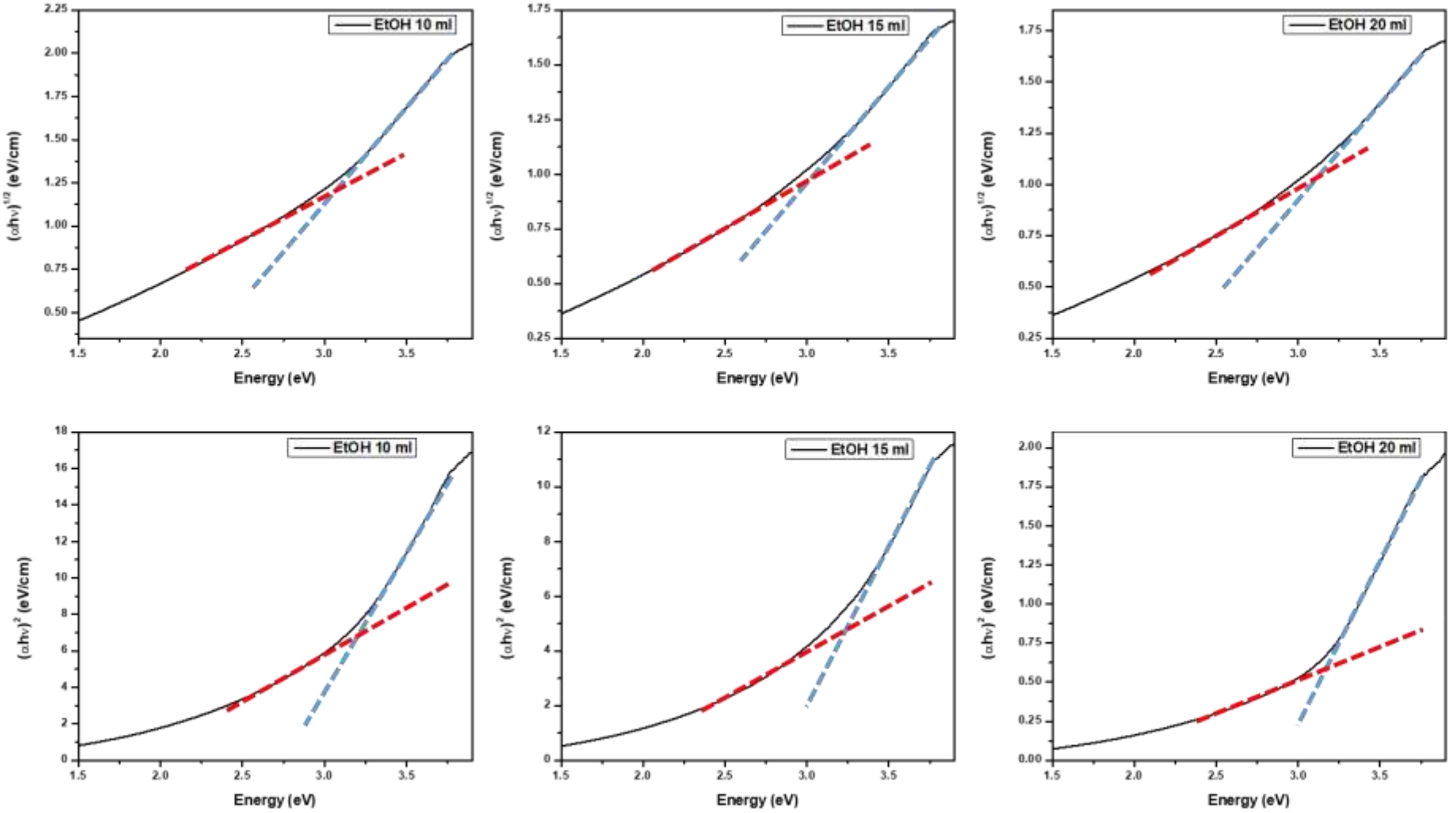


Figure 7.12: Tauc plots for direct and indirect band gaps of MWCNTs in EtOH.

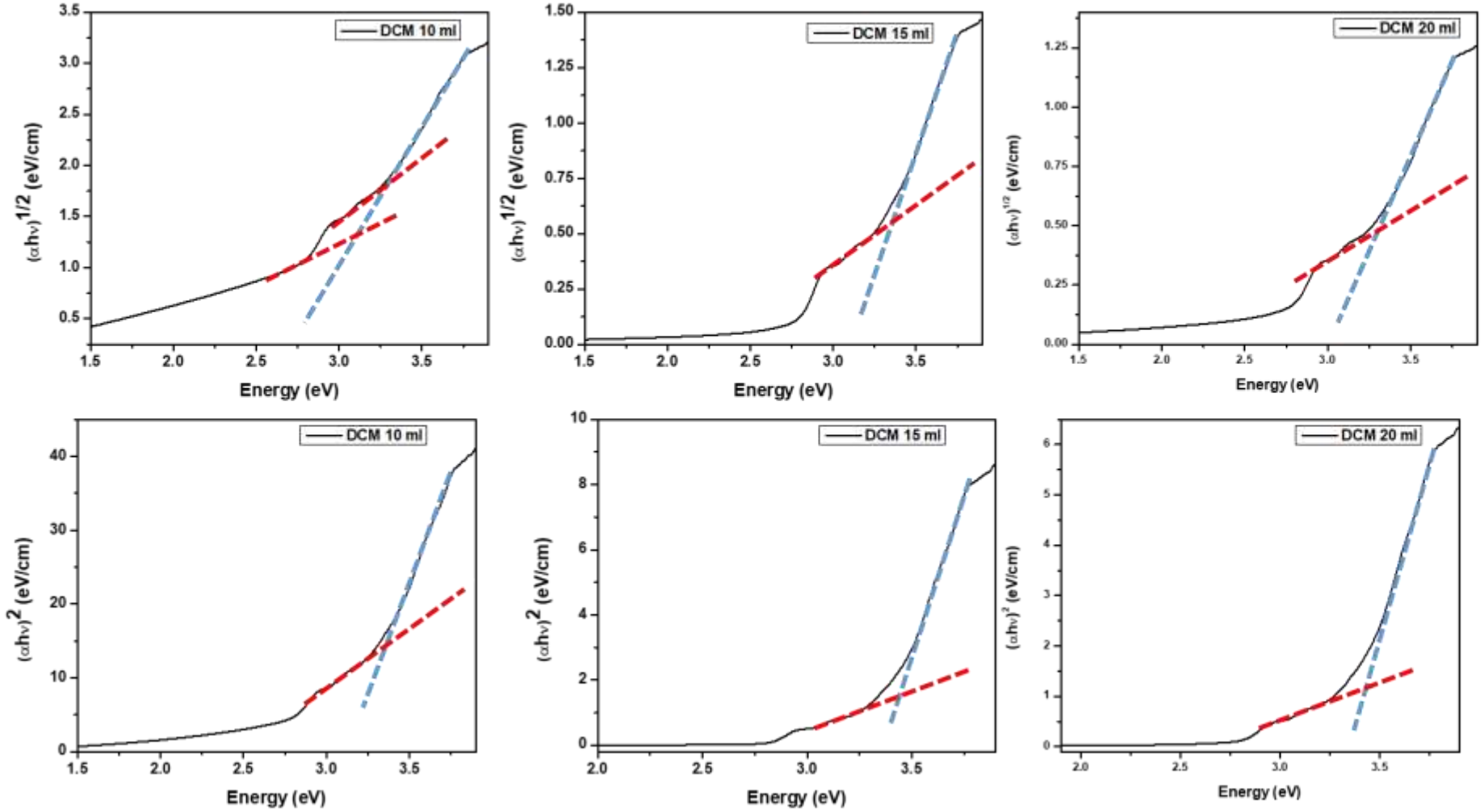


Figure 7.13: Tauc plots for direct and indirect band gaps of MWCNTs in DCM.

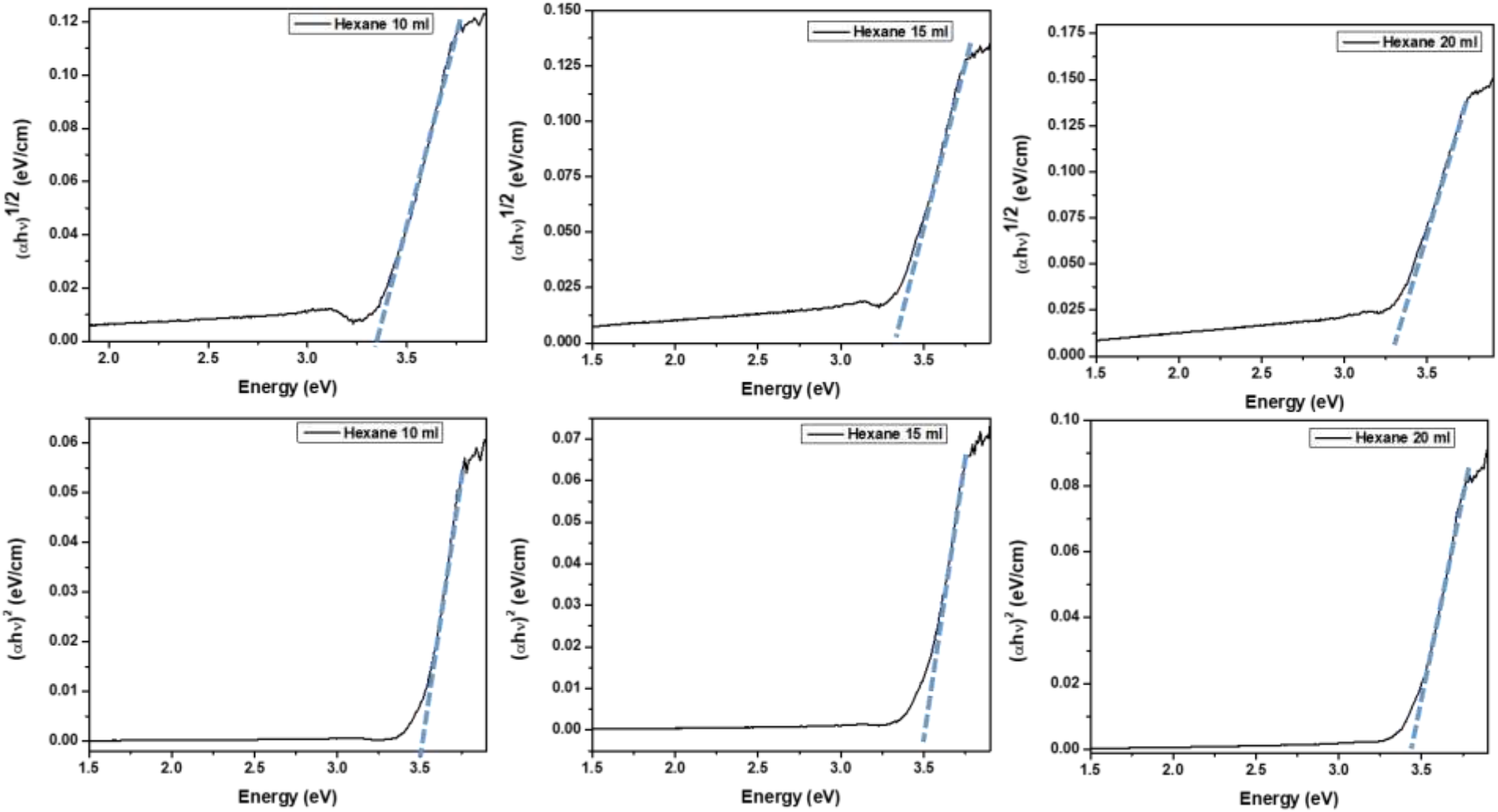


Figure 7.14: Tauc plots for direct and indirect band gaps of MWCNTs in Hexane.

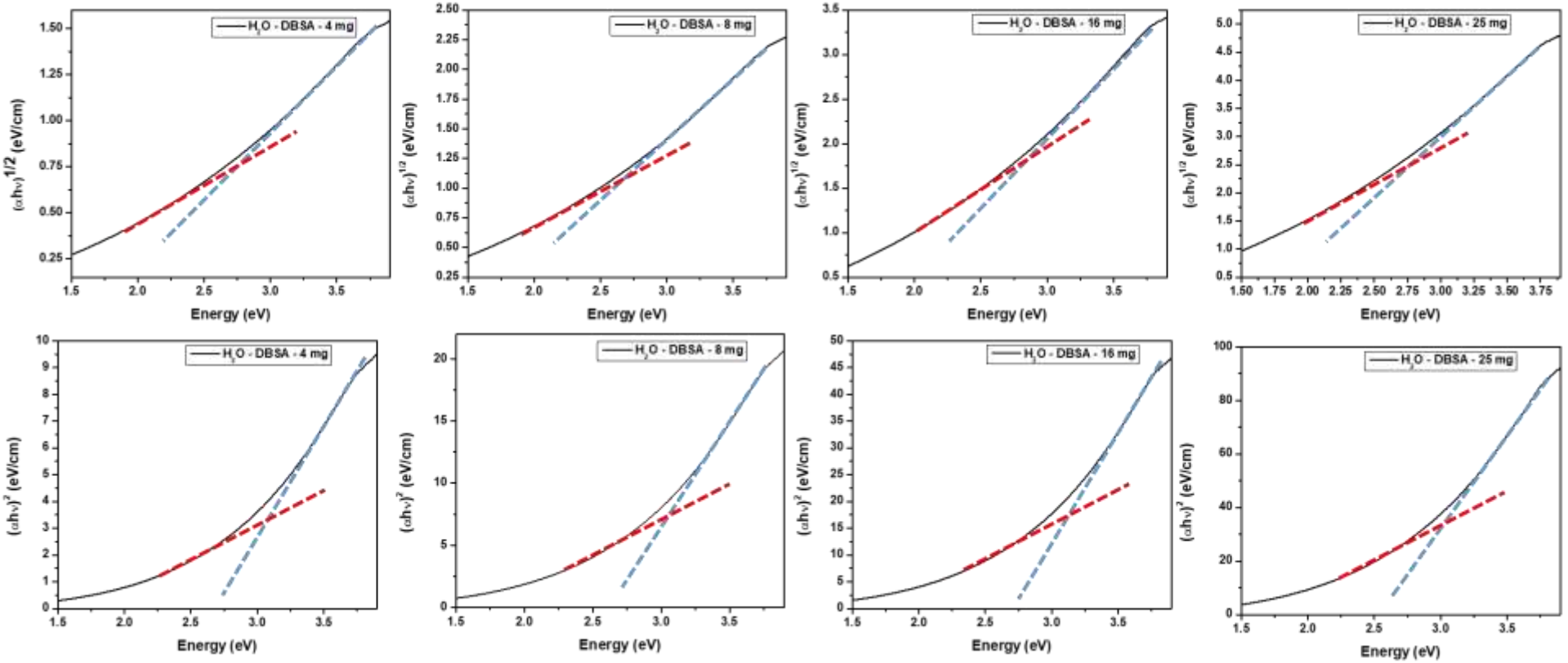


Figure 7.15: Tauc plots for direct and indirect band gaps of MWCNTs in DBSA-water mixture.

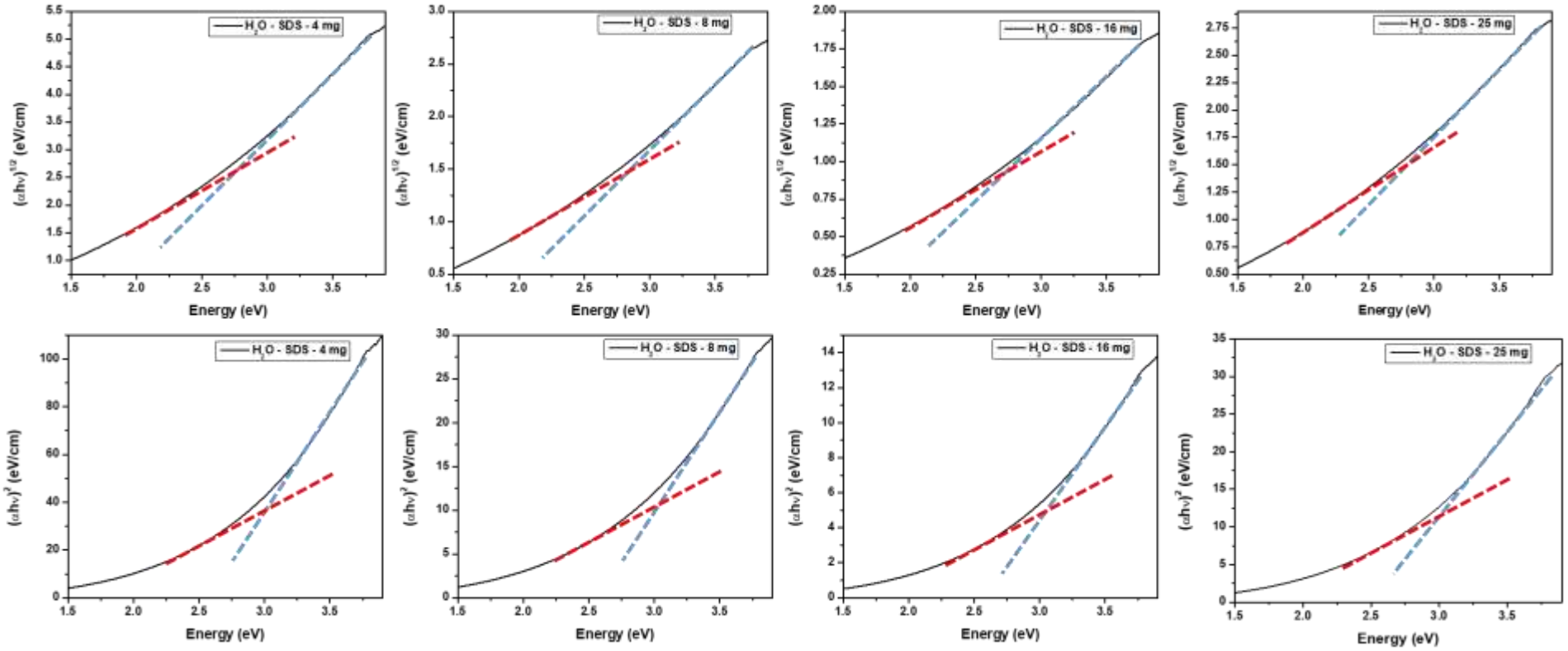


Figure 7.16: Tauc plots for direct and indirect band gaps of MWCNTs in SDS-water mixture

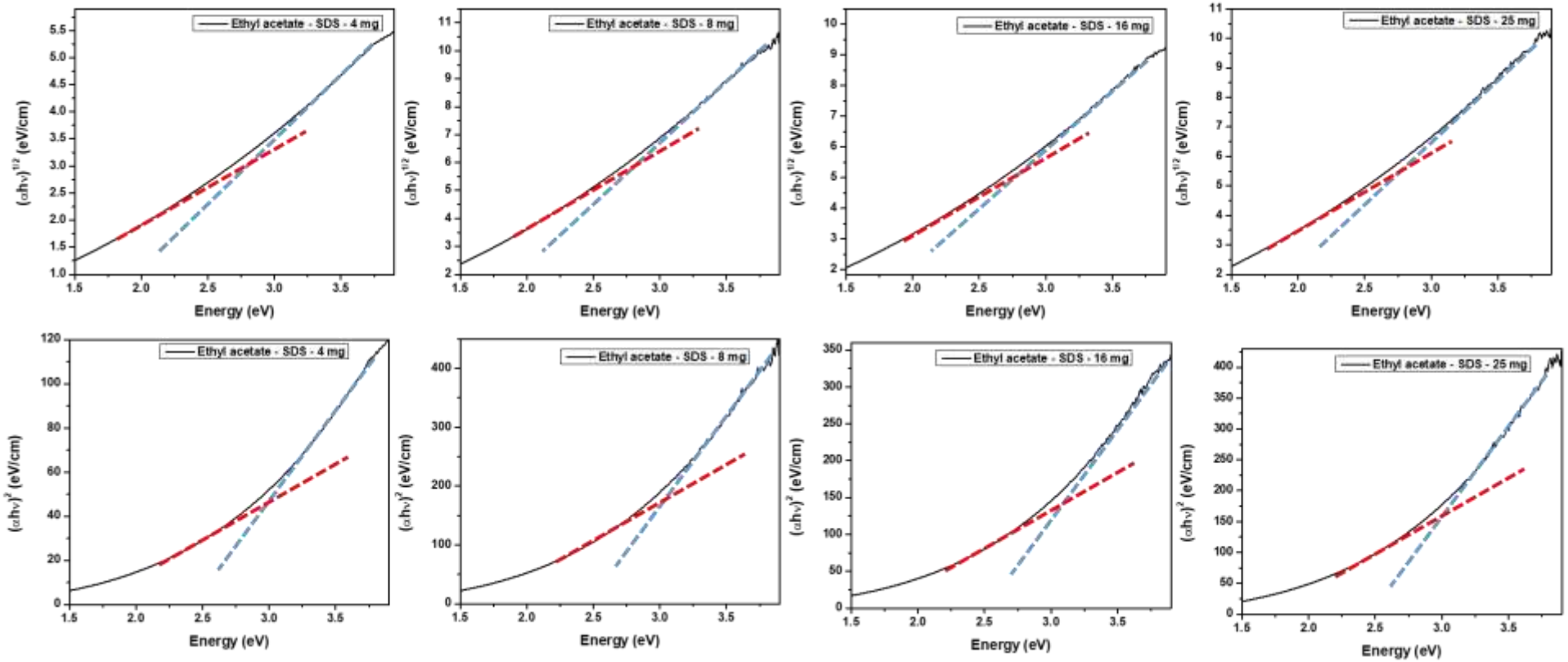


Figure 7.17: Tauc plots for direct and indirect band gaps of MWCNTs in SDS-ethyl acetate mixture

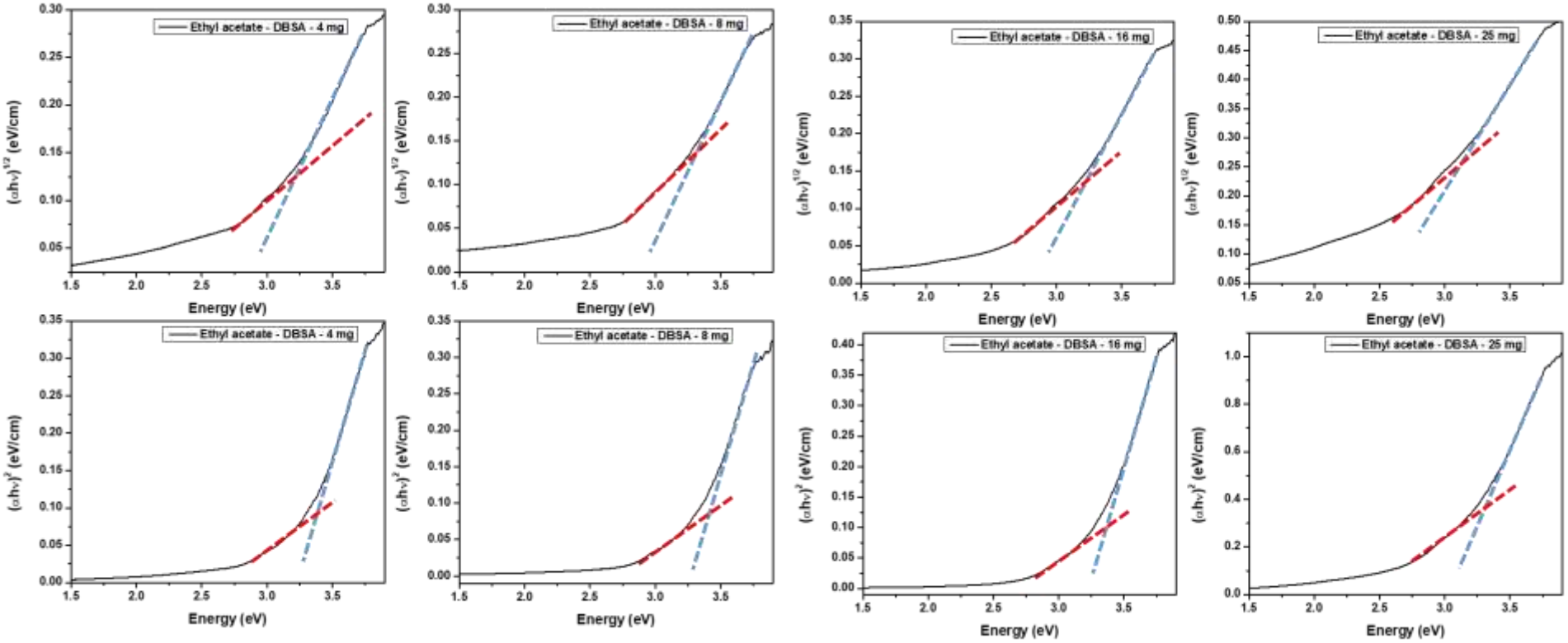


Figure 7.18: Tauc plots for direct and indirect band gaps of MWCNTs in DBSA-ethyl acetate mixture

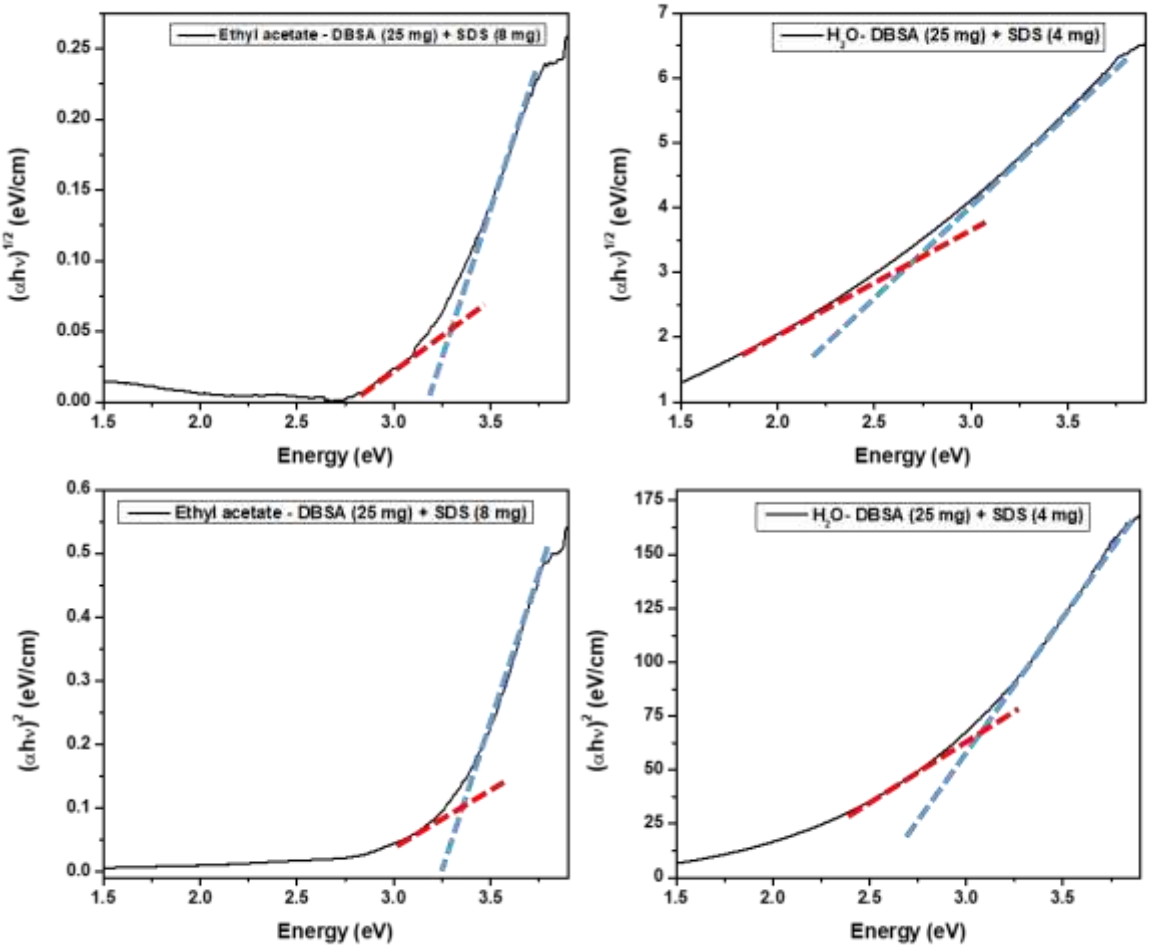


Figure 7.19: Tauc plots for direct and indirect band gaps of MWCNTs in SDS-DBSA-water and ethyl acetate mixtures.

Chapter 7 References.

1. G. Sun, Z. Liu, G. Chen. *Nano; Brief Reports and Reviews.* 2010, **5,** 103-109.
2. K. Jagadish, S. Srikantaswamy, K. Byrappa, L. Shruthi, M. R. Abhilash. *Journal of Nanomaterials.* 2015, **2015**, 381275 (1-6).
3. K. S. Park, J. R. Youn. *Carbon.* 2012, **50**, 2322-2330.
4. M. S. Dresselhaus. D. Dresselhaus. *Carbon Nanotubes; Synthesis, Structure Properties and Applications. Springer Science and Business Media.* P. Avorousi (Editor). 2001.
5. Q. Li, J. S. Church, A. Kafi, M. Naebe, B. L. Fox. *Journal of Nanoparticle Research.* 2014, **16**, 2513(1-12).
6. X. Huang, W. Liang, S. Zhang. *Nanoscale Research Letters.* 2011, **6**, 1-6.
7. B. Fei, H. Lu, Z. Hu, J. H. Xin. *Nanotechnology.* 2006, **17**, 1589-1593.
8. A. Krueger. *Carbon Nanotubes. In Carbon Material and Nanotechnology. Weinheim: Wiley-VCH*. 2010, page 123-281.
9. K. B. Ustinovich, V. V. Ivanov, Y. M. Tukonov, A. A. Loshkarev, N. I. Sapronova, A. M. Vorobei, O. O. Parenago, M. G. Kiseley. *Molecules.* 2020, **25**, 4061-4072.
10. K. E. Geckeler, T. Premkumar. *Nanoscale Research Letters.* 2011, **6**, 136-138.
11. R. Vajtai. *Springer Handbook of Nanomaterials. Springer-Verlag.* 2013.
12. J. Yu, N. Grossiord, C. E. Koning, J. Loos. *Carbon.* 2007, **45**, 618-623.
13. H. J. Gao, S. H. Zhang, D. P. Huang, L. Q. Zheng. *Colloid and Polymer Science.* 2012, **290**, 757-762.
14. X. L. Xie, W. Y. Mai, X. P. Zhou. *Materials Science and Engineering R: Reports.* 2005, **49**, 89-112.
15. G.-X. Chen, Y. Li, H. Shimizu. *Carbon.* 2007, **45**, 2334-2340.
16. J. O. Aguilar, J. R. Bautista-Quinjano. F. Avilés. *Express Polymer Letters.* 2010, **4**, 292-299.

17. K. H. Maria, T. Mieno. *Carbon Nanotubes; Recent Progress. Web of Science*. Chapter 12, 235-256.

18. O. V. Karissova, B. I. Kharisov, E. G. de Casas Ortiz. *RSC Advances.* 2013, **3**, 24812-24852.

19. T. Premkumar, R. Mezzenga, K. E. Geckler. *Small*. 2012, **8**, 1299-1313.

20. M. J. Green. *Polymer International.* 2010, **59**, 1319-1322.

21. H. Gamsjager, J. W. Lorimer, P. Scharlin, D. G. Shaw. *Pure and Applied Chemistry.* 2008, **80**, 233-276.

22. L. Cui. *Advanced Material Research.* 2013, **641-642**, 436-439.

23. T. Yasumitsu, G. Liu, J.-M. Leveque, S. Aonuma, L. Duclaux, T. Kimura, N. Komatsu. *Ultrasonics Sonochemistry.* 2013, **20**, 37-39.

24. M. S. Strano, V. C. Moore, M. K. Miller, M. J. Allen, E. H. Haroz, C. Kittrell, R. H. Hauge, R. E. Smalley. *Journal of Nanoscience and Nanotechnology.* 2003, **3**, 81-86.

25. M. S. Arnold, A. A. Green, J. F. Hulvat, S. I. Stupp, M. C. Hersam. *Nature Nanotechnology.* 2006, **1**, 60-65.

26. P. Zhao, E. Einarsson, R. Xiang, Y. Murakami, S. Maruyama. *The Journal of Physical Chemistry C.* 2010, **114**, 4831-4834.

27. M. Nadler, T. Mahrholz, U. Riedel, C. Schilde, A. Kwade. *Carbon*. 2008, **46**, 1384-1392.

28. N. Hordy, S. Coulumbe, J.-L. Meunier. *Plasma Processes and Polymers.* 2013, **10**, 110-118.

29. Y. Kim, H. Ma, Q. Yu. *Nanotechnology.* 2010, **21**, 295703 (1-7).

30. Y. Jiang, Y.-F. Zhu, F.-Y. Wang, W.-J. Chen. *Plasma Chemistry and Plasma Processing.* 2011, **31**, 441-448.

31. B. I. Kharisov, O. V. Kharissova, U. O. Mendez. *CRC Press.* 2013, page 586.

32. A. A. Vetcher, J.-H. Fan, I. A. Vetcher, T. Lin, S. M. Abramov, R. Draper, M. E. Kozlov, R. H. Baughman, S. D. Levene. *International Journal of Nanoscience.* 2007, **6**, 1-7.

33. B. R. Burg, J. Schneider, M. Muoth, L. Durrer, T. Helbling, N. C. Schirmer, T. Schwamb, C. Hierold, D. Poulikakos. *Langmuir.* 2009, **25**, 7778-7782.

34. M. D. Rossell, C. Kuebel, G. Ilari, F. Rechberger, F. J. Heiligtag, M. Niederberger, D. Koziej, R. Erni. *Carbon.* 2013, **61**, 401-411.

35. Q. Cheng, S. Debnath, E. Gregan, H. J. Byrne. *The Journal of Physical Chemistry C.* 2010, **114**, 8821-8827.

36. R. Arrigo, R. Teresi, C. Gambarotti, F. Parisi, G. Lazzara, N. T. Dintcheva. *Materials.* 2018, **11**, 383-396.

37. W. Chen, X. Liu, Y. Liu, H.-I. Kim. *Materials Letters.* 2010, **64**, 2589-2592.

38. H.-S. Kim, W.-I. Park, M. Kang, H.-J. Jin. *Journal of Physics and Chemistry of Solids.* 2008, **69**, 1209-1212.

39. A. Ghozatloo, A. M. Rashidi, M. Shariaty-Niasar. *International Communications in Heat and Mass Transfer.* 2014, **54**, 1-7.

40. L. Vaisman, G. Marom, H. D. Wagner. *Advanced Functional Materials.* 2006, **16**, 357-363.

41. M. Bricha, K. E. Mabrouk. *Colloids and Surfaces: Physicochemical and Engineering Aspects.* 2019, **561**, 57-69.

42. K.-Y Chun, S. K. Choi, H. J. Kang, C. Y. Park, C. J. Lee. *Carbon.* 2006, **44**, 1491-1495.

43. S. Dumonteil, A. Demortier, S. Detriche, C. Raes, A. Fonseca, M. Rühle, J. B. Nagy. *Journal of Nanoscience and Nanotechnology.* 2006, **6**, 1315-1318.

44. L. F. Wah, U. Hashim, W.-W. Liu, T. Adam. *Journal of Applied Science Research.* 2013, **9**, 3411-3416.

45. M. Gupta, S. Malhotra, S. Chopra, R. Maheshwari. *API Conference Proceedings.* 2010, **1324**, 394-398.

46. L. N. Lisetski, S. S. Minenko, A. P. Fedoryako, N. I. Lebovka. *Physica E.* 2009, **41**, 431-435.

47. J. H. Kim, J.-Y. Hwang, H. R. Hwang, H. S. Kim, J. H. Lee, J.-W. Seo, U. S. Shin, S.-H. Lee. *Scientific Reports.* 2018, **8**, 1375-1384.

48. M. Shahabuddin, N. A. Madhar, N. S. Alzayed, M. Asif. *Materials.* 2019, **12**, 3044-3053.

49. J. Li, Y. J. Lu, Q. Ye, M. Cinke, J. Han, M. Meyyappan. *Nano Letters*. 2003, **3**, 929-933.

50. I.-Y. Jeon, D. W. Chang, N. A. Kumar, J.-B. Baek. *Web of Science: Carbon Nanotubes-Polymer Composites.* 2011. Chapter 5, page 91-110.

51. N. F. Braga, H. M. Zaggo, L. S. Montagna, F. R. Passador. *Journal of Composite Science.* 2020, **4**, 44-61.

52. G. Rahman, Z. Najaf, A. Mehmood, S. Bilal, A. H. A. Shah, A. A. Mian, G. Ali. *Journal of Carbon Research.* 2019, **5**, 3-31.

53. Y. Zhou, Y. Fang, R. P. Ramasamy. *Sensors.* 2019, **19**, 392-421.

54. A. Oskoueian, K. A. Matori, S. Bayat, E. Oskoueian, F. Ostovan, M. Toozandehjani. *Journal of Nanomaterials.* 2018, 8417016 (1-13).

55. L. Meng, C. Fu, Q. Lu. *Progress of Natural Science.* 2009, **19**, 801-810.

56. A. Hirsch. *Angewadte Chemie International Edition.* 2002, **41**, 1853-1859.

57. S. B. Sinnot. *Journal of Nanoscience and Nanotechnology.* 2002, **2**, 113-123.

58. Y.-P. Sun, K. Fu, Y. Lin. *Accounts of Chemical Research.* 2002, **35**, 1096-1104.

59. S. Mallakpour, S. Soltanian. *RSC Advances.* 2016, **6**, 109916-109935.

60. A. G. Osorio, I. C. L. Silveira. V. L. Bueno, C. P. Bergmann. *Applied Surface Science.* 2008, **255**, 2485-2489.

61. K. Hernadi, A. Siska, L. Thiên-Nga. L. Forró, I. Kiricsi. *Solid State Ionics*. 2001, **142-142**, 203-209.

62. V. Datsyuk, M. Kalyva, K. Papagelis, J. Parthenios, D. Tasis, A. Siokou, I. Kallitsis, C. Galiotis. *Carbon*. 2008, **46**, 833-840.

63. E. S. Yeo, G. I. Mathys, N. Brack, E. T. Thostenson, A. N. Rider. *Journal of Visualized Experiments.* 2017, **123**, e55614 (1-9).

64. S. Banerjee, S. S. Wong. *Journal of Physical Chemistry B.* 2002, **106**, 12144-12151.

65. M. Holzinger, O. Vostrowsky, F. Hennrich, M. Kappes, R. Weiss, F. Jellen. *Angewandte Chemie International Edition*. 2001, **40**, 4002-4005.

66. E. P. Jackson, T. J. Sisto, E. R. Darzi, R. Jasti. *Tetrahedron.* 2016, **72**, 3754-3758.

67. A. Bianco, M. Prato, K. Kostarelos, A. Bianco. *Accounts of Chemical Research.* 2008, **41**, 60-68.

68. E. T. Mickelson, C. B. Huffman, A. G. Rinzler, R. E. Smalley, R. H. Hauge, J. L. Margrave. *Chemical Physics Letters.* 1998, **296**, 188-194.

69. W. Francisco, F. V. Ferreira, E. V. Ferreira, L. de Simone Cividanes, A. dos Reis Coutinho, G. P. Thim. *Journal of Aerospace Technology and Management.* 2015, **7**, 289-293.

70. M. Pandurangappa, G. K. Raghu. *Web of Science: Carbon Nanotubes Applications.* 2011, chapter 21, pages 549-525.

71. C. Klumpp, K. Kostarelos, M. Prato, A. Bianco. *Biochimica et Biophysica Acta (BBA)-Biomembranes.* 2006, **1758**, 404-412.

72. H. Touhara, J. Inahara, T. Mizuno. *Fluorine Chemistry.* 2002, **114**, 181-188.

73. K. F. Kelly, I. W. Chiang, E. T. Mickelson, R. H. Hauge, J. L. Margrave, X. Wang, G. E. Scuseria, C. Radloff, N. J. Halas. *Chemical Physics Letters.* 1999, **313**, 445-450.

74. P.-C. Ma, N. A. Siddiqui, G. Marom, J.-K. Kim. *Composites Part A: Applied Science and Manufacturing.* 2010, **41**, 1345-1367.

75. C. Wei, B. Akinwolemiwa, L. Yu, D. Hu, G. Z. Chen. *Nanoparticles Synthesis, Properties, and Application.* 2019, 211-248.

76. Y.-A. Leu, M.-H. Yeh, L-Y. Lin, T.-J. Li, L.-Y. Chang, S.-Y. Shen, Y.-S. Li, G.-L. Chen, W.-H. Chiang, J.-J. Lin. K.-C. Hao. *ACS Sustainable Chemistry and Engineering.* 2017, **5**, 537-546.

77. S. Peng, L. Tian, J. Liang, S. G. Mhaisalkar, S. Ramakrishna. *ACS Applied Materials and Interfaces.* 2012, **4**, 397-404.

78. M. Sireesha, V. Jagadeesh Babu, S. Ramakrishna. *Materials Science and Engineering: B.* 2017, **223**, 43-63.

79. Q. Fu, C. Lu, J. Liu. *Nano Letters.* 2002, **2**, 329-332.

80. R. Ramasubramaniam, J. Chen, H. Liu. *Applied Physics Letters.* 2003, **83**, 2928-2930.

81. J. Chen, H. Liu, W. A. Weimer, M. D. Halls, D. H. Waldeck, G. C. Walker. *Journal American Chemical Society.* 2002, **124**, 9034-9035.

82. D. Baskaran, J. W. Mays, M. S. Bratcher. *Chemistry of Materials.* 2005, **17**, 3389-3397.

83. J. H. Rouse. *Langmuir*. 2015, **21**, 1055-1061.

84. X. W. Jiang, Y. Z. Bin, M. Matsuo. *Polymer*. 2005, **46**, 7418-7424.

85. D. Tuncel. *Nanoscale.* 2011, **3**, 3545-3554.

86. P. Kumar, H. B. Bohidar. *Colloids and Surfaces A: Physicochemical and Engineering Aspects.* 2010, **361**, 13-24.

87. R. P. Singh, S. Jain, P. Ramarao. *Journal of Nanoparticle Research.* 2013, **15**, 1985 (1-19).

88. A. O. Borode, N. A. Ahmed, P. A. Olubambi. *Physics of Fluids.* 2019, **31**, 071301 (1-24)

89. D. Mendoza-Cachú, C. Mercado-Zúñiga, G. Rosas. *Advances in Condensed Matter Physics.* 2017, **2017**, 1751768 (1-7).

90. K. Yang, Z. L. Yi, Q. F. Jing, R. L. Yue, W. Jiang, D. Lin. *Chinese Science Bulletin.* 2013, **58**, 2082-2090.

91. Q.-Y. Tang, Y.-C. Chan, N.-B. Wong, R. Cheung. *Polymer International.* 2010, **59**, 1240-1245.

92. M. S. Strano, V. C. Moore, M. K. Miller, M. J. Allen, E. H. Haroz, C. Kittrell, R. H. Hauge, R. E. Smalley. *Journal of Nanoscience and Nanotechnology.* 2003, **3**, 81-86.

93. H. Wang. *Current Opinion in Colloid and Interface Science.* 2009, **14**, 364-371.

94. L. Vaisman, H. D. Wagner, G. Marom. *Advances in Colloid and Interface Science.* 2006, **128-130**, 37-46.

95. B. R. Priya, H. J. Byrne. *The Journal of Physical Chemistry C.* 2008, **112**, 332-337.

96. C. M. Damian, S. A. Garea, E. Vasile, H. Lovu. *Composites Part B: Engineering.* 2012, **43**, 3507-3515.

97. J. Shiju, F. Al-Sagheer, A. Bumajdad, Z. Ahmad. *Nanomaterials.* 2018, **8**, 308-327.

98. I. Kalinina, K. Worsley, C. Lugo, S. Mandal, E. Bekyarova, R. C. Haddon. *Chemistry of Materials.* 2011, **23**, 1246-1253.

99. F. Bourdiol, F. Mouchet, A. Perrault, I. Fourquaux, L. Datas, C. Gancet, J.-C. Boutonnet, E. Pinelli, L. Gauthier, E. Flahaut. *Carbon*. 2013, **54**, 175-191.

100. P. Bilalis, D. Katsigiannopoulos, A. Avgeropoulos, G. Sakellariou. *RSC Advances.* 2014, **4**, 2911-2934.

101. D. W. Steuerman, A. Star, R. Narizzano, H. Choi, R. S. Ries, C. Nicolini, J. F. Stoddart, J. R. Heath. *Journal of Physical Chemistry B.* 2002, **106**, 3124-3130.

102. H. S. Woo, R. Czerw, S. Webster, D. L. Carroll, J. Ballato, A. E. Strevens, D. O' Brien, W. Blau. *Applied Physics Letters.* 2000, **77**, 1393-1395.

103. C.X. Liu, J.-W. Choi. *Nanomaterials (Basel).* 2012, **2**, 329-347.

104. M. T. Müller, B. Krause, P. Pötschke. *Polymer*. 2012, **53**, 3079-3083.

105. F. N. A. M. Sabri, M. R. Zakaria, H. M. Akil. *API Conference Proceedings.* 2020, **2267**, 020043 (1-6).

106. M. Khazaee, W. Xa, G. Lackner, R. G. Mendes, M. Rümmeli, M. Muhler, D. C. Lupascu. *Scientific Reports.* 2016, **6**, 26208 (1-10).

107. Y. Kim, S.-M. Kwon, D.-Y. Kim, H.-S. Kim, H.-J. Jin. *Current Applied Physics.* 2009, **9**, e100-e103.

108. S. Alrekabi, A. Cundy, A. Lampropoulos, I. Savina. *International Journal of Civil, Environmental, Structural, Construction and Architectural Engineering.* 2016, **10**, 261-267.

109. H. Li, Y. Qiu. *Royal Society Open Source.* 2019, **6**, 190241.

110. M. Bricha, K. El Mabrouk. *Colloids and Surfaces A: Physiochemical and Engineering Aspects.* 2019, **561**, 57-69.

111. S. Javadian, A. Motace, M. Sharifi, H. Aghdastinat, F. Taghavi. *Colloids and Surfaces A.* 2017, **531**, 141-149.

112. S. Kim, B. Tserengombo, S.-H. Choi, J. Noh, S. Huh, B. Choi, H. Chung, J. Kim, H. Jeong. *International Communications in Heat and Mass Transfer.* 2018, **91**, 95-102.

113. O. V. Kharissova, B. I. Kharisov, E. G, de Casis Ortiz. *RSC Advances.* 2013, **3**, 24812-24852.

114. T. L. Brown, H.E. LeMay, Jr. B. E. Bursten, C. J. Murphy. *Chemistry the Central Science 10th edition: Pearson Education, Inc.* 2005, chapter 13, pages 558-562.

115. M. S. Z. Shiri, W. Henderson, M. R. Mucalo. *Materials.* 2019, **12**, 1896-1922.

116. X. Cui, S. Mao, M. Liu, H. Yuan, Y. Du. *Langmuir.* 2008, **24**, 10771-10775.

117. X. Cui, Y. Jiang, C. Yang, X. Lu, H. Chen, S. Mao, M. Liu, H. Yuan, P. Luo, Y. Du. *The Journal of Physical Chemistry B.* 2010, **114**, 7808-7816.

118. J.-M. Bonard, T. Stora, J-P. Salvetat, F. Maier, T. Stöckli, C. Duschl, L. Forró, W. A. de Heer, A. Châtelain. *Advanced Materials.* 1997, **9**, 827-831.

119. S. Ou, S. Patel, B. A. Bauer. *Journal of Physical Chemistry B.* 2012, **116**, 8154-8168.

120. A. I. Frolov, R. N. Arif, M. Kolar, A. O. Romanova, M. V. Federov, A. G. Rozhin. *Chemical Science.* 2012, **3**, 541-548.

121. A. P. Periasamy, Y.-H. Ho, S.-M. Chen. *Biosensors and Bioelectronics.* 2011, **29**, 151-158.

122. A. Heidari, M. H. Beheshty, H. Rahimi. *Fullerenes, Nanotubes, Carbon Nanostructures.* 2013, **21**, 516-524.

123. C. Tang, T. Zhou, J. Yang, F. Chen, Q. Fu, L. Yang. *Colloids and Surfaces B: Biointerfaces.* 2011, **86**, 189-197.

124. A. L. Ahmad, Z. A. Jawad, S. C. Low, S. H. S. Zein. *Current Nanoscience.* 2013, **9**, 93-102.

125. B. Wang, Y. Han, K. Song, T. Zhang. *Journal of Nanoscience and Nanotechnology.* 2012, **12**, 4664-4669.

126. A. K. Sharma, R. Sharma, R. Prajapati, S. Chaudhary. *Fullerenes, Nanotubes and Carbon Nanostructures.* 2016, **24**, 332-338.

127. J. Njuguna, O. A. Vanli, R. Liang. *Journal of Spectroscopy.* 2015, 463156 (1-11).

128. N. Grossiord, O Regev. J. Loos, J. Meuldijk, C. E. Koning. *Analytical Chemistry.* 2005, **77**, 5135-5139.

129. N. Grossiord. P. van der Schoot. J. Meuldijk. C. E. Koning. *Langmuir*. 2007, **23**, 3646-3653.

130. J. A. Fagan, C. Y. Khripin, C. A. Silvera Batista. *Advanced Materials.* 2014, **26**, 2800-2804.

131. L. Jiang, L. Gao, J. Sun. *Journal of Colloid and Interface Science.* 2003, **260**, 89-94.

132. X. Wang, Y. Cao. *Journal of Industrial and Engineering Chemistry.* 2020, **82**, 324-332.

133. L. Hu, D. S. Hecht, G. Grüner. *Chemical Review.* 2010, **110**, 5790-5844.

134. R. J. Grow. *Carbon Nanotubes; Properties and Applications.* Taylor and Francis Group, New York. 2006, Chapter 7.

135. R. Heyd, A. Charlier, E. McRae. *Physical Review B (Condensed Matter)*. 1997, **55**, 6820-6824.

136. L. Yang, M. P. Anantram, J. Han, J. P. Lu. *Physical Review B*. 1999, **60**, 13874-13878.

137. P. Makula, M. Pacia, W. Macyk. *The Journal of Physical Chemistry Letters.* 2018, **9**, 6814-6817.

138. J. I. Pankove. *Optical Process in Semiconductors; Courier Corporation.* 1971.

139. C. M. E. Kane. *Physics Review Letters.* 1997, **78**, 1932.

140. E. J. Wanless, W. A. Drucker. *Journal of Physical Chemistry.* 1996, **100**, 3207.

141. R. J. Hunter. *Introduction to Morden Colloid Science*. Oxford University Press, Oxford. 1993.

142. M. P. Aronson. *Langmuir*. 1989, **5**, 494.

143. J. Bibette, D. Roux, B. F. Naliet. *Physics Review Letters.*1990, **65**, 2470.

144. M. Bystrzejewski, A. Huczo, H. Lange, T. Gemming, B. Büchner, M. H. Rümmeli. *Journal of Colloid and Interface Science.* 2010, **345**, 138-142.

Chapter 8: The fabrication of pristine and heteroatom doped MWCNTs thin films; an electrochemical study.

Thin film technologies have a comprehensive scope of application which have led to significant advances in fields such as biomedicine[1-2], optoelectronics[2-3], and magnetic data storage - devices[4-6] (e.g., hard disks, video tapes). They are widely utilized in semiconducting technologies that are central to advancements in the development of various devices.[7-18] A thin film is a low dimensional (2D) thin layer of material on a substrate can possess characteristics different from the bulk material of the same chemical composition, giving it distinct optical, mechanical, magnetic, and electrical (conductive or non-conductive) properties relative to its bulk component.[19-23]

A good example of the indispensable contribution of thin film technologies in industry is in its use in photovoltaic (PV) technologies. Different factors inform the great interest observed in their use in photovoltaic cells (PVCs), and why they provide a pivotal contribution to the rise of new generations of PVCs.

(i) Their superior light harvesting ability is essential and this can also be enhanced through the design and tailoring of the physical structure or geometry (size, shapes, area) of the film.[24-27]

(ii) Less material is required to produce a thin film, for example, a silicon wafer used in a first-generation PVCs has a thickness of approximately 350 μm and thus would require more silicon than a 1 μm amorphous silicon thin film used in a 2nd generation PVC.[28-29]

(iii) The availability of a variety of substrates (e.g., ceramic) diversifies their application.

(iv) They allow for surface modification leading to tailoring of optical properties such as reflection, scattering and transmission, and for the passivation of grain boundaries.[30-31]

(v) They can be used to produce different types of electronic junctions; from single to multi/tandem junctions to enhance photon harvesting commensurate with the solar emission spectrum or to act as mobility filter for different charge carriers. The ability to create multi-junctions has been a large contributor to the high and

improved efficiencies of the different PV cells, like frontier perovskite PVCs with a reported efficiency greater than 30% to date.[31-32]

This makes thin film technologies attractive in the use of CNTs for diverse technological applications. Available techniques for thin film fabrication are classified into two broad categories; physical deposition and chemical vapor deposition (also referred to as the direct growth method), and both techniques have been utilized in the preparation of CNT thin films. The chemical vapor deposition method generally involves the reaction or decomposition of volatile precursors on a suitable substrate, usually in a presence of a metallic catalyst at an elevated temperature.[33-37] It can produce thin films with random or aligned CNTs. Compared to randomly distributed CNT thin films, aligned CNT thin films have demonstrated a lack of statistical reproducibility.[38] Different techniques have been used to obtain aligned CNT thin films, and these include the use of patterned catalysts, directional gas flow, and utilizing a substrate that has a determined lattice structure.[39-41]

Physical deposition techniques are largely solution based and they involve initially the dissolution of a material in a solvent and subsequent condensation of the solution on a substrate.[42-53] The quality of CNT thin films obtained from these techniques (as measured by high conductivity) depends on the quality of CNTs and their dispersion (i.e., homogeneity and stability) prior to deposition on a substrate. Given the high aspect ratio of CNTs, obtaining a homogenous and stable dispersion may be aided and improved by the addition of surfactants or polymers, which also makes their removal a crucial factor.[33-34] Excellent dispersions result in smooth thin films that exhibit relatively high conductivity because they have fewer electron scattering centres such as small grain boundaries, and they provide better electron pathways and transport than their counterpart. [31, 34, 54]

Additionally, the type of substrates used are essential and may determine where and how the thin film may be applied (e.g., transparent conducting oxides on glass such as tin indium oxide (ITO) and fluorine-doped tin oxide (FTO)). The wettability of the substrate's surface is a significant factor in the quality of the thin film produced, failure to take this into account may lead to limited film substrate adhesion (in the case of CNTs) or delamination. In some cases, this is improved through the treatment/activation of the substrate's surface before deposition to improve the interaction between the material and substrate.[33, 55-59] Seeman *et al.* activated the substrate's surface by applying an electric field to the substrate, thus managing to control the deposition characteristics and pattern resolution by allowing the assembly of the CNTs onto

the charged surface to be governed by Coulombic interactions.[60] Saran and co-workers improved the surface adhesion of the polyethylene terephthalate (PET) substrate after treating the substrate with amino-propyl-tri-ethoxy-silane (APTES).[44]

The physical deposition and chemical deposition methods differ in the type and quality of the film they produce. Direct growth methods can produce highly conductive thin films with few defects and good CNT-CNT contacts, resulting in the presence of individualized CNTs in the thin film. However, the methods are performed at high temperatures and under vacuum, thus restricting their application in certain fields by being incompatible with some substrates (plastic). On the other hand, despite challenges associated with individualizing CNTs in different dispersion media for solution-based methods, they can produce CNT thin films at reduced costs due to the low temperature and vacuum conditions used.[33-34]

The application of CNT as thin films in devices is determined by its physical properties amongst other significant factors. The thickness of the film is crucial; high electrical conductivity and optical transparency are observed for a thickness in the 10-100 nm range, and this has allowed them to be used as a photoanode in place of indium tin oxide electrodes.[61-62] Micro-meter thick films are suitable for application in supercapacitors, batteries, and fuel cells.[63-64] The nanotube density of the thin film also influences their area of application. Given that a sample of CNTs consists of semiconducting and metallic nanotubes, a transition between semiconducting and metallic behaviour is observed when the density of the materials changes. A density close to the percolation threshold has semiconducting behaviour and restricts the application of the film to transistors and sensors.[65-66]

Different techniques are available for the modification of CNT thin films to improve their quality and properties, and thus diversify their application. *Patterning* of the films can be employed in both the CVD and solution-based methods to design and tailor their morphology. Thin films obtained using the CVD method can be patterned by using techniques such as inkjet printing, micro contact printing, photolithography etc., while those obtained from solution-based methods can use additional techniques such as laser ablation and E-beam lithography.[33, 67-70] *Doping and functionalization* techniques have also been utilized; covalent functionalization is not ideal as it has a great impact on the materials transport characteristics, and it tends to lower electron mobility. On the other hand, non-covalent functionalization has a lesser effect on the intrinsic electron transport properties of the CNT thin film provided that the materials used for functionalization are removed.[33] The doping of CNT thin films is a

simple process that alters the charge distribution and the position of the Fermi-level in the band structure of the material. It involves exposure of the thin film to a dopant, normally by immersion in a solution of the dopant, but gas-based doping has also been reported.[33, 71-72] Eda and co-workers reported a 5-fold increase in the conductivity of their CNT thin film after treatment with HNO_3 and $SOCl_2$.[73] CNT thin films can also have their properties and functionality improved by incorporating different materials that allow them to form hybrids or composites. This technique has been used to improve the surface properties of CNT thin films such as roughness, without negatively affecting the surface's electrical conductivity.[33, 74] Polymer coatings have been useful in improving their mechanical strength by filling the pores of the thin films.[33] This technique offers great utility and versatility for making CNT thin films provided they are applied in fields where the removal of the incorporated dopant is not required. Although CNT thin films with regular network arrangements of CNTs have been developed, most films have random network arrangements. However, this can be limiting to their scope of application, particularly in their use as electrodes in different fields. Their use as electrodes is governed primarily by their electrochemical properties, which are in turn determined by the morphology (thickness, smoothness) of the film.[61-66]

CNT thin films have shown great potential in their application as counter electrodes (CEs) in DSSCs (i.e., this allows for the potential replacement of the costly platinum CE). Thus far, Pt has reported high catalytic activity for the reduction of the unrivalled I^-/I_3^- redox couple electrolyte of the device. CNTs have recorded successful reduction of the DSCC-I^-/I_3^- redox couple electrolyte, comparable and in some cases, superior to Pt.[48, 75-76] Different types of promising redox couple electrolytes made of transition metal complexes such as Co(III)/Co(II) $Co(II)[dbbip]_2/(ClO_4)_2$ (where dbbip is 2,6-bis(1'-butylbenzimidazol-2'-yl)pyridine), Cu(II)/Cu(I), Fe(III)/Fe(II), Ni(IV)/Ni(III), and Os(III)/Os(II) have been investigated, and were found to present sluggish mass transport. However, they have given improved efficiencies, primarily under low lighting compared to full light conditions, when using I^-/I_3^- redox couple.[77-83] Organic redox shuttles such as the 2,2,6,6-tetramethyl-1-piperidinyloxy radical ($TEMPO/TEMPO^+$) and organic disulfide/thiolate redox couples have also been introduced. They have shown several advantages such as higher open circuit voltage and lower competitive visible light absorption efficiency, respectively. However, both the $TEMPO/TEMPO^+$ and disulfide/thiolate redox couple exhibit an inferior regeneration efficiency to the I^-/I_3^- redox couple. The low device efficiency from the disulfide/thiolate redox couple was found to be due to the high charge transfer resistance and low fill factor relative to the I^-/I_3^- redox couple.[81, 83-

[85] Hence, the I^-/I_3^- redox couple has achieved an almost universal usage in DSSCs. This is due to their high overpotential in the reduction of titanium dioxide (TiO_2) and high current densities on the surfaces of DSSCs electrodes such as Pt and graphite.[86] The use of CNT thin films in conjunction with this redox system have shown electrochemical properties and device conversion efficiencies comparable to or greater than devices that use Pt as a CE.[87-97]

Thin film technologies offer indispensable techniques in producing new and versatile 2D materials with unique, and in some cases better properties, than their bulk form. The work in this chapter is focused on the fabrication of pristine, and heteroatom doped (N, O, B, N-B, P) MWCNTs thin films using a drop casting solution-based method. Their electrochemical properties in the reduction of the iodide-triiodide electrolyte were evaluated and reported.

8.1. Materials and methods.

8.1.1. Starting material

Lithium iodide (LiI, 99.9%), lithium perchlorate ($LiClO_4$), iodine (I_2, 99.8%), acetonitrile (anhydrous, 99.8%), polyethylene glycol and fluorine doped tin oxide (FTO) glass were used as obtained from the suppliers. The pristine, boron doped, nitrogen-boron co-doped and phosphorous doped MWCNTs were prepared and reported in chapters 3, 4, 5 and 6, respectively.

8.1.2. Preparation of the thin films.

The FTO glass was cleaned by submersion in isopropyl alcohol under sonication for 20 min, followed by washing with acetone under sonication for an additional 20 min. The glass was left to dry in air. Pristine or heteroatom doped MWCNTs (20 mg) were added to 20 ml of distilled water and left to stir for 24 h. The resulting mixtures were sonicated for 1 h and were allowed to stand for 1 h without any agitation. A solution of polyethylene glycol (7.4 g) in 20 ml of water was prepared. The supernatant portion of the MWCNTs dispersion (0.5 ml) was added to 0.5 ml of the polyethylene glycol solution and left to stir for 5 min. Then, 0.5 ml of the resulting mixture was collected using a syringe and drop casted onto an FTO glass on a 180℃ hot plate, once the water evaporated off the FTO glass, successive drop casting was performed until the full 0.5 ml mixture was used. Every successive drop was preceded by the removal of the FTO glass from the hot plate followed by replacement back on the hot plate. The FTO glass was then placed at 250℃ in an oven for 2 h to remove polyethylene glycol; this resulted in the formation of a thin black film on the glass.

8.1.3. Electrochemical analysis of MWCNTs thin films.

The iodide tri-iodide electrolyte was prepared by dissolving LiI (0.27 g), I_2 (0.1 g) and $LiClO_4$ (2.1 g) in acetonitrile (50 ml). A three-electrode system with a silver/silver chloride electrode as a reference electrode and platinum wire as a working electrode (diameter of 2.0 mm and are area of 3.14 mm^2) were used in obtaining cyclic voltammetry (CV) data at a scan rate of 100 mV/s and a potential window of -1.5-1.0 eV, and the electrochemical impedance spectroscopy (EIS) properties were determined from 100 KHz to 0.200 Hz.

8.2. Results and discussion.

The use of water for the dispersion of MWCNTs has several challenges: (i) The relatively high boiling point of water (100 ℃), and (ii) the high surface tension of water (72 mM/m, 25 ℃).[98-101] The latter was found to be detrimental for the fabrication process as it facilitated the creation of islands on the surface of the substrate leading to the formation of a non-uniform thin film. The high surface tension of water results in a low wettability of the substrate surface.[98-102] These effects are illustrated in **Figure 8.1,** in which the role of the surface energies on the wettability of a film is depicted.

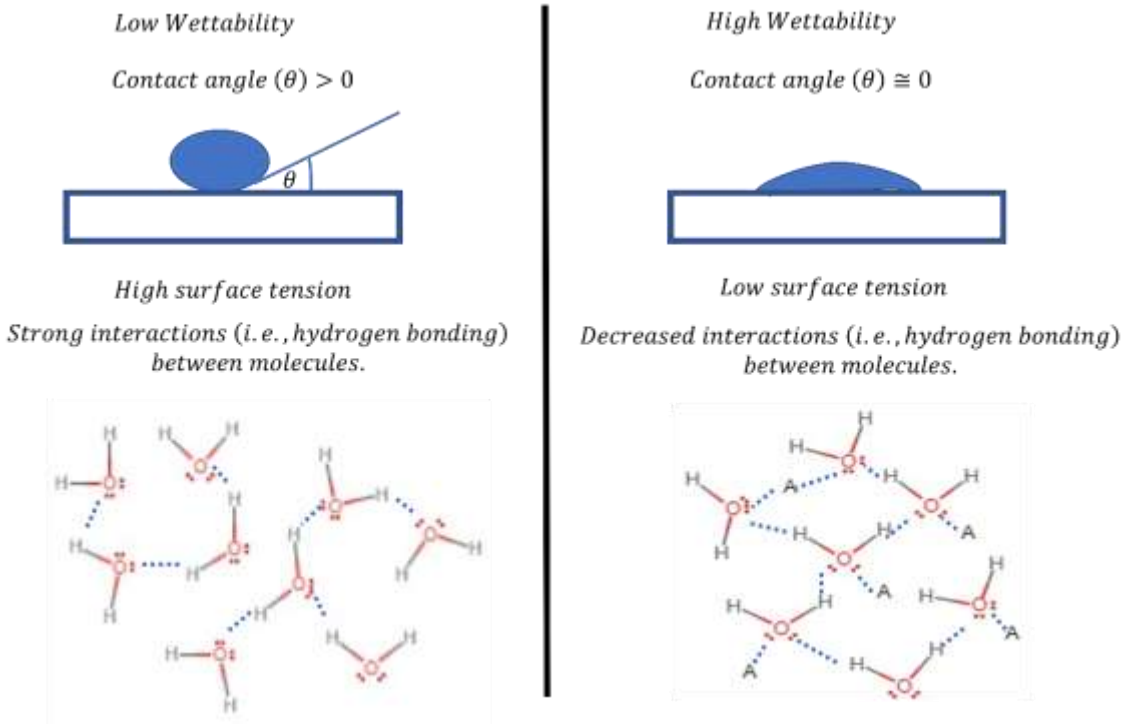


Figure 8.1: The wettability of a liquid on a surface.

The high surface tension of water is a consequence of the strong hydrogen bonding interaction between the molecules resulting in large cohesion forces that cause it to behave as if it is

covered by an elastic membrane.[98-102] The surface tension can be decreased by adding a material/chemical (denoted A in **Figure 8.1**) that will disrupt the strong hydrogen bonding interactions. A near saturated solution of polyethylene glycol (PEG) was chosen (small amounts of PEG are required for crystallization to occur) to achieve the desired wettability. PEG was chosen for its low melting point (60-63℃) and decomposition temperatures that allowed it to be removed during the annealing of the thin film.

The values of experimental parameters and conditions (i.e., potential window and scan rate) for electrochemical analysis were based on initial analysis data obtained from Pt reduction of the iodide triiodide electrolyte (**Figure 8.2a**). The use of Pt as a CE gives four redox processes, in the narrow potential window of -1.5 to 1.0 V:

Oxidation 1: $3I^- \rightarrow I_3^- + 2e^-$ $E_{a,1}$ = 0.25 V.

Reduction 1(RED 1): $3I_2 + 2e^- \rightarrow 2I_3^-$ $E_{c,1}$ = 0.60 V.

Oxidation 2: $2I_3^- \rightarrow 3I_2 + 2e^-$ $E_{a,2}$ = 0.75 V.

Reduction 2 (RED 2): $I_3^- + 2e^- \rightarrow 3I^-$ $E_{c,1}$ = -0.11 V.

This narrow window indicates that Pt has a relatively low barrier for electron transfer in reducing the electrolyte. In this study, RED 1 generated a current density ($J_{pc,1}$) of -0.65 mA/cm^2, while RED 2 produced a current density ($J_{pc,2}$) of -1.27 mA/cm^2. Multiple scanning cycles were performed, and a successive decrease in both current densities was observed with the number of cycles. This could be attributed to the formation of a diffusion layer on the electrode surface, which slowed down the mass transport and diffusion of the analyte to the electrode. EIS data was fitted with a Randles equivalent circuit for an interfacial reaction, and measurements (**Figure 8.2b**) of the Pt material reported a relatively high charge transfer resistance (R_{CT}) of 1853 Ω/cm^2.

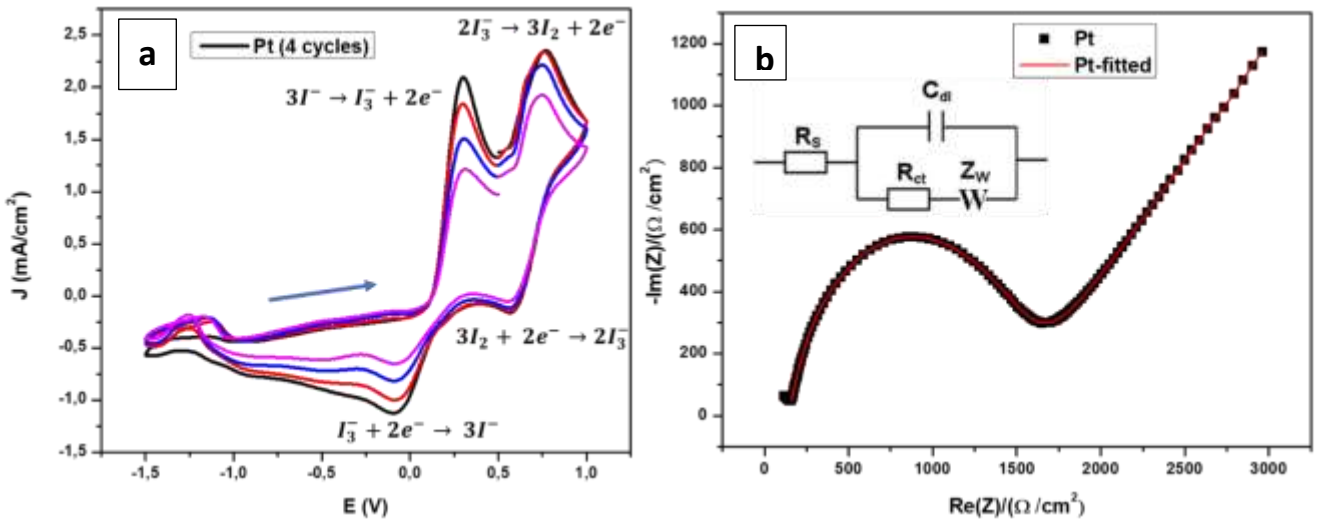


Figure 8.2: *a)* CV analysis of Pt, *b)* EIS analysis of Pt. Scan rate: 100 mV/s.

All the CV scans for the electrochemical analysis of the pristine and heteroatom doped MWCNTs thin films were restricted to the Pt potential window. Any material that did not report electrocatalytic activity within this potential window was considered not to be a suitable replacement for Pt as a CE, and the data thereto is not presented or discussed in this chapter. All the EIS data was fitted using the Randles equivalent circuit.

8.2.1. Electrochemical analysis of pristine and heteroatom doped MWCNTs.

8.2.1.1. The electrochemical analysis of pristine and nitrogen doped MWCNTs thin films.

CV scan (multiple) for pristine and nitrogen doped MWCNTs (**Figure 8.3**) reported two expected reduction peaks (Red 1 and Red 2). The reduction potentials of both films were observed at a more negative value than that of Pt (Table 8.1), with both films generating a current density lower than Pt. A more negative reduction potentials indicates that both films have a higher barrier to electron transfer. This was corroborated by the EIS measurements (Table 8.1, **Figure 8.3**) that revealed that pristine and N-doped MWCNT thin films had significantly higher charge transfer resistance (R_{CT}) than the Pt based electrode. This indicated that both thin films had poor electrocatalytic activity than Pt for both reduction processes and are not an appropriate replacement for Pt in DSSCs. However, both materials registered a lower extent of a decrease in the current density than Pt over multiple cycles, indicating the MWCNTs can maintain their electrocatalytic activity over a longer period than Pt.

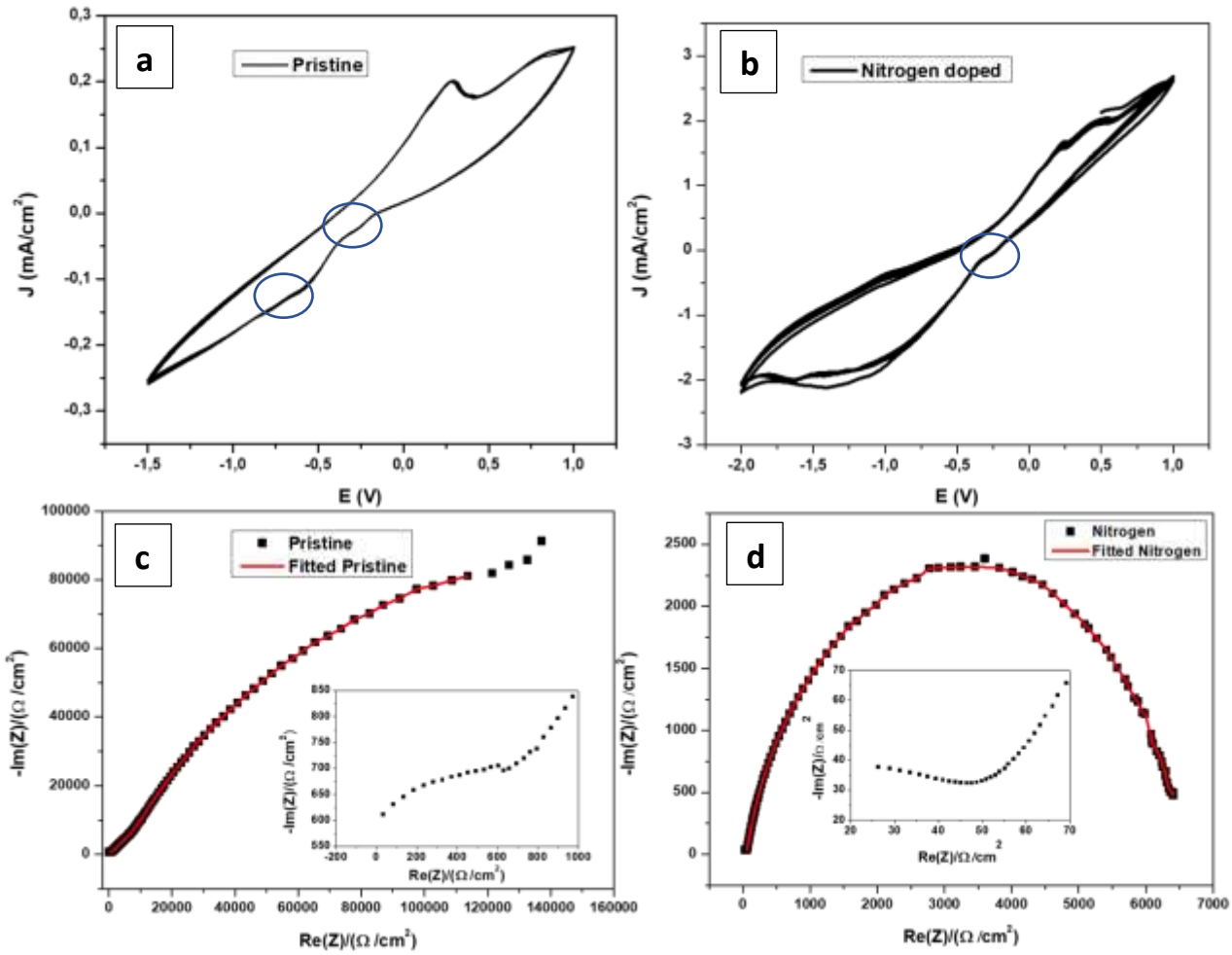


Figure 8.3: *a)* CV analysis of pristine MWCNTs thin film, *b)* CV analysis of nitrogen doped MWCNTs thin film, *c)* EIS scan of pristine MWCNTs thin film, *d)* EIS scan of nitrogen doped MWCNTs thin film. Scan rate: 100 mV/s.

The pristine and N-doped MWCNTs presented with a small semi-circle at lower resistances, which indicated that there MWNCTs in the films were not homogenous in their electrical properties. In addition, the non-vertical line at high Re(Z) for pristine MWCNTs thin films indicates limited ion transport in the electrolyte.

Table 8.1: Electrochemical data of pristine and nitrogen doped MWCNTs thin films.

Sample	$J_{pc,1}$ (mA/cm^2)	$J_{pc,2}$ (mA/cm^2)	$E_{c,1}$ (V)	$E_{c,2}$ (V)	R_s (Ω/cm^2)	R_{ct} (Ω/cm^2)
Pt	-0.65	-1.27	0.60	-0.11	147	1853
Pristine MWCNTs	-0.01	-0.11	-0.35	-0.61	398	299 000

N-doped MWCNTs	-0.05	-0.58	-0.26	-1.40	45	6555

The N-doped MWCNTs thin film had a higher current density (i.e., 5 times more) than the pristine MWCNTs thin film. The R_s and R_{CT} values were also found to be consistent with this observation. This indicates that the addition of nitrogen to the lattice structure of MWCNTs improved the electrocatalytic activity of the MWNCTs. The R_{CT} value was improved by the lone electron pairs due to nitrogen, which act as delocalized charges for electron transport across the network structure. Additionally, the R_s value was also improved due to nitrogen providing additional electrocatalytic active sites for the reduction reaction. As evidenced by the low current density, both thin films reported significantly lower electrocatalytic activity for iodine (Red 1) than for the tri-iodide (I_3^-) ion (Red 2). In addition, despite the significantly lower R_s and R_{CT} values, Red 2 occurred at a more negative potential for the N-doped MWCNTs thin film than the pristine MWCNTs.

8.2.1.2. The electrochemical analysis of MWCNTs thin films prepared from MWCNTs produced at different reaction times.

Samples produced from the attempted synthesis of B-doped MWNCTs using tri-isopropyl borate and trimethyl borate at different reaction times (see full discussion and results in **Chapter 4, section 4.3.1**) were used to fabricate thin films whose electrochemical properties were evaluated below (**Figure 8.4a,c**). The MWCNTs thin films (BP800-15-*i*, BP800-30-*i*, BP800-*i*) were successful in reducing the tri-iodide electrolyte. Both reduction processes (I_2/Red 1 and I_3^-/Red 2) were found at more negative reduction potentials than Pt (**Figure 8.4a**, Table 8.2). They all produced lower current densities than Pt for both reduction processes, which made them inappropriate replacements for Pt as a counter electrode (CE). The current densities of BP800-15-*i* (-0.51 Ω/cm^2) and BP800-30-*i* (-0.57 Ω/cm^2) thin films were similar (difference of 0.06 Ω/cm^2), while that of the BP800-*i* thin film (-1.09 Ω/cm^2) was found to be approximately double that of both films. Additionally, all three films recorded higher R_{CT} values than Pt. The small differences in electrocatalytic performance between the BP800-15-*i* and BP800-30-*i* thin films was in line with the difference in the R_{CT} value (**Figure 8.4c,** Table 8.2) of 0.5 kΩ/cm^2. Furthermore, just as the current density for BP800-*i* thin film was approximately double that of the BP800-15-*i* and BP800-30-*i* thin films, the R_{CT} value was found to be approximately half that of both values observed for the thin films. Although all

three samples did not contain any boron in their lattice structure, they still reported higher current densities and lower R_{CT}, and consequently better electrocatalytic activity than the pristine MWCNTs. This was attributed to the presence of nitrogen and high concentrations of oxygen (> 10%, with BP800-*i* reporting the highest concentration of 14%) in the lattice structure of each material, which provided additional active sites for reduction, and participation in the electron transport across the conjugated network structure.

The BP800-15-*m* and BP800-30-*m* thin films produced from materials prepared from trimethyl borate reported larger current densities and lower R_{CT} values than Pt (**Figure 8.4b, d**, Table 8.2) in the reduction of I_3^-(Red 2), but still fell short in the reduction of I_2 (Red 1). Despite having better electrocatalytic activity than Pt and thus being a potentially suitable replacement, both thin films reported more negative reduction potentials than Pt. A difference of 0.05 mA/cm^2 in current density was reported between the BP800-15-*m* and BP800-30-*m* thin films, this was not reflected in the marginal difference (1425 Ω/cm^2) recorded between their R_{CT} values. This could be ascribed to BP800-15-*m* containing boron (0.31%) in its lattice structure, which may play a compensatory role in the performance of the material by providing additional active sites for the reduction reaction on the material.

Table 8.2: Electrochemical data of B-doped MWCNTs thin films for samples prepared at different reaction times.

Sample	$J_{pc,1}$ (mA/cm^2)	$J_{pc,2}$ (mA/cm^2)	$E_{c,1}$ (V)	$E_{c,2}$ (V)	R_{ct} (Ω/cm^2)
Pt	-0.65	-1.27	0.60	-0.11	1853
Pristine MWCNTs	-0.01	-0.11	-0.35	-0.61	299k
BP800-15-*i*	-0.05	-0.51	-0.25	-1.35	9.9k
BP800-30-*i*	-0.11	-0.57	-0.25	-1.25	9350
BP800-*i*	-0.05	-1.09	-0.25	-1.45	4720
BP800-15-*m*	-0.05	-1.42	-0.25	-1.35	1710
BP800-30-*m*	-0.05	-1.47	-0.25	-1.25	285

BP800-*m*	-0.11	-0.35	-0.25	-1.22	245

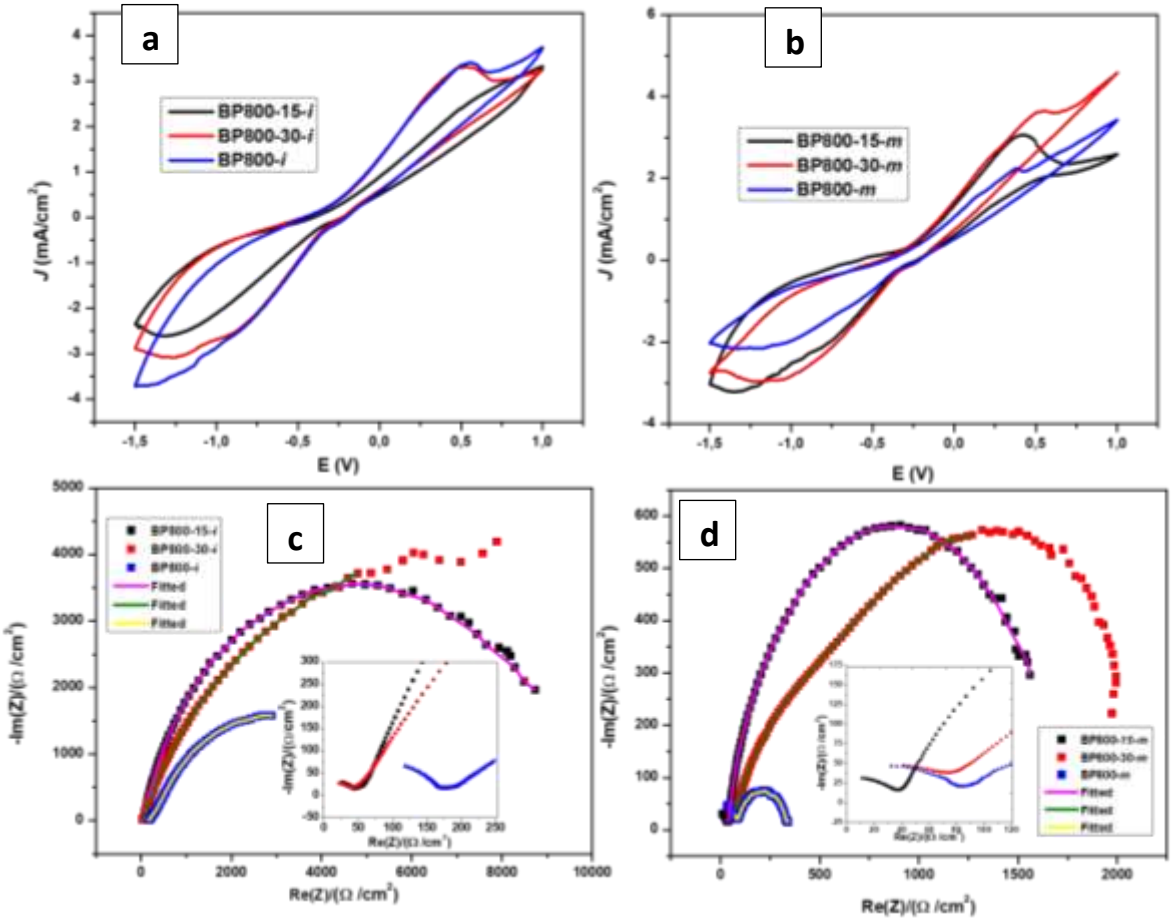


Figure 8.4: *a)* CV analysis of heteroatom doped MWCNTs (prepared from tri-isopropyl borate at different reaction times) thin films, *b)* CV analysis of heteroatom doped MWCNTs (prepared from trimethyl borate at different reaction times) thin films, *c)* EIS scans of heteroatom doped MWCNTs (prepared from tri-isopropyl borate at different reaction times) thin films, *d)* EIS scans of heteroatom doped MWCNTs (prepared from trimethyl borate at different reaction times) thin films. Scan rate: 100 mV/s.

The BP800-*m* thin film not only reported lower electrocatalytic activity than Pt, but values lower than BP800-15-*m* and BP800-30-*m* thin films. This was despite it reporting the lowest R_{CT} (245 Ω/cm^2) value, and the highest boron concentration (0.99%) in its lattice structure. However, a large portion of that boron was found to exist in as B_2O_3. It could have contributed to the low catalytic activity by blocking the active sites of the material. All six thin films presented with better electrocatalytic activity than the pristine MWCNTs thin film. The better performance of the BP800-15-*m* and BP800-*m* thin films were largely attributed to the presence

of both the boron and oxygen atoms in the structure of the MWCNTs. However, the remaining samples predominantly had oxygen in the lattice structure and no boron, including the one with the highest electrocatalytic activity (BP800-30-*m*). This indicated that the boron sources played little role in modifying the electrode activity, but their presence in the reaction process was essential in producing MWCNTs with high performance.

8.2.1.3. The electrochemical analysis of MWCNTs thin films prepared with material produced at different temperatures.

Samples produced from the attempted synthesis of B-doped MWNCTs using tri-isopropyl borate and trimethyl borate at different reaction temperatures (see full discussion and results in **Chapter 4, section 4.3.2**) were used to fabricate thin films whose electrochemical properties were evaluated below (**Figure 8.5,** Table 8.3). Tri-isopropyl borate was found to be successful in producing B-doped MWCNTs at 700℃ (BP700-*i*) and 750℃ (BP750-*i*) but failed at 800℃ (BP800-*i*).

Table 8.3: Electrochemical data of B-doped MWCNTs thin films for samples prepared at different temperatures

Sample	$J_{pc,1}$ (mA/cm^2)	$J_{pc,2}$ (mA/cm^2)	$E_{c,1}$ (V)	$E_{c,2}$ (V)	R_{ct} (Ω/cm^2)
Pt	-0.65	-1.27	0.60	-0.11	1853
Pristine MWCNTs	-0.01	-0.11	-0.35	-0.61	299k
BP700-*i*	-0.04	-0.62	-0.25	-1.26	879
BP750-*i*	-0.04	-0.45	-0.25	-1.26	290
BP-60-*i*	-0.05	-1.09	-0.25	-1.45	4720
BP700-*m*	-0.05	-0.10	-0.25	-0.63	250
BP750-*m*	-0.05	-0.78	-0.25	-1.30	295
BP-60-*m*	-0.11	-0.35	-0.25	-1.22	245

All three thin films prepared from these samples reported lower current densities than Pt. This is despite the R_{CT} values of the BP700-*i* (879 Ω/cm^2) and BP750-*i* (290 Ω/cm^2) thin films being marginally lower than both the Pt (1853 Ω/cm^2) and BP800-*i* (4720 Ω/cm^2) thin films. This

could be attributed to the presence of B_2O_3 in both samples, which may exist on the surface of the nanotubes, and thus impede the electrochemical reaction at the surface of the electrode.

Trimethyl borate did not produce B-doped MWCNTs at 700℃ and 750℃ but was successful at 800℃. Despite having some of the lowest R_{CT} values, thin films fabricated from these samples reported lower current density, and consequently poorer electrocatalytic activity relative Pt. In the case of the BP800-*m* this was ascribed to the presence of B_2O_3 on the surface of the nanotubes. This indicates that the low performance could be attributed to several other factors that were not evaluated in this work. These include (i) the smoothness of the film formed, (ii) the thickness of the film (iii) the density percolation pathway, and (iv) diameter and length of MWCNTs used.[19-23, 61-66] Although the BP700-*m* thin film had the lowest electrocatalytic activity, it reported a more positive potential for the reduction of I_3^-(Red 2) than all the thin films produced from the tri-isopropyl borate derived samples, the BP800-*m* and BP750-*m* thin films. This is consistent with its low R_{CT} value.

Both sets of thin films, except BP700-*m*, had better electrocatalytic activity than the pristine MWCNTs thin films, even when no boron was added to the lattice structure. This corroborates that the two boron sources, using our synthetic methodology, do not fulfil their role in the reaction but significantly influence the nature of material produced, and ultimately their electrochemical performance.

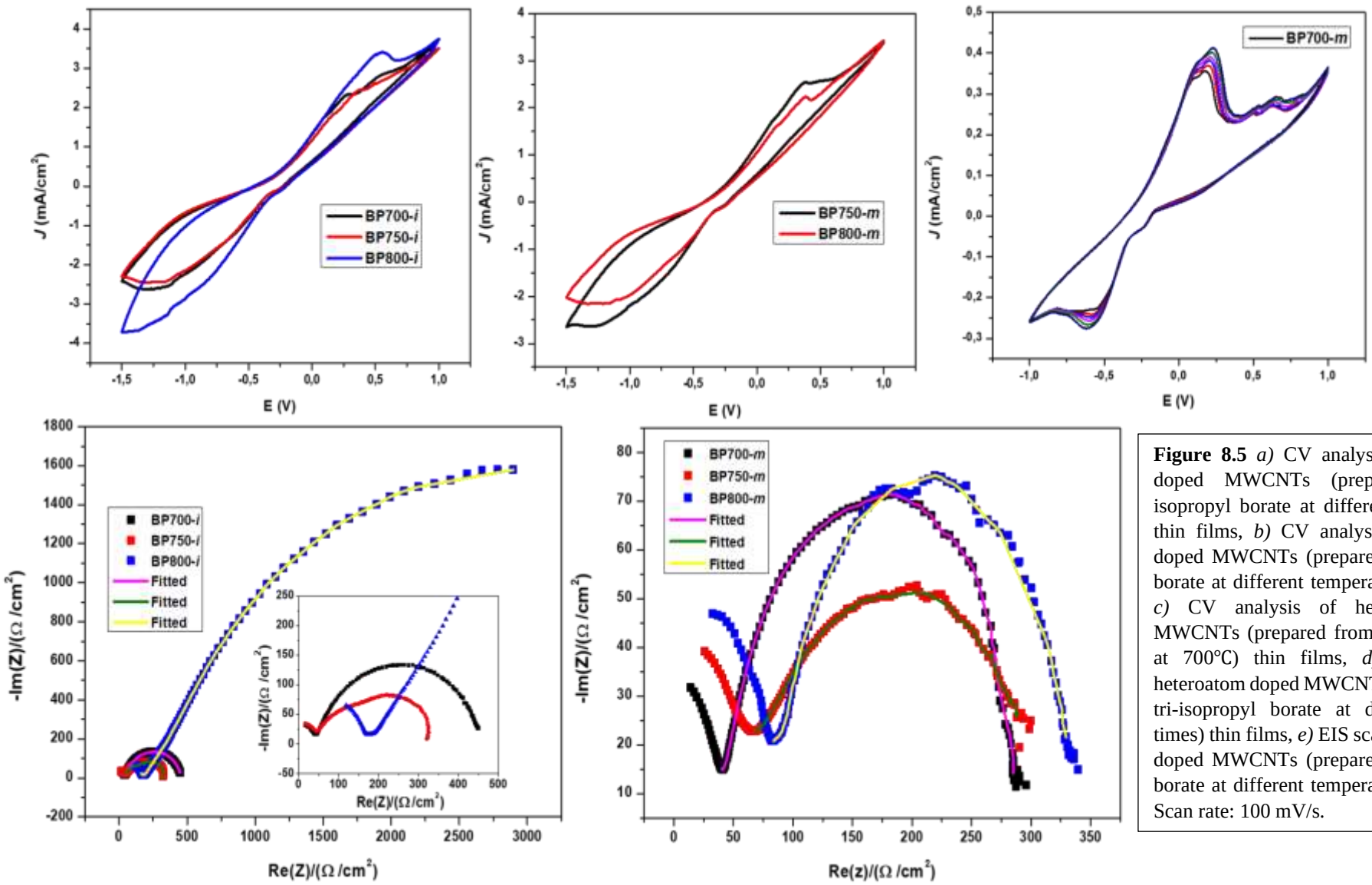


Figure 8.5 *a)* CV analysis of heteroatom doped MWCNTs (prepared from tri-isopropyl borate at different temperatures) thin films, *b)* CV analysis of heteroatom doped MWCNTs (prepared from trimethyl borate at different temperatures) thin films, *c)* CV analysis of heteroatom doped MWCNTs (prepared from trimethyl borate at 700°C) thin films, *d)* EIS scans of heteroatom doped MWCNTs (prepared from tri-isopropyl borate at different reaction times) thin films, *e)* EIS scans of heteroatom doped MWCNTs (prepared from trimethyl borate at different temperatures) thin films. Scan rate: 100 mV/s.

8.2.1.4. The electrochemical analysis of boron-nitrogen co-doped MWCNTs thin films.

In the attempt to synthesise boron-nitrogen co-doped MWCNTs, the addition of boron to nitrogen doped MWCNTs (NP800) using tri-isopropyl borate was attempted and produced a sample labelled NB800. The resulting NB800 thin film made from NB800 gave a lower electrocatalytic performance than Pt (**Figure 8.6**, Table 8.5). This was corroborated by its larger R_{CT} value of 3655 Ω/cm^2 compared to that of Pt (1853 Ω/cm^2). However, it recorded better electrocatalytic performance than the pristine MWCNTs thin film, and the N-doped MWCNTs thin film from which the sample was derived. Although it still fell short of being a replacement for Pt, this indicated that an addition of both nitrogen and boron to the lattice structure of pristine MWCNTs can improve their electrochemical performance. This was corroborated by the trend in the R_{CT} values as addition of nitrogen led to a significant decrease in R_{CT} from 299k Ω/cm^2 to 6555 Ω/cm^2, which was followed by a further decrease to 3655 Ω/cm^2 when boron was added to N-doped MWCNTs. This was ascribed to both heteroatoms producing additional actives sites for the reduction process and to partake in electron transport through the lone pairs on nitrogen and through the empty p-orbital on boron. The data can also be attributed to two additional factors; (i) the presence of the N-B bond in the lattice structure (the bond between these two may lead to a neutralization of the lone pair of electrons on the nitrogen by the empty p-orbital on boron). (ii) The low surface area of 2.1 m^2/g compared to 21.1 m^2/g for the N-doped MWCNTs.

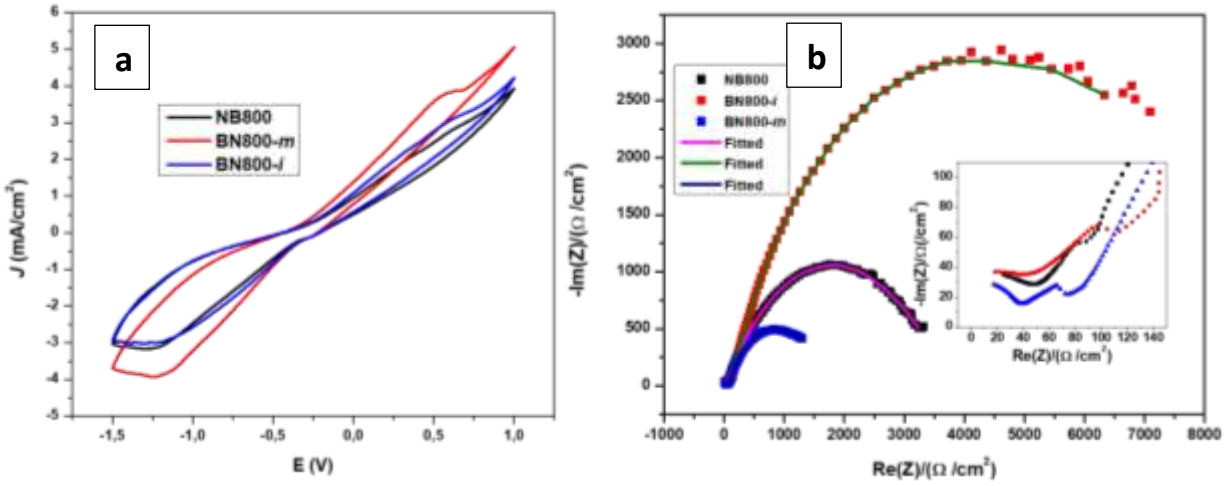


Figure 8.6: *a*) CV analysis of nitrogen-boron co-doped MWCNTs thin films, *b)* EIS scan of nitrogen-boron co-doped MWCNTs thin films. Scan rate: 100 mV/s.

Table 8.5: Electrochemical data of boron-nitrogen co-doped thin films

Sample	$J_{pc,1}$ (mA/cm^2)	$J_{pc,2}$ (mA/cm^2)	$E_{c,1}$ (V)	$E_{c,2}$ (V)	R_{ct} (Ω/cm^2)
Pt	-0.65	-1.27	0.60	-0.11	1853
Pristine MWCNTs	-0.01	-0.11	-0.35	-0.61	299k
N-doped MWCNTs	-0.05	-0.58	-0.26	-1.40	6555
NB800	-0.12	-0.71	-0.37	-1.25	3655
BP700-*i*	-0.04	-0.62	-0.25	-1.26	879
BN800-*i*	-0.11	-0.57	-0.27	-1.25	8720
BP750-*m*	-0.05	-0.78	-0.25	-1.30	295
BN800-*m*	-0.05	-1.47	-0.30	-1.25	1617

The B-doped samples BP700-*i* and BP750-*m* prepared from tri-isopropyl borate and trimethyl borate, respectively, were also used in an attempt to produce boron-nitrogen co-doped MWCNTs. The boron found in the lattice structure was lost due to the high reaction temperature and by possible substitution with nitrogen as reaction produced N-doped MWCNTs (BN800-*i*) instead. The BN800-*i* thin film showed a poor electrochemical performance relative to Pt and the BP700-*i* thin film, as evidenced by the lower current density (0.57 mA/cm^2) and higher R_{CT} (8720 Ω/cm^2) value. BP750-*m* did not produce boron-nitrogen co-doped MWCNTs. It was found that more nitrogen was added (2.47%, NB800-*m*) than in the production of NP800 (0.97%). Consequently, the NB800-*m* thin film had a higher current density (1.47 mA/cm^2) and slightly lower R_{CT} value (1617 Ω/cm^2) than found for Pt. This indicates that higher concentrations of nitrogen in the lattice structure of MWCNTs are sufficient for better electrocatalytic activity than Pt. The higher concentration of nitrogen in the lattice structure provided more actives sites and led to a larger degree of activation of the π-conjugated system.

8.2.1.5. The electrochemical analysis of phosphorous doped MWCNTs thin films.

A post doping and *in-situ* method were used in the attempted production of P-doped MWCNTs using PPh_3. The *in-situ* method was unsuccessful and led to the production of pristine MWCNTs (PhP800). However, The PhP800 thin film reported higher current density (0.57 mA/cm^2) and lower R_{CT} (24k Ω/cm^2) than found for the pristine MWCNTs thin film (**Figure 8.7,** Table 8.6). Sample Ph(1:2)800 was the only one that confirmed the successful incorporation of phosphorus (0.29%) into the lattice structure. Both Ph(1:1)800 and Ph(1:2)800 thin films had better electrocatalytic activity than the pristine MWCNTs thin film. The Ph(1:1)800 thin film reported lower current density (0.82 mA/cm^2) than Pt, while Ph(1:2)800 has a current density (1.20 mA/cm^2) comparable to that of Pt. This was attributed to phosphorous increasing the number of active sites for the reduction reaction. It also confirmed that phosphorus improved the electrochemical performance of pristine MWCNTs.

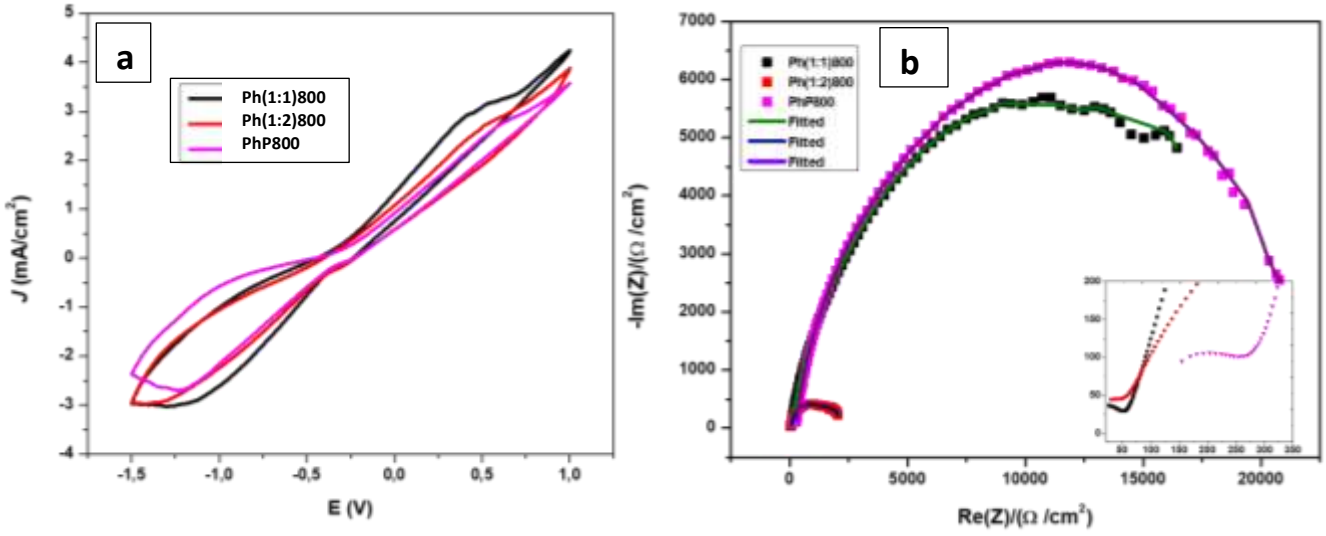


Figure 8.7: *a)* CV analysis of phosphorous-doped MWCNTs thin films, *b)* EIS scans of phosphorous-doped MWCNTs thin films. Scan rate: 100 mV/s.

Table 8.6: Electrochemical data of P-doped MWCNTs thin films.

Sample	$J_{pc,1}$ (mA/cm^2)	$J_{pc,2}$ (mA/cm^2)	$E_{c,1}$ (V)	$E_{c,2}$ (V)	R_{ct} (Ω/cm^2)
Pt	-0.65	-1.27	0.60	-0.11	1853

Pristine MWCNTs	-0.01	-0.11	-0.35	-0.61	299k
Ph(1:1)800	-0.14	-0.82	-0.26	-1.24	23k
Ph(1:2)800	-0.02	-1.20	-0.30	-1.32	2451
PhP800	-0.18	-0.59	-0.26	-1.24	25k

8.3. Conclusion.

The aim of this chapter was to assess the electrochemical properties of heteroatom doped MWCNTs for the replacement of Pt as a counter electrode in the reduction of the iodide-tri-iodide electrolyte. All the thin films investigated were prepared from MWNCTs prepared under different reaction conditions using different reagents. Pt recorded a current density of -1.27 mA/cm^2, and only three thin films (BP800-15-*i*, BP800-30-*i*, and BN800-*m*) reported a higher current density, and consequently better electrocatalytic performance than Pt. Two thin films (BP800-*i*, -1.09 mA/cm^2 and Ph(1:2)800, -1.20 mA/cm^2) reported current densities comparable to that of Pt. The better performance of the BP800-15-*m* (-1.42 mA/cm^2) and BN800-*m* (-1.47 mA/cm^2) thin films were attributed to presence of boron (0.31%) and high concentration of nitrogen (2.47%) in the lattice structure of the MWNCTs, respectively. However, it was established that the presence of boron did not translate into a high electrocatalytic performance, as evidenced by the poor performance of BP700-*i* (-0.62 mA/cm^2), BP750-*i* (-0.45 mA/cm^2), and BP800-*m* (-0.35 mA/cm^2) thin films. This was corroborated by the performance of BP800-30-*m* (-1.47 mA/cm^2), which had no boron reported in its lattice structure but a high concentration of oxygen (14%). All heteroatom (O, N, B and P) containing MWCNTs, had a higher performance than the pristine MWCNTs thin films. This indicated that addition of these heteroatoms and the method used to add them determines their electrochemical performance.

Chapter 8 References

1. V. Vedra, L. Wu, S. Krishnan. *Nanotechnology of Life Sciences; polymer thin films for biomedical applications.* 2011, **5**, 1-51.
2. E. Bekyarova, Y. Ni, E. B. Malarkey, V. Montana, J. L. McWilliams, R. C. Haddon, V. Parpura. *Journal of Biomedical Nanotechnology.* 2005, **1**, 3-17.
3. J. Zhao, Z. Chi, X. Chen, M. S. Arnold, Y. Zhang, J. Xu, Z. Chi, M. P. Aldred. *Nanoscale.* 2018, **10**, 5764-5792.
4. P. Avouris. J. Chen. *Materials Today.* 2006, **9**, 46-54.
5. T. Thomson. *Metallic Films for Electronic, Optical and Magnetic Applications.* 2014, 454-546.
6. P. Sheng, B. Wang, R. Li. *Journal of Semiconductors*. 2018, **39**, 011006 (1-13).
7. S. Sharma, K. K. Jain, A. Sharma. *Material Science and Applications.* 2015, **6**, 1145-1155.
8. T. D. Lee, A. V. Ebong. *Renewable and Sustainability Reviews.* 2017, 1286-1297.
9. H. A. Alturaif, Z. A. Al Othman, J. G. Shapter, S. M. Wabaidur. *Molecules.* 2014, **19**, 17329-17344.
10. H. Sun, J. Wei, Y. Jia, X. Cui, K. Wang, D. Wu. *Nanoscale Research Letters.* 2014, **9**, 514-520.
11. M. Rapaso, P. A. Ribeiro. *Chemsensors.* 2019, **7**, 37-38.
12. Z.-D. Lin, S.-J. Young. S.-J. Chang. *IEEE Sensors Journal.* 2015, **15**, 7017-7020.
13. C. D. Lokhande, D. P. Dubal. O.-S. Joo. *Current Applied Physics.* 2011, **11**, 255-270.
14. T. Bohneberger. U. Schmid. *Procedia Engineering.* 2015, **120**, 1037-1041.
15. S. Lu, A. D. Franklin. *Nanoscale.* 2020, **12**, 23371-23390.
16. W. Huang, Y. Wang, Y. Zhang, J. Zhu, D. Liu, J. Wang, L, Fan, R. Qui, M. Zhang. *Carbon*. 2022, **189**, 386-394.
17. P. Charturvedi, A. Chouksey, S. Malik, M. Lal, P. K. Chaudhury, Harsh. *Fullerenes, Nanotubes and carbon Nanostructures.* 2013, **21**, 888-893.
18. L. Jin, A. Chortos, F. Lian, E. Pop, C. Linder, Z. Bao, W. Cai. *Proceedings of the National Academy of Sciences of the United States.* 2018, **115**, 1986-1991.
19. D. Schlettwein. *Supramolecular Photosensitive and Electroactive Materials.* 2001, chapter 3, 211-338.
20. A. Abdelhalim, A. Abdellah, G. Scarpa, P. Lugli. *Carbon.* 2013, **61**, 72-79.

21. K. Mylvaganam, Y. Chen, W. Liu, M. Liu, L. Zhang. *Anti-abrasive Nanocoatings, Current and Future applications.* 2015, chapter 21, 543-567.
22. M. Benelemekki, A. Erbe. *Frontiers of Nanoscience.* 2019, chapter 1, 1-34.
23. M. C. Rao. *International Journal of Modern Physics; Conference Series.* 2013, **22**, 576-582.
24. A. M. Bagher, M. M. A. Vahid, M. Mohsen. *American Journal of Optics and Photonics.* 2015, **3**, 94-113.
25. A. M. Green. *Third Generation Photovoltaics: Advanced Solar Energy Conversion.* (2003). Springer, page 65.
26. C. J. Petti, M. M. Hilali, G. Prabhu. *Handbook of Thin Film Deposition (3rd edition).* 2012, chapter 10, 313-359.
27. R. E. Camacho, A. R. Morgan, M. C. Flores, T. A. Mcleod, V. S. Kumsomboone, B. J. Mordecai, R. Bhattacharjea, W. Tong, B. K. Wagner, J. D. Flicker, S. P. Turano, W. J. Ready. *JOM.* 2007, **59**, 39-42.
28. V.-M. Airaksinen. *Handbook of Silicon Based MEMS Materials and Technologies (2nd edition); Micro and Nano technologies.* 2015, chapter 15, 381-390.
29. National Renewable Energy Laboratory (NREL), Best research-cell efficiencies (Date accessed: 14-04-2017). www.commons.wikimedia.org/wiki/file:best_research-cell_efficiencies.png
30. M. T. Kibria, A. Ahammed, S. M. Song., F. Hossain., Shams-Ul-Islam. *Proceedings of the 5th International Conference on Environmental Aspects of Bangladesh.* 2014.
31. K. L. Chopra, P. D. Paulson, V. Dutt. *Progress in Photovolatics; Research and Application.* 2012, **12**, 69-92.
32. Tandem cells approaching 30% efficiency. (Date accessed: 14-04-2017) www.pv-magazine.com/2020/01/30/tandems-cells-approaching-30-efficient/
33. L. Hu, D. S. Hetch, G. Grüner. *Chemical Reviews.* 2010, **110**, 5790-5844.
34. L. Fu, A. M. Yu. *Reviews of Advanced Materials.* 2014, **36**, 40-61.
35. A. E. Aliev, J. Oh, M. E. Kozlov, A. A. Kuznetsov, S. Fang, A. F. Fonseca, R. Ovalle, M. D. Lima, M. H. Haque, Y. N. Gartstein, M. Zhang, A. A. Zakhidov, R. H. Baughman. *Science. I209,* **323**, 1575-1578.
36. A. Aguilar-Elguézabal, W. Antúnez, G. Alonso, F. P. Delgado, Espinosa, M. Miki-Yoshida. *Diamond and Related Materials.* 2006, **15**, 1329-1335.
37. Y. S. Li, T. J. Pan, Y, Tang, Q. Yang, A. Hirose. *Diamond and Related Materials.* 2011, **20**, 187-190.

38. G. Gruner. *Journal of Material Chemistry.* 2006, **16**, 3533-3539.
39. P. Liu, Q. Sun, F. Zhu, K. Liu, K. Jiang, L. Liu, Q. Li, S. Fan. *Nano Letters*. 2008, **8**, 647-651.
40. P. Saini, V. Choudhary, B. P. Signh, R. B. Mathur, S. K. Dhawan. *Materials Chemistry and Physics.* 2009, **113**, 919-926.
41. S. S. Xie, B. H. Chang, W. Z. Li, Z. W. Pan, L. F. Sun, J. M. Mao, X. H. Chen, L. X. Qian, W. Y. Zhou. *Advanced Materials.* 1999, **11**, 1135-1136.
42. E. Ramasamy, W. J. Lee, D. Y. Lee, J. S. Song. *Electrochemistry Communications.* 2008, **10**, 1087-1089.
43. A. Schindler, J. Brill, N. Fruehauf, J. P. Novak, Z. Yaniv. *Physica E: Low-dimensional Systems and Nanostructures.* 2007, **37**, 119-123.
44. N. Saran, K. Parikh, D.-S. Suh, E. Muñoz, H. Kolla, S. K. Manohar. *Journal of American Chemical Society.* 2004, **126**, 4462-4463.
45. V. Bliznyuk, S. Singamaneni, R. Kattumenu. *Applied Physics Letters*. 2006, **88**, 164101 (1-3).
46. J. W. Jo, J. W. Jang, J. U. Lee, W. H. Jo. *ACS Nano*. 2010, **4**, 5382-5388.
47. D. Wu, M. Wei, R. Li, S. Gong, Z. Xiao, Z. Zhu, Z. Li. *Composites Part B; Engineering.* 2019, **174**, 107034.
48. Y.-A. Leu, M.-H. Yeh, L-Y. Lin, T.-J. Li, L.-Y. Chang, S.-Y. Shen, Y.-S. Li, G.-L. Chen, W.-H. Chiang, J.-J. Lin. K.-C. Hao. *ACS Sustainable Chemistry and Engineering.* 2017, **5**, 537-546.
49. M. Eslamian, F. Soltani-Kordshuli. *Journal of Coatings Technology and Research.* 2018, **15**, 271-280.
50. N. Alexeyeva, J. Kozlova, V. Sammelselg, P. Ritslaid, H. Mändar, K. Tammeveski. *Applied Surface Science.* 2010, **256**, 3040-3046.
51. L. Tammveski, H. Erikson, A. Sarapuu, J. Kozlova, P. Ritslaid, V. Sammelselg, K. Tammeveski. *Electrochemistry Communications.* 2012, **20**, 15-18.
52. B. Gao, G. Z. Yue, Q. Qui, Y. Cheng, H. Shimoda, L. Fleming, O. Zhou. *Advanced Materials.* 2001, **13**, 1770-1773.
53. A. K. Pal, R. K. Roy, S. K. Mandal, D. Deb. *Thin Solid Films*. 2005, **476**b, 288-294.
54. S. Peng, L. Tian, J. Liang, S. G. Mhaisalkar, S Ramakhrisna, *ACS Applied Materials and Interfaces.* 2012, **4**, 397-404.
55. S. S. Fan, M. G. Chapline, N. R. Franklin, T. W. Tombler, A. M. Cassell, H. J. Dai. *Science*. 1999, **283**, 512-514.

56. M. Hazani, F. Heinrich, M. Kappes, R. Naaman, D. Peled, V. Sidorov, D. Shvarts. *Chemical Physics Letters.* 2004, **391**, 389-392.
57. M. Shimoda, L. Fleming, K. Horton, O. Zhou. *Physica B.* 2002, **323**, 135-136.
58. W. Xue, T. H. Cui. *Nanotechnology*. 2007, **18**, 145709 (1-6).
59. Y. V. Gulyaev, N. I. Sinitsyn, G. V. Torgashov, S. T. Mevlyut, A. I. Zhabanov, Y. F. Zacharchenko, Z. Y. Kosakovskaya, L. A. Chernozatonskii. O. E. Glukhova, I. G. Torgashov. *Journal of Vacuum Science and Technology.* 1997, **15**, 422-424.
60. L. Seeman, A. Stemmer, N. Naujoks. *Nano Letters.* 2007, **7**, 3007-3013.
61. Q. Cao, S. H. Hur, Z. T. Zhu, Y. G. Sun, C. J. Wang, M. A. Meitl, M. Shim, J. A. Rogers. *Advanced Materials.* 2006, **18**, 304-309.
62. H. E. Unalan, G. Fanchini, A. Kanwal, A. Duu Pasquier, M. Chhowalla. *Nano Letters.* 2006, **6**, 677-682.
63. R. N. Das, B. Liu, J. R. Reynolds, A. G. Rinzler. *Nano Letters.* 2009, **9**, 677-683.
64. C. S. Du, N. Pan. *Nanotechnology.* 2006, **17**, 5314-5318.
65. J. Vaillancourt, H. Y. Zhang, P. Vasinajindakaw, H. T. Xia, X. J. Lu, X. L. Han, D. C. Janzen, W. S. Shih, C. S. Jones, M. Stroder, M. Y. H. Chen, H. Subbaraman,R. T. Chen, U. Berger, M. Renn. *Applied Physics Letters.* 2008, **93**, 243301 (1-3).
66. C. F. Zhou, S. Kumar, C. D. Doyle, J. M. Tour. *Chemistry of Materials.* 2005, **17**, 1997-2002.
67. M. Zheng, A. Jagota, E. D. Semke, B. A. Diner, R. S. Mclean, R. S. Lustig, R. E. Richardson, N. G. Tassi. *Nature Materials.* 2003, **2**, 338-342.
68. D. G. P. Arthur, *Patent application*. 2006.
69. K. H. An, W. S. Kim, Y. S. Park, Y. C. Choi, S. M. Lee, D. C. Chung, D. J. Bae, S. C. Lim, Y. H. Lee. *Advanced Materials.* 2001, **13**, 497-500.
70. Q. Cao, J. A. Rogers. *Advanced Materials.* 2009, **21**, 29-53.
71. J. E. Fischer, H. Dai, A. Thess, R. Lee, N. M. Hanjani, D. L. Dehaas, R. E. Smalley. *Physical Reviews B.* 1997, **55**, R4921 (1-4).
72. A. Tselev, M. Woodson, C. Qian, J. Liu. *Nano Letters.* 2008, 152-156.
73. G. Eda, G. Fanchini, A. Kanwal, M. Chhowalla. *Journal of Applied Physics.* 2008, **103**, 093118 (1-7).
74. M. W. Rowell, M. A. Topinka, M. D. Mcgehee, H. J. Prall, G. Dennler, N. S. Saraciftci, L. B. Hu. *Applied Physics Letters.* 2006, **88**, 233506 (1-3).
75. S. U. Lee, W. S. Choi, B. Hong. *Solar Energy Materials and Solar Cells.* 2010, **94**, 680-685.

76. I. Ahmed, J. E. McCarthy, M. Bari, Y. K. Gun'ko. *Solar Energy*. 2014, **102**, 152-161.
77. K. S. Sirvishnu, S. Prasanthkumar, L. Giribabu. *Materials Advances.* 2021, **2**, 1229-1247.
78. Y. Liu, S.-C. You, C.-L. Ho, W.-Y. Wong. *Coordination Chemistry Reviews.* 2018, **375**, 514-557.
79. S. Carli, E. Benazzi, L. Casarin, T. Bernardi, V. Bertolasi, R. Argazzi, S. Caramoria, C. A. Bignozzi. *Physical Chemistry Chemical Physics.* 2016, **18**, 5949-5956.
80. F. Bella, S. Galliano, G. Gerbaldi, G. Viscardi. *Energies.* 2016, **9**, 384 (1-22).
81. H. Tian. L. Sun. *Journal of Materials Chemistry.* 2011, **21**, 10592-10601.
82. T. Li, A. M. Sponkyny. C. She, O. K. Farha, C. A. Mirkin, T. J. Marles. J. T. Hupp. *Journal of the American Chemical Society.* 2010, **132**, 4580-4582.
83. M. Wang, C. Grätzel. *Energy and Environmental Science*. 2012, **5**, 9394-9405.
84. Z. Zhang, P. Chen, T. N. Murakami, S. M. Zakeeruddin, M. Grätzel. *Advanced Functional Materials.* 2008, **18**, 341-346.
85. K. Oyaizu, H. Tabuhira. H. Nishide. *Polymer Journal.* 2015, **47**, 212-219.
86. K. R. Millington. *Encyclopedia of Electrochemical Power Sources.* 2009, 10-21.
87. P. A. Mithari, A. C. Mendhe, B. R. Sankapal, S. R. Patrikar. *Journal of Indian Chemical Society.* 2021, **98**, 100195 (1-8).
88. J. Y. Ahn, J. H. Kim, J. M. Kim, D. Lee, S. H. Kim. *Solar Energy.* 2014, **107**, 660-667.
89. X. Luo, J. Y. Ahn, Y. S. Park, J. M. Kim, H. W. Lee, S. H. Kim. *Solar Energy.* 2017, **150**, 13-19.
90. M. Younas, M. A. Gondal, M. A. Dastageer, K. Harrabi. *Solar Energy.* 2019, **188**, 1178-1188.
91. M. Younas, M. A. Gondal, M. A. Dastageer, U. Baig. *Ceramics International.* 2019, **45**, 936-947.
92. M. Batmunkh, M. J. Biggs, J. G. Shapter. *Nano Micro Small.* 2015, **11**, 2963-2989.
93. L. C. Brennan, M. T. Byrne, M. Bari, Y. K. Gun'ko. *Advanced Energy Materials.* 2011, **1**, 472-485.
94. H. Hanaei, M. K. Assadi, R. Saidur. *Renewable and Sustainable Energy Reviews.* 2016, **59**, 620-635.
95. S. Yun, A. Hagfeldt, T. Ma. *Advanced Materials.* 2014, **26**, 6210-6237.
96. S. Mahalingam, H. Abdullah, A. Manap. *Electrochemica Acta.* 2018, **264**, 275-283.
97. K. Jiang, R. A. Gerhardt. *Journal of Carbon Research.* 2021, **7**, 1-38.
98. J. G. Speight. *Natural Water Remediation Chemistry and Technology.* 2020, 131-163.

99. A. Laaksonen, J. Malila. *Nucleation of Water*. 2022, 31-44.

100. I. M. Hauner, A. Deblais. J. K. Beattie, H. Kellay, D. Bonn. *The Journal of Physical Chemistry Letters.* 2017, **8**, 1599-1603.

101. J. G. Speight. *Natural Water Remediation Chemistry and Technology*. 2020, 53-89.

102. X. Domingo. *A Guide to the Surfactants World.* 1995, Edicions Proa, S.A. Barcelona.

Chapter 9: Conclusion and recommendations.

The trajectory of global energy production and consumption, coupled with the environmental impact of the current dominant modes of energy production necessitates the investigation and development of new energy production technologies. Renewable energy-based technologies, in particular photovoltaic devices have been the driving force for sustainable and clean global energy production. Photovoltaic devices have gone through various forms and stages of development accompanied by incremental improvements in their performance, cost, and environmental footprint. Dye sensitized solar cells (DSSCs) form part of a cohort of devices that could revolutionize energy production from solar energy. The challenges faced in the development of photovoltaic devices and their performance is related to their architecture, and predominantly by the characteristics of the "optoactive" layer and associated materials that are used in the PV device. The investigation and development of these devices is spoilt for choice in the diversity of materials that are available for use. However, the overall performance of the material of choice relies on its synergy with the constituents' layers of the device. Since their identification/discovery, CNTs have been poised to have a profound impact on the different industries, including energy production and storage due to their unique, tunable, and superior properties. Their use in photovoltaic devices is not only informed by their potential, but their versatility too. Photovoltaic devices have multiple components that use different types of material, however, CNTs are quite adaptable for use as different components of a given device. In addition, their versatility can still be expanded through different types of physical and chemical modifications to tune them to a specific application or photovoltaic device.

This work investigated and reported on the synthesis and modification of MWCNTs under different parameters. The catalytic chemical vapor deposition (CCVD) method was utilized in the successful synthesis of pristine and heteroatom doped MWCNTs. In the synthesis of pristine MWCNTs, two reaction parameters were explored: (i) catalyst preparation method (microwave irradiation versus thermal heating), (ii) reaction temperature. Catalyst preparation method was found to have significant impact on the properties of pristine MWCNTs produced. The catalysts prepared from microwave irradiation produced higher yields of pristine MWCNTs compared to those obtained from a catalyst prepared from thermal heating. In addition, longer irradiation times (i.e., larger amount energy used) gave the highest yield of pristine MWCNTs relative to shorter irradiation times. The XRD and Raman analysis of all

three samples revealed that microwave irradiation in catalyst preparation produced MWCNTs with better crystallinity and least amount of density of defects than thermal heating. Shorter irradiation time in catalyst preparation produced MWCNTs with better crystallinity and lower density of defects than longer irradiation times. The most thermally stable pristine MWCNTs were obtained from a catalyst prepared using microwave irradiation, at longer irradiation times. Higher surface area was reported for samples produced from the catalysts prepared by microwave irradiation, with longer irradiation times producing MWCNTs with the highest surface area. This work has highlighted that altering the preparation methods of the catalyst led to the production of pristine MWCNTs with different properties. Additionally, for the highest yields, good crystallinity, high thermal stability, and surface area in pristine MWCNTs, microwave irradiation in catalyst preparation was a more suitable choice than thermal heating. The catalyst prepared from longer microwave irradiation time was used in the investigation of reaction temperature (700, 750 and 800 ℃) to produce pristine MWCNTs. This study illustrated that variation in reaction temperature, using one type of catalyst produces MWCNTs with different properties; the % yield, crystallinity/density of defects, and surface area decreased with an increase in reaction temperature. The highest thermal stability was recorded for the sample prepared at 700℃, followed by 800℃. The higher thermal stability of the sample prepared at 800℃ compared to 750℃ was attributed to the geometric and structural characteristics of MWCNTs (larger diameters, and long-range order in its lattice structure).

The synthesis of pristine MWCNTs was proceeded by the attempted fabrication of heteroatom doped MWCNTs. Tri-isopropyl borate and trimethyl borate were used as boron sources, and the influence of reaction time (15, 30, 60 min), reaction temperature (700, 750, 800℃) and gas flow rates (total flow rate and individual gas flow rates) were investigated. The use of both boron sources had varying influences on the nature of material produced. XPS analysis of both sets of samples revealed that trimethyl borate was successful at producing B-doped MWCNTs at 15- (0.31%) and 60-min (0.99%) reaction times, while tri-isopropyl borate failed under all attempts undertaken. As the reaction time increased, the % yield and surface area decreased when both sources were used. When tri-isopropyl borate was used, greater yields were obtained, but higher surface areas were reported when trimethyl borate was used. A general increase in density of defects were reported with an increase in reaction time when both sources were used, with 60 min and 30 min reporting the lowest crystallinity when trimethyl borate (I_D/I_G = 2.22) and tri-isopropyl borate (I_D/I_G = 2.01) were used, respectively. Both boron sources produced the most thermally stable material at a reaction time of 30 min. Significant

thermal stability differences in the samples were observed in the use of trimethyl borate than tri-isopropyl borate.

In the temperature dependent study, reaction temperature is a significant parameter in the production of boron doped MWCNTs. XPS analysis revealed that tri-isopropyl borate was successful at producing B-doped MWCNTs at lower temperatures of 700℃ (0.39%) and 750℃ (0.29%), while trimethyl borate was only successful at 800℃ (0.99%). When tri-isopropyl borate was used, the % yield was inversely proportional to reaction temperature, with 700℃ producing the highest yield. The use of trimethyl borate produced the highest yield at 750℃. A general decrease in crystallinity and density of defects with reaction temperature was observed when tri-isopropyl borate was used, while the use trimethyl borate gave samples that had an inverse relation to reaction temperature. The thermal stability of both sets of samples was inversely related to reaction temperature. The best thermal stability was reported for products made at reaction temperatures 700℃ and 750℃ for tri-isopropyl borate and trimethyl borate derived samples, respectively. All B-doped material prepared at 750℃ and 800℃ had better thermal stability than their corresponding pristine MWCNTs. Samples prepared at 700℃ recorded the highest surface area for both sets of samples. The surface area of both sets of samples was inversely correlated to reaction temperature, with each sample reporting larger surface area than their corresponding pristine MWCNTs.

The influence of gas flow rates on the production MWCNTs was investigated in two ways; keeping the total flow rate constant and varying the total flow rate. It was found that varying the individual flow rates of the carbon source and carrier gases, while keeping the total flow rate constant led to no significant differences in % yield. Lower flow rates of the carbon source (90 sccm) and higher flow rates of the carrier gas (260 sccm) gave MWCNTs with the highest crystallinity. When the total flow rate was not kept constant, an increase in % yield was observed from 270 sccm to 370 sccm. XRD and Raman analysis reported a general increase in crystallinity with total flow rate. The thermal stability trend was consistent with XRD and Raman determinations of crystallinity, with the lowest total flow rate reporting the highest thermal stability. The surface area of the obtained samples was inversely correlated with the total flow rate.

The effects of incorporating boron and nitrogen to the same lattice structure of MWCNTs was investigated. A two-step process was used in the attempted synthesis of boron-nitrogen co-doped MWCNTs; (i) synthesis of nitrogen doped MWCNTs, followed by the addition of boron,

The addition of boron (0.79%) using tri-isopropyl borate to the lattice structure of nitrogen doped MWCNTs was followed by a decrease in crystallinity, surface area, and an increase in thermal stability of the resulting material. (ii) synthesis of boron doped MWCNTs, followed by the addition of nitrogen. The addition of nitrogen to the lattice structure of boron doped MWCNTs derived from tri-isopropyl borate not only led to the loss of boron, but a decrease in thermal stability and surface area in the resulting sample. However, a decrease in crystallinity was observed when nitrogen was added to the lattice structure. Trimethyl borate failed to add boron to the lattice structure at 750℃, the resulting sample led to the addition of higher concentration (2.47%) of nitrogen than the direct synthetic method for nitrogen doped MWCNTs (0.97%). The addition of nitrogen to the structure of this material resulted in a decrease in crystallinity, temperature, and surface area.

All three studies revealed that the CVD method was successfully used in the production of pristine and heteroatom doped MWCNTs. However, it was predominantly unsuccessful in the production of boron doped MWCNTs, and it was found that the boron sources predominantly modified the surface of the material and modulate the amount of nitrogen and oxygen.

Attempts were made to add phosphorus to the lattice structure of MWCNTs using a post doping and method. Post doping pristine MWCNTs with a solution of triphenyl phosphine in toluene produced material with 0.07% of phosphorus in the lattice structure, lower crystallinity, and thermal stability compared to when solid (i.e., not in solution) triphenyl phosphine was used. Additionally, it reported a considerable difference in crystallinity and thermal stability relative to pristine MWCNTs. The use of solid triphenyl phosphine resulted in samples with comparable thermal stability to pristine MWCNTs, but higher surface area and lower crystallinity, with one of the samples recording 0.29% of phosphorus in the lattice structure.

Due to their high aspect ratio (i.e., length to diameter ratio), the solubilization or dispersion of MWCNTs is a non-trivial process. Various methods of functionalization and use of dispersive agents have been investigated to aid this process. The influence of different solvents (ethanol, toluene, ethyl acetate, water, hexane, and dichloromethane) at different volumes and surfactants (sodium dodecyl sulphate and dodecyl benzenesulfonic acid) at different concentrations on the dispersion of pristine MWCNTs was investigated. Water and ethyl acetate reported the highest dispersive ability, while hexane and ethanol reported the lowest dispersive ability, respectively. The use of SDS in ethyl acetate was found to be a superior aid in the dispersion of MWNCTs than DBSA in ethyl acetate at 4 different concentrations of each

surfactant. The aiding ability of DBSA in water was found to be higher than when used in ethyl acetate and it was directly correlated to the concentration of DBSA used. The increase of SDS concentration in water was detrimental to the dispersion of MWCNTs. However, the lowest concentration of SDS (4 mg) reported better dispersive ability than the highest concentration of DBSA (25 mg) in water. A mixture of both surfactants at different concentrations in water reported the highest dispersibility relative to when it was used in ethyl acetate. Assuming the Fermi-golden rules of the electron transition for a direct and indirect electron transition, the band gap of the dispersions was evaluated using the Tauc plot. Hexane contained MWCNTs with the highest estimated band gap energy of all the dispersions. The use of SDS in both water and ethyl acetate contained MWCNTs with the same estimated band gap energy (2.74-2.76). The variations in the band gap energies suggest that the average tubal diameter is a major factor in the dispersion of MWCNTs in different solvents. Additionally, the MWCNTs dispersed in water and ethyl acetate had the largest average diameter in the samples. DCM and toluene dispersions reported larger band gap energies (3.20-3.70), and consequently had affinity for smaller average diameter MWCNTs in the sample. The use of surfactants to aid in the dispersion also demonstrated a similar dependence to diameter of the nanotubes. The use of SDS and DBSA, and combination thereof, led to the suspension of MWCNTs of the same larger average diameter MWCNTs in the sample. The dispersion study revealed that in a sample containing MWCNTs with different diameters could be separated by using different solvents and surfactants.

Pristine and heteroatom doped MWCNTs thin films were prepared using a drop casting method, their electrochemical properties were evaluated to determine their potential as replacements of Pt as a counter electrode in the reduction of the iodide-tri-iodide electrolyte. Similar to Pt, all fabricated thin films reported two reduction peaks that occurred at more negative potential than those of Pt. Pt recorded a current density of -1.27 mA/cm^2, and only three thin films; material with a boron (0.31%) and nitrogen (2.47%) reported higher current densities of 1.42 mA/cm^2 and 1.47 mA/cm^2, respectively. It was established that the presence of boron did not translate into a high electrocatalytic performance, as evidenced by the poor performance of BP700-*I* (-0.62 mA/cm^2), BP750-*i* (-0.45 mA/cm^2), and BP800-*m* (-0.35 mA/cm^2) thin films with boron concentrations of 0.39%, 0.29%, and 0.99%, respectively. Furthermore, the performance of BP800-30-*m* (-1.47 mA/cm^2) was superior to that of Pt, and it had no boron reported in its lattice structure but a high concentration of oxygen (14%). Although most of the MWCNTs thin films had poorer electrocatalytic activity than Pt, they all

had a higher performance than the pristine MWCNTs thin films. This indicated that addition of these heteroatoms (O, N, B, P) and the method used to add them determines their electrochemical performance.

9.1. Recommendations and future work.

Pristine MWCNTs and heteroatom doped MWCNTs were successfully synthesized. In the synthesis of heteroatom doped MWCNTs other boron sources should be explored in order to increase the concentration of boron. The dispersion study identified the development of a method that would allow for the separation of nanotubes according to their diameter. This method can be refined and expanded using chromatography. The method will involve (i) performing thin layer chromatography to determine the retardation factor (R_f) using different solvents, (ii) followed by column chromatography using silica gel.

Although a fabrication of MWCNTs thin films was achieved, future work will involve the exploration of additional methods to make the films such as dip coating and spray pyrolysis. Additionally, comprehensive surface area studies using instruments such as the atomic force microscopy (AFM) to evaluate the smoothness of the films and how that impacts their electrochemical performance will also be investigated. The MWCNTs thin films that reported superior electrochemical performance will be used in the fabrication of DSSCs. However, given that the overall performance of the devices is also reliant on the synergy that exists between the different components of both devices, thin films that reported poor performance should not be discarded. They will be used in a broad study that attempts to match them with components of the device that may contribute to improving their performance in the device.